Empirical Cross-Calibration of XMM-Newton's EPIC Effective Areas
and
Search for a Compact Object Associated with the SNR G96.0+2.0

Dissertation
der Mathematisch-Naturwissenschaftlichen Fakultät
der Eberhard Karls Universität Tübingen
zur Erlangung des Grades eines
Doktors der Naturwissenschaften
(Dr. rer. nat.)

vorgelegt von

Cornelia Bettina Heinitz

aus Weingarten

Tübingen
2021

Gedruckt mit Genehmigung der Mathematisch-Naturwissenschaftlichen Fakultät
der Eberhard Karls Universität Tübingen.

Tag der mündlichen Qualifikation:	22.10.2021
Dekan:	Prof. Dr. Thilo Stehle
1. Berichterstatter:	Prof. Dott. Andrea Santangelo
2. Berichterstatter:	Prof. Dr. Klaus Werner

"That sky above me looks as though it could not change, and yet it will."

(Elizabeth Gaskell – *North and South*)

Abstract

The X-ray satellite XMM-Newton, also called the X-ray Multi Mirror Mission, is a highly successful mission of the European Space Agency (ESA). It was launched in 1999 and is expected to continue to provide high sensitivity observations in the soft to mid-energy X-ray range for several more years to come. This thesis is dedicated to two XMM-related topics.

Three X-ray cameras on board the satellite together constitute XMM-Newton's European Photon Imaging Camera (EPIC). Differences between the fluxes measured with the individual cameras indicated a discrepancy in their effective area calibration, which sets a limit to the quality that the scientific analysis of XMM data can have. Until now, a reliable correction of the effective area calibration to reconcile the three EPIC cameras is missing. The first part of this thesis is concerned with the further development of the CORRAREA tool included in the standard data reduction and analysis software for XMM-Newton, pursuing the aim of making it fit to serve as a default correction for the EPIC on-axis effective area calibration in the future. CORRAREA applies an energy-dependent, multiplicative correction factor to the data, based on correction functions determined by empirical cross-calibration of the EPIC cameras with the stacked residual ratio method. The underlying procedure was revised and extended in the scope of this work to suit the purpose of a default correction tool. A script package was developed to largely automate the necessary steps for validation purposes and future updates. From the hundreds of thousands of source detections in the XMM database, 163 sources were identified as being suitable to be included in the analysis to determine the required correction functions. The dependence of the results on different factors was investigated for validation, revealing that the combination of different XMM science modes requires an adjustment of the originally applied stacking method. New correction functions were determined for an updated, recalibrated non-default application. It was successfully shown that the procedure performed with the developed scripts can, in addition, be used for an independent validation of other calibration works. The presented routine also offers the potential to be extended to involve a cross-calibration with instruments on other X-ray observatories in the future.

In the second part of this thesis, the first search for a compact object associated with the Galactic supernova remnant (SNR) G96.0+2.0, using an XMM-Newton observation, is presented. Compact objects are astronomical objects with very high densities and include neutron stars (NSs), which are prominent X-ray sources. NSs are the most dense objects that can be directly observed and are, thus, extremely interesting for the study of superdense matter. An identified SNR-NS-pair can provide information about each of the two objects that would otherwise be inaccessible. A special focus was set on searching for one particular kind of compact object, a so-called central compact object (CCO), which is an isolated, purely thermally emitting NS located in the centre of a SNR. Because CCOs offer an undisturbed view onto their surface, they

are considered ideal targets to obtain constraints on NS parameters and the properties of their superdense matter. Both, identifying SNR-NS-pairs and increasing the small number of known CCOs, are an important contribution to the study of NSs and of the fundamental physics concerning superdense matter. A source detection was carried out for each image in the XMM observation of G96.0+2.0 and 22 X-ray point sources were identified. A possible NS nature of the individual sources was investigated by conducting a cross-match with optical catalogues to search for potential counterparts, by performing a spectral and timing analysis for each source and by analysing their X-ray-to-optical flux ratios as well as their positions in a hardness ratio diagram. The results led to the exclusion of the possibility of the SNR having an associated CCO. In addition, 17 of the identified X-ray point sources could be dismissed as potential candidates for any type of associated NS altogether. Of the remaining sources, one was found to be a particularly promising candidate for a potentially associated NS, with all characteristics being consistent with a NS nature.

Zusammenfassung

Der Röntgensatellit XMM-Newton (die *X-ray Multi Mirror Mission*) ist eine äußerst erfolgreiche Mission der Europäischen Weltraumorganisation ESA. Der Start der Mission erfolgte 1999 und es wird erwartet, dass der hochempfindliche Satellit noch über mehrere Jahre hinweg Beobachtungen im weichen bis mittleren Röntgenbereich liefert. Diese Arbeit widmet sich zwei Themen im Zusammenhang mit XMM-Newton.

Drei Röntgenkameras an Bord des Satelliten bilden gemeinsam die *European Photon Imaging Camera* (EPIC). Abweichungen zwischen den mit den einzelnen Kameras gemessenen Flüssen ließen eine Diskrepanz in der Kalibrierung ihrer effektiven Flächen erkennen, durch welche die Qualität, welche bei der wissenschaftlichen Analyse von XMM-Daten erreicht werden kann, eingeschränkt wird. Bisher fehlt eine verlässliche Korrektur der Kalibrierung der effektiven Flächen, um die drei EPIC-Kameras aufeinander abzustimmen. Der erste Teil dieser Arbeit beschäftigt sich mit der Weiterentwicklung des Corrarea Tools, welches in der Standardsoftware für die Reduktion und Analyse von XMM-Daten enthalten ist, um dem Ziel näher zu kommen, es zukünftig als Standardkorrektur für die Kalibrierung der effektiven Flächen auf den optischen Achsen der drei EPIC-Kameras anwenden zu können. Corrarea wendet einen energieabhängigen, multiplikativen Korrekturfaktor auf die Daten an, welcher auf Korrekturfunktionen basiert, die durch empirische Kreuzkalibrierung der EPIC-Kameras anhand der *stacked residual ratio* Methode bestimmt werden. Die zugrundeliegende Verfahrensweise wurde im Rahmen dieser Arbeit überarbeitet und erweitert, um dem Anspruch einer Standardkorrektur gerecht zu werden. Ein Skriptpaket wurde entwickelt, um die nötigen Schritte zu Validierungszwecken und für künftige Aktualisierungen weitgehend zu automatisieren. Aus den hunderttausenden detektierten Quellen im XMM-Datenbestand wurden 163 Quellen ermittelt, welche für die Analyse zur Ermittlung der benötigten Korrekturfunktionen als geeignet erachtet werden. Die Abhängigkeit der Ergebnisse von verschiedenen Faktoren wurde zur Validierung untersucht, wobei aufgezeigt wurde, dass die Kombination verschiedener Beobachtungsmodi eine Anpassung des ursprünglich angewandten *stacking* Verfahrens notwendig macht. Neue, aktualisierte und rekalibrierte Korrekturfunktionen für die nicht standardmäßige Anwendung wurden bestimmt. Es konnte gezeigt werden, dass das mit den entwickelten Skripten angewandte Verfahren zusätzlich für eine unabhängige Validierung anderer Kalibrierungsarbeiten verwendet werden kann. Der vorgestellte Programmablauf bietet zudem die Möglichkeit, erweitert zu werden, um in Zukunft eine Kreuzkalibrierung mit Instrumenten anderer Röntgenobservatorien mit einzuschließen.

Im zweiten Teil dieser Arbeit wird die erste Suche nach einem kompakten Objekt, welches mit dem galaktischen Supernovaüberrest G96.0+2.0 assoziiert werden kann, vorgestellt. Hierfür wurde eine zu diesem Zweck mit XMM-Newton durchgeführte Beobachtung verwendet. Kompakte Objekte sind astronomische Objekte mit sehr hohen Dichten. Hierzu gehören Neutronensterne, die bekannte Röntgenquellen

sind und die größte Dichte aller Objekte, die direkt beobachtet werden können, haben. Sie sind deshalb äußerst interessant, um extrem dichte Materie zu untersuchen. Ein identifiziertes Paar aus Supernovaüberrest und dem dazugehörigen Neutronenstern kann Informationen über jedes der beiden Objekte liefern, die ansonsten nicht zugänglich wären. Ein besonderer Schwerpunkt wurde auf die Suche nach einer bestimmten Art von kompaktem Objekt gelegt, einem sogenannten *central compact object* (CCO). Dabei handelt es sich um einen isolierten Neutronenstern mit rein thermischer Strahlung, der sich im Zentrum eines Supernovaüberrestes befindet. Da CCOs einen ungestörten Blick auf ihre Oberfläche ermöglichen, stellen sie ideale Beobachtungsobjekte dar, um Parameter von Neutronensternen und die Eigenschaften ihrer extrem dichten Materie einzugrenzen. Sowohl das Auffinden von Supernovaüberrest-Neutronenstern-Paaren als auch die Erweiterung der kleinen Gruppe bekannter CCOs stellen einen wichtigen Beitrag zur Untersuchung von Neutronensternen und der grundlegenden Physik extrem dichter Materie dar. Für jedes Bild der XMM-Beobachtung von G96.0+2.0 wurde eine Suche nach Quellen durchgeführt und 22 Röntgen-Punktquellen wurden identifiziert. Um einen möglichen Neutronenstern unter den Quellen zu ermitteln, wurde eine Kreuzkorrellation mit optischen Katalogen und eine Spektral- und Zeitanalyse für jede Quelle durchgeführt sowie das Verhältnis von Röntgenfluss zu optischem Fluss und die Lage der Quellen in einem Härtegraddiagramm analysiert. Die Ergebnisse zeigen, dass das Vorhandensein eines zum Supernovaüberrest gehörenden CCO unwahrscheinlich ist. Zudem konnten 17 der identifizierten Punktquellen insgesamt als potenzielle Kandidaten für einen Neutronenstern, der mit dem Supernovaüberrest assoziiert werden kann, ausgeschlossen werden. Unter den verbleibenden Quellen konnte ein Kandidat ermittelt werden, der für einen potenziell zum Supernovaüberrest gehörenden Neutronenstern besonders vielversprechend ist, da alle festgestellten Charakteristiken mit einem Neutronenstern vereinbar sind.

Contents

List of Figures

List of Tables

CHAPTER 1

Introduction

Since its beginnings in the 50's and early 60's of the last century, X-ray astronomy has developed rapidly and has continuously gained in importance. Its relevance in modern science has been acknowledged, in particular, almost 20 years ago, in 2002, when Riccardo Giacconi, who was a driving force behind the early detections of cosmic X-ray sources and also the necessary technological developments, received the Nobel Prize in physics for his pioneering work.[1] Nowadays, X-ray astronomy constitutes an established astronomical sub-discipline and contributes to research on many topics and to the understanding of fundamental physics, including the structure and evolution of the Universe, accretion physics and matter under extreme conditions (like temperatures of more than a million degrees, the strongest magnetic fields known and the exceptional densities and gravitational fields that neutron stars and black holes can have).

XMM-Newton, the X-ray Multi-Mirror Mission launched in 1999, is one of the current leading missions in X-ray astronomy and operates in the energy range from 0.1 keV to 15 keV. With its combined imaging capabilities, high spectral resolution and unprecedented collecting area, it has since then contributed significantly to the enhancement of knowledge in high-energy astrophysics (Güdel, 2009; Santos-Lleo et al., 2009; Schartel et al., 2017) and is expected to continue to do so for several more years to come. In this work, two XMM-related topics are addressed. The first one concerns the improvement of the on-axis effective area calibration of XMM's three X-ray cameras. The effective areas basically describe the cameras' ability to actually detect incoming photons at different energies. This part of the thesis particularly deals with instrumental aspects. The second topic, concerning the search for a compact object associated with the supernova remnant (SNR) G96.0+2.0 using an XMM observation, has a stronger astrophysical focus.

To give the reader an idea of the state of the art and the value of current missions like XMM-Newton, Chapter 2.1 contains a short overview of the history of observational X-ray astronomy (limited to the energy range relevant here) with a focus on technological developments. In this context, also an introduction to the basic working principles of the main instrumentation is provided. Understanding these and keeping the properties of the instruments in mind is always advisable when analysing and interpreting observational data but is absolutely essential when working on the calibration[2] of the instruments as done in this work.

In Chapter 2.2 some basic information on the astrophysical background underlying the processing and analysis of the data is given. First, this involves the main processes

[1] shared with Raymond Davis Jr. and Masatoshi Koshiba, who discovered cosmic neutrinos (`https://www.nobelprize.org/prizes/physics/2002/summary/`)

[2] which involves analysing the instruments' properties and correcting the data accordingly

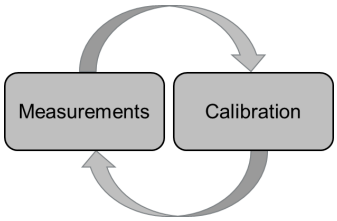

Figure 1.1: Interdependence between measurements and calibration.

which can generate X-rays in astronomical objects. To understand them is fundamental to the interpretation of a source's observed properties, concerning, for example, spectral and timing features. Typical models and methods for the analysis are based on these processes and can also only be understood and reasonably applied if the theoretical background is known. The second part of the chapter contains some general remarks on source types relevant in this thesis, including not only astronomical target sources but also background components.

1.1 The Importance of Calibration

The calibration work done in the scope of this work is presented in Chapter 3. Calibration is an important task to supply scientific users with reliable data. The properties of the instruments and their interaction with incoming photons affect the data. These instrumental features need to be understood to correct for them and extract the undistorted scientific data for an astronomical source. A sufficient reliability of the scientific analysis and outcome, thus, requires a high-quality calibration of the instruments used to obtain the data. And particularly when a source's observation has a high signal-to-noise ratio and consequently small statistical errors, the systematic calibration uncertainties may be the defining, limiting factor for the overall precision of the data.

One might wonder why calibration is still necessary once a satellite is in space, especially when it has already been operated for over 20 years as in the case of XMM-Newton. First of all, given the development and construction schedule of a mission, ground-based calibration always has a rather strict time limit. Advanced calibration tasks are, thus, usually postponed to the in-orbit phase. Also, the actual in-orbit performance of the instruments can, of course, only be analysed after launch. But calibration also has to be adjusted over time. Both because the instrument performance is subject to change and because of an improved understanding of the instruments (Arnaud et al., 2011), which are usually developed for a particular satellite mission so that at first there are no empirical values to draw on. In addition, as illustrated in Figure 1.1, calibration is determined by measurements, which, however, are based on the calibration. And there are several different calibration issues which are correlated so that changing the calibration concerning one of them might make a recalibration at some other point necessary. All in all, calibration is never fully finished but is a continuous process which always leaves room for improvement.

To prevent an over- or misinterpretation of scientific data, the included calibration uncertainties should always be taken into account in the analysis. In the case of XMM-Newton, these uncertainties even lead to obvious discrepancies between astrophysical parameters obtained with the three X-ray cameras on board (Guainazzi et al., 2014),

which, combined, make up the European Photon Imaging Camera (EPIC). Details on the satellite and its instruments are given in Chapter 3.2. For almost the entire energy range, the dominating factor in XMM's calibration uncertainties is the effective area. Since no tool had been available to scientific users to get an estimate of the effective area calibration uncertainties, Guainazzi et al. (2014), together with Read et al. (2014), introduced CORRAREA (described in detail in Chapter 3.3) to provide such an option for sources located at the on-axis positions of the cameras. So far, however, CORRAREA could only be used for estimation purposes and has not been considered fully validated. It is now a priority issue of the calibration team at the *European Space Astronomy Centre* (ESAC) to develop CORRAREA further so that it can be used as a default correction instead of an estimation tool to increase the reliability of the data. The first part of this thesis concerns this task, which involved a recalibration with a revised procedure and the newest calibration status, different analyses for validation as well as the automation of various steps for validation and future update purposes.

1.2 Isolated Neutron Stars as Unique Laboratories

Chapter 4 is dedicated to the astrophysical analysis of X-ray point sources. One type of these sources are neutron stars (NSs). They have played an important part in X-ray astronomy since its beginnings, with the first extrasolar X-ray source discovered (Scorpius X-1) having been identified as an accreting binary with a NS primary. Throughout, NSs have proved to be very fascinating objects, showing some very interesting and extreme properties and phenomena. One is that NSs have the highest densities of any directly observable object, with almost $10^{15}\,\mathrm{g\,cm^{-3}}$ reached in their cores, which is higher than the density of atomic nuclei. Since these conditions cannot be reproduced in a laboratory frame on Earth, the nature of matter at such densities and the density-pressure-relation, defined by its equation of state, are unknown.

One class of NSs particularly suitable to study these objects and the equation of state of superdense matter are the so-called central compact objects (CCOs). They are a type of isolated NSs which, by definition, can always be associated with a SNR and which are considered to provide a unique, undisturbed view onto the thermally emitting NS surface without the dominant radiation caused by accretion and strong magnetic fields as in the case of other NS classes (Klochkov et al., 2015). With the aim of increasing the still small number of CCOs known, the Galactic SNR G96.0+2.0 was observed with XMM-Newton in 2017 because with its properties like age and type the SNR offered a good chance for finding such a NS. But also the prospect of finding any kind of compact object which might be associated with G96.0+2.0 supported the potential scientific value of the observation since, generally, any such association provides information exceeding the one obtained from separate objects.

With this in mind, the data analysis and interpretation for the point sources in the aforementioned observation were performed in the context of this work. Based on the conducted search for optical counterparts, the spectral and timing analysis as well as an analysis of the X-ray-to-optical flux ratios and hardness ratios, the number of potential candidates could be significantly reduced, leading to the identification of one source that particularly stands out as a NS candidate that might be associated with the SNR.

The overall results of both topics covered in this thesis are summarized and concluded with the future outlook in Chapter 5.

CHAPTER 2

The Sky in X-rays

2.1 Observational X-ray Astronomy

Especially when compared with the long tradition of observing the sky in the optical, X-ray astronomy, which deals with photon energies between 0.1 keV and a few 100 keV, is a relatively young field of science. The reason is not simply that X-rays are not visible to our naked eyes, but they cannot be observed from Earth's surface due to absorption in the atmosphere. In the energy range this work is concerned with, namely soft to mid-energy X-rays with energies below 15 keV, rockets and satellites need to be used in order to be able to detect the photons.[3]

First steps into observational X-ray astronomy were taken in the late 1940s, when rockets originally developed in the course of World War II were available. In 1949, Friedman et al. (1951) successfully detected solar X-rays for the first time using one of these rockets, equipped with radiation detectors. However, at the time, their findings rather led to a loss of interest in the search for other astronomical X-ray sources amongst scientists, since many did not believe that more distant sources could be sufficiently bright in X-rays to be observable from Earth (Seward & Charles, 2010). Assuming extrasolar sources to have about the same intensity in X-rays as the Sun, these sources would have been too faint by three orders of magnitudes to be detectable with the instrumentation available at the time (Santangelo & Madonia, 2014).

Things changed when, in 1962, Giacconi et al. (1962) tried to find X-ray emission from the moon[4] but instead made the first discovery of an extrasolar X-ray source, which was later identified as Scorpius X-1 (Giacconi et al., 1964). Back then, the typical detector used for the experiments was a Geiger counter, which they had mounted on an Aerobee high-altitude research rocket. Geiger counters have a tube-shaped chamber filled with a noble gas and a central wire along its longitudinal axis. A high voltage is applied with the wire serving as the anode and the tube itself or a conducting coating on its inside wall being the cathode. X-ray radiation can pass through an entrance window and ionizes the gas, creating ions and free electrons. While the ions move towards the cathode, the electrons are accelerated towards the anode and, due to the high electric field, they release additional electrons when colliding with the gas molecules, which amplifies the signal. The signal is registered in the end due to the voltage which is generated when the electrons pass through a connected resistor. With this type of

[3] Also balloon flights played an important part in the early days of X-ray astronomy (and are still conducted sometimes these days). However, due to the lower altitude at which they can be operated, X-ray studies conducted with balloons are limited to hard X-rays and, thus, they are not discussed further at this point.

[4] expected in the form of fluorescence of lunar material after being excited by solar X-rays

detector, the early experiments provided information on the occurrence and the time of an event, but no information on the energy of the incident X-ray photon was gained (Seward & Charles, 2010).

Another limitation was given due to the use of rockets: not only is soft X-ray radiation still affected by absorption to a considerable degree at the rockets' flight altitude, but, from today's point of view, they also only allowed for rather short observations times of a few minutes (Staubert & Trümper, 2008). Satellites, equipped with further developed technologies, offered solutions to these problems and led to a big progress in observational X-ray astronomy - justifying the much higher costs of these missions. It would be beyond the scope of this work to list all satellite missions carrying X-ray detectors. An overview of the main missions can be found in e.g. Santangelo & Madonia (2014) and Seward & Charles (2010). Here, the developmental stages which can be considered the major steps towards modern imaging telescopes for soft to mid-energy X-rays shall be focussed on.[5]

The first satellite dedicated to X-ray astronomy was Uhuru (Jagoda et al., 1972), sent into space by NASA in 1970 and operating in the 2–20 keV range. For this mission, collimated gas proportional counters were used as X-ray detector systems. Proportional counters are quite similar to Geiger counters, but the applied voltage, which separates ions and free electrons and accelerates the electrons towards the anode, is substantially lower. Fewer electrons are released by collisions of electrons and gas molecules so that the overall increase in free electrons is smaller. As a result, the number of free electrons is proportional to the energy of the incident photon, providing spectral information. For large proportional counters providing a large collecting area, the counter was divided into individual cells (using a cathode grid) with each cell having its own anode wire (Pfeffermann, 2008). A collimator, which basically consists of adjacent round or comb-shaped tubes, was mounted in front of the detector and ensured an almost parallel incidence of X-rays, thus limiting the field of view (FOV) and making a rough location determination possible. These non-focussing optics allowed for a spatial resolution of about 0.5° (Giacconi, 2003) – a value that could be significantly improved with the invention of focussing X-ray optics.

The difficulty with trying to focus X-rays is that they easily penetrate into mirrors and are absorbed when the angle of incidence is too large. A solution was found in using grazing incidence optics as originally suggested for X-ray microscopy by Wolter (1952) and adapted for X-ray astronomy by Giacconi et al. (1969) in the form of mirror tubes pointing towards the radiation's direction of arrival. The basic principle of the mirror design of the now commonly used, so-called Wolter type I telescopes is illustrated in Figure 2.1. Since quite small incidence angles are necessary to reflect X-rays, the focal length resulting from a single reflection is rather large. By combining a parabolic shape and a hyperbolic shape for the mirror design, X-rays are reflected twice, and the focal length is decreased (typically to values around 10 m and below), which is an important matter for telescope construction. The critical incidence angle θ_c below which total

[5] For a more thorough explanation of the different instrumentation technologies, including those used for observing hard X-rays, see for example Trümper & Hasinger (2008).

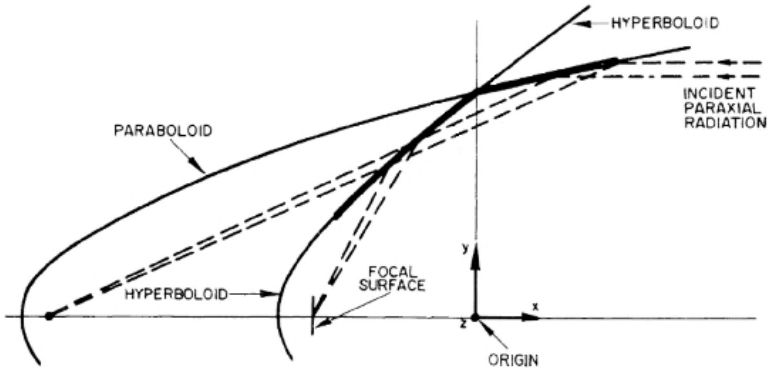

Figure 2.1: Schematic illustration of the Wolter type I grazing incidence mirror design. The mirrors (bold line) are composed of a parabolically-curved front part and a hyperbolically-curved back part. Due to this setup, the incident X-ray radiation is reflected twice and the focal length is reduced considerably. (Giacconi et al., 1969, modified)

reflection of X-rays on the mirror surface occurs depends on the energy E of the X-ray photons and the atomic number Z of the reflecting material (Schwartz, 2011):

$$\theta_\mathrm{c} \propto \frac{\sqrt{Z}}{E}\,. \tag{2.1}$$

Thus, the mirrors are coated with a material that has a high atomic number and provides large critical angles over the whole soft to mid-energy X-ray range, e.g. gold or iridium, to be able to collect a large amount of X-ray photons. To increase the collecting area further, several mirror tubes of different sizes can be nested concentrically into each other.

With this technology on board, the first focussing X-ray satellite, Einstein (Giacconi et al., 1979), was launched in 1978. It observed in the soft 0.1–4 keV range, for which nickel was used as a mirror coating back then. Since now the determining factor for the collecting capability of the telescopes were the mirrors, instead of the sensor area, smaller and position sensitive detectors could be used for observatories. One of Einstein's detectors was an imaging proportional counter, for which the anodes, still used for measuring the event energy, are combined with two layers of cathodes. The cathode wires of the two layers are oriented orthogonally with respect to each other so that the signal generated by the ions gives the position of the event (Pfeffermann, 2008). For Einstein observations conducted with this detector, a spatial resolution of $1'$ was achieved.

During the same decade, also gas scintillation proportional counters were developed (Policarpo et al., 1972; Pfeffermann, 2008).[6] But these detectors were used predominantly on missions focussing on mid-energy to hard X-rays.[7] Amongst Einstein's instruments, however, were two other types of detectors whose development played a

[6] In contrast to the proportional counters already presented, gas scintillation proportional counters are operated with a lower electrical field so that the electrons created in the gas by absorption of X-rays do not cause an electron avalanche but only excite atoms in a scintillation region of the detector. The emission when the atoms de-excite is then amplified and measured using a photomultiplier.

[7] e.g. BeppoSAX with an energy range of 4–120 keV and EXOSAT with 2–40 keV (Pfeffermann, 2008)

crucial role with respect to the detectors used in soft to mid-energy X-ray astronomy today: a microchannel plate detector and a solid state spectrometer.

Microchannel plates typically consist of thousands to millions of microscopic tubes within which electrons liberated by incident X-rays cause an electron avalanche by hitting the tube walls and generating more free electrons when moving down the tube towards the anode, where the signal is read out. The design of this detector type allows for an unparalleled spatial resolution. In the case of Einstein, the same spatial resolution as given by the focussing mirrors, about $5''$ (on the optical axis), was achieved with the microchannel plate detector (Seward & Charles, 2010). Today, a microchannel plate detector is mounted on board Chandra (the current soft to mid-energy X-ray mission of the *National Aeronautics and Space Administration*, NASA, operating in the 0.08–10 keV range; Weisskopf et al., 2002), leading to an unprecedented spatial resolution of $\sim 0.5''$. But because of the high amplification of the signal in microchannel plates, these types of detectors are not the first choice when it comes to achieving a high energy resolution for spectral analysis.

Rather, a high energy resolution is one of the advantages when using solid state detectors, which are made of a doped semiconductor, usually silicon. X-rays excite electrons in the semiconducting material from the valence band to the conduction band due to the internal photoelectric effect. Because of the solid material and a low voltage being applied, no electron avalanche is created; but the X-rays themselves create more electron-hole-pairs in the solid detector than they create electron-ion-pairs in gas, resulting in the Einstein solid state detector having a spectral resolution about three times better than Einstein's proportional counter (Seward & Charles, 2010). Today, technology has further advanced and solid state detectors can be considered the predecessors of the now widely used charge-coupled devices (CCDs).

The first X-ray satellite equipped with CCDs was the Advanced Satellite for Cosmology and Astrophysics (ASCA, Tanaka et al., 1994), which was launched in 1993 (Arnaud et al., 2011). CCDs consist of a doped semiconductor bulk which is divided into thousands of microscopic pixels by electrodes attached on top (for a more detailed description see, for example, Strüder & Meidinger, 2008, and Grant, 2011). In principle, each pixel works like a solid state detector but with a common readout anode for each pixel row. Usually a pixel has three electrodes, for which the applied voltage can be regulated. Depending on the detector design, CCDs can either be front-illuminated (with the X-rays entering the semiconductor bulk through the X-ray-transparent electrodes) or back-illuminated (which leads to a higher sensitivity but also to a more complicated and more expensive production process). To collect the electrons liberated when X-rays are absorbed in the semiconductor material, potential wells are created in the semiconductor by applying a higher voltage to the central electrode of each pixel.[8] The additional electrodes are needed to shift the collected charges from pixel to pixel within each row towards the readout anode by adjusting the applied voltage.

To excite an electron from the valence band to the conduction band, the energy of an incoming photon needs to meet a material-specific minimum energy.[9] An X-ray photon usually excites a large number of electrons, with the total number being directly

[8] The free electrons resulting from a single X-ray event are not necessarily all collected in a single pixel but can spread to two or more pixels, creating an event pattern.

[9] In the case of silicon, the average energy needed to create an electron-hole-pair is 3.7 eV (Strüder & Meidinger, 2008).

correlated with the photon energy. Together with the small pixel size, CCDs, thus, offer both, a high energy resolution and a high spatial resolution, combined with a high sensitivity over the whole soft to mid-energy range. So it is not surprising that CCDs play a crucial role in X-ray astronomy today. For example, the CCD technology is also used on the aforementioned Chandra satellite as well as on XMM-Newton, the X-ray Multi-Mirror Mission of the *European Space Agency* (ESA), which is in the focus of this work. Also, eRosita (extended Roentgen Survey with an Imaging Telescope Array, Predehl et al., 2021), a German X-ray telescope for the 0.5–10 keV range just launched in 2019, has CCD detectors mounted. Even though the development of new detector technologies continues[10], CCDs offer many advantages which also recommend their use for future X-ray missions (Grant, 2011).

However, with the higher quality of data that can be obtained today, also a high quality of the instrument calibration has become even more important to ensure the data can be interpreted with the necessary precision. The first part of this work, as presented in Chapter 3, is, thus, dedicated to contribute to improving the calibration of XMM-Newton's X-ray cameras.

2.2 Astrophysical Background

2.2.1 X-ray Generating Processes

To analyse and classify detected sources in an observation, as done in the second part of this thesis (presented in Chapter 4), the processes which are the origin of X-ray radiation from astrophysical sources need to be known. Each process leads to a specific spectral shape. By spectral fitting with models intended to reproduce the respective spectral shapes, some light can be shed on the possible nature of a source and, likewise, an understanding of the processes is necessary to choose from and evaluate the applicability of the model components available.[11] The major astrophysical processes which generate an X-ray continuum are (Seward & Charles, 2010):

- *Blackbody radiation*: Blackbody radiation is of thermal origin. In general, an object with a temperature above 0 K emits electromagnetic radiation. The thermal emission of astrophysical sources like stars can be approximated by the radiation of an idealized black body in thermal equilibrium[12], which absorbs all incoming radiation and whose resulting thermal emission depends on its temperature alone. The spectrum peaks at a temperature-dependent energy. With an increasing temperature, the overall intensity of the radiation increases and the maximum intensity in the spectrum shifts towards higher energies.[13] The peak is in the X-ray regime if the temperature is around 10^6–10^7 keV, as in the case of the hot surface of young neutron stars.

[10] like the development of the so-called active pixel sensors, which will be used on board ATHENA (Advanced Telescope for High Energy Astrophysics), ESA's mission currently planned to be launched in 2031

[11] The precise models applied in this work are described in later chapters.

[12] In thermal equilibrium, the temperature in a system is homogeneous and all particles basically have the same energy.

[13] as stated by Wien's displacement law

- *Thermal bremsstrahlung*: Thermal bremsstrahlung is emitted by optically thin, hot plasmas in thermal equilibrium and it leads to a spectrum with an exponential decay at higher energies. When there is a Coulomb collision between free electrons and the positively charged, ionized atoms in a plasma, the electrons get deflected and decelerated by the electrostatic force. The kinetic energy they lose in these encounters is emitted in form of electromagnetic radiation. Since the energy of the photons depends on the velocity of the electrons in the plasma, it increases with higher temperatures. Thermal bremsstrahlung can be observed as X-rays if the temperature of the plasma reaches at least 10^6 K. Examples where thermal bremsstrahlung can be observed in X-rays are the intergalactic medium in clusters of galaxies, accretion discs in low-mass X-ray binaries and plasma heated by SNR shocks.

- *Synchrotron radiation*: Synchrotron radiation, also called magnetic bremsstrahlung, occurs when fast charged particles move in a magnetic field at an angle to the field lines. In an astrophysical context, these particles are usually relativistic electrons. The Lorentz force, which is perpendicular to both a charged particle's velocity vector and the magnetic field lines, causes the electrons to spiral around the lines. This deflection constitutes an acceleration due to which the electrons emit electromagnetic radiation. Usually, the resulting spectrum of an astronomical source of synchrotron radiation can be described with a power law and it depends on the magnetic field strength and the electron energy only. The conditions for synchrotron radiation are met, for example, in pulsar wind nebulae around highly magnetic neutron stars.

- *Inverse Compton scattering*: According to the Compton effect, a photon transfers energy to a charged particle when being scattered by it. When the charged particle has a higher energy than the photon, however, inverse Compton scattering takes place and the photon gains energy from the charged particle. This effect on the photons and on the overall spectrum is called Comptonization. It can also play an important part in the production of X-rays in an astrophysical setting since the relativistic electrons present in some astronomical X-ray sources usually have higher energies than the photons they interact with. Again, the resulting spectrum follows a power law. One example for sources of X-ray radiation caused by inverse Compton scattering are active galactic nuclei (AGNs), where optical and ultraviolet radiation coming from an accretion disc around a supermassive black hole is Comptonized by relativistic electrons in a surrounding hot corona.

Besides these continuum-generating processes, X-ray spectra can also show emission lines, which are due to spontaneous emission from bound electrons in a hot gas that is not completely ionized. As long as the gas temperature does not exceed about 5×10^7 K, there are still electrons bound in the atoms of heavy elements (Seward & Charles, 2010). They can get excited to higher energy levels either by collisions with the fast, free electrons in the gas or by absorbing photons from a source of high-energy radiation, as in the case of an accretion disc that is irradiated by a compact primary in an X-ray binary, for example. Inner shells in an atom which are left unoccupied in the process can then be filled by electrons from the outer shells. When an electron, thus, de-excites, it emits a photon with an energy according to the energy difference between the levels,

which is distinctive of the respective element and transition. The resulting emission lines in the overall spectrum can often be modelled using Gaussian model components.

2.2.2 Remarks on Types of X-ray Sources

In the previous section, some examples for astronomical objects emitting X-rays generated by the presented processes were already given. It would be far beyond the scope of this work to go into detail about the properties of every possible type of X-ray source which might be included in an observation used here and to discuss the possible combinations of different processes present in various source types. An extensive overview of different types of X-ray sources, including their respective nature, properties and the general understanding of the underlying physical processes (which, of course, is subject to a continuous scientific progress), can, for example, be found in Trümper & Hasinger (2008), Seward & Charles (2010) and Longair (2011).

Neutron stars and their association with SNRs are presented in more detail in Chapter 4 since they are the objects of interest in the second part of this thesis. For the calibration topic presented in Chapter 3, suitable sources were selected according to defined selection criteria (see Chapters 3.3.1 and 3.5.2). The actual nature of these sources is of marginal importance in this regard as long as they fulfil the criteria. One important aspect to be named here, however, is the distinction between point-like sources and extended sources, which, in this case, refers to the appearance of a source in an image rather than its actual physical shape and extent. With the spatial resolution that has been achieved for instrumentation used in X-ray astronomy today, it has been made possible to differentiate between point sources and diffuse, extended emission within the resolution's limits – for example, to look for an associated compact object in a Galactic SNR. But distant, strong X-ray sources like X-ray binaries, galaxies and clusters of galaxies can appear point-like as well, even though they are not actual point sources (in the case of XMM-Newton, if their extent radius[14] is smaller than $6''$). Thus, the numerous sources included in Chapter 3 are of various different types, with their specific nature not being subject of this thesis. For a classification of the individual sources, the *XMM-Newton Serendipitous Source Catalogue*[15] may be consulted.

[14] for example, as determined by the task `emldetect` of the XMM-Newton Science Analysis System (SAS)

[15] available, for example, at `https://heasarc.gsfc.nasa.gov/w3browse/all/xmmssc.html`. See also `http://xmmssc.irap.omp.eu/cat.html`.

CHAPTER 3

Cross-Calibration of XMM-Newton's EPIC Effective Areas

High-quality calibration of scientific instruments is essential in order to obtain reliable analysis results. The satellite XMM-Newton, the X-ray Multi-Mirror Mission, is considered one of the most successful missions of the *European Space Agency* (ESA), but its observational data are still affected by calibration uncertainties which lead to discrepancies in the results obtained with the different instruments on board. Over almost the complete energy range which XMM's instruments cover, the dominating factor for these calibration uncertainties is the effective area. In the scope of this work, a tool to improve the on-axis[16] effective area calibration was worked on as presented in this chapter. In the first section, the necessity to address the topic and the aim of this work are explained. The internal configuration of the spacecraft, details on its instruments and on the processing of the data as well as different relevant calibration issues, including a definition of the effective area, are given next to provide the background underlying this calibration project. The presentation of the calibration process includes an introduction of Corrarea, the tool this work is based on, a variety of steps performed in order to achieve a reliable effective area correction and even the use of the script package developed in this context to also support the improvement of other calibration issues. The overall outcome of this project is discussed in the final section.

3.1 Motivation

As already mentioned in Chapter 1.1, calibration is based on measurements, which need to be continuously performed in order to take instrument changes and previous calibration improvements into account. This dependence on measurements leads to systematic errors involved in the measuring process affecting the calibration. To any data analysis, which requires the application of calibration corrections, these calibration uncertainties are then introduced and resulting model predictions should be interpreted with caution. Combining an incorrect spectral model with insufficiently calibrated instrument response files can still lead to a good spectral fit (Natalucci, 2013) and, as a consequence, to a misinterpretation of the data. Therefore, the quality of the data analysis in observational science can only be as good as the underlying calibration of the instruments (Guainazzi, 2014).

It is, thus, important to know the calibration uncertainties contained when analysing data to be able to fully evaluate the reliability of the results. As for XMM-Newton's

[16] meaning the position on a detector where the optical axis of the telescope meets the focal plane

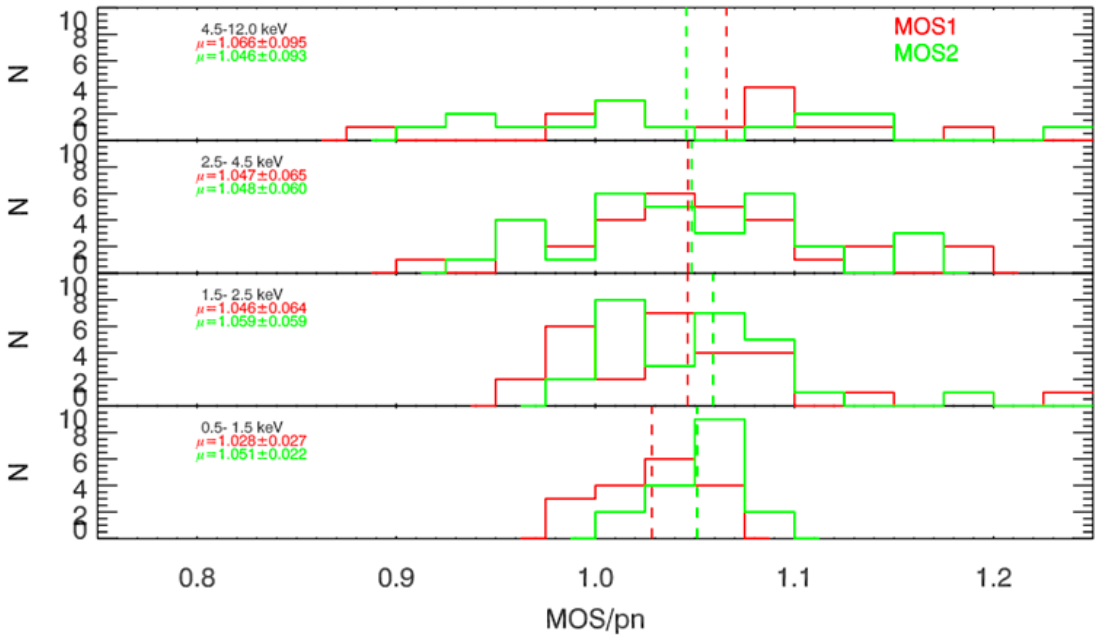

Figure 3.1: MOS-to-pn flux ratio for a selected sample of 46 on-axis point sources in different energy bands, obtained using SAS version 13.5 and corresponding calibrations. Shown is the number N of sources for a certain flux ratio value. A flux ratio of 1.0 corresponds to the same flux being detected for the MOS and the pn instruments. The dashed lines show the respective mean value μ. (Guainazzi et al., 2014)

European Photon Imaging Camera (EPIC), which comprises the main X-ray instruments, above 0.5 keV these uncertainties are dominated by the effective area calibration (Read et al., 2014), which makes a good understanding and calibration of the effective area absolutely essential. Presenting a tool named CORRAREA, which allows users to estimate the on-axis effective area calibration uncertainties contained in their data, Guainazzi et al. (2014) showed a discrepancy between the three X-ray instruments that make up EPIC, two metal oxide semiconductor (MOS) CCDs and one pn-type detector, in the source flux of 46 on-axis point-sources[17] as can be seen in Figure 3.1. In case of an ideal calibration of XMM's two MOS detectors and its pn CCD, the MOS-to-pn flux ratio would equal 1.0, which, obviously, it does not. On average, the flux detected with the MOS instruments is about 5% higher than the one detected with pn. Also, the deviation of the mean value from 1.0 gets larger at higher energies and the single values are more widely spread.

As mentioned by Guainazzi et al. (2014), the intention behind the CORRAREA tool is to align the on-axis effective areas of XMM's X-ray detectors with each other by applying an energy-dependent multiplicative correction factor determined empirically by cross-calibrating the instruments based on already available observations. The details of the tool and its application are given in Chapter 3.3. It is pointed out by the creators of the original CORRAREA tool themselves that the tool is so far only considered to offer users an idea of the systematic uncertainties in the effective area calibration to be

[17] Details on how the sources were selected are given in Chapter 3.3.1.

able to assess their impact on astrophysical outcomes. This is why CORRAREA, which was implemented into the Science Analysis System (SAS) for XMM data processing from version 14 onwards, is so far only available as a non-default option, which should only be applied on data to get an estimate of the effective area uncertainties but not to produce final results. To be used as a default correction, CORRAREA is not yet considered sufficiently validated and it needs to be updated because corrections regarding other important calibration issues which affect the effective area calibration as well, like the correction of the point spread function (PSF), have been conducted in the meantime.

But a correction in the effective area calibration is still needed. Figure 3.2 shows the MOS-to-pn flux ratio for the same 46 sources contained in Figure 3.1, this time with the flux taken from the 4th *XMM-Newton Serendipitous Source Catalogue* (Webb et al., 2020), which was obtained using SAS version 18 and corresponding calibrations. As before, there are discrepancies between the flux values obtained with the different X-ray detectors of XMM. Though the results for the different observations now show a MOS-to-pn flux ratio more densely concentrated around the mean value, the flux values between the MOS instruments and pn differ with an even higher discrepancy of almost up to 10%, though one has to be aware that the fluxes obtained with the pipeline of the *XMM-Newton Serendipitous Source Catalogue* contain larger errors compared to the values included in the previous plot. Nevertheless, the noticeable general tendency of the MOS CCDs detecting a higher flux than pn shows that the effective area calibration still requires further inspection.

Until now, a way to reliably reconcile the effective areas of XMM's three X-ray instruments amongst themselves is missing. To meet this issue, it was decided to develop the CORRAREA tool further in order to make it a default correction, which is considered a current high priority calibration topic amongst the XMM calibration team at the *European Space Astronomy Centre* (ESAC) of the *European Space Agency* (ESA). To do so, not only a recalibration and further validation of the tool is necessary but also an automation of the process to get the correction function underlying CORRAREA is required so that it can easily be run repeatedly for different validation steps and also for keeping the tool up-to-date in the future. This automation of the process as well as the recalibration and validation of the CORRAREA tool were addressed within the scope of this work. Effective area calibration uncertainties and discrepancies between astrophysical parameters obtained with different instruments are not a topic exclusive to XMM but constitute a general problem in X-ray astronomy so that the methods presented here can also be applied to other missions to achieve an overall alignment of the instruments operated in the same energy range.

3.2 XMM-Newton

3.2.1 The Mission

The X-ray Multi-Mirror Mission (Jansen et al., 2001), also referred to as XMM-Newton or just XMM, was launched by ESA in December 1999 as a cornerstone mission in its Horizon 2000 science programme. Intended to offer new possibilities for X-ray spectroscopy, the observatory is equipped with an unprecedented large collecting area to allow for high throughput of soft X-ray photons and, thus, the observation of a variety of X-ray sources, including fainter ones than those that could be detected with previous

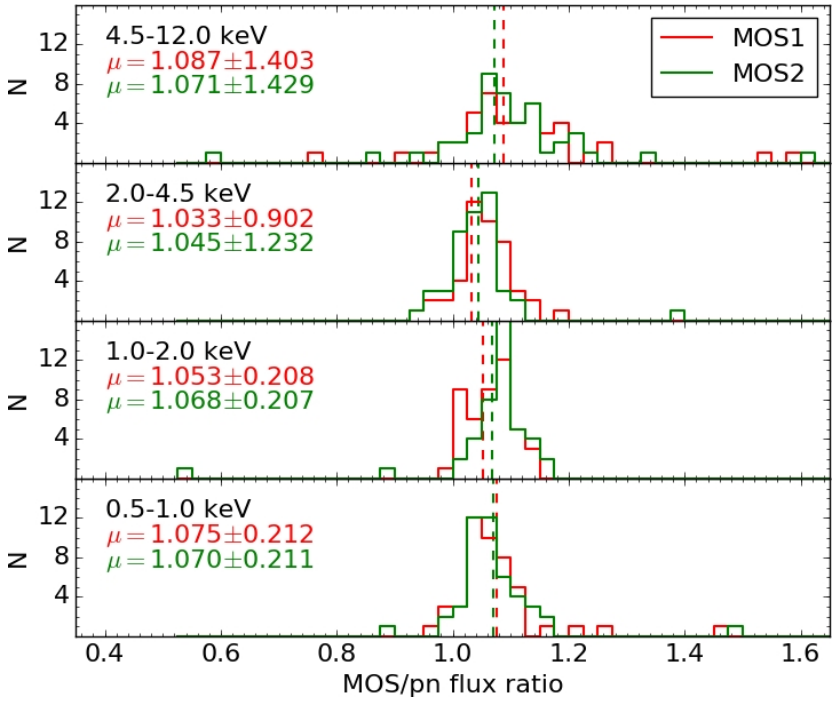

Figure 3.2: MOS-to-pn flux ratio for a selected sample of 46 on-axis point sources in different energy bands, using the flux values given in the fourth *XMM-Newton Serendipitous Source Catalogue* (4XMM-DR9), which made use of SAS version 18 and corresponding calibrations. Shown is the number N of sources for a certain flux ratio value. A flux ratio of 1.0 corresponds to the same flux being detected for the MOS and the pn instruments. The dashed lines show the respective mean value μ.

X-ray missions. At the same time, the satellite's highly elliptical orbit around Earth provides the conditions for long, uninterrupted observations with a total observation time of up to 40 hours per cycle. Considering its high timing resolution as well, XMM-Newton combines the capabilities to perform high-sensitivity imaging spectroscopy and high-quality timing analysis.

Since the beginning of its time in space, the satellite has contributed to enhancing our understanding of many different astrophysical fields like, for example, hot stars and star formation, accretion processes and properties of compact objects, the evolution of supernova remnants (SNRs) and the distribution of elements in them as well as the structure and composition of clusters of galaxies (e.g. Santos-Lleo et al., 2009; Schartel et al., 2017). After more than 20 years, the satellite is still in operation and set a record in September 2018 as the mission which has been operated by the *European Space Operations Centre* (ESOC) in Darmstadt, Germany, longer than any other ESA satellite before. Together with a publication rate of around 300 refereed papers per year based on XMM data (Ness et al., 2014)[18], XMM-Newton can be called one of ESA's most successful missions of all time.

According to the Mission Operations Centre (MOC) at ESOC, the satellite can most likely be operated for another decade.[19] Given the good condition of the instruments, the still very high number of observation proposals, which exceeds the available observation time by a factor of more than five and the good prospects of innovative scientific results, a continuation of the mission over this period can be expected (Schartel et al., 2017). This promising outlook of the mission makes an improvement of the calibration of the detectors not just relevant for already existing data but also for future observations.

3.2.2 The Spacecraft and its Payload

The following sections summarise those aspects of the XMM-Newton instruments and the data processing relevant with respect to this work. A more detailed description can be found in the *XMM-Newton Users Handbook*[20] (ESA: XMM-Newton SOC, 2018b).

For calibrating the EPIC instruments, the whole light path within the spacecraft plays an important role as different hardware components have an effect on the X-rays before they reach the detectors. Figure 3.3 shows a sketch of the satellite's interior. It has three Wolter type I X-ray telescopes (see Chapter 2.1), each of which has a mirror module and one of the EPIC detectors, either a MOS or the pn detector, in its focus. The name of XMM refers to the many mirrors of the mirror modules, with each consisting of 58 gold-coated, nested mirror shells that have a focal length of 7.5 m and account for the largest total collecting area of a focussing X-ray telescope so far.[21] One of the modules can be seen in Figure 3.4. The mirror shells all have a length of 0.6 m and their diameters vary from 0.3 m to 0.7 m (Gondoin et al., 1998). Also visible is the spider arm structure supporting the mirrors, which can cause a similar shape to appear in images of observed sources.

[18] this still holds true with almost 6700 refereed papers according to `https://www.cosmos.esa.int/web/xmm-newton` as of March 2021

[19] as noted by the XMM Spacecraft Operations Manager M. Kirsch at the *X-ray Topics in Astronomy: from History to the Future* Workshop in Tübingen on 16 April 2019

[20] available at `https://xmm-tools.cosmos.esa.int/external/xmm_user_support/documentation/uhb/XMM_UHB.pdf`

[21] with 4650 cm^2 at 1.5 keV and 1800 cm^2 at 8 keV

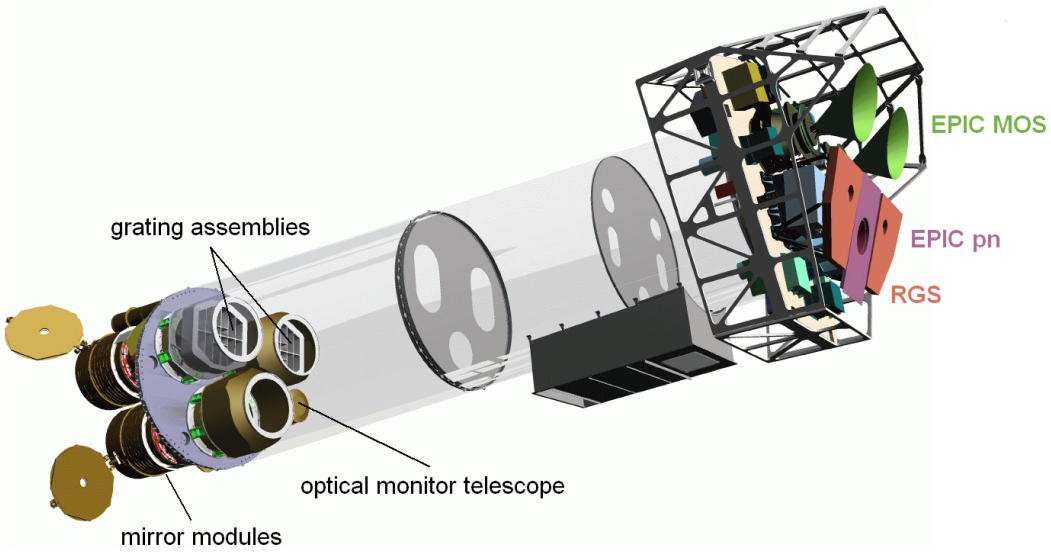

Figure 3.3: Sketch of the interior of the XMM-Newton satellite. The EPIC and RGS detectors are positioned in front (i.e. as seen from the mirror module entrance window) of their cooling radiators, which are coloured according to the matching label. (Credit: Dornier Satellitensysteme GmbH, *XMM-Newton Users Handbook*, ESA: XMM-Newton SOC, 2018b, modified)

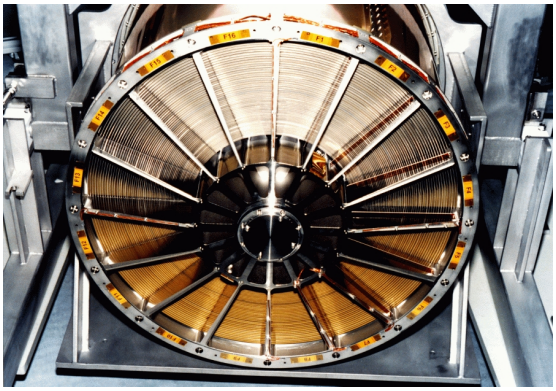

Figure 3.4: Mirror module of one of the XMM Wolter I telescopes. (Credit: D. de Chambure, ESA/ESTEC, `https://heasarc.gsfc.nasa.gov/docs/xmm/xmmhp_gal_hard_photo_mir.html`)

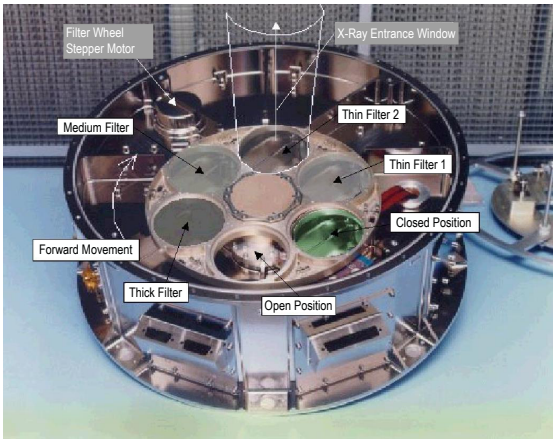

Figure 3.5: An XMM filter wheel in its mount structure. The wheel contains six positions, namely an open position, a closed position and a position for the two thin filters, the medium filter and the thick filter, respectively. (Turner et al., 2001, modified)

The two X-ray telescopes with the MOS detectors have grating assemblies in their light path which directs part of the X-rays to the detectors of the reflection grating spectrometer (RGS, Den Herder et al., 2001). The RGS offers the possibility for high resolution spectroscopy (with $E/\Delta E$ ranging from 500 to 100) in the 0.3–2.1 keV range. This work is not concerned with RGS data but it is important to keep in mind that, in contrast to the pn camera, only about half of the X-rays captured with the telescopes of the MOS cameras actually reach the MOS detectors due to the grating assemblies dispersing light towards the RGS detectors.

The three EPIC detectors themselves, the main instruments in the focus of this work, are presented in more detail in the next section. Before the X-rays reach the detectors, however, they also need to pass through a filter wheel positioned in front of each detector. Each filter wheel contains two thin filters, a medium filter and a thick filter besides the open and closed positions (Figure 3.5). As the X-ray detectors are also sensitive to ultraviolet, optical and infrared radiation, the filters are needed to prevent contamination of the data. But inevitably the filters also absorb some of the X-ray photons, particularly at lower energies (Lumb et al., 2012). Thus, their permeability to X-rays is a matter of calibration as well.

Last but not least, an optical telescope, the optical monitor (OM, Mason et al., 2001), is located at the mirror module mount platform. This Ritchey-Chrétien telescope has an aperture of 30 cm in diameter and can be used in the wavelength range from 180 nm to 600 nm to detect objects with an optical brightness as high as 7.4 mag[22] within a field of view (FOV) of $17'$. The OM allows for simultaneous observations in X-rays and optical light and, even though OM data was not used in the calibration work done here, it was used to support the analysis presented in Chapter 4, as the spatial resolution in the optical, $\sim 1''$ in the case of OM, is generally better than the spatial resolution that can be achieved in X-rays.

[22] in case of an A0 star observed with the V filter

3.2.3 The European Photon Imaging Camera

The European Photon Imaging Camera is the main instrument of XMM-Newton. It provides observations for imaging as well as spectral and timing analysis in the 0.1–15 keV range, with a spatial resolution of about 6″ (FWHM), good timing capabilities and a moderate spectral resolution. As mentioned before, EPIC actually consists of three detectors, each being located in the focal point of its own telescope. With two different types of detectors involved, they have different designs, properties and advantages.

Two of the detectors consist of metal oxide semi-conductors (MOS, Turner et al., 2001), which were developed at the *Space Research Centre* of the *University of Leicester*. Their design can be seen in Figure 3.6 (left). Each MOS detector is made up of seven charge-coupled devices (CCDs), with one central CCD and the others arranged around it. The two MOS detectors, called MOS1 and MOS2, are oriented in a 90° angle with respect to each other to reduce the overlap of the chip gaps. The on-axis position where the optical axis meets the detector is centrally located on CCD1. This is the position of interest for the effective area calibration in this work. A proposed target, in case it is a single point source, is usually positioned here. Also, the position allows for the best overall calibration as it has also been in the focus of the work on other calibration issues and outer regions generally suffer from additional negative effects that add to the calibration uncertainties, like e.g. vignetting.

When analysing scientific data in general but especially for calibrating the instruments it is important to not include data from any CCD not functioning properly. As for MOS1, two of the CCDs were damaged in micrometeoroid hit events, CCD6 in March 2005 and CCD3 in December 2012, so that they have been switched off for scientific observations since then. The 2012 event also led to an increased background in half of the adjacent MOS1 CCD4, for which the possibility to exclude only this part of the CCD was introduced. In addition to this, MOS CCDs can sometimes be in a so-called anomalous state with an increased noise at low energies below 1 keV and should then be deselected. This is frequently the case for MOS1 CCD4 and MOS2 CCD5.

The pn detector (Strüder et al., 2001), which was developed by the *Max Planck Institute for Extraterrestrial Physics* in Garching in cooperation with the *Institute for Astronomy and Astrophysics Tübingen*, shows a different CCD geometry (Figure 3.6). It consists of 12 CCDs arranged in two rows on a single wafer. As this arrangement results in a chip gap in the centre of the detector, the on-axis position is slightly shifted onto CCD4.

For a comparison of the characteristics of the two detector types, some key figures are given in Table 3.1. Besides their better spectral resolution, the MOS detectors also have a better spatial resolution (in part due to their smaller pixel size but mainly due to their smaller point spread function, which will be described in detail in Chapter 3.2.4). The pn detector, on the other hand, slightly extends the upper limit of the observable energy range to 15 keV and is more sensitive to photons as it is back-illuminated. In addition, the pn detector has a readout node for each pixel column of each CCD, resulting in 768 readout nodes as opposed to a total of 14 readout nodes for one of the MOS detectors, which have two readout nodes per CCD. Thus, the pn detector allows for a much faster readout and a better time resolution. The exact time resolution value depends on the science mode used for an observation.

The science modes define the parts of a detector that are active during an observation (Figure 3.7) and are chosen depending on the target source and the scientific aim.

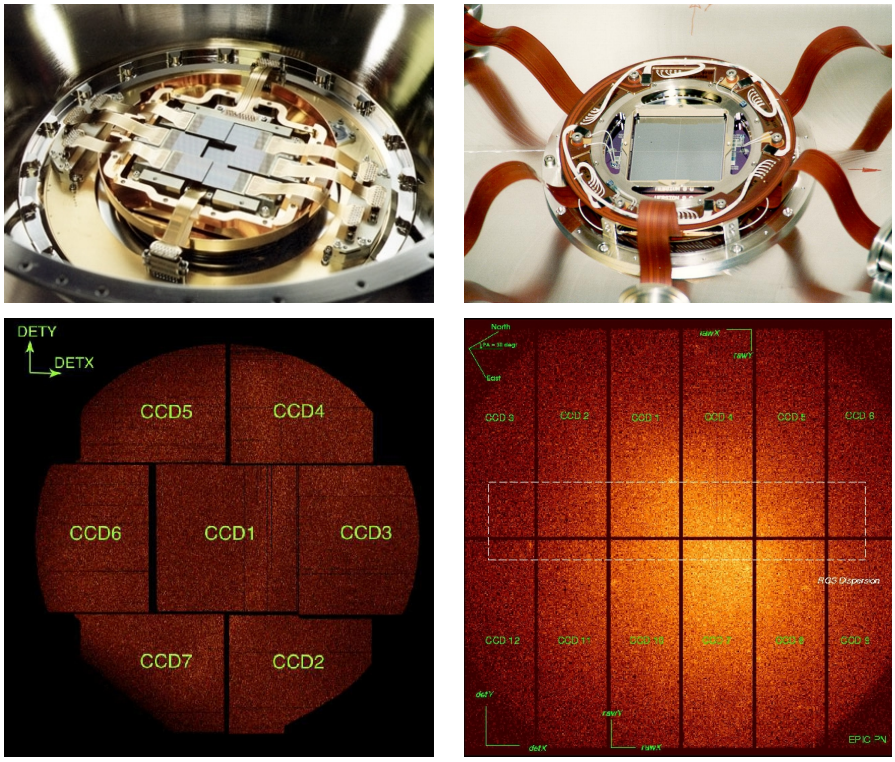

Figure 3.6: CCD configuration of the EPIC detectors. A MOS detector is shown on the left, the pn detector on the right. *Top*: photographs of the detectors (credit: ESA, `https://www.cosmos.esa.int/web/xmm-newton/technical-details-epic`); *bottom*: images taken by the illuminated detectors (*XMM-Newton Users Handbook*, ESA: XMM-Newton SOC, 2018b). The CCD labels shown are the official numbers provided in the data products to address data of individual CCDs. The MOS CCDs have a size of 2.5 cm × 2.5 cm, the pn CCDs of 1 cm × 3 cm, respectively.

Table 3.1: Selected key characteristics of the two EPIC camera types.

	MOS	pn
FOV	$33' \times 33'$	$27.5' \times 27.5'$
energy range	0.1–12 keV	0.15–15 keV
number of pixels per CCD	600×600	64×200
pixel size	$40\,\mu\text{m} \times 40\,\mu\text{m}$	$150\,\mu\text{m} \times 150\,\mu\text{m}$
spectral resolution at 1 keV	∼70 eV	∼80 eV
spectral resolution at 6.4 keV	∼150 eV	∼150 eV
illumination arrangement	front-illuminated	back-illuminated

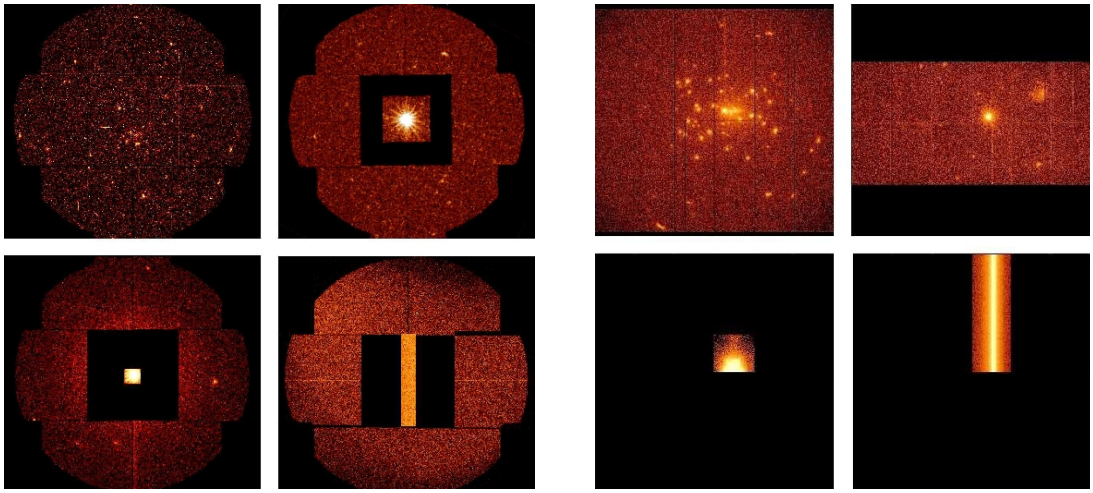

Figure 3.7: Science modes of the MOS detectors (four images on the left) and the pn detector (four images on the right). The modes shown for each detector type are: Full Frame mode (top left), Large Window mode (top right), Small Window mode (bottom left) and Timing mode (bottom right). (*XMM-Newton Users Handbook*, ESA: XMM-Newton SOC, 2018b)

Different modes can be selected for the different EPIC detectors. All detectors have a Full Frame (FF) mode, a Large Window (LW) mode, a Small Window (SW) mode and a Timing mode. In FF mode the whole detector is active and the whole FOV is observed. In case of the MOS detectors the readout region of the central CCD is reduced in the two window modes (to 300×300 pixels in the LW mode and 100×100 pixels in the SW mode). As for pn, in LW mode the active regions of all CCDs are reduced by half. In pn SW mode only an area of 63×64 pixels around the on-axis position on CCD4 is active. The window modes can be used to observe brighter sources and achieve a better time resolution as the respective values in Table 3.2 show. The last mode displayed in Figure 3.7 is the Timing mode with which the time resolution can be further improved at the expense of spatial information, which is reduced to one dimension. For the MOS detectors the readout region of the central CCD is then reduced to a column of 100×600 pixels, for the pn detector CCD4 is fully used with the other CCDs being inactive. The science modes available for the pn detector are augmented by the Extended FF mode and the Burst mode. With the whole detector being active as for the normal FF mode, the Extended FF mode has a longer integration time, which can be useful for observing extended sources. The Burst mode is a special version of the Timing mode but it excludes the last 20 pixel rows where the source is located and a time resolution of $7\,\mu$s is achieved with it.

For calibration it is important to not assume that the same corrections can be applied to data of all science modes alike. Possible differences which the instruments show depending on the modes need to be investigated. In this respect, this work is only concerned with the imaging modes, namely the (extended) FF, LW and SW modes. As Table 3.2 shows, the modes do not only differ in the time resolution but also in the maximum count rate a source can have to be observed with the respective mode. Above that threshold, serious pile-up will affect an observation. Pile-up is one of the major

Table 3.2: Characteristics of the EPIC detectors for different science modes.

	MOS		pn	
Mode	Time resolution (ms)	Count rate limit* (cts s^{-1})	Time resolution (ms)	Count rate limit* (cts s^{-1})
Extended Full Frame	–	–	199.1	0.3
Full Frame	2600	0.5	73.4	2
Large Window	900	1.5	47.7	3
Small Window	300	4.5	5.7	25
Timing	1.75	100	0.03	800
Burst	–	–	0.007	60 000

* limit given to prevent pile-up

calibration issues which are relevant in the process of calibrating the effective area and which are described in the next section.

3.2.4 Calibration Issues

The focus of this work is on the calibration of the XMM EPIC on-axis effective area. The effective area is a measure for the combined ability of the components of each camera to collect photons at different energies. It is the product of the detector quantum efficiency (a detector's capability to actually register an incoming photon), the mirror effective area (the capability of the mirrors to collect photons) and the filter transmission (the capability of the filters to let X-rays pass through). Figure 3.8 shows the resulting, energy-dependent on-axis effective area of the EPIC cameras. The lower effective area values of the MOS cameras are mainly a result of the grating assemblies in their light path, which direct part of the light to the RGS detectors. Also, being a back-illuminated sensor, the pn detector has a slightly higher sensitivity. The effective area of the pn camera is slightly more stable over a broader energy range, which resembles the more stable behaviour of the pn detector's quantum efficiency shown in Strüder et al. (2001) (in combination with ESA: XMM-Newton SOC, 2018b).

Uncertainties in the effective area calibration are the dominant factor of the relative systematic uncertainties in the instruments above 0.5 keV; at lower energies, uncertainties in the calibration of the detector response, which deals with the probability that a photon of a specific energy is allocated as a count in a particular spectral bin, have a strong influence (Read et al., 2014). To not include these response related uncertainties in the effective area correction, lower energies were excluded from the analysis. Also, this work initially mainly focuses on energies below 7.5 keV as an improvement of the point spread function (PSF) calibration was worked on simultaneously at ESAC, which turned out to have a significant effect at higher energies (see Chapter 3.8).

The PSF reflects a telescope's capability to focus photons. In Figure 3.9 the shape of the on-axis PSF of each EPIC camera can be seen. Each camera shows a slightly different shape, which is most obvious for MOS2. The core region of the PSF does not entirely contain all photons detected from a source and generally source counts are missed when extracting data from a source region. The radial structures surrounding

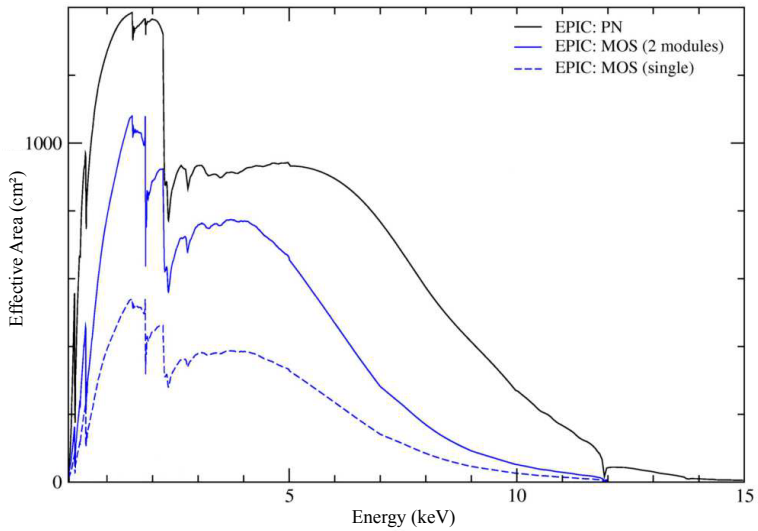

Figure 3.8: On-axis effective area of the EPIC cameras. (*XMM-Newton Users Handbook*, ESA: XMM-Newton SOC, 2018b, modified)

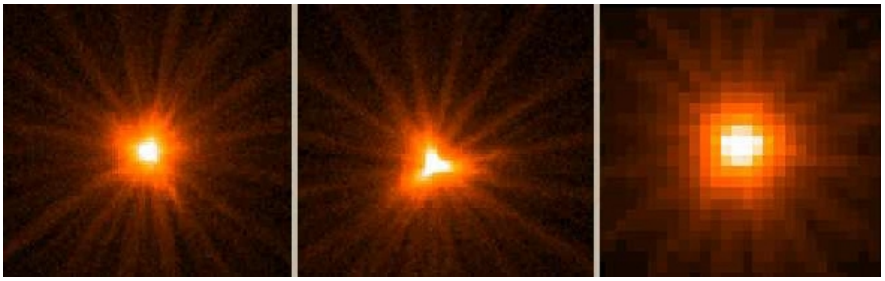

Figure 3.9: Illustration of the on-axis point spread function for the MOS1 (left), MOS2 (centre) and pn (right) camera. The MOS images were taken in Small Window mode, the pn image in Large Window mode. Each image displays a width of about 110″. (*XMM-Newton Users Handbook*, ESA: XMM-Newton SOC, 2018b)

the PSF core are a result from the spider arm structure which supports the mirrors (ESA: XMM-Newton SOC, 2018b) and indicate the positions between the spider arms, where source counts are also present due to scattering.

For the bright source used in Figure 3.9, the very centre of the core is piled-up, which is another major issue that has to be carefully considered in order to not get a distorted correction for the effective area calibration in the end. Pile-up occurs when two or more photons are detected in either the same pixel or in adjacent pixels in a single read-out cycle. Accordingly, there are two different types of pile-up, both illustrated in Figure 3.10. When energy pile-up (also called photon pile-up) occurs, the photons arrive in the same pixel and are ascribed to a single event with an energy equal to the sum of the individual photon energies. Pattern pile-up refers to photons in adjacent pixels, thus forming a pattern that is registered as originating from only one event, again with an energy equalling the sum of the individual photon energies. As a result, pile-up leads to flux loss as high count rates are suppressed and to a hardening of the observed

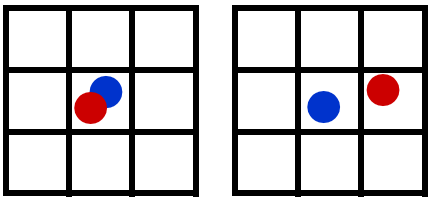

Figure 3.10: Energy pile-up (left) and pattern pile-up (right). (Image based on Mück, 2014)

spectrum, with too many events at higher energies while the actual events at lower energies were not noticed accordingly. The likelihood for a detector to be subject to pile-up depends not only on the brightness of the source but also on the chosen science mode. The shorter the readout-time is, the brighter the observed source can be.

Two more calibration issues, which mainly concern the pn camera, shall be described at this point. One of these issues concerns out-of-time (OoT) events. When a CCD is read out, photons continue to be registered. This results in a notable amount of source counts being present along the readout column as Figure 3.11 demonstrates. There is a tool that corrects for out-of-time events based on a model file. But to not introduce additional uncertainties, OoT events should be avoided for the effective area calibration by ensuring background regions do not include parts of the OoT streak along the readout line.[23] The second issue to be mentioned has to do with the charge transfer inefficiency (CTI), meaning the loss of charges during readout.[24] Data processing involves application of a calibrated correction for the CTI. But the CTI depends on the distance of the respective position on a CCD from its readout node and so does the correction. Both of these issues, OoT events and the CTI correction, need to be considered when choosing a suitable region to determine the local X-ray background as described in detail in Chapter 3.5.4.

Compared with off-axis positions, the calibration of the on-axis position on the detectors is easier to be conducted as the overall calibration is most advanced here and does not suffer much from additional border effects like vignetting or PSF distortion. Still, there are many calibration issues that can also affect the on-axis effective areas, like the transmission factors of the RGS reflection grating assemblies or contamination of the mirrors and detectors. They have not been relevant with respect to developing the Corrarea tool, though, but might rather have an effect on future recalibrations. As a general remark, the performance of the pn camera has been quite stable over XMM-Newton's entire operational time (Sartore et al., 2012; Read et al., 2014) while the performance of the MOS cameras is more subject to variation. The following section introduces the form in which calibrated corrections are provided, the general tools used for XMM-Newton data processing and the definition of event patterns as already mentioned in the context of pile-up.

[23] The MOS CCDs have frame store areas which largely reduce the impact of OoT events.

[24] Compared with the pn detector, the MOS detectors are not affected as much by CTI (Briel et al., 2000).

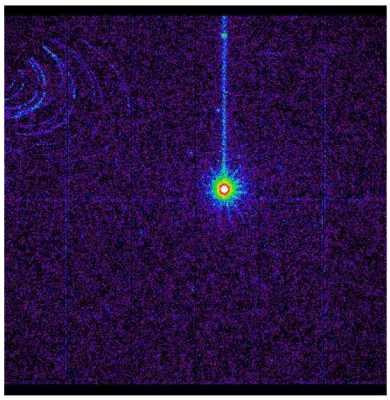

Figure 3.11: Effect of out-of-time events on pn images. Shown is a bright source in the 2–10 keV range observed in FF mode. The streak above the source is the result of the out-of-time events along the readout line of the CCD. The arc-shaped structures in the upper left corner are caused by straylight. (*XMM-Newton Users Handbook*, ESA: XMM-Newton SOC, 2018b, modified)

3.2.5 Data Handling

XMM-Newton observations are numbered with distinctive observation identifiers (IDs). An observation does not automatically consist of only one exposure for each camera but can be interrupted and contain a number of consecutive exposures. Data for a specific observation come in two forms of datasets: the raw observation data files (ODFs), which this analysis is based on, and the Pipeline Processing Subsystem (PPS) files. The ODFs comprise the raw event files of an observation in FITS[25] format for all XMM cameras (EPIC, OM and RGS), as well as the housekeeping, radiation monitor and spacecraft files, so that users can reprocess the data of an observation from scratch. Opposed to that, the files created with the PPS of the *XMM Science Operations Centre* (SOC) already include processed data and data products, like calibrated event files, images, source lists and general information about the observation. These pipeline products offer an easy way for a first overview of an observation but, depending on when an observation was done, will at some point be outdated with respect to the calibration status applied. Also, the use of the ODF files makes it possible to have control over the individual data reduction steps.

The standard programme to reduce the data is the Science Analysis Software (SAS), which is a software package introduced for XMM data in particular. The available tools, their application and the data reduction procedure are described in detail in the *Users Guide to the XMM-Newton Science Analysis System*[26] (ESA: XMM-Newton SOC, 2018a) and in *The XMM-Newton ABC Guide*[27] (NASA/GSFC XMM-Newton Guest Observer Facility, 2018). With the initial data reduction calibrated photon event files are obtained by making use of the publicly available current calibration files (CCFs), which contain the calibration data for all of XMM's cameras. The calibrated event files

[25] Flexible Image Transport System

[26] available at `https://xmm-tools.cosmos.esa.int/external/xmm_user_support/documentation/sas_usg/USG/`

[27] available at `https://heasarc.gsfc.nasa.gov/docs/xmm/abc/`

are the basis to produce products for analysis, for which SAS also provides a variety of tasks. For example, it allows to filter data according to different selection criteria or to produce auxiliary files necessary for spectral analysis.

Amongst other selection criteria, filtering can be done to select only data that follow a certain event pattern. Valid event patterns are predefined to identify pixel patterns that constitute an isolated X-ray event. The 31 valid event patterns defined for the imaging modes of the MOS detectors are shown in Figure 3.12, the 13 valid patterns defined for the pn detector in Figure 3.13. Events are searched for by scanning for pixels with a charge above a set threshold within a matrix of 5×5 pixels.[28] If the respective pixels form one of the defined patterns, the signal is regarded as a valid event presumably caused by X-rays.

But to analyse an astronomical object not all event patterns should be included. For the MOS detectors a limitation to patterns 0–12 is strongly recommended for the imaging modes as the majority of the detected soft X-rays photons produce these patterns and they are better calibrated. The reduction of the detection efficiency caused by the exclusion of pattern types is, thus, made up for by the improvement of the spectral resolution. Patterns 26–29 constitute the diagonal events. They can sometimes be caused by X-ray induced silicon fluorescence from the detectors but are almost exclusively the result of pile-up of more than one event. Patterns 30 and 31 can indicate pile-up, too, if there is an enhanced occurrence of them in the PSF centre. But, as opposed to the diagonal event patterns, there is not such a definite origin of these patterns. They are primarily intended for detecting cosmic ray events and, also, X-rays at higher energies[29] can generate a notable amount of pattern 31 events with an increasing probability, depending on their energy.

For the pn detector, all 13 patterns shown in Figure 3.13 can be generated by valid X-ray events from single photons. Other patterns are mainly ascribed to pile-up. To perform spectral analysis, a limitation to patterns 0–4 is strongly recommended as only these patterns are considered to be calibrated well enough. Unlike the MOS detectors with their diagonal event patterns, the pn detector does not have patterns defined which are almost entirely the result of pile-up.

Filtering for patterns is, of course, only one small step in the process of reducing and analysing the data. The overall procedure that has been carried out is presented in the following chapters. For the spectral analysis done in this work, also the X-ray spectral fitting package XSPEC[30] (Arnaud, 1996; Dorman & Arnaud, 2001) was used.[31] XSPEC is part of the High Energy Astrophysics Software (HEASOFT) package, which also includes FTOOLS[32] (Blackburn, 1995), which was used for FITS file alteration where required. For image analysis, the SAOImage DS9[33] tool (Joye & Mandel, 2003), also simply called DS9, for astronomical imaging purposes was made use of.

Before spectral analysis can be performed, though, further preparations have to be made based on the obtained calibrated event lists. For example, spectral fitting with XSPEC requires two auxiliary files which contain instrument models needed for

[28] with the exception of the pn single event pattern, which is defined within a 3×3 pixel matrix
[29] starting from $\sim$6 keV
[30] `https://heasarc.gsfc.nasa.gov/xanadu/xspec/`
[31] The *XSPEC Users' Guide* (Arnaud et al., 2018) is available at `https://heasarc.gsfc.nasa.gov/xanadu/xspec/manual/`
[32] `http://heasarc.gsfc.nasa.gov/ftools`
[33] `https://sites.google.com/cfa.harvard.edu/saoimageds9`

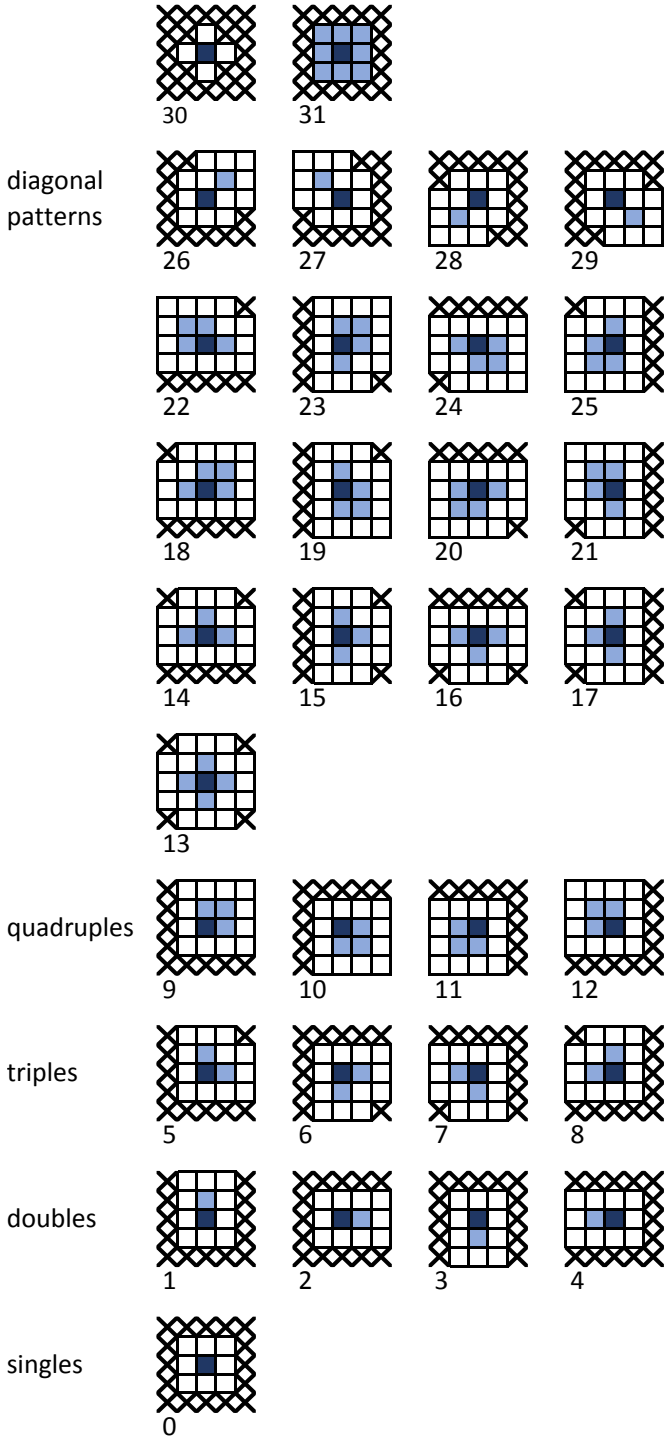

Figure 3.12: Valid event patterns for the imaging modes of the MOS detectors. Each pattern is defined within 5×5 pixels. All coloured pixels have a charge above the set threshold. The centre of a pattern is located at the pixel with the highest charge (dark blue), the adjacent pixels coloured in light blue have a lower charge which is still above the threshold and the pixels coloured in white must have a charge below the threshold. Pixels that are indifferent are crossed out. The number given below each pattern is the pattern code used in SAS. (Image based on the *Users Guide to the XMM-Newton Science Analysis System*, ESA: XMM-Newton SOC, 2018a)

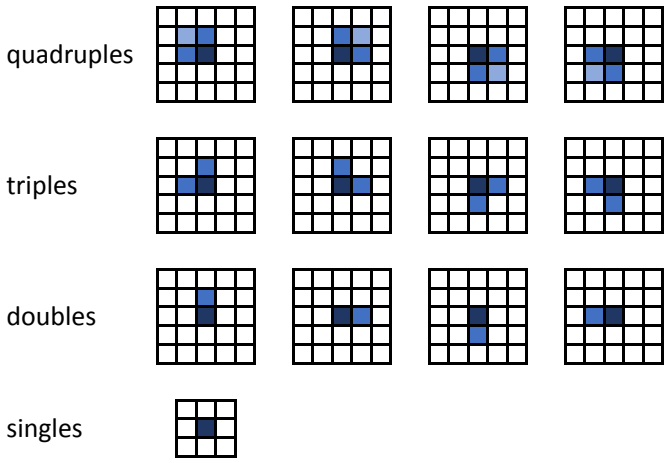

Figure 3.13: Valid event patterns for the pn detector. Each pattern is defined within 5×5 pixels, 3×3 pixels in the case of single pixel events. All coloured pixels have a charge above the set threshold. The centre of a pattern is located at the pixel with the highest charge (dark blue). The other pixels coloured in blue have a lower charge which is still above the threshold. In case of the quadruple patterns also the position of the pixel with the lowest charge above threshold is defined (light blue). Pixels coloured in white must have a charge below the threshold. In SAS the pattern code 0 refers to single events, 1–4 to the double patterns, 5–8 to the triple patterns and 9–12 to the quadruple patterns. (Image based on Dennerl et al., 1999)

simulating spectra and which also need to be produced with SAS. One of these files is the response matrix file (RMF), which contains the respective detector response as a function of spectral channel and energy. The second file is the ancillary response file (ARF), which contains the energy-dependent effective area model. The product of these two files gives the probability that a photon with a given energy will be detected in a specific spectral channel. As the content of these files is based on the instrument calibration, they are inevitably affected by calibration uncertainties. To estimate the on-axis effective area calibration uncertainty, the Corrarea tool was introduced with SAS version 14. It comes in form of a correction function implemented as an extension in the effective area CCFs, namely the XAREAEF constituents, and can be accessed when creating an ARF with the `arfgen` SAS task by setting `applyxcaladjustment` to true, which is currently a non-default option.

3.3 Corrarea

3.3.1 The Original Source Sample

It is intended to make Corrarea a default correction for the effective area calibration uncertainties rather than solely a tool to estimate their impact. The original Corrarea version by Guainazzi et al. (2014) is, of course, the starting point to do so and shall, thus, be presented in the following sections. It was developed based on a source sample compiled by Read et al. (2014) according to a number of selection criteria set in order to find suitable sources. The sources were selected from the *XMM-Newton Serendipitous*

Source Catalogue[34] in its 2XMMi-DR3 version (Watson et al., 2009), which contains almost 5000 observations obtained with XMM-Newton between February 2000 and October 2009. These observations include more than 350 000 source detections, which comprise more than 260 000 unique sources (XMM-Newton Survey Science Centre Consortium, 2010). Please note that in the context of the CORRAREA source sample the term *source* does not automatically imply distinct sources. One and the same source can be added to the sample multiple times if it has been observed more than once with the selection criteria being met. As the focus lies on the analysis of the instruments' performance and not on the physical properties of the sources, the identification of the sources is not of interest here and each of their observations is treated as if concerning an individual source, being referred to with the respective observation ID. The seven selection criteria to add a source to the sample were defined in Read et al. (2014) as follows:

- *extent*: Only **point-like** sources, meaning sources which show no extension according to the catalogue, were included in the sample. This limitation eases the analysis considerably and these sources offer a high signal-to-noise ratio (S/N).
- *position on the detector*: As the current concern of CORRAREA is the calibration of the on-axis effective area, only sources with a near **on-axis** position on the detectors were selected. To do so, the smallest boresight-to-source distance amongst the three detector values, meaning the smallest angular distance between the on-axis position and the source detection position, was set to be below $2'$.
- *filters*: For a consistency in the filters involved, the sources were limited to encompass only those observed with the **thin and/or medium filters** as these filters are most commonly used.
- *modes*: To also have a consistency in the modes involved, only **FF mode** observations were allowed in the sample. FF is the most commonly used science mode, it is best suited for background subtraction since the CCD regions around the on-axis sources are all active and the best CTI calibration can be expected for it.
- *count rates*: With pile-up being an issue, it was made sure that the sources' count rates do not exceed the values given as **pile-up limits** in the *XMM-Newton Users Handbook*. These limits depend on the science mode used. According to the handbook version referred to, namely version 2.10, these limits are at $0.7\,\mathrm{cts\,s^{-1}}$ for the MOS FF mode and at $6\,\mathrm{cts\,s^{-1}}$ for the pn FF mode.
- *total counts*: To reduce the impact of background issues, like differences in the effective area of source and respective background regions, a **minimum number of counts** in the 0.2–12 keV range was required. Only sources with more than 5000 counts in the case of the MOS cameras and more than 15 000 counts in the case of the pn camera were included.
- *Galactic latitude*: A Galactic latitude either below $-15°$ or above $15°$, as shown in Figure 3.14, was defined as a last criterion to ensure the selected sources lie **out of the plane of the Galaxy** and, thus, reduce effects due to Galactic absorption.

[34] accessible in its current version via the XMM-Newton Science Archive at `https://www.cosmos.esa.int/web/xmm-newton/xsa` or via `https://heasarc.gsfc.nasa.gov/W3Browse/xmm-newton/xmmssc.html`

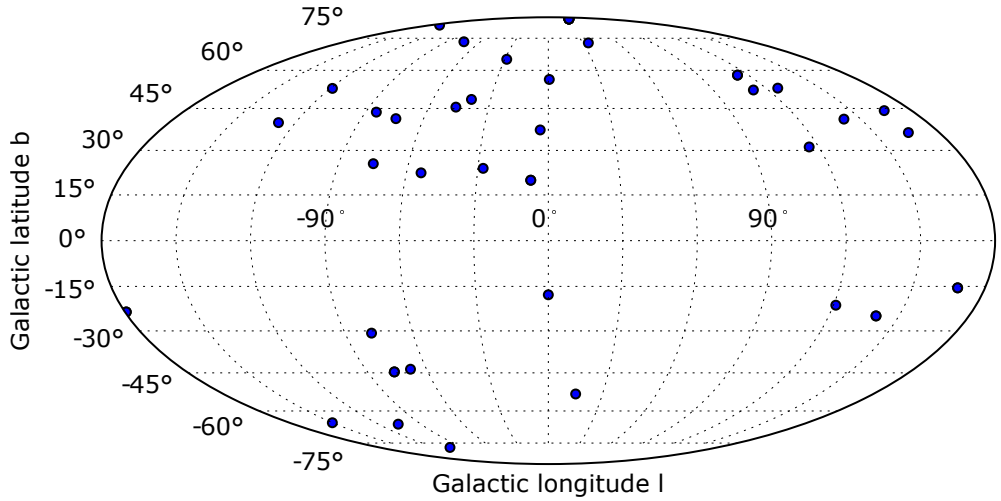

Figure 3.14: Galactic coordinates of the final 46 sources included in the original Corrarea source sample. Only 36 locations are shown due to multiple occurences in the sample (i.e. seven unique sources were observed twice or several times so that they actually amount to 17 sources in the sample). Sources with a Galactic latitude between $-15°$ and $15°$ were considered ineligible for the sample.

These selection criteria, taken together, are quite restrictive and already led to a reduction of the potentially suitable sources down to 87 out of the more than 350 000 source detections in the catalogue. A follow-up screening of the sources led to further exclusions from the sample. This screening involved a filtering for so-called good time intervals (GTIs) as well as an examination of images.

GTIs are those intervals in which observations are free from background flares. To filter out times affected by background flaring, Read et al. (2014) used their calibrated event lists and, excluding the CCDs with the on-axis position, created lightcurves in the 10–15 keV band with a binning of 100 s. To define the GTIs, a fixed limit of 40 counts per bin was set for the MOS cameras and of 130 counts per bin for the pn camera. Bins with an exceeding number of counts were rejected. The single GTI files defining the individual GTIs of the MOS1, MOS2 and pn camera, respectively, were then combined to one common GTI file including only time intervals that remained for all three cameras. The reason to do so is the comparability of the cameras' performances. With the common GTI file, GTI-filtered event lists were created, which were then used to also create images for image screening. In the screening process sources were dismissed in case of:

- a **GTI-filtered exposure time** below 1 ks.
- **crowded fields** in which either other sources were too close to the target source or which led to the intended background region (see Chapter 3.3.2) not being source free.
- **CCD chip gaps or bad CCD columns** being too close to the source region.
- **extended emission**, either from the target source itself or of another origin.
- a **CCD chip loss** or loss of an entire pn quadrant during the observation.

The screening further reduced the 87 initially selected sources down to 46 sources, which constitute the final source sample of the original CORRAREA version. These are the sources which were shown in Figure 3.14. A list of the sources is given in Table A.1 in form of the respective observation ID. The table also includes the common GTI-filtered exposure time for each source. Combined, the source sample amounts to a total exposure time of 1751.9 ks available for the effective area analysis in the original CORRAREA version.

3.3.2 The Stacked Residual Method

Using the final sample of selected sources, the stacked residual method (Longinotti et al., 2008; Kettula et al., 2013; Schellenberger et al., 2015) was applied as the basic method behind CORRAREA. When modelling a spectrum, the residuals represent the deviation between the data and the fitted model. Here, the residuals are defined as the observed spectral data divided by the applied model folded with the respective instrument response, namely the RMF and ARF:

$$\text{residuals} = \frac{\text{data}}{\text{model} \otimes \text{response}} \,. \tag{3.1}$$

If two cameras were equally well calibrated, a specific model would match the observed data of both cameras equally well and the residuals would not differ. Thus, the residual ratio, which compares the residuals obtained for two different cameras, is a good measure for the XMM-Newton effective area calibration uncertainties, since these uncertainties are the dominant ones over almost the whole energy range covered by the satellite. In order to use the residual ratio for a cross-calibration of the three EPIC cameras, one of them has to be chosen as the reference instrument with which the other two are to be compared. Since the pn camera has shown the most consistent performance and collects more photons, due to the lack of an RGS grating assembly in the light path and to it being more sensitive, Read et al. (2014) selected it as the reference instrument. Following Kettula et al. (2013), the residual ratio $\mathcal{R}$ between one of the MOS cameras ($j = \text{MOS1}, \text{MOS2}$) and the pn camera is then defined as

$$\begin{aligned} \mathcal{R} &= \frac{\text{residuals}_j}{\text{residuals}_{\text{pn}}} \\ &= \frac{\text{data}_j}{\text{model}_{\text{pn}} \otimes \text{response}_j} \times \frac{\text{model}_{\text{pn}} \otimes \text{response}_{\text{pn}}}{\text{data}_{\text{pn}}} \end{aligned} \tag{3.2}$$

for each energy bin. As the equation shows, the same model, model_{pn}, is applied for the MOS cameras and the pn camera. The intended model is first fitted to the pn data and then folded with the MOS response with the model parameters fixed to the values from the pn fit. This ensures the comparability of the residuals and the value of the residual ratio would be equal to one in case of a perfectly conform cross-calibration.

For the residual ratio to be generally representative of the cameras' performance, an empirical analysis is necessary, including not only one but several observations. In case of the original CORRAREA version, the source sample as introduced in the previous section was used. To combine the data of all observations, Read et al. (2014) applied the stacked residual method using the *stack and fit* approach. For each camera, the

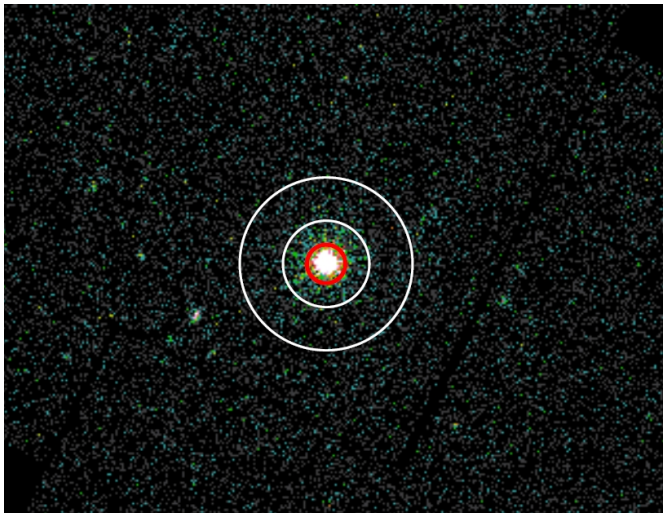

Figure 3.15: Example of the extraction regions as used for the original CORRAREA version. The circular source extraction region is shown in red, the white annulus marks the background extraction region. This is a slightly zoomed-in MOS1 image.

extracted source spectra of all observations were first stacked to one spectrum, which was then fitted with a phenomenological model.

The extraction regions for the source and background spectra were defined for all observations and all three EPIC cameras alike (see Figure 3.15 for an example): a circle with a radius of 40″ was used for the source regions, an annulus with an inner radius of 90″ and an outer radius of 180″ around the source region was used for the background regions. Besides the source spectra and the background spectra, an RMF and an ARF file were created for each observation and camera, as would have been necessary for an individual fitting for each source. The complete stacking process then involved the creation of one stacked source spectrum, one stacked background spectrum, one average RMF and one average ARF for each camera, respectively. More details on the procedure are given in Chapter 3.4.1.

With these files, the spectral fitting for the stacked spectra of the whole source sample could be performed. The spectra and fitted model for MOS1, MOS2 and pn are shown in Figure 3.16. From several phenomenological models tested, Read et al. (2014) found that

$$\texttt{wabs} \times [\texttt{power} + \texttt{power} + \texttt{Gauss} + \texttt{Gauss} + \texttt{Gauss}] \times \texttt{edge} \tag{3.3}$$

resembled their stacked pn data well, with a reduced chi-squared (χ^2_{red}) of 1.19 for 1888 degrees of freedom (dof). The `wabs` component is intended to take account of photo-electric absorption, `Gauss` stands for a Gaussian line profile, `edge` is an absorption edge component and `power` is a power law $\mathcal{F}_{\texttt{pow}}$, which is defined as

$$\mathcal{F}_{\texttt{pow}}(E) = K_{\texttt{pow}} E^{-\Gamma} \,, \tag{3.4}$$

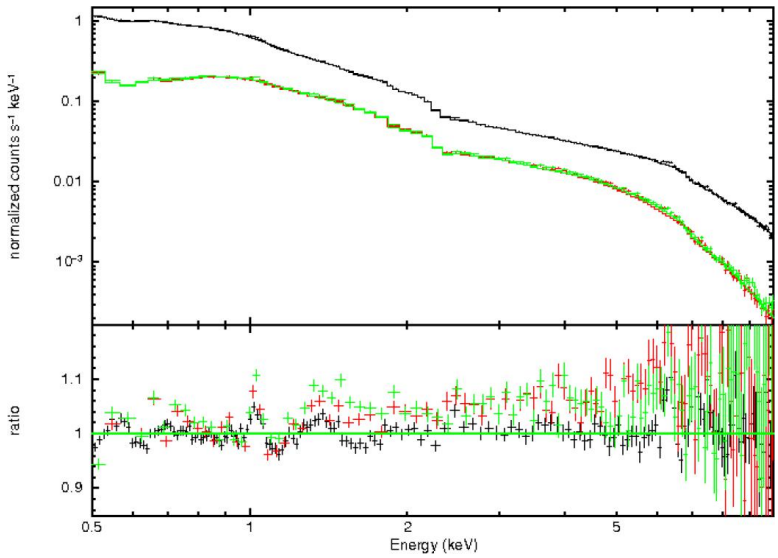

Figure 3.16: Fit of the stacked spectra for the original source sample. The upper panel shows the source spectra and model, the lower panel the residuals (MOS1: red, MOS2: green, pn: black). The phenomenological model was first fit with the pn spectrum and then, with fixed parameter values, convolved with the MOS responses. Please note that the axis label *ratio* in the lower panel does not refer to the residual ratio but to the residuals being defined as the ratio of data and fitted model. (Read et al., 2014)

with the energy E, the normalization parameter $K_{\texttt{pow}}$ and the photon index Γ.[35]

Read et al. (2014) pointed out that the exact choice of the model did not influence their final residual ratio results. Since the same model is applied to both, MOS and pn, any model-based variation of the residuals is cancelled out in equation 3.2, where the MOS residuals are divided by the pn residuals.

3.3.3 The Correction Function

Once the residual ratio values are determined, they can be used to find a correction function for the effective area calibration. While Read et al. (2014) used SAS version 12.0.0 and the corresponding calibrations for their residual ratio analysis, Guainazzi et al. (2014) re-extracted the spectra with SAS version 13.5 and the then-public calibrations, before they repeated the stacking procedure in order to complement the analysis with a function to be used as the CORRAREA correction.

The residual ratios they obtained in the 0.7–7.0 keV range are shown on the left in Figure 3.17. There is an excess of the MOS residuals with respect to the pn residuals of mostly around 5%. This matches the discrepancy already indicated by the flux ratio discussed in Chapter 3.1. Since the pn camera is the reference instrument, its residual ratio would be unity, which is indicated by the dashed line in the plot.

[35] A larger photon index indicates a softer spectrum.

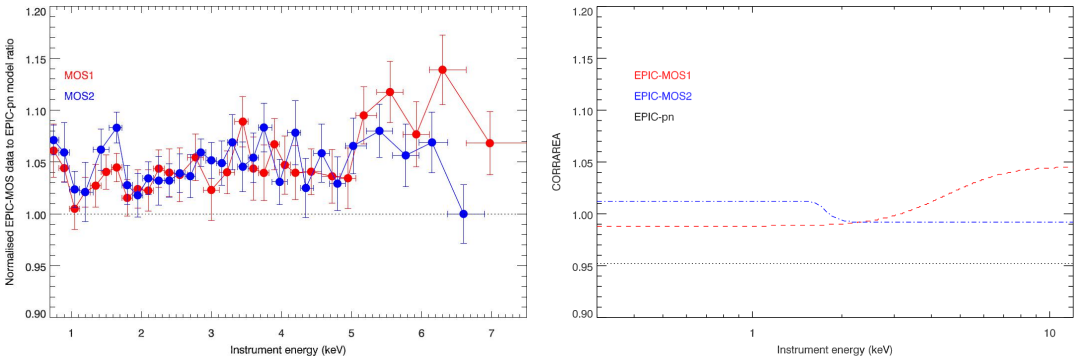

Figure 3.17: Residual ratios (left) and correction functions (right) of the original CORRAREA version. The black, dotted lines show the pn correction factor. The correction functions on the right are generally lower than than the residual ratios on the left since the pn correction factor α_{pn} was set to a value not equal to one to account for the relative difference of the EPIC performance compared to other observatories operating in a soft X-ray band. (Guainazzi et al., 2014, modified)

To get the energy (E)-dependent CORRAREA correction function $\mathcal{C}$ for the two MOS cameras (j = MOS1, MOS2), Guainazzi et al. (2014) used a Gompertz function to fit the general trend the residual ratios follow:

$$\mathcal{C}_j\,(E) = \alpha_j + \alpha_{\mathrm{pn}} + \beta_j \times \exp\left(-\gamma_j \times \exp\left(-\delta_j \times E\right)\right), \tag{3.5}$$

where α_j, β_j, γ_j and δ_j are the best fit parameters. The current CORRAREA functions are shown in the right plot in Figure 3.17. An energy-independent correction factor α_{pn} was added for the reference camera, pn, to account for the relative difference in performance between EPIC and cameras on board other X-ray observatories. This correction factor was based on cross-calibration studies between the corresponding instruments of XMM-Newton, Chandra, Suzaku, BeppoSAX and Swift (Nevalainen et al., 2010; Ishida et al., 2011; Tsujimoto et al., 2011).

For CORRAREA as a mere estimation tool, this constant, energy-independent pn correction factor can be sufficient. To apply CORRAREA as a default correction, it is considered to be too vague. To include a cross-calibration with other satellites, a more thorough, energy-dependent study would be necessary. Before this can be done, a reliable cross-calibration of the three EPIC cameras has to be achieved first. As far as this work is concerned, the pn correction factor is, thus, fixed to unity.

In order to make CORRAREA a default correction, the tool requires a reconsideration of the source selection and data reduction choices made, a thorough validation of its applicability and recalibration with an updated calibration status. A set of scripts was developed in the course of this work so that the required reruns of the different steps in the process can be performed more easily and faster, both for the current analysis and for future recalibrations of CORRAREA.

3.4 Automation

3.4.1 The Procedure

In this work, the original procedure to determine the CORRAREA correction function has been expanded. On the one hand, a targeted objective was to be able to reproduce the original CORRAREA correction to validate the developed scripts and the stacking process included. On the other hand, for a new CORRAREA version suitable to be used as a default correction, revised selection criteria and additional screening steps to examine the selected observations were considered to be necessary. A detailed description of the changes made and the additions to the procedure follows in Chapter 3.5.

At this point, an overview of the necessary steps and of the sequence in which they are performed is given. The main procedure is shown in Figure 3.18 and Figure 3.19. Besides a major part of the process being automated with the scripts, there are still manual steps included where personal assessment is required. These manual steps are mainly only necessary for sources newly added to the source sample. Also, some of these steps comprise methods for the recalibration and are, thus, not needed for running the mere procedure of the original CORRAREA version, as indicated by the dashed lines in the figures.

As for the automated steps, they are implemented in several separate scripts, which allows for the desired flexibility. The validation of the procedure and methods used for CORRAREA sometimes just requires reruns of individual steps and often only changes of parameters at one stage in the process are necessary so that not always the whole procedure needs to be rerun. The script package is mainly written in Python[36] and Bash, but use was also made of IDL and C Shell to draw on specific routines. SAS, HEASOFT and DS9 are called from within the scripts where needed. To define the source sample to be used, a list of the observation IDs needs to be given as input. The manual screening steps usually lead to the exclusion of observations, realized by continuing with a reduced observation list from which these observations were excluded. Corresponding to the numbering in Figure 3.18 and Figure 3.19, the individual steps included in the procedure are as follows:

1. **getting the data of the selected source sample**
   After the source sample has been selected based on the defined selection criteria – either the criteria as defined for the original CORRAREA version (as described in Chapter 3.3.1 before) or revised criteria (see Chapter 3.5.2) – the list of the observation IDs is given as an input file to download all required ODFs from ESA's XMM-Newton Science Archive in one go and unpack the data into a separate folder for each observation, respectively.
2. **performing the initial data processing**
   Following the instructions in *The XMM-Newton ABC Guide* and the *Users Guide to the XMM-Newton Science Analysis System* for the initial data processing, this script creates the calibration index files (using the SAS task `cifbuild`), the ODF summary files (`odfingest`) and the calibrated event files (`emproc`/`epproc`) for each observation. Calibration index files contain the location of the CCFs and information on which of them are relevant for a specific observation. The ODF

[36] To be precise, the Anaconda Python distribution was used, which already includes the Astropy package for astronomy-specific tasks.

summary files provide SAS with necessary information on the observations. Finally, calibrated event files are obtained for each of the three EPIC cameras and each exposure, respectively. As it is an extensive step to process the data for a large number of observations, the script logs the output of all tasks so that any errors occurring in the processing can be detected. By default, the latest calibration status is applied to process the data in this step. But the script allows for setting a past analysis date, which is useful to compare different calibration stages and, in this particular case, was needed to test if the script package can reproduce the results of the original CORRAREA version (as done in Chapter 3.4.2).

3. **filtering out periods of high particle background**
In this step, periods of soft proton flares are filtered out from the calibrated event lists. This is necessary because these flares constitute a background component strongly varying over the course of an observation. To define good time intervals (GTIs) without flaring, a limit to the counts per time bin needs to be set. Only time bins with less counts are then considered to be GTIs. To ensure comparability of the MOS and pn cameras in the end, only good time intervals (GTIs) common to all three EPIC cameras within an observation are used here to filter the data.

   The script consists of two main parts. In the first part, the light curves necessary for the filtering are created, if they do not already exist from a previous run, and the GTIs are defined for each camera and exposure. Empty GTI files, resulting from an exposure being entirely affected by flaring, are dismissed by being shifted into a separate folder. Two options are provided to define the GTIs: using either the GTI filtering method applied for the original CORRAREA version or a revised approach. Following the original method described by Read et al. (2014), the light curves are created with the SAS task `evselect` in the 10–15 keV band, using only single patterns, the #XMMEA_EM (for MOS) or #XMMEA_EP (for pn) filter[37] as well as a binning of 100 s and excluding the CCDs covering the on-axis position. The maximum counts per bin value is then set to the same value for all observations and the respective GTI files are created using TABGTIGEN. For reproducing the original CORRAREA version, the maximum is set to 40 counts per bin in the case of MOS, to 130 counts per bin in the case of pn.

   The revised method (see Chapter 3.5.1) allows for a GTI filtering individually adjusted to each observation. First, the light curves are created similarly, but, following the instructions in the *Users Guide to the XMM-Newton Science Analysis System*, an upper energy limit of 12 keV was set for the pn data and no CCDs were excluded. The basic principle behind this revised method is the determination of two limiting thresholds for the counts per bin in a lightcurve (one based on the Gaussian distribution of the data and one on the signal-to-noise ratio, S/N), and selecting the more conservative threshold for the filtering and creation of the GTI files (see Chapter 3.5.1 for details). The two thresholds are determined with the implemented `deflare` subscript.[38] As shown in Chapter 3.5.1, the S/N threshold can fail in a few exceptional cases, making a fixed selection of the Gaussian threshold, available as an option in the script, necessary for them. For

[37] The #XMMEA_EM and #XMMEA_EP filters provide a set of conditions for events to be excluded, like being outside of the FOV or on bad pixels.

[38] The `deflare` script is based on a script by M. Smith at ESAC, which was adjusted to be used in the routine and meet the requirements here.

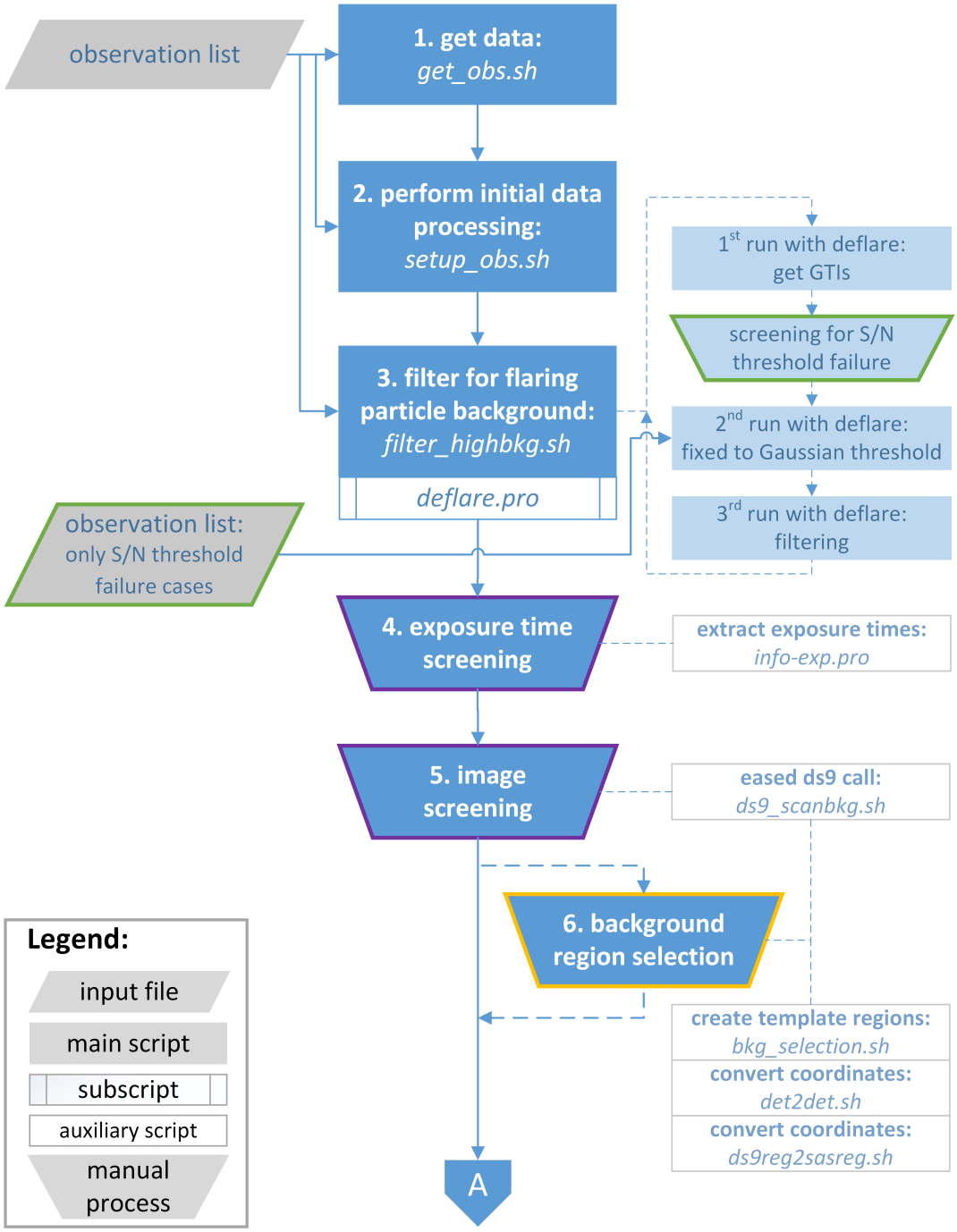

Figure 3.18: The main procedure and script package to determine the CORRAREA correction function. Individual steps are numbered according to their description in the text. The names of the corresponding scripts are given in italics. Input files with a coloured frame result from the manual processes framed accordingly. Steps linked with dashed lines are optional as they are needed almost exclusively for executing a revised procedure (as compared to the original CORRAREA version), depending on new methods and data processing options chosen. For reasons of clarity, auxiliary scripts and required input files are not connected. The chart is continued in Figure 3.19.

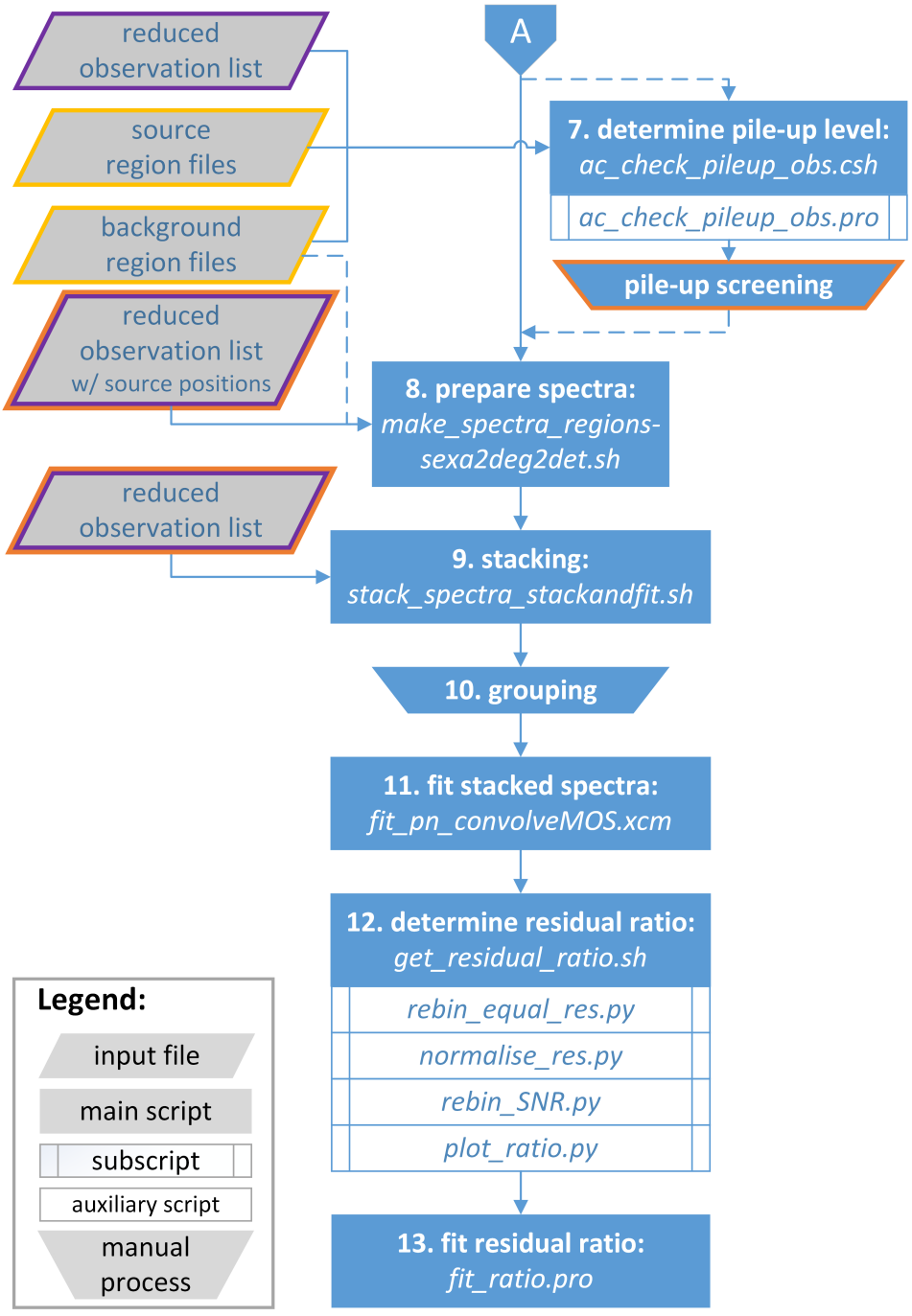

Figure 3.19: Continuation of Figure 3.18.

this purpose, the two parts of the script can be run separately, so that the correct GTI definition can be ensured before the actual filtering is done.

In the second part of the script, the common GTI file with time intervals remaining for all cameras alike is created with `mgtime` for each observation and then used to filter the event files of each camera and exposure with `evselect`. Like the empty GTI files before, event files that end up empty, which can happen if an exposure does not contain any time intervals covered by all three cameras, are dismissed. Besides the new, filtered event files, also images are created in both, sky and detector coordinates, again for each EPIC camera and exposure.[39] These images are needed for further processing to check the general suitability of observations and to define source and background regions. To avoid anomalous MOS CCDs to be used when defining the regions for data extraction, events from potentially affected CCDs are excluded from the images in detector coordinates.[40]

4. **ensuring the remaining exposure time is sufficiently high**
To ensure each observation has sufficiently high statistics to evaluate its suitability for the analysis in the following steps, a minimum exposure time limit was set. As for the original CORRAREA version, this limit was kept at 1000 s throughout this work. Observations with a shorter common GTI-filtered exposure time than the defined value are excluded from the observation list in this step. To extract the exposure times, the `info-exp` auxiliary script can be used, which sums up all time intervals included in the common GTI file for each observation, respectively, and writes them into a single output file for assessment.[41]

5. **screening of images to exclude unsuitable observations**
With the images created in step 3, the observations can now be screened for their general suitability. Following the procedure for the original CORRAREA version, the cases checked for here are the aforementioned crowded fields, CCD chip gaps or bad CCD columns, extended emission and CCD chip or quadrant loss. Affected observations are, again, dismissed from the observation list that is used as input for following steps. Of course, if the whole procedure is rerun with new settings, calibrations etc., this step does not have to be repeated for observations that have already been screened for the defined cases. But any observation of a potential new addition to the source sample (see Chapter 3.5.2) has to pass through this stage and, also, new criteria to exclude observations might make a new screening round necessary for the whole sample. The results of the screening for a revised, recalibrated CORRAREA version are presented in Chapter 3.5.3.

Together with the following selection of individual background regions, this is the most extensive manual step included in the procedure since all images of each detector, exposure and observation should be screened. The auxiliary script `ds9_scanbkg` helps to speed up the process by offering an easy call of the

[39] For the MOS cameras, the images are created in the 0.2–12.0 keV band, using patterns 0–12 and setting the #XMMEA_EM filter. For pn, the 0.2–15.0 keV band, only single and double events and the FLAG==0 setting (which besides #XMMEA_EP also rejects events close to bad pixels and CCD gaps) are used to create the images.

[40] CCD4 in the case of MOS1 and CCD5 in the case of MOS2, which are often found to be in an anomalous state, are generally excluded. Also, CCDs tagged as being in an anomalous state by the SAS task `emtaglenoise` are not used here.

[41] The `info-exp` script is based on a script by S. Saeedi, which was extended for the required purpose in the routine.

individual images with display parameters that immediately show the images clearly in DS9 and allow for a quick evaluation.

6. **selection of individual background regions**
   In contrast to a generalized background region definition applied for the original CORRAREA version, background regions selected individually for each observation and detector were considered preferable for the recalibration. The approach and criteria to select suitable regions are described in detail in Chapter 3.5.4. Region files already containing potential regions to choose from are provided by the `bkg_selection` script and are automatically loaded when using the previously mentioned `ds9_scanbkg` script for displaying the images. For each image the selected background region then needs to be saved in a background region file.

   The `det2det` script is a minor script to copy and convert a background region file of one detector to a region file for one of the other detectors. This can be useful for the two MOS detectors, if the same region in the sky is suitable for both of them.[42] Finally, the `ds9reg2sasreg` auxiliary script converts the region definitions from all DS9 background files to the region syntax required by SAS.

7. **screening for pile-up**
   For the original CORRAREA version, a maximum count rate limit was set as a criterion for selecting suitable sources in order to obtain a pile-up free source sample. However, the pile-up limits given in the *XMM-Newton Users Handbook* only indicate above which count rate a high pile-up level is to be expected but it does not imply that the observations of sources with lower count rates are completely pile-up free. A method to evaluate the pile-up level more thoroughly was, thus, pursued in the course of this work. For this purpose, a couple of scripts, provided by M. Stuhlinger at ESAC, were adjusted so they could be integrated into the procedure. Among other things, these scripts make use of the fraction of pile-up-exclusive MOS diagonal events and provide an output file with which the observations of the whole sample can be screened for pile-up (see Chapter 3.5.5 for an in-depth description of the pile-up analysis). Observations of affected sources are then excluded from the observation list for further processing.

8. **preparing the individual spectra**
   Once the final source sample to be used for the stacked residual method has been defined after passing the screening steps, the source spectra and all related files needed for spectral analysis can be prepared. The dedicated script automatically creates all source spectra, background spectra, RMFs and ARFs and sets the so-called BACKSCAL keyword in the headers of the spectral files, which gives the extraction area size taking chip gaps and bad pixels into account.[43] With respect to the region selection, the script offers options corresponding to the different region definitions required for reproducing the original CORRAREA version, as described by (Read et al., 2014), and for creating a revised and recalibrated tool.

   For the source regions, generally a circle is defined which is centred on a source's position given in the observation list input file. In the present work,

[42] For the pn detector, different criteria apply to the background region selection and chip gaps usually require different sky regions compared to the MOS detectors.

[43] Also source and background event files as well as images of the extracted regions are created as side-products as they can be used for further examination.

the source positions were extracted from the *XMM-Newton Serendipitous Source Catalogue* and are converted from equatorial to detector coordinates by the script, also making use of the `ecoordconv` SAS task. In case of the original CORRAREA version, a radius of 40″ was used for all sources. But the parameter can be set to a different value in the script and, also, different values can be given for MOS and pn, respectively. This way, sources which only allow for a smaller source extraction radius may be kept in the sample, improving the statistics, and an analysis of possible effects different source region radii have on the final result can be done.[44]

As for the background regions, one option is to select an annulus of equal size for each observation and detector around the respective source. This follows the original CORRAREA version, for which an annulus with an inner radius of 90″ and an outer radius of 180″ was selected. The parameters for these radii can be set to different values in the script to keep this approach for a general background region definition that is the same for all observations more flexible. Besides this approach, the option to use the individual background region files created for each observation and detector in step 6 can be selected. The extraction of background spectra can also be disabled in the script. If source spectra are created for different source region sizes, a repeated creation of the background spectra is usually not necessary and would only slow down the process.

Following the recommendations for creating spectra in the *Users Guide to the XMM-Newton Science Analysis System*, as was done for the original CORRAREA version, spectra for source and background regions are created with `evselect` with a spectral bin size of 5 eV and using patterns 0–12 and the #XMMEA_EM flag set for MOS, patterns 0–4 and the FLAG==0 setting for pn. Once the spectra are extracted, the BACKSCAL value is calculated and saved in the FITS file headers for each spectrum using the SAS task `backscale`. All corresponding RMF and ARF files are created with the standard SAS tasks `rmfgen` and `arfgen`. After the script has been run, each observation folder contains the source and background spectra as well as RMFs and ARFs for each exposure of each EPIC detector.

9. **stacking the spectra and related files**
The stacking script, which makes use of various FTOOLS, stacks the prepared source spectra, background spectra, RMFs and ARFs, respectively, for each EPIC camera, following the description in Read et al. (2014). In order to obtain a stacked source spectrum, the counts per bin of all sources are summed up as are the exposure values to get the total exposure time. The BACKSCAL value for the stacked spectrum is obtained by exposure-weighting the individual values. The same is done with the background spectra to get a stacked background spectrum. To get an average ARF that corresponds to the stacked source and background spectra of the respective camera, the exposure-weighted values of all sources are merged for each bin, respectively. As for the RMF, the ftool `addrmf` is used to stack the exposure-weighted values (with the exposure-weights as a fraction of a total of one as required by the task). With one stacked source spectrum, background

[44] An auxiliary source region file is prepared for screening purposes using the `bkg_selection` script during the background region selection, step 6. But it is not used for the extraction of the source counts as changes to the source region definition can be much quicker made if it is directly set in the script for creating the spectra.

spectrum, RMF and ARF for each of the three EPIC cameras, spectral fitting can be performed to get the empirical residual ratios.

10. **grouping the data in the stacked spectra**
Before the fitting with XSPEC, the `grppha` command needs to be run for each spectral source file. The task defines the grouping of the counts in a spectrum and adds necessary information to the file, such as the BACKFILE, RESPFILE and ANCRFILE keywords in the spectral file header, which need to be set to the file names of the corresponding background spectrum, RMF and ARF, respectively. The chosen binning factor for the grouping depends on the intended purpose. If a model shall be tested first to see how well it fits the spectra (using the chi-squared test), a rebinning with a sufficient minimum number of counts per bin should be done. For calculating the residual ratios, keeping the bins as they are, without rebinning them at this point, offers the largest flexibility for the residual ratio resolution later on but cannot always be fitted equally well.

11. **fitting the stacked spectra**
The corresponding script for fitting the stacked spectra (`fit_pn_convolveMOS` in Figure 3.19) is in a format to be directly executed in XSPEC. The phenomenological model to be used needs to be defined in this file first before being automatically fit to the stacked pn spectrum and then convolved with the MOS1 and MOS2 instrument responses. Usually, the model used in this work is the same as for the original CORRAREA version. As mentioned earlier, the precise choice of the model does not change the final result in form of the CORRAREA correction as any differences are cancelled out when the residual ratio is calculated. But any chosen model should still represent the data properly so its use can be justified. Therefore, adjusting the model is sometimes necessary, for example when observations done in other science modes are included for the revision of the CORRAREA tool or when a broader energy range is used.

    To reproduce the original CORRAREA version, the energy range selected for the fitting was set to 0.5–10.0 keV as given by Read et al. (2014). This range was kept unless a broader energy range became necessary. In general, the energy range depends on the energy range for which the residual ratios, and, thus, the applicability of the correction function, shall be obtained. The energy range at this point needs to be at least slightly wider than the range for which the residual ratios are to be calculated so that the marginal values are included.

    Once the model has been fit to the stacked pn spectrum and convolved with the MOS responses, the resulting residual values per energy bin are automatically saved to a text file for each camera, respectively, for further processing. Also, the fit results, together with an image of the fitted spectra, are saved for inspection.

12. **determining the residual ratio**
Using the residual files provided before, the ratios of the MOS residuals to the pn residuals are calculated. As this requires the division of the values for the two different camera types, MOS and pn, the residuals first need to be reallocated to a new, uniform energy grid because, even though the same binning factor was used when creating the spectra with `evselect`, the energy ranges of the bins differ slightly due to the different redistributions of MOS and pn. For the reallocation, the `get_residual_ratio` script does not only load the residuals, corresponding

energies and respective errors from the residual files but also reads in the lower and upper energy boundaries for each bin from the stacked RMF of each EPIC camera, respectively. During the process of reproducing the original CORRAREA results with the scripts, two options for the reallocation of the energy channels were developed. One is to keep the MOS bin ranges and only adjust the distribution of the pn residuals to them. The second, and in the end more commonly used, option is to define the total energy range and total number of bins wanted in the script, which then determines the respective lower and upper energy boundaries of the new bins of equal size and reallocates the residuals of all three cameras to this new linear energy grid. For the reallocation the subscript `rebin_equal_res` is called for each camera. It determines the coverage fraction of the original energy bins with respect to the newly defined bins and reallocates the residuals accordingly.

With `normalise_res` the MOS residuals are then divided by the reference pn residuals for each new bin, respectively, to get the MOS-to-pn ratio. The resulting output file is used to determine the CORRAREA correction function in the next, final step. For illustration purposes, the two additional subscripts can be enabled optionally. The `rebin_SNR` script provides an adaptive binning for clearer presentation by rebinning the data in a SNR-like manner.[45] With `plot_ratio` a plot of the residual ratios is automatically created (either with or without prior rebinning).

13. **fitting of the residual ratio**
Finally, the CORRAREA correction function, respectively for MOS1 and MOS2, can be determined. The `fit_ratio` script asks for the intended function and start parameters and fits it separately to the MOS1 and MOS2 residual ratios. The final parameters values are saved in an output file and also plots are created automatically for immediate inspection.

3.4.2 Reproduction of Results from the First CORRAREA Version

To validate the stacking performed with the scripts, a test to see if the results of the original CORRAREA version could be reproduced was first approached. Only steps 1–4 and 8–13 from the previous chapter had to be performed to do so as particularly most of the manual steps were introduced later to obtain a recalibrated, more reliable tool.

Guided by the date of the CORRAREA release note, which is 19 September 2014 (Guainazzi et al., 2014), SAS version 13.5 was used and the analysis date was set accordingly in the initial data processing step so that only the public calibration files valid at the time were employed. Also, the analysis was performed with the original sample of 46 sources as defined by Read et al. (2014, see Chapter 3.3.1). The same model (numbered 3.3 in Chapter 3.3.2) was used to fit the stacked pn spectrum. It led to an equally good fit as is shown in Table 3.3, in which the resulting parameters are compared with those given in Read et al. (2014). Figure 3.20 shows the stacked spectra with the model, fit to the pn spectrum and convolved with the MOS responses, as well as the resulting residuals.

The MOS-to-pn residual ratios are illustrated and compared with the residual ratios obtained for the original CORRAREA version in Figure 3.21. In general, the reproduced

[45] so that the ratio between the calculated residual ratio values and the corresponding, calculated errors reach a chosen, constant threshold in each new bin

Table 3.3: Comparison of the parameters given for the fit of the original stacked spectrum in Read et al. (2014) and obtained for the fit of the reproduced stacked spectrum in this work.

parameter	Read et al. (2014)	reproduced
`wabs`: N_{H} (10^{21} cm^{-2})	1.84	1.01
`power`$_1$: Γ	4.09	3.09
`power`$_2$: Γ	1.43	1.28
`gauss`$_1$: E (keV)	0.59	0.58
`gauss`$_2$: E (keV)	0.88	0.91
`gauss`$_3$: E (keV)	5.03	0.01
`edge`: E (keV)	6.85	6.84
χ^2_{red} (dof)	1.19 (1888)	1.08 (1888)

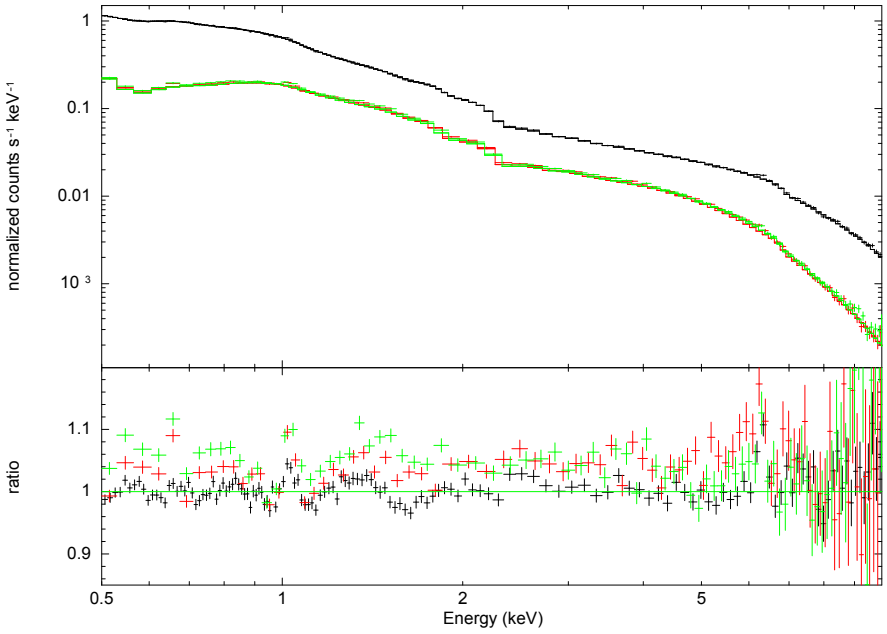

Figure 3.20: Stacked spectrum and residuals for the reproduction of the original Corrarea results using the original sample of 46 sources. MOS1 data are shown in red, MOS2 in green and pn in black. The fit of the model to the pn data resulted in a reduced chi-squared (χ^2_{red}) of 1.08 for 1888 degrees of freedom (dof).

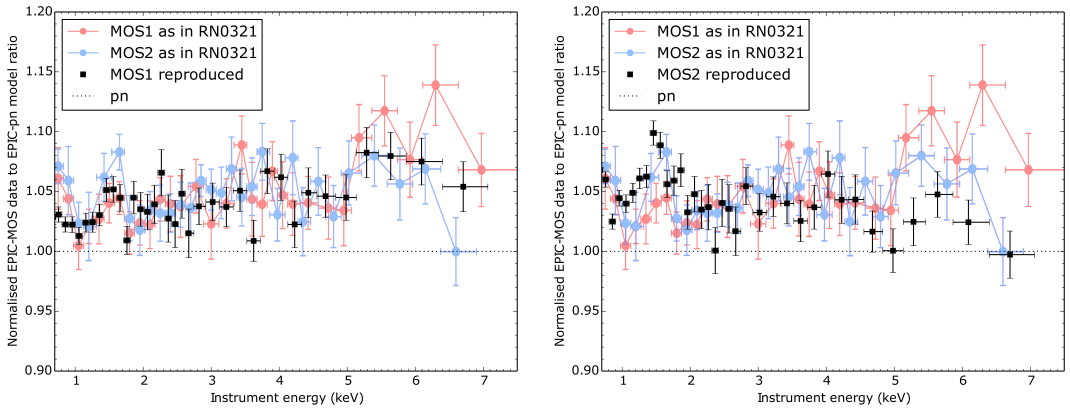

Figure 3.21: Comparison of the residual ratios from the original CORRAREA version and the reproduced residual ratios for MOS1 (left) and MOS2 (right). The illustration of the original data points (coloured) was taken from the CORRAREA release note (RN0321, Guainazzi et al., 2014, modified). The dotted line represents the ratio for the pn camera, which is unity as it is the reference instrument.

data of both MOS cameras show about the same values and shape as for the original version, particularly when taking the errors into account. Slight deviations can, however, occur either due to different binning factors being set at some stages or due to the applied calibration status not being precisely the same. To calculate the reproduced residual ratios, the residuals were redistributed to a new energy grid with a bin size of 0.1 keV and then redistributed for illustration purposes to achieve a SNR of 50. With this, a similar, but not precisely matching, distribution of the data points as shown for the original data could be achieved. As for the calibration status, the date of the CORRAREA release note was set for the reproduction of the results, but the precise calibration status with which the original analysis was performed might be of an earlier date. For example, also in 2014 calibration updates for the MOS and pn CTI and the PSF of the pn telescope had already been made public prior to the CORRAREA correction[46] but might not have been included in the original CORRAREA analysis since the analysis had to be performed some time before the release.

Finally, the residual ratios were fitted with the same function used for the original correction (introduced as equation 3.5 in Chapter 3.3.3). Figure 3.22 shows the original correction functions again, this time compared with the reproduced functions. As mentioned before, a constant factor was additionally added for the original correction to account for differences between the XMM-Newton cameras and instruments on other observatories. For this reason, the pn line is below unity and the MOS residual ratios are lowered accordingly in the original plot. But such a comparison with other observatories would require a much more extensive and detailed analysis before it can be included in a default correction. Therefore, the focus for a default CORRAREA correction has to lie in achieving a reliable, thorough reconciliation of the three EPIC cameras first, as aimed for in this work. The correction functions in the right plot of Figure 3.22, thus, do not show such an offset. But the general shapes of the reproduced correction

[46] an overview of the XMM-Newton calibration release notes is given at `https://www.cosmos.esa.int/web/xmm-newton/ccf-release-notes`

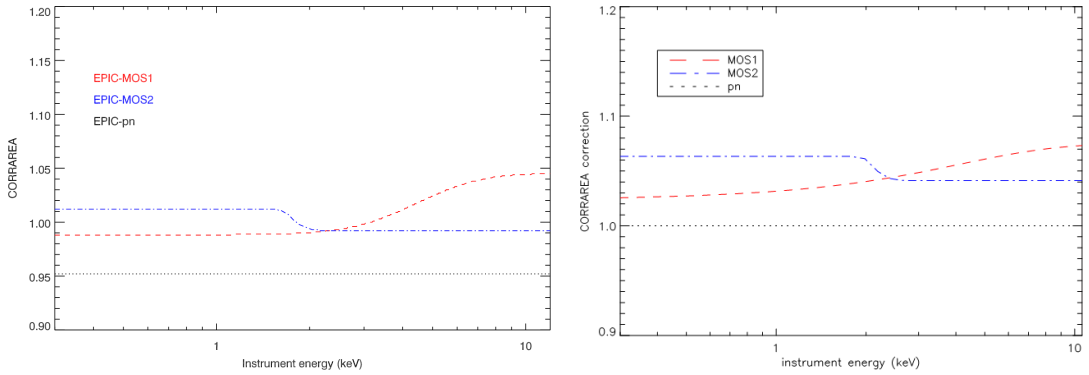

Figure 3.22: Comparison of the original CORRAREA correction functions (left) and the reproduced functions (right). The original functions include a constant factor to account for discrepancies between the effective areas of instruments from different observatories. Such a constant factor is not included in the reproduced results of this work. (Credit for the left image: Guainazzi et al., 2014)

functions match the original functions to a sufficient degree, with the expected slight deviations due to the possible reasons described before. In addition, the precise outcome of fitting processes can depend on initial parameter values given, the underlying fitting algorithms and sometimes even the computers used.

All in all, the original CORRAREA correction could be reproduced successfully with the developed script package and the stacking process performed with them could be validated. Once this was established, the scripts were used to further develop, validate and recalibrate the CORRAREA tool, as described in the following chapters.

3.5 Recalibration of the CORRAREA Correction

In the previous chapter, the same procedure as applied for the original CORRAREA version to process the data and obtain the correction functions in the end was followed. To make CORRAREA a default correction, a simple recalibration by using the newest calibration files is not sufficient but requires reconsideration of the choices made regarding the source selection and the procedure. These changes and additions for a revised CORRAREA version, which were already mentioned in the course of the script package description in Chapter 3.4.1, are explained and illustrated in detail here.

3.5.1 Revised GTI Filtering

The first change that was done to the procedure was to implement a method to individually define GTIs for each observation and camera. While for the original CORRAREA version fixed limits were set for the counts per time bin to filter out periods of high background flaring, the new method defines individual thresholds either based on the count abundance distribution or the SNR. This is done with light curves created as suggested officially for the GTI filtering (ESA: XMM-Newton SOC, 2018a), selecting energies $> 10\,\mathrm{keV}$ for MOS and 10–12 keV for pn and using a 100 s binning. An example of such a light curve is given in the top panel of Figure 3.23, which is an output of the

`deflare` script.[47] The mid-panel shows a histogram with the distribution of the counts per time bin. A Gaussian threshold is set at three times the standard deviation above the mean value, $\mu + 3 \times \sigma$. The bottom panel in the figure shows the SNR distribution with a second threshold being set at the maximum SNR. Of the two thresholds, the more conservative one is chosen as the counts-per-bin-limit to define the GTI periods for the respective exposure. Just as for the original GTI filtering method, a common GTI file, which only includes GTIs covered by all three EPIC cameras alike, is created for each observation first to ensure the MOS residuals and pn residuals are comparable. This common GTI file is then used to obtain the GTI-filtered event files.

A screening of the `deflare` output proved to be necessary as in few cases determining the SNR threshold fails. Drops in the light curve due to temporary detector outages can lead to an absolute SNR maximum at a count value of only zero or one, which would result in empty event lists with all events of an observation being filtered out erroneously. Figure 3.24 shows such a case. To correct for this, the option to force the filtering script to use the Gaussian threshold was introduced. Usually this is necessary for a minority of observations. For example, in the original sample of 46 sources only three were affected.

In Table A.1 in the appendix the remaining GTI-filtered exposure times obtained for the original sample with this new method are compared with the exposure times obtained with the original method using a fixed count limit value. Usually the new method leads to a more conservative filtering and, with the count limit being individually adjusted for each exposure, can be considered more reliable with respect to filtering out periods affected by flaring.

3.5.2 Source Selection for the Extended Sample

The *XMM-Newton Serendipitous Source Catalogue*, from which the sources in the sample were selected according to the defined criteria, is updated regularly. The 3XMM-DR7 version of the catalogue (Rosen et al., 2016) was used in this work to include a larger number of sources in the sample and improve the statistics and the validity of the Corrarea tool. Compared to the originally used 2XMMi-DR3 catalogue (Watson et al., 2009), the newer version provided about twice as many observations (∼9700 compared to ∼5000 before) and source detections ($> 725\,000$ compared to $> 350\,000$ before) to look for suitable source candidates for the sample.[48]

The selection of sources from the catalogue according to defined criteria is the first step to single out suitable sources.[49] Basically, the original criteria defined for the first Corrarea version as described in Chapter 3.3.1 were adopted for this work, with some alterations made as described below. As before, sources had to be point-like, near the EPIC on-axis position and out of the plane of the Galaxy to be selected. The remaining four selection criteria were altered as follows:

- *filters*: Besides sources that were observed using the thin and/or medium filters, also those observed with the thick filters were now included since there was

[47] The examples shown here were created with SAS version 16.1 and the calibration files public in December 2017.

[48] The statistics of the catalogue versions can be accessed via `http://xmmssc.irap.omp.eu/cat.html`.

[49] The search was conducted using the query form provided at `https://heasarc.gsfc.nasa.gov/db-perl/W3Browse/w3table.pl?tablehead=name%3Dxmmssc&Action=More+Options`.

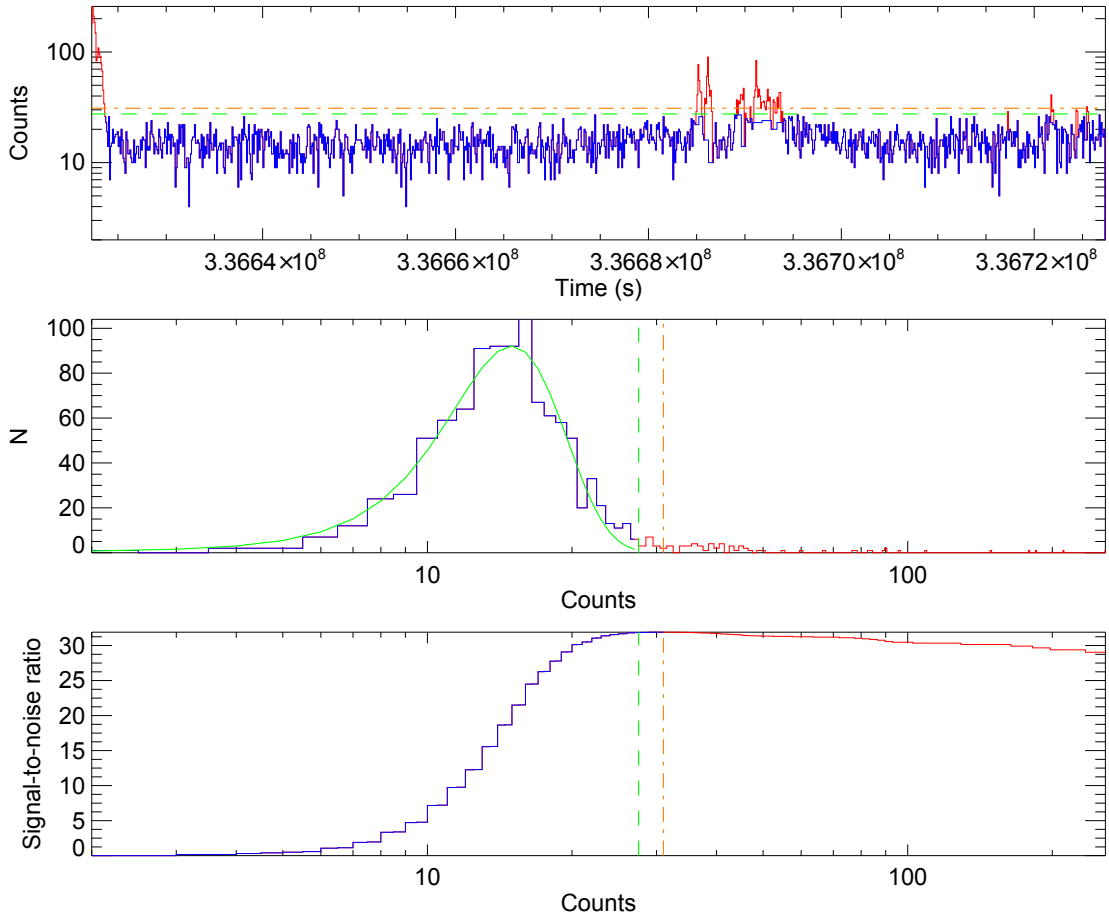

Figure 3.23: Example for the revised GTI filtering method showing the output of the `deflare` script for the MOS2 exposure of observation 0555650301. *Top panel:* light curve for energies $> 10\,\mathrm{keV}$ with a binning of 100 s; *Middle panel:* histogram showing the corresponding abundance distribution of the counts per bin with N occurences; *Bottom panel:* distribution of the corresponding SNR. The green, dashed line shows the Gaussian threshold at three times sigma above mean. The orange, dash-dotted line indicates the threshold set by the maximum SNR. In this case, the Gaussian threshold is the more conservative one and is selected to define the GTIs for this exposure. The blue data lie within the GTIs, the red data are not included. Note, however, that this does not automatically represent the final filtering since that is performed using the common GTI file, which might exclude further time frames.

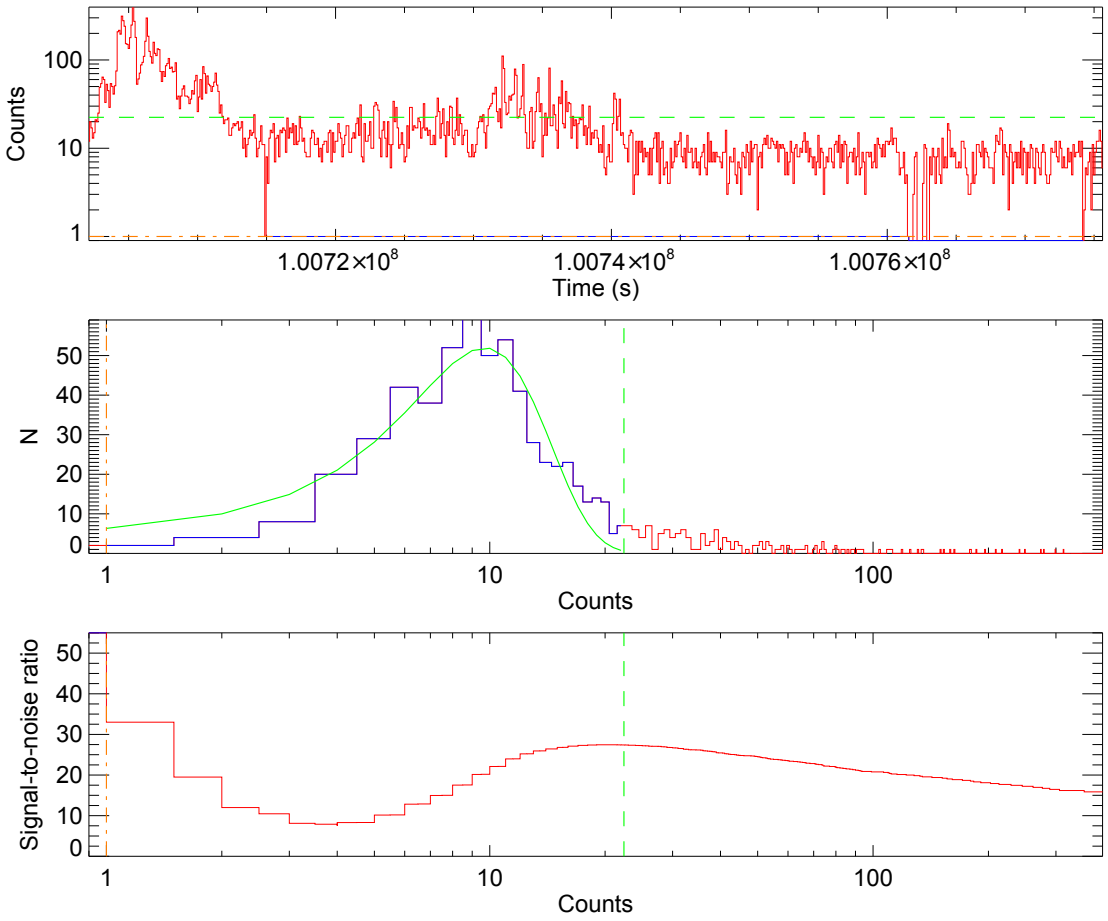

Figure 3.24: Example for a failed definition of the SNR threshold showing the output of the `deflare` script for the MOS2 exposure of observation 0086360301. The same description for the panels and colouring as given for Figure 3.23 applies.

no conclusive reason to exclude them and their exclusion rather leads to an unnecessary worsening of the statistics.

- *modes*: For a truly representative correction function, a high number of counts in the empirical dataset is important. However, using only sources observed in FF mode automatically excludes bright sources since usually the window modes are used for their observation. Thus, not only the FF mode but also the LW mode and SW mode were allowed in the new search for suitable sources (with the intention of comparing the outcome for the individual modes before combining them).

- *count rates*: The pile-up limits of the count rates are mode dependent. Following version 2.13 of the *XMM-Newton Users Handbook*, the count rate limits for LW mode observations were set to $1.5\,\mathrm{cts\,s^{-1}}$ (MOS) and $3.0\,\mathrm{cts\,s^{-1}}$ (pn) and for the SW mode observations to $4.5\,\mathrm{cts\,s^{-1}}$ (MOS) and $25.0\,\mathrm{cts\,s^{-1}}$ (pn), respectively. Regarding the FF mode, lower count rate limits than used before were given in the newer handbook version. Instead of $0.7\,\mathrm{cts\,s^{-1}}$ set for MOS for the original sample, a limit of $0.5\,\mathrm{cts\,s^{-1}}$ was now given in the handbook, for pn the limit had changed from $6\,\mathrm{cts\,s^{-1}}$ to $2\,\mathrm{cts\,s^{-1}}$. However, the older values were kept for the search conducted in this work to include all sources of the original sample (and similar ones) for diverse comparisons and validating analysis steps. Keeping the higher count rate limits at this point did not constitute a problem because the count rate limit is not an absolute guarantee for sources to be pile-up free and, thus, an additional, more thorough step to screen for pile-up was introduced to the routine in this work anyway (see Chapter 3.5.5).

- *total counts*: Again, to have all of the original sources included in the new search, the minimum number of counts in the 0.2–12 keV range was cut down to 13 500 for pn, which is not a big difference compared to the original 15 000 counts. In the case of MOS, the original value of 5000 counts could be kept.

Searching the catalogue for potentially suitable sources with these criteria led to some observation IDs appearing more than once since several of the contained sources fulfilled the criteria. However, since this means more than one bright source was detected at the on-axis position, the respective 14 observations (47 sources) were directly excluded from any data processing as the presence of crowded fields was obvious.

In the end, the criteria resulted in 347 sources being selected from the catalogue. Table 3.4 shows the number of observations for the different combinations of science modes present in the sample. Sources observed with all three EPIC cameras operating in FF mode are clearly the largest group. The number almost doubled compared to the 87 sources considered potentially suitable by Read et al. (2014) before excluding further sources in the manual image screening process.

Initial data processing was performed for all 347 sources with the respective scripts, SAS version 16.1 and the calibration files public in December 2017 to prepare the observational data for the different screening steps. One source (observation 0743070201) had to be dismissed since no event files could be created, probably due to corrupt ODF files.[50] Also, the GTI-filtering led to a remaining exposure time below 1 ks in

[50] However, the image available in the *XMM-Newton Science Archive* already shows two close, bright sources at the on-axis position, meaning the observation is unsuitable to be included in the CORRAREA sample anyway.

Table 3.4: Number of potentially suitable sources for the new CORRAREA sample per science mode combination (FF: Full Frame mode, LW: Large Window mode, SW: Small Window mode). The results are based on the updated selection criteria being applied to the 3XMM-DR7 version of the *XMM-Newton Serendipitous Source Catalogue*. The numbers in parentheses are the numbers of sources which have FF count rates that also meet the more restrictive pile-up limits given in the newer handbook version. Mode combinations which are not listed here did not occur in the search.

Mode			number of sources
pn	MOS1	MOS2	3XMM-DR7
FF	FF	FF	166 (122)
FF	FF	LW	3 (3)
FF	FF	SW	2 (2)
FF	LW	FF	2 (1)
FF	LW	LW	29 (7)
FF	LW	SW	2 (1)
FF	SW	SW	15 (1)
LW	FF	FF	6 (3)
LW	LW	LW	50
LW	SW	SW	9
SW	LW	LW	8
SW	SW	SW	55

two cases (observations 0103861501 and 0303550901), leaving 344 potentially suitable sources/observations, for which the manual image screening was performed.

3.5.3 Image Screening

Following the selection from the catalogue, the remaining sources had to be screened manually to evaluate their actual suitability. This required viewing each image taken of each source with each of the three EPIC detectors separately, since also detector-specific issues like chip gaps, had to be taken into account. The images created in detector coordinates with the respective scripts in the procedure were used to do so.[51]

As done by Read et al. (2014) for the original sample, the new sample of potential sources was screened for crowded fields, chip gaps or bad CCD columns close to the source, extended emission of or around the sources and chip losses. In the case of crowded fields, the decision to exclude sources did not have to be as conservative as for the original sample since a maximum source region radius and individual background regions were also defined for each source in this work (see Chapter 3.5.4). Fixed, uniform source region radii and background regions mean a source definitely has to be excluded from the sample if another source (even if it is just a weak one) lies within the extraction regions. A more flexible region definition, on the other hand, allows for keeping several sources in the sample which otherwise would have to be excluded.

[51] using patterns 1–12, 0.2–12 keV, the #XMMEA_EM filter and excluding potentially anomalous CCDs in the case of MOS; using patterns 1–4, 0.2–15 keV and the FLAG==0 filter for pn

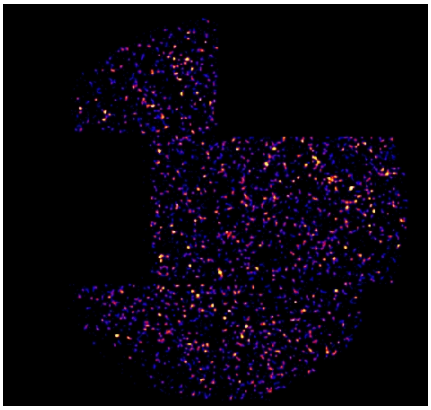

Figure 3.25: Example for an excluded exposure. The data is not sufficient to identify sources, not even the bright, central target source. Thus, the useability of the observation and the suitability of selected extraction regions cannot properly be evaluated.

Besides the screening for the issues mentioned above, three further issues made an exclusion of sources necessary. First, for a couple of observations there were several exposures conducted with the same detector but with different science modes being used and in which case the main mode exposure (being the one providing the longest GTI-filtered exposure time) did not overlap with the main exposures of the other detectors. Second, the source of interest was too far off from the on-axis position in some cases, which led to the pn source region covering a region of inhomogeneous background (see Chapter 3.5.4). Third, in one case the GTI-filtered exposure time was still too short to make a proper screening of the images possible.

All in all, the image screening led to the exclusion of another 82 sources. These are listed in Table A.2 in the appendix, together with the reason for their exclusion. 262 sources remained for the new, extended sample. They are given in Tables A.3, A.4 and A.5 (the division into three tables already follows the designation of the sources as pile-up free, vague pile-up cases and piled-up sources, as described in detail in Chapter 3.5.5). Among other things, the tables also show the used source position from the *XMM-Newton Serendipitous Source Catalogue*, the science mode, filter and source count rate for each EPIC camera and the GTI-filtered exposure time.

In the case of multiple exposures performed with a single detector within an observation, the exposures are merged by the scripts when stacking the spectra. But there are cases in which single exposures should not be used (but which do not require discarding a whole observation), like multiple modes used for a single detector or data that is insufficient for the screening. An example for the latter case is shown in Figure 3.25. All excluded exposures are listed in Table A.6 in the appendix.

3.5.4 Revised Region Selection

For the 262 sources that were not excluded from the sample, also a background extraction region and the maximum source region radius were defined for each source and EPIC detector, respectively, during the image screening process. As described in Chapter 3.3.2, Read et al. (2014) used a common background region for each source, an annulus

with an inner radius of 90″ and an outer radius of 180″ around the source position, regardless of the detector used. However, it was decided to select individual background regions in this work since the use of a common region poses the following problems. Such an annulus would cover inactive MOS CCD areas in case of the newly included window mode observations. As for the pn detector, the annulus generally includes chip gaps, is sometimes not entirely located on only one CCD, involves areas with different CTI corrections and often covers regions with an inhomogeneous background due to the so-called copper hole. The copper hole is an instrumental feature caused by the shape of the electronics board below the CCDs, as Figure 3.26 illustrates. Due to X-ray fluorescence emission from materials located close to the CCDs inside the camera (Briel et al., 2000), there is a strong copper line around 8 keV. But this spectral feature is not present where the inner gap in the electronics board is located, leading to the inner copper hole and the spatially inhomogeneous background. Since the on-axis position is located in the copper hole, a suitable background region for the sources used here must not cover any areas affected by the copper fluorescence.

For the new, individual background regions for each source and detector, different region options that were given successive priorities were defined depending on the detector type and science mode used. These options are illustrated in Figure 3.27. However, before having to dismiss an option and move on to the next priority region instead, the potential background regions were usually adjusted with respect to their size and exact position within the limits of the following background region definitions and rules, which were specified for a consistent region selection throughout the sample:

Full Frame mode

MOS:
- 1st choice: an annulus around the source, with an inner radius of at least 90″ and within the borders of the central CCD.
- 2nd choice: a circle in any corner of the central CCD.
- There might be further limitions to the positioning of the background region. An example, a 'hole' in an image, is shown on the left in Figure 3.28.
- The minimum annular width for an annular background region is 20″, the minimum radius for a circular background region is also 20″ (though usually a larger background region can be used for MOS here).
- The background regions for the two MOS detectors do not have to cover the same sky regions so that no conversion of detector coordinates or double checking for chip gaps is necessary.

pn:
- In general, the background region has to lie within the area marked by the yellow hexagon in Figure 3.27, which surrounds the detector parts that are free of the instrumental copper line feature.
- 1st choice: a circle on CCD4, centred on the same Y-position of the CCD (RAWY) as the source (positioned to either the left or right of the source) to ensure the same CTI correction is applied; bright PSF spokes, which are contaminated by source emission (see right side of Figure 3.28), should be avoided.
- 2nd choice: a circle on CCD4 with a different RAWY-position and a different RAWX-position as the source, avoiding the pixel columns affected by the readout of the source counts (see right side of Figure 3.28); the background

region can be positioned to either the left or right of these pixel columns; the RAWY-position should only be as far off from the source's RAWY-position as necessary (e.g. due to point sources or bright PSF spokes), to limit the difference in the CTI correction applied.
- 3rd choice: a circle on CCD1, located on the same RAWY-position as the source on CCD4.
- The minimum radius for the background region is 20″.

Large Window mode

MOS:
- 1st choice: an annulus around the source, with an inner radius of at least 90″ and within the borders of the active pixels of the central CCD.
- 2nd choice: a circle on any other CCD visible in the image.
- With respect to the minimum region size and differences between the MOS1 and MOS2 regions the same rules apply as for the FF mode.

pn:
- The same rules apply as for the FF mode.

Small Window mode

MOS:
- 1st choice: a circle on any of the outer CCDs visible in the image.
- With respect to the minimum region size and differences between the MOS1 and MOS2 regions the same rules apply as for the FF mode.

pn:
- The same rules apply as for the FF mode but without the third background option.

With the new, individual background region selection, even some observations could be kept in the sample which otherwise would have had to be excluded because of the old, uniform background region not being source free. Besides the revised background region selection, all sources were also checked for the maximum source radius that might be used for the circular source extraction region. A total limit was set at a radius of 60″, which is the overall maximum radius that is intended to be used in any further validation analysis or future update of CORRAREA. But the use of different extraction radii can always be required in the validation process and a smaller extraction radius might be selected for the CORRAREA correction at any time (like the fixed value of 40″ radius of the original CORRAREA version). So it has to be known which observations can be kept in a subsample when a certain extraction radius is to be used. In many cases, the maximum source radius is below the limit of 60″, particularly in the case of the pn exposures, where only four cases actually allow for an extraction radius of that size. Reasons for a limitation of the source region radius to a value below 60″ were:

- other point sources close to the target
- the source region overlapping with detector parts that are not read out in the MOS window modes (particularly in case of the small window mode)
- the source region overlapping with chip gaps of the pn detector
- part of the source region reaching into pn detector parts that are contaminated by the copper-line feature

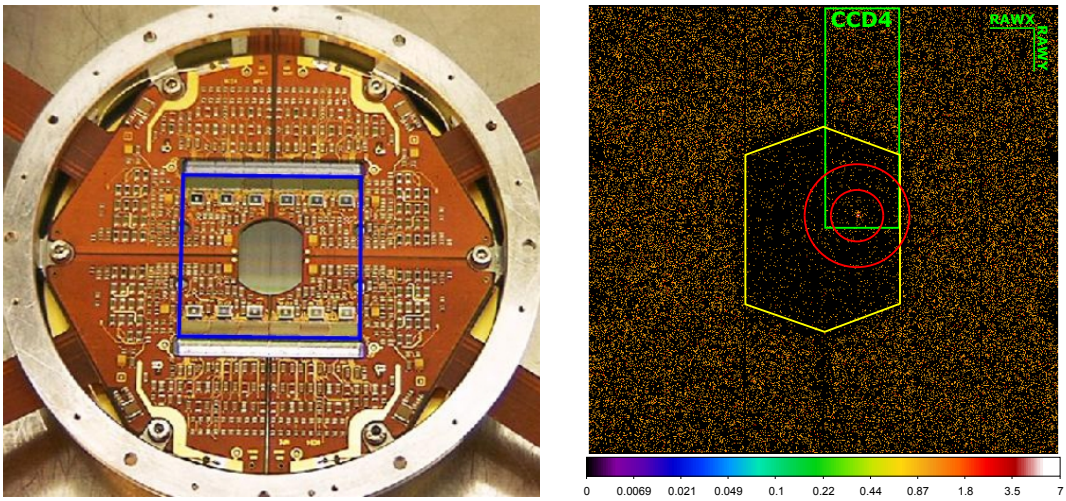

Figure 3.26: Illustration of the pn copper hole in the instrumental background. *Left*: Image of the pn detector showing the electronics board for readout and power supply. The blue frame marks the position of the CCD plane below. Clearly visible is the central gap in the board structure, which leads to the absence of the copper fluorescence line in the respective CCD parts (credit: X-ray Group at MPE, Garching, `http://www.mpe.mpg.de/xray/wave/xmm/epic/images/image_08.php`, modified). *Right*: Example of a pn image in the 7.8–8.2 keV range showing the presence of the copper fluorescence. The image frame corresponds to the blue frame on the left. The copper hole, which is not covered by the electronics board, is roughly marked by the yellow hexagon. CCD4, on which the on-axis position is located, is shown in green and the annulus shown in red marks the originally used background region for this observation, which extends beyond the copper hole border. (Observation 0306630201 was used here since its high GTI-filtered exposure time makes the copper feature more apparent.)

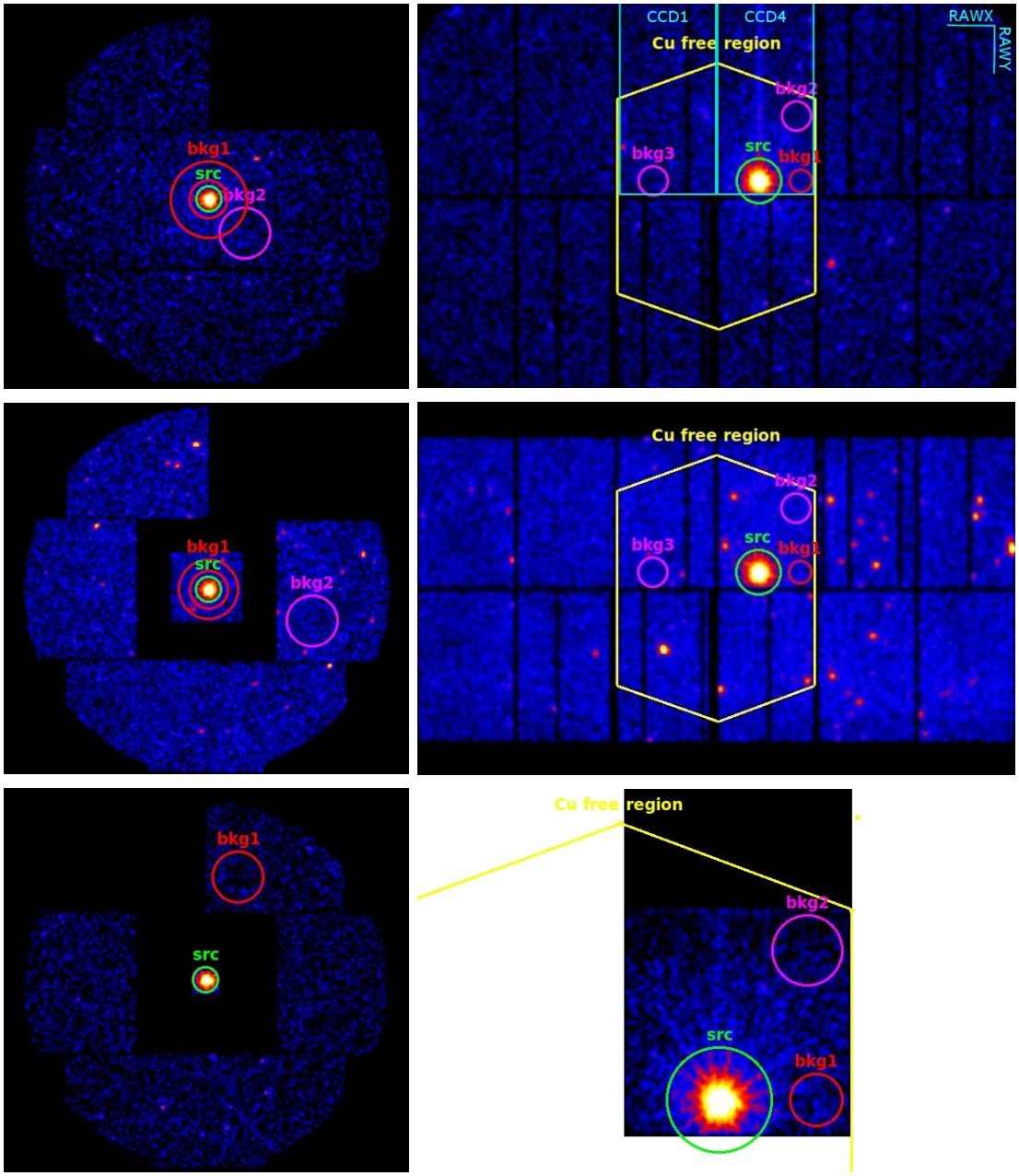

Figure 3.27: Detector and mode dependent background region options. The MOS modes are shown on the left, the pn modes on the right, with the FF modes in the top row, the LW modes in the second row and the SW modes in the bottom row. The potential background regions to be given first priority are shown in red (bkg1), second and third priority regions are shown in magenta (bkg2 and bkg3). The yellow hexagon surrounds the pn region free from the instrumental copper-line feature. The X- and Y-directions on the concerned pn CCDs are indicated by the CCD-related coordinates RAWX and RAWY. The green circles show the source position with a radius of 60″, the maximum radius intended to be used in the analysis in general. Note that, for an enlarged illustration, the pn images do not show the whole CCD plane but are cut on top and bottom.

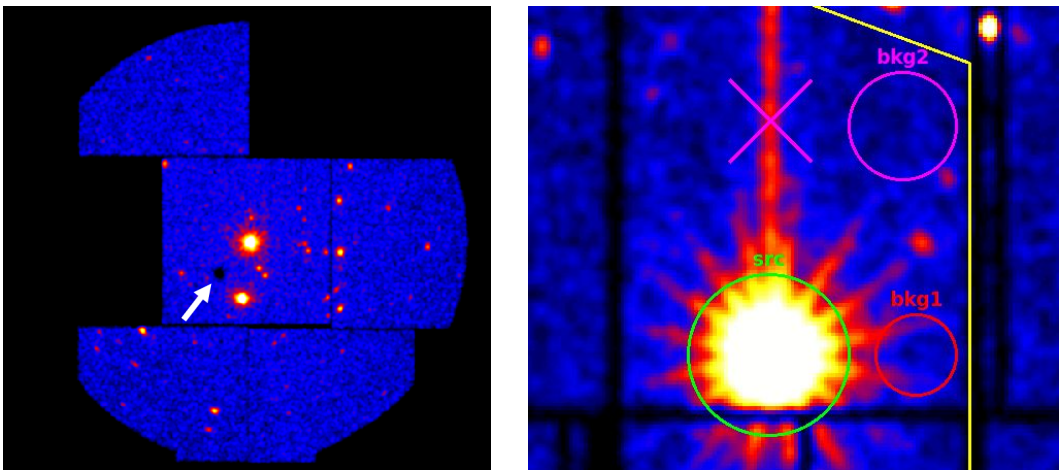

Figure 3.28: Limitations to the background region selection. *Left*: Example of a MOS image. In rare cases, a 'hole' in the MOS image can be seen and the affected area should be avoided when defining the background region. Such a 'hole' is most likely due to local optical loading, which is the excitation of a significant number of electrons in a CCD caused by optical photons from optically extremely bright sources (for the various impacts optical loading can have see the *XMM-Newton Users Handbook*). *Right*: Example of a pn image. When choosing the first priority background region (red circle), the visible PSF spokes should not reach into it since they contain source counts. The second priority region (magenta circle) must not be positioned at the same RAWX position (magenta cross) as the source due to OoT events in the readout direction. The image also shows that the chip gap visible below the source usually limits the maximum radius for the source region of the on-axis sources (green circle).

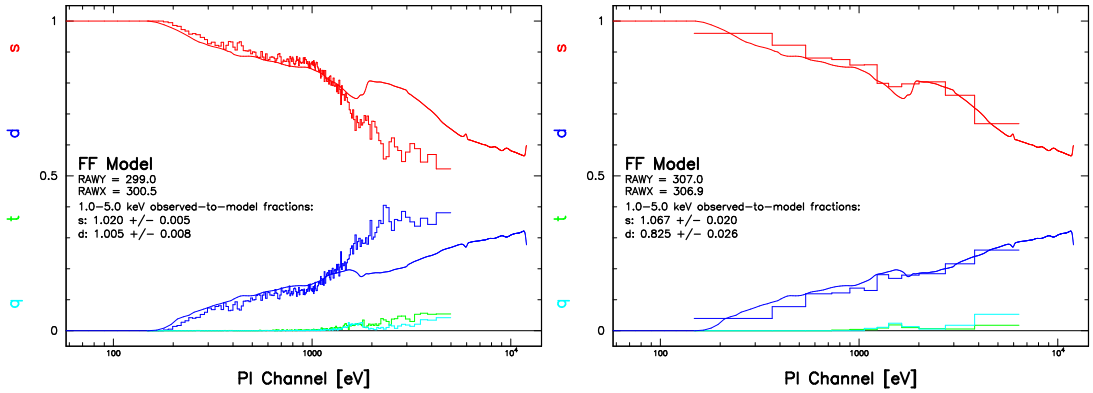

Figure 3.29: Example of `epatplot` pattern fraction outputs for piled-up exposures. *Left*: Strongly piled-up example where the single and double pattern fractions differ clearly from the fraction models (observation 0134540601, MOS2). *Right*: Example where pile-up is present but no clear deviation of the single and double pattern fractions from the model curves is visible (observation 0555020201, MOS2). Fractions and model curves of single pattern events are shown in red (s), of double pattern events in blue (d). Fractions of triple pattern events are shown in green (t) and of quadruple pattern events in cyan (q).

As the limitation depends on the detector and to be able to use different radii for the MOS and pn detector if wanted, separate values for the maximum radius were registered not only for each source but also each detector. These are also given in Tables A.3, A.4 and A.5, together with the source positions from the *XMM-Newton Serendipitous Source Catalogue*, on which the source extraction regions were centred.

3.5.5 Pile-up Screening

Since the count rate limits given in the *XMM-Newton Users Handbook* for each detector and mode are only approximate values to limit the presence of pile-up but do not guarantee pile-up free exposures, another method to identify pile-up was aimed for. The already existing SAS task `epatplot`, which uses the deviation of the single and double pattern fractions from fraction model curves to indicate pile-up, is not sufficiently precise to detect all pile-up cases, particularly when working on the instruments' calibration. Figure 3.29 shows examples of `epatplot` outputs, one plot of a strongly piled-up case and one plot which does not clearly show the presence of pile-up even though the exposure is affected as can be revealed with the method applied in this work.

For the method used here, the diagonal patterns of the MOS detectors (see Chapter 3.2.5) serve as an indicator for pile-up, since these patterns are almost exclusively due to the pile-up of two single pixel events. Similar to Jethwa et al. (2015), for each exposure an image of diagonal pattern events was divided by a clean image of plausible single events to determine the pile-up fraction. The images were created for the events within a circle with a radius of 30″ around the position of the respective source in question. Since the diagonal pattern events only represent part of the piled-up events, the values in the diagonal pattern image were multiplied by a factor of 2.25. This factor results from double pattern events that are due to pile-up and can be estimated to be equally

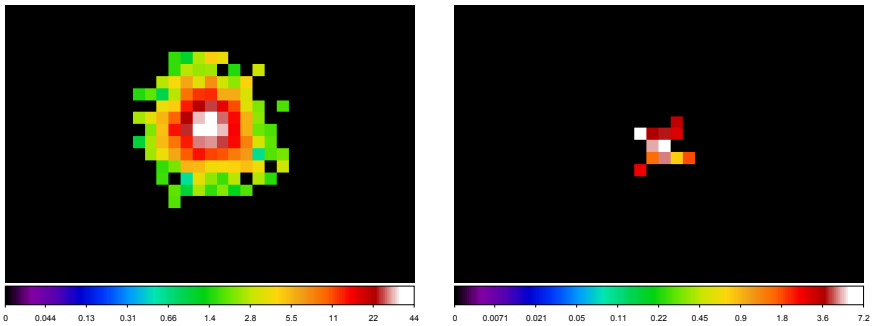

Figure 3.30: Two examples for pile-up fraction images, giving the percentage of piled-up to clean events. Only the central image sections are shown since only events within a 30″ radius around the on-axis sources were included in the pile-up fraction calculation. *Left*: Highly piled-up on-axis source in the MOS1 exposure of observation 0134540601. *Right*: On-axis source in the MOS2 exposure of observation 0555020201, for which no pile-up could be identified using `epatplot`.

high as the number of diagonal events[52], as well as from energy pile-up events in the central pixel, which can be estimated to contribute another 1/9 of piled-up events. For the clean single event images the (FLAG & 0x766ba001)==0 selection expression was used, excluding the diagonal pattern events.

Figure 3.30 shows two examples of the resulting pile-up fraction images after the piled-up events were divided by the clean image events. The left image shows an example of a highly piled-up MOS1 FF mode exposure of a source which is not part of the source sample but was selected from the *XMM-Newton Serendipitous Source Catalogue* due to its high count rate of > 8 cts/s, considerably larger than the given MOS FF mode count rate limit of 0.5 cts/s (ESA: XMM-Newton SOC, 2018b), to illustrate the typical distribution of the pile-up fractions. In the central part of the observed source the fractions are highest and, similar to a PSF distribution, decrease towards the outer areas of the source. The right image in Figure 3.30 shows the corresponding pile-up pattern fraction for the exposure for which no pile-up was visible in the `epatplot` output shown in Figure 3.29 before. A non-negligible presence of pile-up is obvious here, with a pile-up fraction of up to 7% visible in individual pixels in the image.

To ease the process of deciding whether or not an observation can be kept in the sample or is too much affected by pile-up, the total number of piled-up events calculated from a diagonal pattern image divided by the total number of clean events in the corresponding clean event image was defined as the overall pile-up fraction. Having one pile-up fraction value rather than the values in individual pixels allows for a consistent decision making process and makes it unnecessary to screen through and evaluate each single image. For the evaluation of the pile-up significance a threshold of 2% was set and only sources with an overall pile-up fraction below this threshold were considered pile-up free. That this threshold is indeed a reasonable estimate is shown in Figure 3.31, which compares the MOS pile-up fractions thus determined for all sources in the sample with the count rates for each of the MOS imaging modes, respectively. The threshold of 2%

[52] since the diagonally neighbouring pixels around one central pixel make up only four out of the eight adjacent pixels

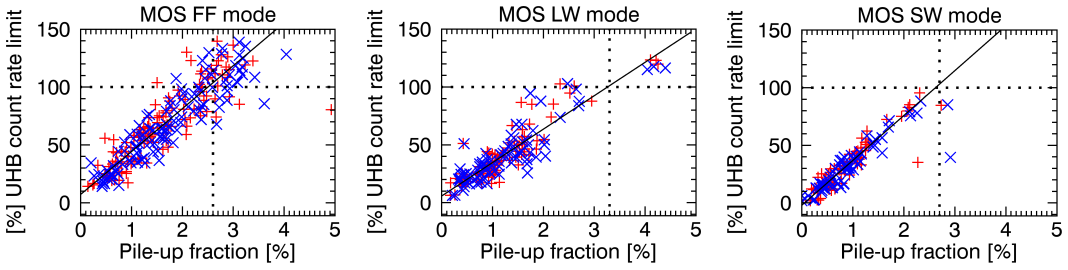

Figure 3.31: MOS1 (red) and MOS2 (blue) count rates to pile-up fractions of all sources that have remained in the sample so far and for each of the three imaging modes, respectively. The count rates are given as a fraction of the count rate limits specified in the *XMM-Newton Users Handbook* (UHB). The dashed lines indicate which pile-up fractions the count rate limits correspond to. (Image courtesy of M. Stuhlinger, ESA/ESAC, modified)

is close to but actually more conservative than the pile-up fraction which corresponds to the count rate limit in the *XMM-Newton Users Handbook*.

Unfortunately, this method can only be applied to estimate the pile-up in MOS exposures because the diagonal patterns are only defined for the MOS detectors. Since the pn detector allows for higher count rates when operated in the same mode as the MOS detectors and is, thus, less susceptible to pile-up in comparison, the MOS pile-up fraction is a sufficient indicator as long as the pn detector has been operated in either the same mode as the MOS detectors or in a faster mode.[53]

However, when the pn detector has been operated in a slower mode than both of the MOS detectors, a pile-up free state of the pn exposure cannot be guaranteed based on the MOS diagonal pattern outcome. Figure 3.32 compares the pn count rates with the MOS pile-up fractions and count rates for those observations in the sample which have faster MOS than pn exposures. All the mode combinations concerned show that the slower pn mode is much more restrictive than the faster MOS modes. While both the 2% MOS pile-up fraction limit as well as the MOS count rate limit suggest that almost all of the respective MOS exposures are pile-up free (with only a few exceptions amongst the MOS LW mode exposures), the pn count rate limit is exceeded for the majority of pn FF mode exposures. As for the pn LW mode exposures, the limit is barely exceeded but the limits of the slower MOS SW mode are much less exhausted.

With only the count rate limit available as an indicator for the presence of pile-up in pn exposures at this point, the pile-up status of those observations with a pn mode slower than the MOS modes had to be evaluated based on the pn count rate alone. Because the count rate limit is a generally suggested value and not a direct indication of pile-up (like the MOS diagonal patterns), only observations of sources in the sample with a count rate up to 90% of the count rate limit where considered pile-up free with reasonable certainty. Sources with a count rate higher than 120% of the count rate limit where classified as piled-up and sources with an intermediate count rate corresponding to 90–120% of the count rate limit where tagged as vague cases, which might not have

[53] A faster mode being a mode with a faster readout cycle and, consequently, with a higher count rate limit. The FF mode is, thus, the slowest, the SW mode the fastest of the modes considered here, with the LW mode in between.

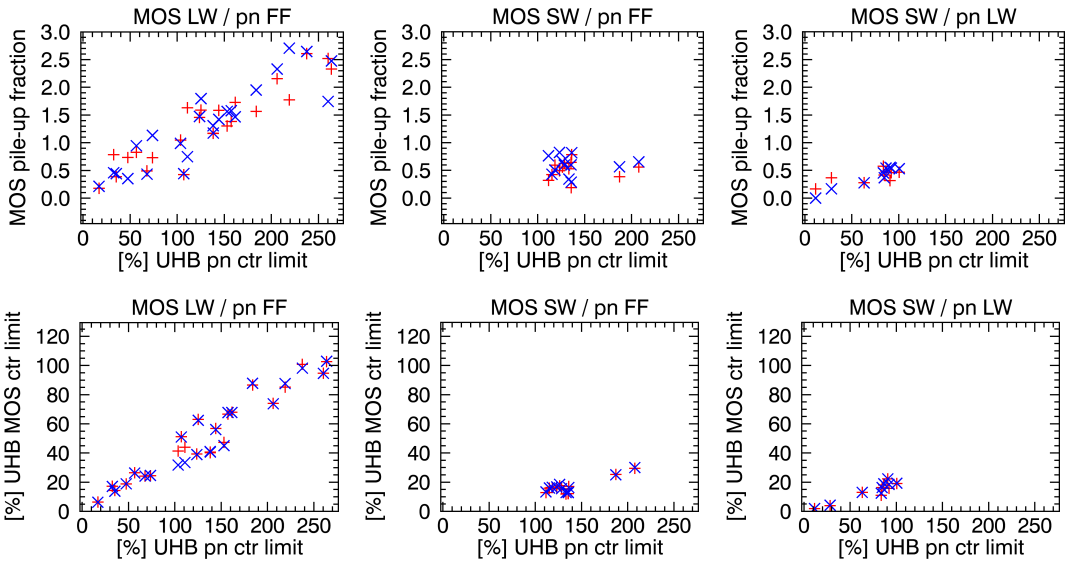

Figure 3.32: Comparison of MOS (MOS1: red, MOS2: blue) and pn pile-up indicators for cases with a slower pn mode. In the top row the MOS pile-up fractions as determined with the method described in this chapter are compared to the pn count rates, in the bottom row the MOS count rates are compared to the pn count rates. The count rates are given as a fraction of the count rate limits specified in the *XMM-Newton Users Handbook* (UHB). Included are all observations with the respective mode combinations that have remained in the sample so far and which only have one remaining exposure for each of the three detectors, respectively. (Image courtesy of M. Stuhlinger, ESA/ESAC, modified)

Table 3.5: Criteria for the pile-up evaluation.

	equal modes or slower MOS mode*	slower pn mode
pile-up free	MOS pile-up fraction $< 2\%$	pn count rate $< 90\%$ of the count rate limit
vague cases	contradictory results for • the two MOS detectors operated in the same mode • two or more exposures with one MOS detector	pn count rate $\geq 90\%$ and $< 120\%$ of the count rate limit
piled-up	MOS pile-up fraction $\geq 2\%$	pn count rate $\geq 120\%$ of the count rate limit

* of either one or both MOS detectors

to be excluded in the end but which would require further analysis before being safe to be included in the final sample for the CORRAREA correction.

Also some observations for which the MOS pile-up fraction method could be used were tagged as vague cases because either the two MOS detectors led to different results (with the pile-up fraction being above 2% for one instrument and below this value for the other one) or because one of the MOS detectors had more than one exposure but the pile-up evaluations for them were contradictory. Table 3.5 summarizes the criteria for the pile-up evaluation for the two distinguished scenarios: 1. the MOS detectors were operated in the same or a slower mode as the pn detector and the pile-up fraction based on the MOS diagonal patterns could be relied on for the pile-up evaluation; 2. the pn detector was operated in a slower mode than both of the MOS detectors and the pn count rate to count rate limit ratio had to be used for the pile-up evaluation instead.

The corresponding scripts in the procedure (see number 7 in Chapter 3.4.1) create an output file that contains the MOS pile-up fractions, MOS and pn count rate and count rate to count rate limit ratio for all observations in the sample and for each exposure, together with information on the respective science mode and a tag classifying each exposure as either pile-up free, piled-up or being a vague case. The 163 observations in the sample which are completely pile-up free are listed in Table A.3, the 70 observations with clearly piled-up exposures are listed in Table A.5 and the 29 vague cases, which cannot be used for a reliable CORRAREA correction without further investigation, are listed in Table A.4.

3.6 Analysis of the Dependence on Certain Selection Criteria

3.6.1 Comparison of Subsamples with Different Filters

One advantage of the automation of the CORRAREA procedure is that the outcome for different subsamples can be easily compared. Thus, any dependence of the MOS-to-pn residual ratio on certain selection criteria can be analysed. Since all three filters are

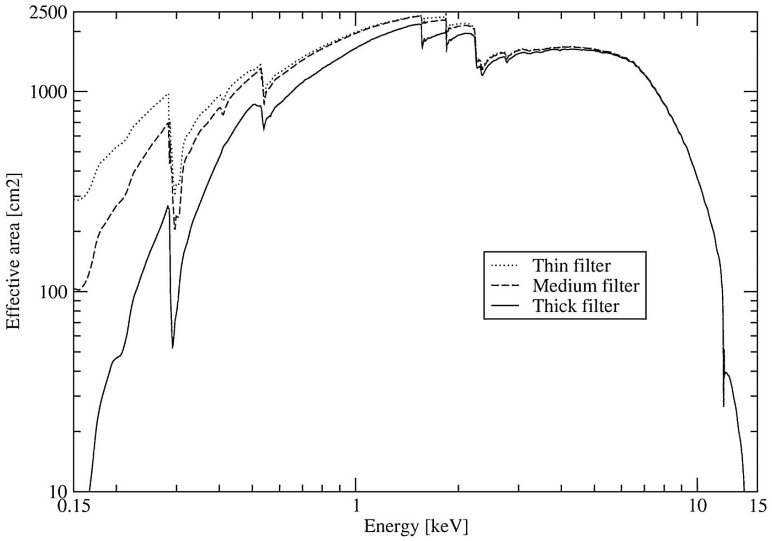

Figure 3.33: EPIC effective area for each filter assuming all three cameras are operated with the same filter type. (*XMM-Newton Users Handbook*, ESA: XMM-Newton SOC, 2018b)

allowed in the new sample (as opposed to the exclusion of thick filter observations in the original sample of the old CORRAREA version), a comparison of the individual results for each filter seems to be advisable. The *XMM-Newton Users Handbook* contains a plot of the effective area showing an increasing dependence on the filters towards lower energies (see Figure 3.33).

However, this does not automatically imply that also the uncertainties in the effective area calibration vary between the different filters. Unfortunately, the sample does not include enough observations at this point to check if the new addition of thick filter observations in the sample has an effect on the MOS-to-pn residual ratios. Only six of the remaining, pile-up free observations were done using the thick filter consistently for all three EPIC cameras. But the relatively small number of thick filter observations in the sample suggested any effect on the residual ratios to be negligible. The inclusion of the respective observations for the purpose of better statistics was, thus, given preference. But a comparison of the results for subsamples with different filters might be possible in the future when further sources can be added to the sample due to the still ongoing operation of XMM-Newton. With an increasing number of thick filter observations included, such an analysis would then also become more significant.

3.6.2 Comparison of Subsamples with Different Science Modes

A currently more important comparison involves the residual ratio outcome and the consequently required correction function for the different science modes. These shall be combined to obtain sufficient statistics for a default correction of the effective area calibration, particularly because of the much higher counts in the SW mode observations. But since the FF mode observations are used for calibration purposes more often and are, consequently, said to be better calibrated, the possibility of a difference between the modes with respect to the residual ratios cannot be eliminated without looking at the topic more closely.

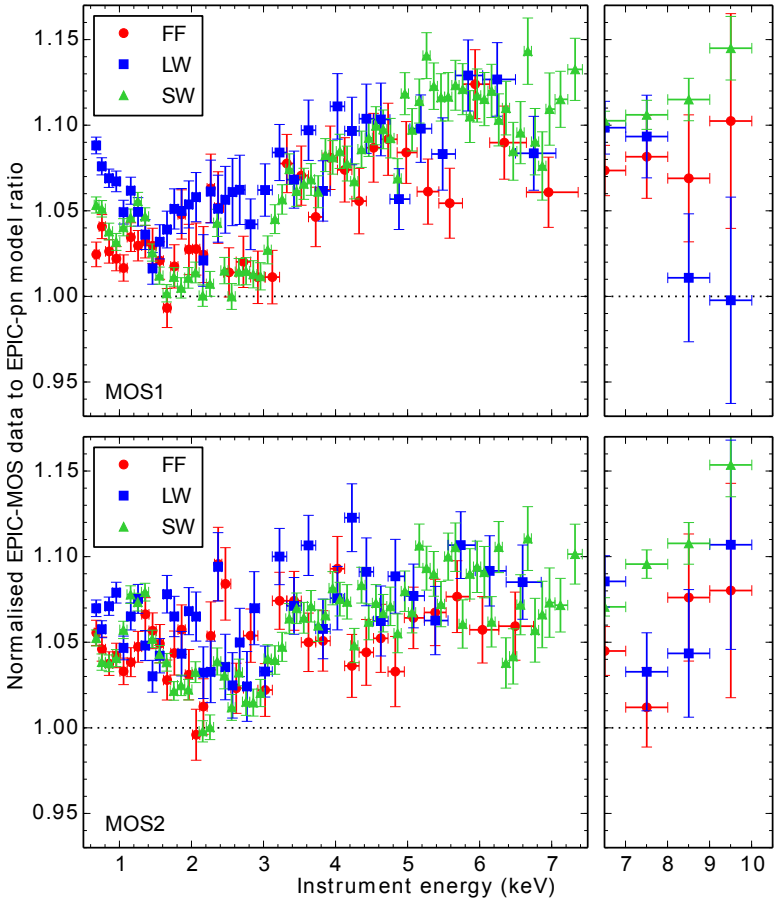

Figure 3.34: Comparison of the MOS-to-pn residual ratios for the different science modes. Included are only observations from the new, pile-up free sample which were conducted using either only the FF mode, only the LW mode or only the SW consistently for all three cameras and which allowed for a MOS source region radius of 40″ and a pn source region radius of 35″. The data were processed with the calibration files public in December 2017. The dotted line indicates the pn ratio.

Figure 3.34 shows the residual ratios for each of the three imaging modes included in the analysis, respectively. In the energy range considered so far, up to about 7 keV, the differences between the three modes are not large. In case of MOS1, the LW mode residual ratio below 3.5 keV is slightly higher than the ratios for the other two modes. The SW mode residual ratio for MOS2 is mostly slightly lower than the FF and LW mode ratios between ∼2 keV and ∼5 keV. At energies above 7 keV the residual ratios for the SW mode are clearly higher than the ones for the other two modes. It is also worth mentioning that the majority of these SW mode observations are observations of the same source, NGC5844, so that source-specific aspects might play a role as well.

Further insight into the overall impact of the modes can most likely be gained when defining both, a correction function for all modes combined and individual correction functions for each mode, and applying them to selected test sources to compare the effect of the correction on the spectra and determined flux. However, the stacking of

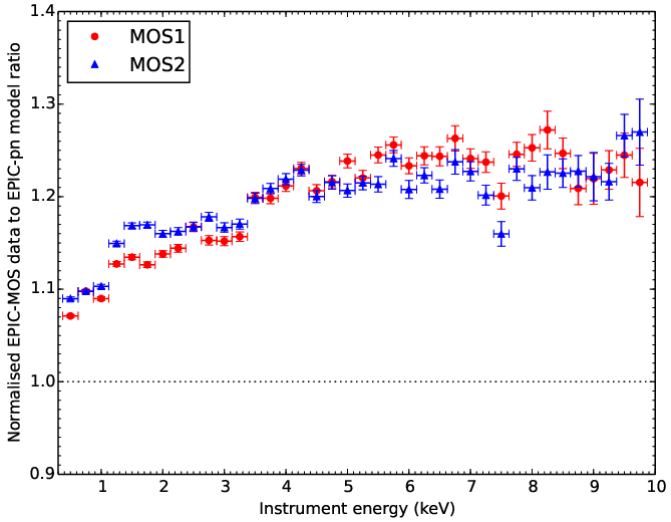

Figure 3.35: Residual ratios for the combined stacking of observations with different science modes. Included are only observations from the new, pile-up free sample which allowed for a MOS source region radius of 40″ and a pn source region radius of 35″. The data were processed with the calibration files public in December 2017. The dotted line indicates the pn ratio.

observations with different modes proved to be problematic with the procedure applied so far. The residual ratios for the combined stacking of observations with different modes are shown in Figure 3.35. It is obvious that the residual ratio obtained with the procedure applied here is much higher for the combined modes, with values up to ∼1.25 as opposed to the typical ∼1.05 to ∼1.10. This is clearly the result of the routine not being suitable to be applied to combined modes yet, particularly because the individual results for the different modes are all at the typical, expected level. So, the problem only occurs when combining the modes, which is an important indication of its origin.

Considering this, a possible explanation are the different, mode-dependent live times, meaning the time in which the detectors collect and shift events (not including the time for the readout). Table 3.6 contains the different MOS and pn live times for the different imaging modes. The live times are smaller for the faster modes, with the smallest value in case of the pn SW mode. This possible explanation for the problem at hand is conform with the further investigation that was done. Combining only FF and LW mode observations, without SW mode observations, led to a much smaller increase in the residual ratio level. The live times are usually corrected for with the effective area calculation in the ARFs. But not taking them into account explicitly when weighting the ARFs and RMFs in the stacking process for Corrarea may lead to the weighting being incorrect. This would easily lead to such large deviations.[54] Another reason for

[54] A comparison with the fit and stack approach in the scope of the current continuation of the project shows no such difference when combining the modes with this other method. This also supports the idea of the weighting being the problem's origin as the ARFs and RMFs are not stacked and weighted when the spectrum of each source is modelled individually and the residual ratios are stacked afterwards. However, the individual modelling of the *fit and stack* approach takes quite some time and can introduce more systematic errors than the *stack and fit* approach.

Table 3.6: EPIC live times for the different imaging modes involved here. The live time (the time when events are collected and shifted) is given as a percentage of the frame time, which is the combined live time and readout time. (Values taken from the *XMM-Newton Users Handbook*.)

	Live time (%)	
Science mode	MOS	pn
Full Frame	100.0	99.9
Large Window	99.5	94.9
Small Window	97.5	71.0

an incorrect weighting of the ARFs and RMFs could be that the number of counts for the individual sources is not taken into account in the weighting factor. It might skew the stacked response files if weak sources with long exposure times contribute more than bright sources with short exposure times. This, again, could explain why the problem is most apparent when adding the SW mode observations, since the sources observed in the SW mode are usually much brighter than the ones observed in the FF mode.

The issue needs to be fully resolved and the script package needs to be adjusted accordingly before all observations in the new, extended sample can be stacked. For the final residual ratios and correction functions presented in this work (see Chapter 3.9), only FF mode observations will, thus, be used.

3.7 Optimization of the Source Extraction Radius

During the manual image screening process, also the maximum source region radius that might be chosen was determined (in steps of 5″) for each exposure. This was done to be able to extract events from a region as large as possible for improved statistics and to also allow for keeping sources which only allow for smaller source region radii in the sample. The respective values are also given in Tables A.3–A.5.

Before spectra for source regions of different sizes can be stacked, however, the possibility of a significant effect of the source region size on the residual ratios needs to be ruled out, particularly because uncertainties in the PSF calibration might affect the results. To analyse the impact of the chosen source region size, data were extracted for source regions with a radius of 30″, 40″ and 50″, respectively, and the resulting residual ratios after stacking and modelling the spectra for each radius were compared with each other (see Figure 3.36).[55] Even though the visible differences are marginal, there seems to be a systematic worsening of the residual ratios towards larger radii.

Its systematic nature indeed indicates that this feature should be an issue of the PSF. Since the PSF calibration was revised at ESAC at the same time this analysis was done, the residual ratio approach and the script package developed for its automation in the process of this work were used to validate the new PSF calibration, as described in the next chapter.

[55] Only the sources from the sample of the original CORRAREA version were included here due to the source selection and screening for the new, extended sample still being carried out at the time of the analysis. SAS version 15 and the calibration files public at the beginning of 2017 were used for the comparison presented here.

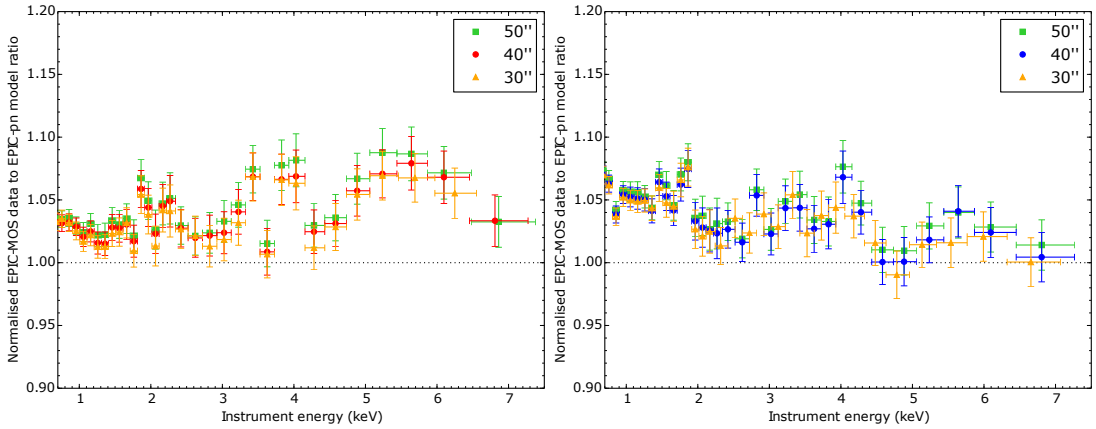

Figure 3.36: Comparison of the residual ratios for different source extraction radii (left: MOS1; right: MOS2). The dotted line indicates the pn ratio.

As long as an impact of uncertainties in the PSF calibration is obvious, consistent source region radii should be selected throughout the sample to obtain the CORRAREA correction function. Given the maximum radii determined in the image screening process, a radius of 40″ for the MOS exposures and of 35″ for the pn exposures proved to be a good compromise between including more events via selecting a larger area while still keeping the majority of sources from the sample for the analysis. These radii for MOS and pn allow for using 134 of the 163 pile-up free sources in the sample.

3.8 Validation of the Point-Spread-Function Calibration

With the PSF calibration publicly available in early 2017 significant differences were seen when comparing EPIC spectra from circular and annular on-axis regions of different sizes.[56] A new set of PSF calibration files was, thus, prepared at ESAC at the time. To analyse the impact of a revised PSF calibration on the residual ratios and to provide an additional, independent validation of the revised PSF calibration, the preliminary, modified PSF CCFs were provided by ESAC so that they could be used to determine the residual ratios with the script package developed in the scope of this work.

Figure 3.37 again shows the residual ratios for source regions with a radius of 30″, 40″ and 50″ being used, respectively, this time with the public PSF CCFs being replaced by the provided, revised files.[57] Comparing the outcome with the previous plots in Figure 3.36 shows an overall increase of the residual ratios towards higher energies but also a slightly smaller deviation between the residual ratios for the different radii at energies above ∼3.5 keV. Particularly in the case of MOS2, the residual ratios no longer seem to be systematically higher for larger radii over the whole energy range considered here. However, the changes are marginal here since the spectra are dominated by the core regions while a different region radius only concerns the PSF wings.

[56] For example, at energies $E \gtrsim 8$ keV, the deficit between a pn spectrum of a circular region and that of an annular region of 30–40″ even amounted to 20–30% as remarked by M. Smith, ESAC, via email communication.

[57] The same sources, SAS version and calibration status (with the exception of the PSF CCFs) were used as in the previous chapter.

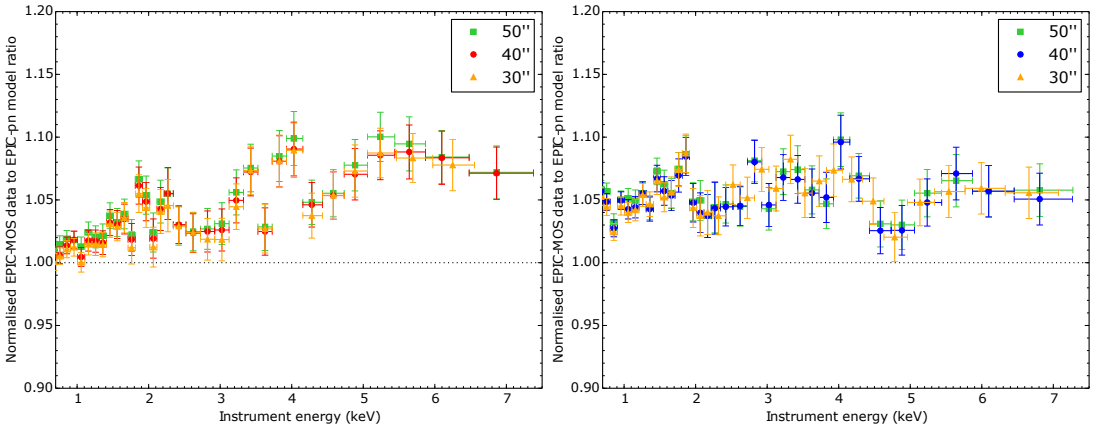

Figure 3.37: Comparison of the residual ratios for different source extraction radii using the provided recalibrated set of PSF CCFs (left: MOS1; right: MOS2). The dotted line indicates the pn ratio.

The changes that come with the new calibration files can, thus, be more easily recognised when comparing the results obtained for different annular source regions rather than the usual circular ones. Figure 3.38 shows the residual ratios for five nested annuli being used as source extraction regions, both with the old public PSF CCFs and the recalibrated ones. It is apparent that the differences between the different annuli improved a lot towards higher energies, as was intended with the new PSF CCFs. The residual ratios for the dominant core region (0–10″) increased with the new PSF calibration, also particularly towards higher energies, which explains why the overall residual ratios for the circular regions presented before were mostly higher using the recalibrated CCFs. This is shown more clearly in Figure 3.39, which directly compares the residual ratios obtained with the CCFs public at the time and the ones obtained with the new PSF CCFs that were tested here.

All in all, the results for different circular extraction regions together with the results for annular extraction regions show an improvement with the new PSF calibration as the extraction radius dependency becomes smaller. With the automation of the residual ratio method in this work, the intended effect of the PSF recalibration could, thus, be confirmed. The new PSF CCFs were made public in August 2017.

Still, the total residual ratios showed a worsening with the new PSF calibration files but these files are actually not expected to improve the EPIC cross-calibration. This is an issue to be dealt with by means of the effective area calibration. It shows how different calibration aspects correlate with each other and, consequently, require constant adjustments.

3.9 A New Correction Function

With the revised procedure, the extended and screened source sample and the comparisons and analyses presented in the previous chapters a first new CORRAREA correction function was determined for each of the two MOS detectors, respectively. Since the stacking of spectra is still problematic when combining different modes, only the pile-up free FF mode observations were used here. Also, since the possibility of remaining

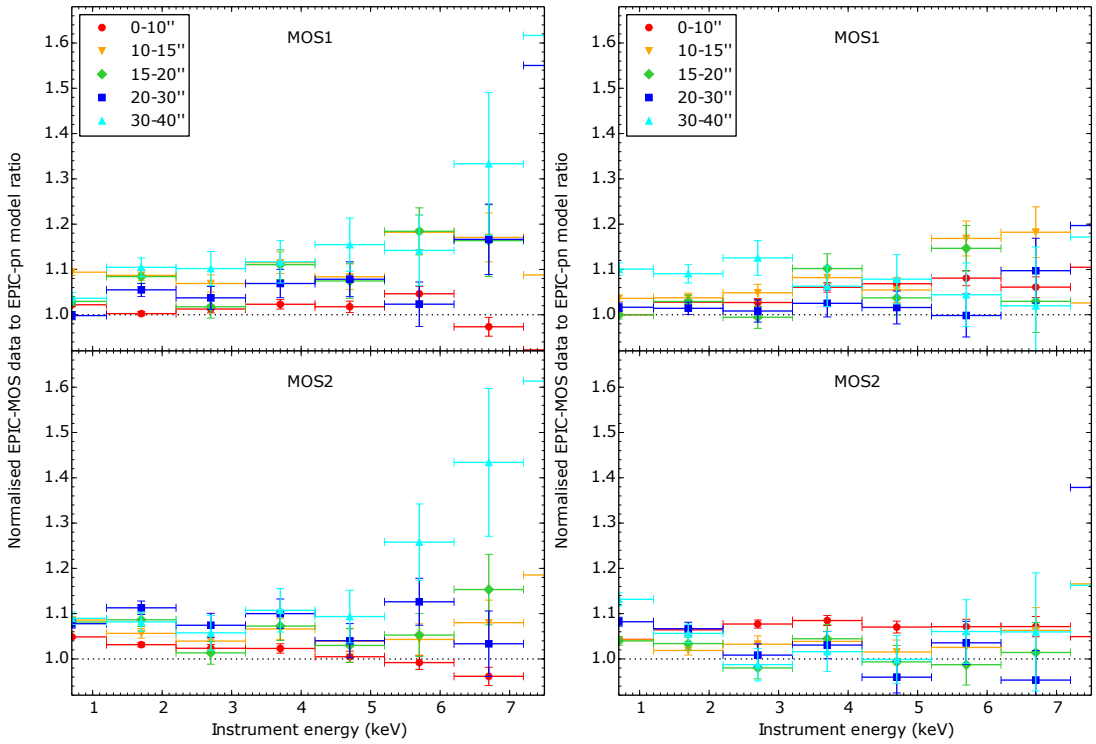

Figure 3.38: Comparison of the residual ratios for nested, annular source regions. *Left*: results using the calibration files public in early 2017. *Right*: results using the provided new PSF CCFs. The dotted line indicates the pn ratio.

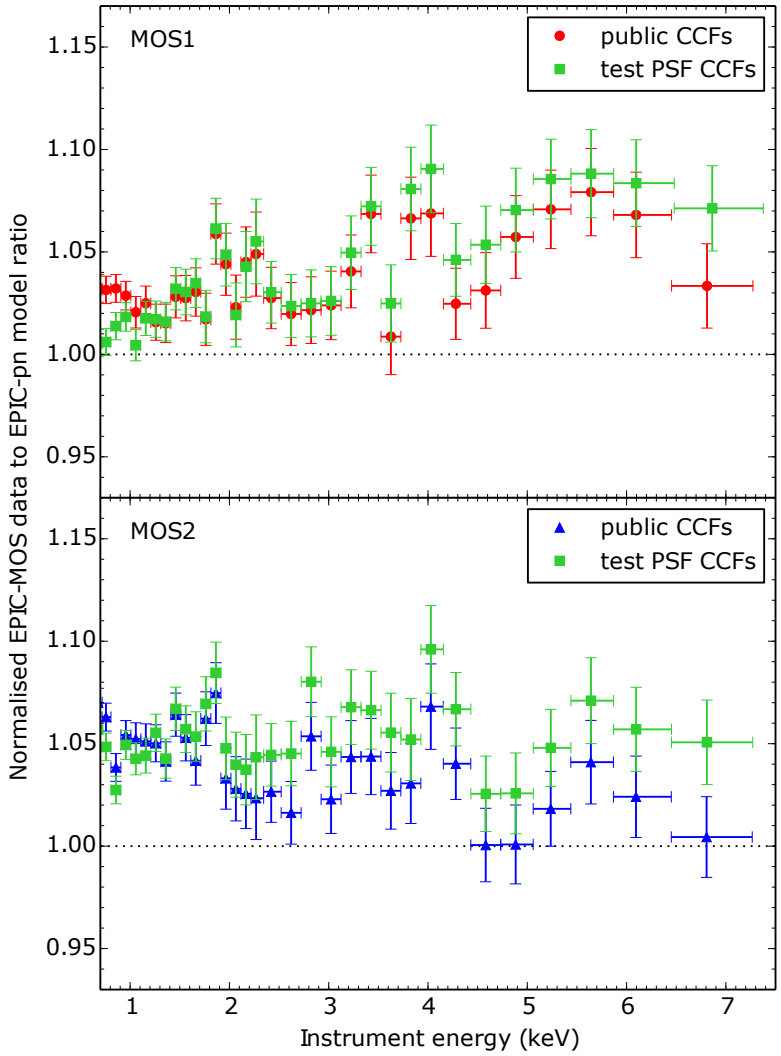

Figure 3.39: Direct comparison of the residual ratios using either the public or the provided test PSF CCFs. A radius of 40″ was used for all source regions. The dotted line indicates the pn ratio.

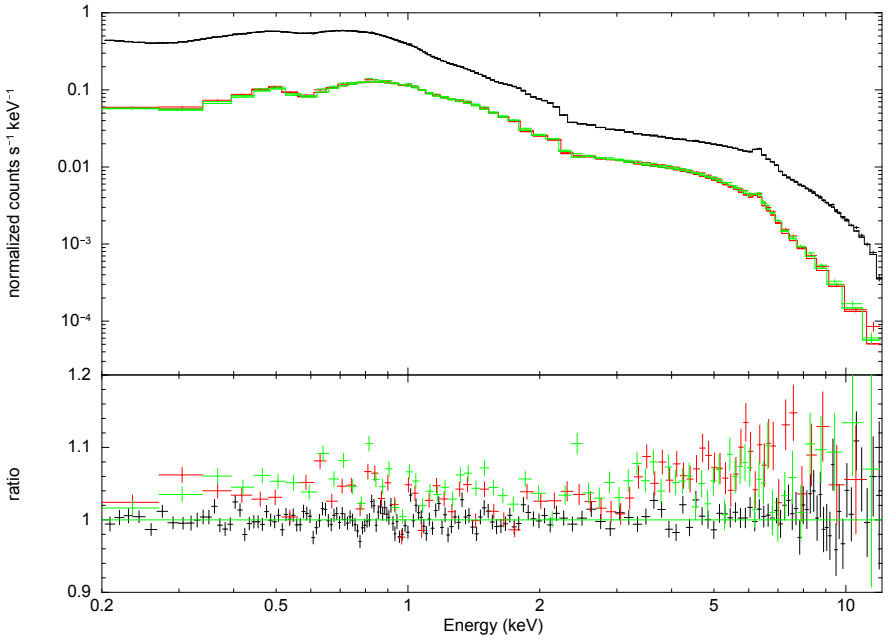

Figure 3.40: Stacked spectrum of 54 selected sources from the new source sample, showing the spectral data and model (top panel) as well as the residuals (lower panel). Used were pile-up free FF mode observations for which source region radii of 40″ (MOS) and 35″ (pn) could be applied. The phenomenological model described in the text was fitted to the pn data (black) and convolved with the MOS1 (red) and MOS2 (green) responses.

PSF calibration uncertainties having an effect on the correction function cannot be eliminated at this point, particularly since also energies $\gtrsim 7\,\mathrm{keV}$ can and should be taken into account for a default effective area correction, the source region radii suggested in Chapter 3.7 were maintained (40″ for MOS exposures, 35″ for pn exposures) and only the sources which allow for these radii were included.

This results in a total of 54 sources with which the stacked spectrum (shown in Figure 3.40) was created using the CCFs public in October 2020 and SAS version 16.1. With 0.2–12.1 keV a wider energy range was used for the fit of the pn spectrum[58], so that more components had to be added to the original model to keep the good quality of the fit and justify the use of a phenomenological model. A close fit to the pn data could be achieved with the following XSPEC model: wabs ($n_\mathrm{H} = 7.56 \times 10^{20}\,\mathrm{cm}^{-2}$) × [pow ($\Gamma = 0.80$) + pow ($\Gamma = 4.57$) + Gauss ($E = 0.24\,\mathrm{keV}$) + Gauss ($E = 0.34\,\mathrm{keV}$) + Gauss ($E = 0.546\,\mathrm{keV}$) + Gauss ($E = 0.554\,\mathrm{keV}$) + Gauss ($E = 6.31\,\mathrm{keV}$)] × highecut ($E_\mathrm{cut} = 1.92\,\mathrm{keV}$) × gabs ($E = 3.28\,\mathrm{keV}$) × edge ($E = 1.09\,\mathrm{keV}$) × edge ($E = 1.46\,\mathrm{keV}$) × edge ($E = 7.03\,\mathrm{keV}$). Fitting this model to the pn data resulted in $\chi^2_\mathrm{red} = 1.09$ for 2105 dof.

After convolving the fitted model with the MOS responses, the residual ratios were calculated for an energy grid with steps of 0.15 keV and fitted in the 0.5–12.0 keV

[58] This energy range was chosen so that residuals were available for the whole 0.3–12.0 keV range, which is of interest for determining the correction function and for further analyses.

range[59] with a Gompertz function, which was already used for the original CORRAREA version (Guainazzi et al., 2014, see Equation 3.5 in Chapter 3.3.3). This function proved to also represent the data sufficiently well at this stage of the project. The residual ratios and the accordingly fitted correction functions are shown in Figure 3.41. In case of MOS1, the fit resulted in a reduced chi-squared of 1.56 for 73 *dof* and led to the following correction function:

$$\mathcal{C}_{\mathrm{MOS1}}(E) = 0.029 + 1.0 + 0.040 \times \exp\left(-2.646 \times 10^{25} \times \exp\left(-17.958 \times E\right)\right). \quad (3.6)$$

For MOS2, the correction function

$$\mathcal{C}_{\mathrm{MOS2}}(E) = 0.048 + 1.0 - 0.005 \times \exp\left(-23\,000 \times \exp\left(-2.280 \times E\right)\right) \quad (3.7)$$

resulted in a reduced chi-squared of 1.47 for 73 *dof*. The requirement for the function used is that it does not introduce any new features into the data. For example, adding Gaussians to the function might help to obtain a better fit for the residual ratios, but they bear the danger of introducing sharp features to spectra when the CORRAREA correction is applied to individual observations. It is, thus, necessary to find a good compromise between a good fit and an overall smoothness of the correction function, with minimal complexity. This is also why one cannot completely rely on the chi-squared statistics in this case but rather has to estimate the usability of the function visually. In addition, the application of a correction function needs to be analysed with a set of selected test sources first before being implemented in the SAS routine, to ensure the absence of any new, correction-related features in the spectra.

It is not necessarily required to stick to the Gompertz function when fitting the residual ratios for the final, default correction. A suggestion for another, slightly less complex (as it does not involve nested exponential components) function which could also represent the data well is

$$\mathcal{C}_j(E) = \alpha_j + \alpha_{\mathrm{pn}} + \beta_j \times \frac{1}{1 + \exp\left(\frac{-E+\gamma_j}{\delta_j}\right)}, \quad (3.8)$$

again with the best fit parameters α_j, β_j, γ_j and δ_j (j = MOS1, MOS2). But deciding on the final function can only be done once all open issues which still prevent a default use of CORRAREA have been solved. In the end, maybe additional terms will be necessary to also represent the data at higher energies better once the window modes have been included. Nevertheless, the general improvement of the data with the correction functions presented here can already be demonstrated, as will be done in the following discussion.

3.10 Discussion

As MOS-to-pn flux ratios served as an indicator for the effective area calibration uncertainties before (see Chapter 3.1), another flux ratio analysis was performed to prove the positive impact of the new correction functions presented in this work. At the time of writing, suitable spectral models were available for 44 of the 54 on-axis,

[59] Lower energies were excluded to eliminate effects of uncertainties in the detector response calibration.

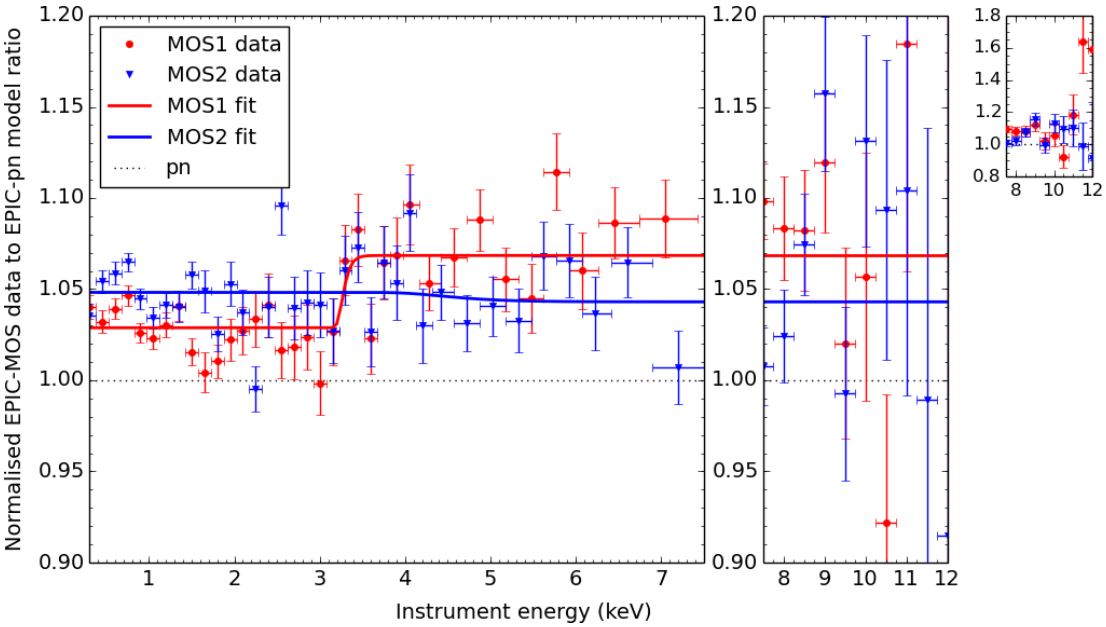

Figure 3.41: Updated residual ratios and correction functions. They were obtained using 54 pile-up free FF mode observations for which source region radii of 40″ (MOS) and 35″ (pn) could be applied. The left panel shows the energy range which was mainly in the focus of this work, with the residual ratios rebinned to a SNR of 50. For the central panel with the higher energies, the residual ratios were redistributed to an energy grid with steps of 0.5 keV for presentation purposes since the errors are much higher here for FF mode observations. The top right panel is an additional display of the higher energies to show the maximum values the residual ratios reach.

FF-mode sources that were used to determine the correction functions.[60] The spectra of these sources which had already been created using the calibration files public in October 2020 were fitted with the models and the resulting fluxes were extracted for different energy bands before dividing each MOS flux value by the corresponding pn flux. The distribution of the MOS-to-pn flux ratios for each energy band is shown in Figure 3.42. Below 2.2 keV the mean deviation between MOS and pn is around 2–4% and, as observed before, rises towards higher energies, reaching values above 10%. Also, even with the updated calibration status, the broader distribution of the flux ratios at higher energies, which had already been noted in Chapter 3.1, is still present. This can be explained by the sole use of FF mode observations, which showed very poor statistics at higher energies due to bright sources not being observable in this mode because they lead to pile-up. At this point, still only FF mode observations were considered for the flux ratio analysis since window mode observations could not yet be fully included to determine the correction functions and it has yet to be confirmed whether or not a correction function which was determined based on one mode can be applied to another mode without problems.

The respective flux ratios with the new correction functions applied are shown in Figure 3.43. As expected, the broad distribution at higher energies due to the use of FF mode observations is present as well, but most notably the mean values show how the flux ratios have been improved by the correction. In the 2.2–4.5 keV band the flux ratios seem extremely well aligned. At lower energies there is even a slight overcorrection, but, nevertheless, the mean values are closer to unity with a deviation of mostly below 2%. The change becomes even more apparent at higher energies where the deviation between the mean values and unity is about halved compared to the uncorrected case. Basically, this shows that the new correction functions obtained with the revised and largely automated routine can be applied successfully to correct for calibration uncertainties of the EPIC on-axis effective areas and improve their cross-calibration accuracy. But so far, the new, updated correction functions presented in the previous chapters should still only be used for a non-default application of Corrarea since there are still open issues which need to be resolved first before the change to a default correction can be completed.

One of these issues is the combination of sources observed in different imaging modes. This would improve the statistics at higher energies considerably and, thus, help to find correction functions which could further improve the effective area cross-calibration at higher energies. In this context, also the analysis of whether or not different, mode-dependent correction functions would be required needs to be performed. The effective area itself should actually not be mode-dependent, but the modes usually require differences in the processing, for example due to limited choices with respect to the location of the background regions or the need for a different model to fit the stacked spectra. Before combining the different modes to get one correction function for each EPIC camera to be applied to all observations, the possibility of a mode-dependency needs to be excluded. This could be done by testing if correction functions obtained with the same mode as the corrected observations lead to similar improvements as functions obtained with a different mode and functions obtained with all modes combined. The new, extended pile-up free sample (Table A.3) which was compiled and carefully screened

[60] The individual models and resulting fluxes were kindly provided by M. Smith (ESAC) and C. Pommranz (IAAT).

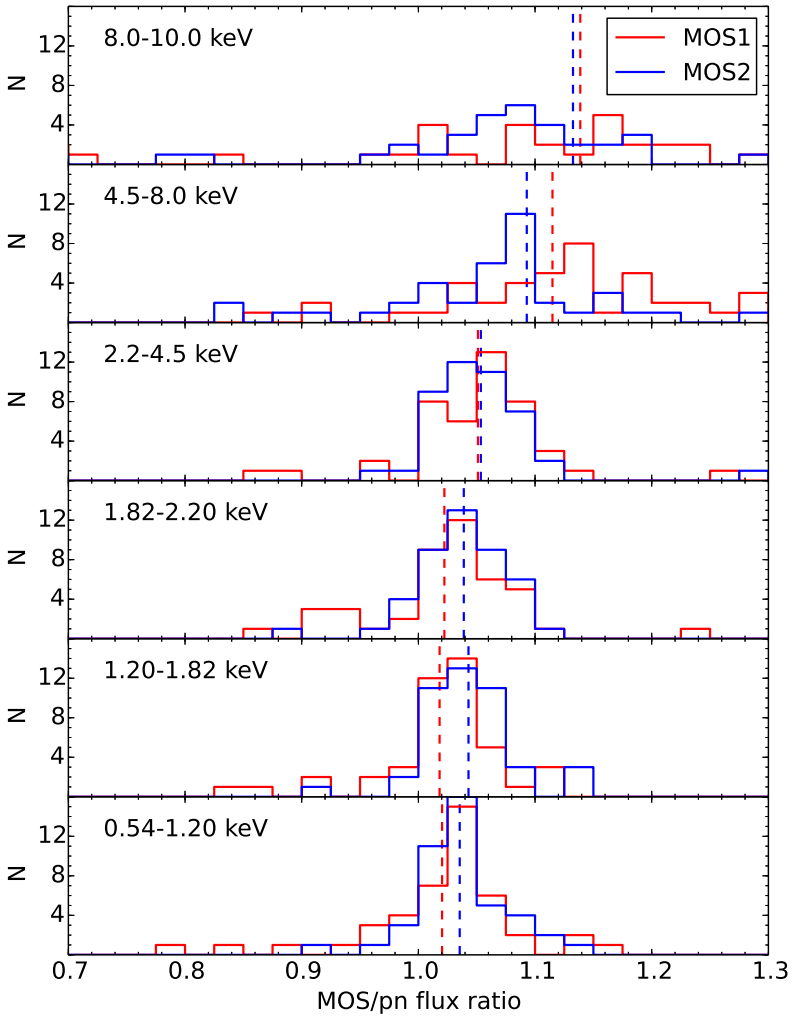

Figure 3.42: Updated MOS-to-pn flux ratios without the CORRAREA correction applied. The fluxes were determined for 44 on-axis point sources observed in FF mode. Shown is the number N of sources for a certain flux ratio, the dashed lines indicate the mean values. To process the data, SAS version 16.1 and the calibration files public in October 2020 were used.

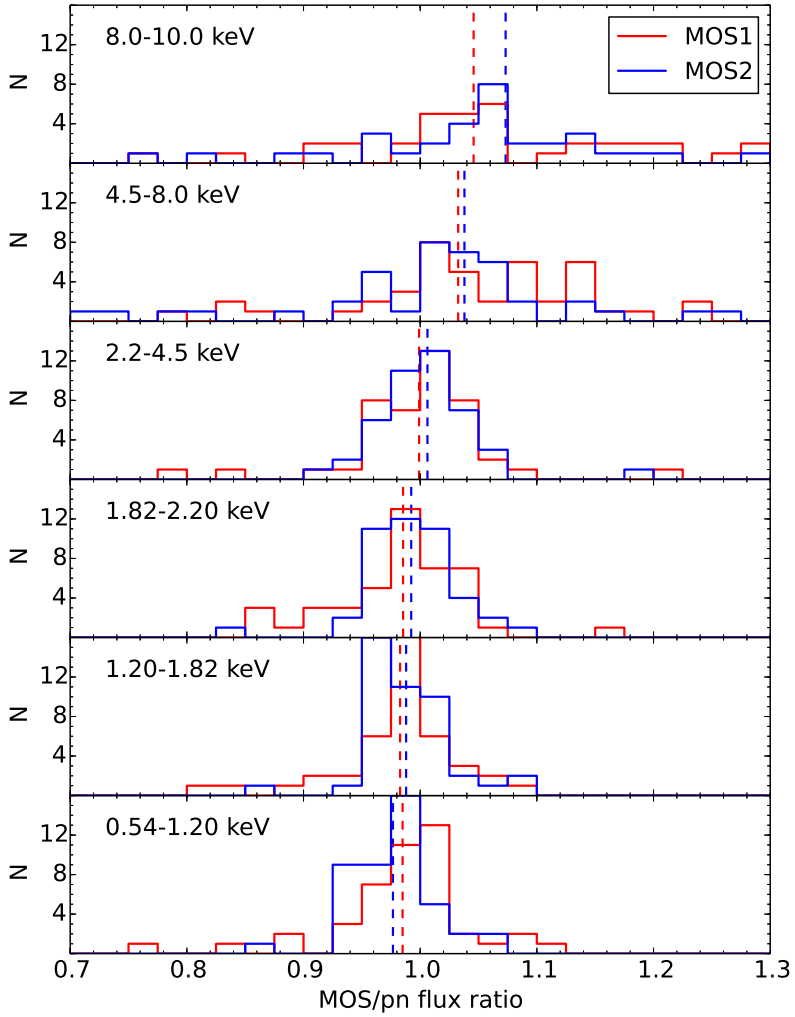

Figure 3.43: Updated MOS-to-pn flux ratios after applying the new correction functions. The fluxes were determined for 44 on-axis point sources observed in FF mode. Shown is the number N of sources for a certain flux ratio, the dashed lines indicate the mean values. To process the data, SAS version 16.1 and the calibration files public in October 2020 were used, with the new correction functions manually implemented in the XAREAEF CCF constituents and applied in the process of creating the ARFs with `arfgen` (setting `applyxcaladjustment` to true).

in the scope of this work already contains a sufficiently high number of sources which were observed with only one mode being used for all three EPICs to perform the required analysis.[61]

To compare the outcome for subsamples of different filters, the number of observations still needs to be higher since only six observations with only the thick filters used are currently available, which is not sufficient for such an analysis. Particularly a change with the thick filters would be of interest here, since they can be expected to have the biggest impact on the observed data and were, thus, excluded by Read et al. (2014) for the original sample of the first CORRAREA version. But at this point, only 11 of the 163 sources in the pile-up free sample were observed with one or more of the thick filters being used. So, their impact, if any, can be expected to be negligible. However, should the sample be extended again in the future and the number of included thick filter observations increase, an analysis of the filter-dependency would be advisable. The current 4XMM-DR10 version of the *XMM-Newton Serendipitous Source Catalogue* (Webb et al., 2020), for example, contains almost 11 700 observations, which means around 2000 additional ones which have not yet been subject to the source selection process.

But to make CORRAREA a default correction, the pile-up free sample of 163 sources presented here is already large enough. By adjusting the original selection criteria to allow for higher statistics while at the same time processing each source in a more individually customized way (GTI-filtering, background region selection, source region size and pile-up screening), the sample offers a well suited base to determine a correction function for a default correction of the on-axis effective area. Besides dealing with the combination of different modes, also a new analysis of the dependence on the choice of the source region radius has to be performed before actually being able to safely combine all sources in the sample. The new PSF calibration files tested with the automated routine in this work showed a reduced discrepancy between the residual ratios of nested annuli, particularly at higher energies. Since the FF mode observations do not offer good statistics at higher energies, the window modes should be included to analyse the outcome for different source region radii and nested annuli with the updated public calibration files. If no substantial differences remain, the data of each source can be extracted with the maximum radius determined for each detector respectively. As a result, none of the sources from the pile-up free sample would have to be excluded to determine the correction functions and for each source and exposure the maximally possible number of events could be extracted for improved statistics.

Currently an implementation of the *fit and stack*[62] approach into the routine and a comparison with the *stack and fit* approach applied so far is in progress. Read et al. (2014) reported a good agreement between the residual ratios obtained with the two different approaches below 5 keV. However, with the changes made here, particularly the new, individual background region selection, a new comparison to confirm that result should be made. Also, the *fit and stack* approach could be a solution to be able to combine sources observed with different science modes as the ARFs and RMFs do not have to be stacked and, thus, the problem of any incorrect weighting would be resolved.

[61] 65 FF-only observations, 41 LW-only observations and 36 SW-only observations when making no limitations to the allowed maximum source region radius

[62] fitting each source separately and calculating the median of the resulting residuals instead of stacking the spectra

But there is a disagreement as to whether or not the *fit and stack* approach leads to a drop of the MOS-to-pn residual ratios at higher energies due to negative spectral bins (probably caused in the background subtraction process due to the low statistics of individual spectra), which are not seen as an issue in the *stack and fit* approach because the stacked spectrum offers higher statistics (Read et al., 2014; Schellenberger et al., 2015). In addition, the individual fitting of each source's spectrum can introduce more systematic errors, though not necessarily to a considerable degree, and it requires more time to add new observations to the sample in the future since physical models have to be determined manually for each new source. So, the *stack and fit* approach provides more ease for further updates of CORRAREA.

All in all, there are three remaining steps that should be done to be able to use the full pile-up free sample and to obtain correction functions suitable for a default application: 1. ensure there is no longer a significant dependence of the residual ratios on the source region radius; 2. compare the two stacking approaches, assess if their respective open issues can be solved successfully (mode combination in the case of *stack and fit*, reliability at higher energies in the case of *fit and stack*) and decide on which approach to stick with; 3. determine the default correction functions and examine their applicability with selected test sources[63] before implementing them into the calibration files. But apart from the steps still necessary to complete the change of CORRAREA into a default correction, the presented new correction functions can already be used for an updated non-default CORRAREA version to give users a revised estimate of the on-axis effective area calibration uncertainties as compared to the originally implemented first version.

In addition, the script package developed in the scope of this work to largely automate the process of obtaining the CORRAREA correction functions eases further analysis steps, like comparing the outcome for different source region radii and screening new observations to further extend the sample in the future. As the testing of the new PSF CCFs prior to their release showed, the scripts can also be used to provide an independent validation of other calibration projects. This illustrates once again the correlation between different calibration issues, which asks for a continuous recalibration, made possible by the automation. Once CORRAREA is fully implemented as a (regularly updated) default correction, the scripts offer the potential to also include other satellite missions to align XMM-Newton's EPIC and other instruments operating in the same energy range with each other. Examples for possible missions and instruments are Chandra's ACIS (Advanced CCD Imaging Spectrometer), eRosita (Extended Roentgen Survey with an Imaging Telescope Array) on-board the satellite SRG (Spectrum-Roentgen-Gamma) and the currently developed WFI (Wide Field Imager) of ATHENA (Advanced Telescope for High-Energy Astrophysics).

[63] particularly to ensure no new features are added to the spectra

CHAPTER 4

Search for an Associated Compact Object in G96.0+2.0

In May 2017, the Galactic supernova remnant (SNR) G96.0+2.0 was observed with XMM-Newton for the purpose of finding a compact object associated with the SNR, preferably a purely thermally emitting NS – a so-called central compact object (CCO). The corresponding analysis of the data has been performed within the scope of this work and is presented in this chapter. First, an explanation is provided as to why the topic is of current interest. After a general introduction on how SNRs and compact objects are related and a characterization of different types of NSs, particularly isolated ones, details about G96.0+2.0 and why it was chosen as a suitable candidate for the intended study are given. Following a short description of the available dataset, the results of the different analysis steps are presented, including the initial data reduction, source detection, a search for optical counterparts, spectral and timing analysis as well as an analysis of the X-ray-to-optical flux ratios and the hardness ratios. In the final section these results are discussed.

4.1 Motivation

Neutron stars are impressive objects of fundamental interest in modern astrophysics. Being not quite compressed enough to have an event horizon, they have the highest density of any directly observable object known. Thus, they offer a unique opportunity to study the properties of matter in such an extreme environment. Even though NSs were already theoretically predicted in the first half of the last century by Landau (1932) and Baade & Zwicky (1934) and first detected in the 1960s (Shklovsky, 1967; Hewish et al., 1968), their nature is not yet fully understood. Today, the theoretically possible values of their mass and radius are well constrained (Lorimer & Kramer, 2012) and the ongoing research has already revealed a lot about their magnetic fields and accretion processes (see Chapter 4.2.2). But the equation of state of the superdense nuclear matter, describing how density and pressure are related, and the composition of the matter in the core of NSs are still uncertain.

While accurate mass measurements are easier to be obtained in observational studies, particularly in binary systems, it is difficult to reliably measure the radii of NSs. Precise measurements of both, mass and radius of a NS, would give an insight into their correlation and, as they are directly related to the nature of the matter inside the NS, into the equation of state by being compared to the mass-radius relations predicted by different theoretical models (e.g. Lattimer & Prakash, 2007). A method to constrain the mass and radius of an observed NS is the spectral fitting of the thermal emission of

the NS surface and deriving the NS mass and the size of the emission region from the models used (e.g. Ho & Heinke, 2009; Klochkov et al., 2015). Unfortunately, a direct observation of the NS surface is often not possible due to its emission being outshined by non-thermal components caused by accretion processes and strong magnetic activity.

A few hundreds of NSs have been identified as accretion-powered pulsars, which are NSs that are part of a binary system and accrete matter from their companion star. The vast majority of the more than 2500 known NSs has been identified as radio pulsars (Tauris et al., 2015), with only part of them having been detected in X-rays as well. They show beamed emission caused by particles being accelerated and material being heated close to the magnetic poles. The latter case usually dominates any thermal emission, while these types of NSs are also often too old, and have, thus, often cooled down too much already, for the thermal emission of the whole surface to be observed.

Our knowledge about the composition of the NS population has been enriched by the detection of new classes of isolated NSs, namely X-ray dim isolated NSs (XDINSs), magnetars and, in recent years, CCOs. So far, there are only a few tens of these objects known, but they offer an excellent view on phenomena which cannot be observed in the more numerously detected radio pulsars and X-ray binaries. While magnetars have the strongest magnetic fields in the universe, XDINSs and CCOs are thermally emitting, cooling NSs, which are ideal for studying the mass-radius relation and, thus, the equation of state as described above. Enlarging the small number of known objects that belong to these classes is therefore of great interest.

Magnetars and CCOs can be associated with SNRs and observing SNRs for which no associated compact object has been found yet are a great opportunity to actively search for such objects. Of the few dozen NSs that can be associated with a SNR so far (Klochkov et al., 2016), only about one third are radio pulsars. The other two thirds are magnetars and CCOs in comparable numbers, which means all three classes of NSs seem to constitute equally significant types of young NSs (Gotthelf & Halpern, 2018). Thus, the search for isolated NSs associated with SNRs does not only potentially increase the small number of magnetars and CCOs known to further study these objects but also contributes to the study of the NS population in our Galaxy.

In addition, the exact nature of both, CCOs and magnetars is not fully understood and open questions remain with respect to some of their properties, like how the constant emission of magnetars and their energetic flares can both be explained by one model (Mereghetti, 2008, 2013). Also, the precise distinction between the different classes of NSs is not clear yet. The first detected radio-quiet isolated NS associated with a SNR, 1E 161348–5055.1 (Tuohy & Garmire, 1980), has long been the prototype of a CCO and is now believed to actually be a magnetar (De Luca, 2017) and there are theories assuming some CCOs might be magnetars hidden by crustal activity (Popov et al., 2015). All in all, the study of CCOs and magnetars is of great current interest and any addition to their samples is highly valuable.

As CCOs have turned out to be ideal objects to study the equation of state (e.g. Ho & Heinke, 2009; Klochkov et al., 2013, 2015), the focus of this work is to search for a potential CCO associated with the SNR G96.0+2.0 based on an XMM-Newton observation that was conducted for this purpose. The SNR was chosen as no compact object has been associated with it so far, its location far from the Galactic centre means low Galactic absorption, its observed radio shape and emission suggest it to be at an early stage of development and, thus, quite young, its size fits into the XMM FOV and

a distance estimate is available for it (Kothes et al., 2005) to support the analysis of potentially associated point sources. Even if no CCO should be found, there is still a good chance to find either a magnetar or a radio pulsar instead. The first case would mean an addition to another underrepresented class of NSs and the latter case, besides adding to the numerous but still very interesting class of radio pulsars, would also be valuable as, generally, the association of a SNR and a compact object offers a great opportunity to gain information about the system and its development from two sources.

4.2 Compact Objects Associated with Supernova Remnants

The approach to achieving the aim of this work is based on a general understanding of SNRs and NSs, their association and their specific properties. The following couple of sections provide an overview of the relevant theoretical background concerning the nature, different types and basic properties of SNRs and NSs. The information given is based on Longair (2011), Seward & Charles (2010) and Trümper & Hasinger (2008), which can be consulted for a more detailed review.

4.2.1 The Late Stages of Stellar Evolution

Neutron stars and supernova remnants are an integral part of stellar evolution. All stars start their lives on the main sequence of the Hertzsprung-Russell diagram (Hertzsprung, 1911; Russell, 1914), burning hydrogen into helium in their cores and being stabilized by the hydrostatic equilibrium between the inward force of gravity and the thermal radiation and gas pressure P:

$$\frac{\mathrm{d}P}{\mathrm{d}r} = -\frac{GM\left(r\right)}{r^2} \times \rho\left(r\right) \,, \tag{4.1}$$

where r is the distance to the centre of the star, G is the gravitational constant[64], M is the stellar mass and ρ is the density. The further development of the stars depends on their individual masses. The time on the main sequence is determined by the nuclear timescale

$$\tau_{\mathrm{nuc}} = f\varepsilon\frac{Mc^2}{L} \tag{4.2}$$

with the luminosity L of the star and the speed of light c.[65] The fraction f of the total mass that is available for fusion in the core is about 10% and the mass energy ε which is released by the fusion of hydrogen into helium is 0.7%. With the mass-luminosity relation of $L \propto M^{3.5}$ for main sequence stars, this results in the stars being on the main sequence on a timescale of

$$\tau_{\mathrm{ms}} \propto 0.1 \times 0.007 \times \frac{c^2}{M^{2.5}} \,. \tag{4.3}$$

Thus, less massive stars develop much more slowly, like our Sun with $\tau_{\mathrm{ms}} \approx 10^{10}\,\mathrm{yr}$, while massive stars already leave the main sequence after only a few million or even

[64] $G \approx 6.67{\times}10^{-11}\,\mathrm{m^3\,kg^{-1}\,s^{-2}}$ (Mohr et al., 2016)
[65] $c \approx 3{\times}10^{8}\,\mathrm{m\,s^{-1}}$ (Mohr et al., 2016)

only a few hundred thousand years. And they have different destinies altogether as well. For simplification, only the two major scenarios are described in the following as details about all possible stellar evolution scenarios that lead to the final stages would be out of the scope of this work.[66]

Stars with masses between $\sim 0.4\,M_\odot$[67] and $\sim 8\,M_\odot$ can undergo one more fusion cycle, converting helium into carbon and oxygen. When the hydrogen in the core is running out, the core starts to contract due to gravity. This leads to a rise in temperature which allows for the hydrogen burning to continue in a shell around the core, consequently causes an expansion of the star's outer envelope and, eventually, triggers the fusion of helium in the core itself. Again, the fusion continues in a shell around the core in the subsequent phase, below the still existing hydrogen shell, which continuously adds more helium. Due to the expansion of the outer envelope that goes with the shell burning phases, the outer layers are less bound by gravity and the star loses a lot of mass in the form of stellar wind. The gravitational potential is not high enough to sufficiently increase the temperature in the core again to start the next fusion cycle. As a result, the core collapses until it is stabilized by the degeneracy pressure of the electrons, resulting from the Pauli exclusion principle, which states that two identical fermions in a quantum system cannot occupy the same quantum mechanical state at the same time. But the fusion in the shells alone gets intense enough to eject the remaining outer layers and reveal the degenerate core, a carbon-oxygen white dwarf (WD), usually keeping a thin hydrogen atmosphere but sometimes ending up with one consisting of almost pure helium (Bischoff-Kim et al., 2019).

With about one solar mass left in total, these Earth-sized WDs have a density of $\sim 10^9\,\mathrm{kg\,m^{-3}}$. The maximum mass that WDs can have is defined by the degenerate nature of its matter as proposed by Chandrasekhar (1931). Above about $1.44\,M_\odot$, known as the Chandrasekhar limit, the degeneracy pressure of the electrons is overpowered by gravity and the core collapses even further. By themselves, the inactive WDs cool over several billions of years, a timescale larger than the current age of the Universe, until they cease to radiate. However, via accretion from a companion star or the merging of two WDs the Chandrasekhar limit can be exceeded, leading to the most energetic stellar event known: a type Ia supernova (SN). The progressing gravitational collapse leads to a temperature high enough to ignite carbon fusion. As the WD consists almost entirely of carbon and oxygen, this leads to a runaway nuclear reaction which releases $10^{52}\,\mathrm{erg}$ and disrupts the WD within seconds, leaving no remaining compact object.

This type of SNe has to be distinguished from core-collapse SNe. Only remnants of the latter one can be expected to potentially host a NS, which is the object of interest in this work. Type Ia SNe are much rarer, making up only about 10–15% of SN events in our Galaxy (Kaspi, 2000), and they all show very similar light curves, hinting at the similarity of their progenitors. The luminosity rises rapidly up to $10^9\,L_\odot$ within two weeks and has a characteristic exponential decline at later times. While type Ia SNe can occur in all kinds of galaxies, core-collapse SNe and their remnants are limited to regions in the vicinity of star-forming regions, the arms of spiral galaxies and irregular galaxies in particular.

[66] The mass limits given here are only approximate values as stellar evolution also depends on other factors like e.g. metallicity.

[67] solar mass: $M_\odot \approx 1.989\times10^{33}\,\mathrm{g}$ (Weigert et al., 2009)

Core-collapse SNe are part of the evolution scenario of more massive stars, which use up their nuclear fuel much more quickly and are, thus, still relatively young at the time the SN explosion happens. When the mass of the progenitor star is above $\sim 8\,M_\odot$, the gravitational force is strong enough for the star to undergo further nuclear fusion cycles, from hydrogen and helium to carbon, neon, oxygen and silicon burning, until the stellar core consists of iron (with the burning of the other elements continuing in the layered shells surrounding the core). As iron is the most stable element with a high nuclear binding energy, it is the final product that can be obtained by exothermic fusion reactions and, thus, no further fusion cycle can take place in stars as it would require an energy input. However, the inactive core continues to gain mass through the burning of silicon into more iron in the outer layers until the electron degeneracy pressure is no longer sufficient to stabilise the core against gravity. As the temperature in the core reaches values of $10^9\,\mathrm{K}$ and higher, iron nuclei are disintegrated into protons and neutrons. The protons p capture electrons e^-,

$$\mathrm{p} + \mathrm{e}^- \rightarrow \mathrm{n} + \nu_\mathrm{e}\,, \tag{4.4}$$

and electron neutrinos ν_e and more neutrons n are created. The number of electrons supporting the core is reduced while at the same time the neutrinos carry away the bulk of the $10^{53}\,\mathrm{erg}$ of binding energy that is released in the core. This energy loss also causes the pressure support to drop, resulting in a runaway process and the collapse of the core within a few seconds. When the impact of the neutron degeneracy pressure sets in, the subsequently infalling material is reflected at the core and a shock wave forms which, together with the energetic neutrinos, accelerates the material of the outer layers and ejects it if the escape velocity is exceeded.

These core-collapse SNe are about two magnitudes less luminous than type Ia SNe and have broader light curves with more diverse decays, indicating the wider range of properties of their progenitor stars. Types of these SNe are Ib, Ic and II. The difference between types I and II is the presence of hydrogen emission lines in their spectra. While type II SNe show broad hydrogen lines, the progenitors of type I SNe have already lost their hydrogen envelopes prior to the SN explosion, either in the process of evolving into a WD in the case of type Ia SNe or via strong stellar winds or accretion by a binary companion as assumed for the progenitors of type Ib/c core-collapse SNe.[68]

The remnants of SNe, extended objects consisting of the ejected material and swept-up surrounding medium, can reach a few tens of parsecs in diameter and are visible on a time scale of 10^5 years as the kinetic energy contained in the shell is dissipated. The type of the original SN can also be found out by investigating the SNR, for example by deriving the abundances and densities of the elements in a remnant's spectrum (see e.g. Sasaki et al., 2014) or by analysing the surrounding structures in the interstellar medium, which might hint at a strong stellar wind (see e.g. Kothes et al., 2005). An overview of the X-ray properties of SNRs is given by Vink (2012). The remnants undergo different stages of development: free expansion, the adiabatic phase, also called the Sedov-Taylor phase, and the radiative phase.

For the first few hundred years, depending also on the local density of the interstellar medium, the ejecta expand freely with typical velocities around $10\,000\,\mathrm{km\,s^{-1}}$. They

[68] the difference between type Ib and Ic is that type Ic progenitors have also already lost their helium layers

sweep up the ambient medium, heating it to several millions of degrees, without being affected by it themselves as the mass of the swept-up material is much lower than the mass of the ejecta. Once the masses are equal, the frontal ejecta are decelerated and the following ejecta bump into them, causing an inward-moving reverse shock, which now heats the ejected material and which marks the transition to the adiabatic phase. The ionized ejecta are now so hot and tenuous that there is no recombination and almost no energy is lost via radiation. The ejected material only cools because of its expansion, driven by the thermal gas pressure, which follows the solution by Sedov (1959) and Taylor (1950) for blast wave explosions. After 10 000 to 20 000 years the temperature has dropped below 10^6 K and the radiative phase sets in, during which ions and electrons recombine, leading to radiative cooling on a time scale of $\sim 10^5$ years until the SNR dissolves as it merges in the interstellar medium.

The analysis of a SNR's evolutionary stage can be used to get an estimate of the remnant's age. Therefore, the evolutionary stage is also an indication of whether or not thermal emission from an associated compact object can be expected to still be strong enough to be detectable (the compact object being the remnant of the original stellar core). If enough material of the outer stellar layers is ejected during the collapse, the degenerate pressure of the neutrons is sufficient to stabilize the core, resulting in a NS, the most dense object that can be directly observed. In case the gravitational force of a star is so strong that the core accretes enough mass to exceed the Tolman-Oppenheimer-Volkoff limit (Tolman, 1939; Oppenheimer & Volkoff, 1939), estimated to be around $2\,M_\odot$ to $3\,M_\odot$, the neutrons cannot stabilize the core against gravity and it collapses into a black hole (BH). This singularity can only be observed by indirect means through its interaction with its environment as even light cannot escape. Neutron stars are, thus, easier to find, easier to observe and easier to analyse in order to advance the study of superdense matter, which cannot be reproduced in a laboratory on Earth.

While their formation and evolution is not yet fully understood (Lattimer & Prakash, 2004), the association of NSs with SNRs was already suggested early in the 20$^{\text{th}}$ century. Chandrasekhar had deduced a maximum mass for a stable WD in 1931. One year later, even before the experimental discovery of the neutron (Chadwick, 1932) had been made public, Landau (1932; Yakovlev et al., 2013) introduced the idea of the existence of NSs. It was first proposed by Baade & Zwicky (1934) that the formation of such NSs could happen in the course of SN explosions of stars, though due to the expected low luminosity and small size it was not believed that these objects could actually be observed. In 1962, almost thirty years later, Giacconi et al. (1962) detected the first extrasolar X-ray source, Sco X-1, for which a NS nature was suggested (Morton, 1964). The proof for the existence of NSs was given in 1967 when Jocelyn Bell detected the first pulsar, PSR1919+21, a pulsating star, in the radio band (Hewish et al., 1968), for which Bell's supervisor Antony Hewish was awarded with the Nobel Prize in 1974. The extremely regular pulses could only be explained by the rotation of objects as compact as NSs (Gold, 1968). Finally, with the detection of the radio pulsars in the Vela (Large et al., 1968) and Crab (Staelin & Reifenstein, 1968) SNRs, there was also observational evidence for the association of SNRs and NSs, supporting the hypothesis developed by Zwicky and Baade. Since then, the interest in these late stellar stage objects has risen and today around 3000 NSs of different types are known.

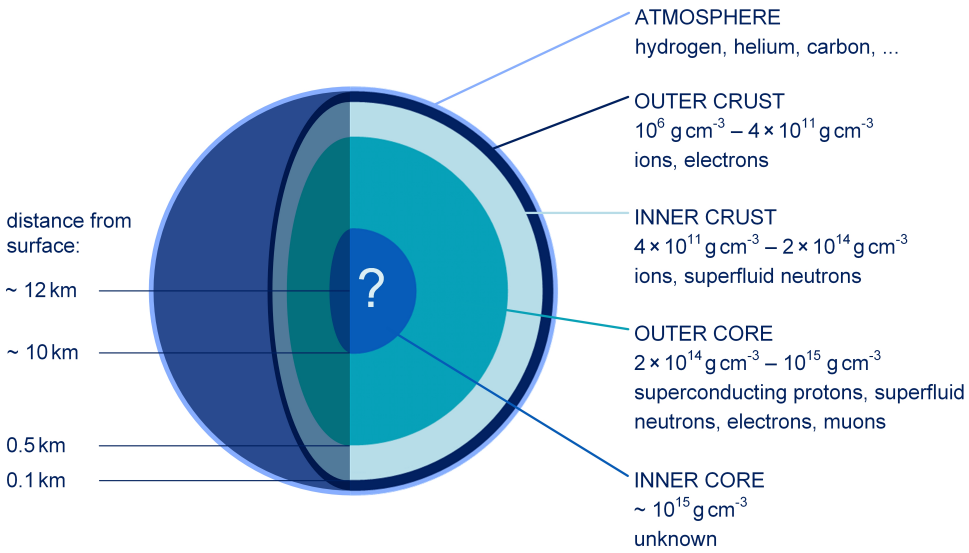

Figure 4.1: Inner structure of a neutron star. (Image loosely based on Gendreau et al., 2012)

4.2.2 Neutron Stars

Although a high number of NSs has been detected so far, the composition of matter in their interior is still unclear. Figure 4.1 shows a schematic view of the inner structure of NSs. It is composed of different layers with increasing density. These stunning objects comprise about 1.4 $M_\odot$ within a radius as small as ∼12 km. In the inner core the density is expected to be so high that the equation of state for the matter is still unknown (see e.g. Lattimer & Prakash, 2001) and it is, thus, an open question if there is a phase transition to some exotic form of matter, like a quark-gluon plasma, or not. This is what makes NSs objects of interest for different fields of physics alike.

As the mass-radius relation of a NS is directly linked with its specific equation of state, a good measurement of these parameters could give a strong constraint on the valid formula. Though the theoretical values for these two parameters are already narrowed down considerably, there is no NS for which observations could reveal sufficiently precise values for both, mass and radius, so far. The problem is that for most types of NSs, as explained below, the observation of at least one of the parameters is complicated by the surroundings. Generally, the radius can be well determined by the thermal emission of a homogeneously emitting stellar object, for example. While NSs, being formed at $\sim 10^{11}$ K during the SN explosion, have a surface temperature of a few times 10^6 K after about a hundred years, they cool down to circa 0.1×10^6 K within $\sim 10^7$ years (Mereghetti, 2011). Thermal emission in the soft X-ray band can, therefore, be observed in young NSs, until $\sim 10^6$ years after their birth, before they have cooled down too much to thermally emit X-rays. The cooling process also depends on the properties of the matter inside (Ofengeim et al., 2015; Beznogov & Yakovlev, 2015), which adds to the usefulness of studying the thermal behaviour of NSs in order to find out more about their interior. Unfortunately, the thermal emission is often partially obscured or outshined by other X-ray producing processes (see Chapter 2.2.1). Besides their high density, NSs have some additional properties which cannot be reproduced on Earth. They have immensely

high magnetic fields, which, with typically around 10^{12} G, are hundreds of billions times stronger than the magnetic field of the Earth, their strong gravitational fields cause relativistic effects and often accretion can be observed. These physical scenarios make NSs even more interesting, but their impact also prevents a direct observation of the neutron star alone. Different types of NSs show different scenarios and some are better suited for the measurement of the mass and/or radius than others.

For measuring the mass, NSs in binary systems offer the opportunity of using orbital dynamics, for example in the form of velocity curves for both objects or of Doppler-shifts in X-ray pulse periods. The proximity of the two objects leads to the accretion of matter. Already Sco X-1, the first extrasolar X-ray source ever discovered, was interpreted as a binary system in which a NS accretes matter from a companion star (Shklovsky, 1967). Today we mainly distinguish between two classes of these accretion-powered X-ray binaries: high-mass X-ray binaries (HMXBs) and low-mass X-ray binaries (LMXBs). In HMXBs, either a NS or a BH accretes matter from the stellar wind of a massive late O or early B type star. LMXBs, on the other hand, have a low-mass main sequence star, like the Sun, as a primary, from which the secondary NS or BH accretes matter via Roche-Lobe overflow. In the optical, this accretion disc outshines the primary star so that HMXBs are better suited for measuring the masses of the two binary companions than LMXBs.[69] But the accretion luminosity in the X-ray band masks the thermal emission of any NS secondary so that no sufficient estimation of the NS radius can be obtained.[70]

Isolated NSs can, thus, offer a better view onto the NS surface. But besides the thermal emission due to their internal heat, they can also have X-ray emission powered by rotational energy, by magnetic field decay and/or by accretion from the surrounding medium. These mechanisms can occur simultaneously with the dominant energy source depending on the physical properties and age of the NS (Mereghetti, 2011), resulting in the definition of different types of isolated NSs.

Radio pulsars are the first type of NSs that has been discovered besides X-ray binaries and the observation of their properties gave proof for the existence of NSs. They were identified as rapidly spinning, strongly magnetized NSs with a beamed emission powered by their rotational energy (Pacini, 1967, 1968; Gold, 1968, 1969) and are not isolated by definition, although only a small fraction is found to be members of the aforementioned accreting binary systems. With $\sim 10^{49}$ erg, the rotational energy stored in rapidly spinning NSs can be compared with the energy released by fusion in a normal star over its entire lifetime (Becker, 2009). The rapid rotation is a result of the conservation of angular momentum during the stellar collapse. Magnetic flux conservation during the collapse and inner dynamics lead to a large magnetic field of $\sim 10^{12}$ G, which accelerates particles along its field lines. While there is still no consensus

[69] Some LMXBs contain accretion-powered millisecond pulsars, which are understood to be the progenitors of rotation-powered millisecond pulsars (see text below). There are also attempts to constrain the equation of state by analysing the pulse-shapes of accretion-powered millisecond pulsars, since these are expected to be affected by thermal emission from the NS surface which is Compton scattered in the accretion column (see e.g. Leahy et al., 2011; Morsink & Leahy, 2011). But the various geometric factors which need to be considered lead to large uncertainties (Özel & Freire, 2016).

[70] The few known binary pulsars that consist of two NSs even offer a more precise measurement of the mass, but the problem that the radius cannot be measured with sufficiently low uncertainties persists (see e.g. Özel & Freire, 2016).

as to the radio emission mechanism (Melrose & Rafat, 2017), high-energy radiation can be caused by several processes. For example, besides the thermal emission from the hot surface, there is soft X-ray emission from the regions around the magnetic poles, which get heated by the relativistic particles that flow back onto the NS surface, non-thermal emission from the optical to the γ-ray band caused by the acceleration of charged, relativistic particles in the magnetosphere and sometimes non-thermal synchrotron emission in the radio to hard X-ray band from an extended pulsar wind nebula (PWN) around the pulsar. But for the majority of pulsars no optical or γ-ray emission has been detected and the thermal X-ray emission is usually outshined or masked by the other emission processes. The characteristic pulsed emission can be observed when the axis of the magnetic dipole is aligned at an angle to the rotational axis and the beam around the magnetic axis passes the line of sight. Typical pulse periods range from a few tens of milliseconds to approximately 8 s. The acknowledged subtype of millisecond pulsars has periods as low as 1–10 ms, but they are believed to be old pulsars that have been spun up by accretion of matter from a companion star and, thus, cannot be expected to show strong thermal emission from their surface anymore. With about 2500 objects known so far[71], radio pulsars constitute the large majority of NSs, but only a few dozen of them have been associated with SNRs.

Magnetars are powered by the decay of their immensely strong magnetic fields. With 10^{14}–10^{15} G they have the strongest magnetic fields known, leading to X-ray luminosities of 10^{35}–$10^{36}\,\mathrm{erg\,s^{-1}}$. At the same time, the enhanced magnetic braking leads to periods of about 5–12 s, which are longer than the typical periods observed for normal pulsars. Only 23 magnetars have been confirmed so far, but almost half of them can be associated with SNRs (Kaspi & Beloborodov, 2017). There are two groups of magnetars: anomalous X-ray pulsars (AXPs) and soft gamma repeaters (SGRs). Each of these two types makes up about half of the magnetar population, respectively. When AXPs were discovered in the 1980s, they were called anomalous because at first they were believed to be accreting objects due to their high X-ray luminosity, even though no companion or orbital motion could be confirmed. SGRs were discovered in γ-rays due to their bursts with $\sim 10^{41}$ erg at unpredictable intervals. When such bursts were observed for one of the AXPs, the two groups were identified as belonging to the same class of NSs, called magnetars. As rare events, magnetars show giant flares, releasing 10^{44}–10^{46} erg within a fraction of a second. The origin of these bursts is believed to lie in occasional cracks in the stellar crust. A direct observation of the thermal cooling emission from the surface is hindered by the influence of the strong magnetic field. But the small number of these objects and the still unresolved question of how their emission features can all be conclusively explained makes the search for magnetars also an issue of current astrophysical interest.

X-ray dim isolated neutron stars are by definition not associated with SNRs. The so-called *Magnificent Seven* have all been discovered within proximity, having a maximum distance of $\sim$500 pc, with the German ROSAT[72] mission. They show a purely thermal X-ray emission with a typical blackbody temperature of a few 10^6 K and

[71] according to the pulsar catalogue of the Australian Telescope National Facility available at `http://www.atnf.csiro.au/research/pulsar/psrcat` (Manchester et al., 2005)

[72] short for Röntgensatellit

a luminosity of $\sim 10^{31}\,\mathrm{erg\,s^{-1}}$, although five of these objects also have pulsations between 3.5 s and 11.4 s (Haberl, 2007). They are, thus, expected to have strong magnetic fields of the order of 10^{13}–10^{14} G. The last of the seven XDINS has been found in 2001 and since then no new member could be added to the class.

Central compact objects are generally found near the centres of young SNRs, as can be seen in Figure 4.2, with ages below a few 10^4 years. They are also cooling NSs that show purely thermal X-ray emission but, with an X-ray luminosity of 10^{32}–$10^{34}\,\mathrm{erg\,s^{-1}}$, they are brighter than XDINS. The blackbody temperature of the spectrum has typical values of $\sim$0.5 keV (Pavlov et al., 2004) and so far they have not been detected in any other electromagnetic waveband (Klochkov et al., 2015). Pulsations have only been found in three of the $\sim$10 CCOs, with periods between 0.1 and 0.4 s (Gotthelf et al., 2013; Gotthelf & Halpern, 2018). But they have no features that would indicate any accretion or strong magnetic activity, like PWNe, flares or non-thermal magnetospheric emission. With 10^{10}–10^{11} G they have the weakest magnetic field of all presented types of NSs. They are, thus, also called anti-magnetars and offer the most unbiased view onto the NS itself, which allows an undistorted analysis of the stellar atmosphere. As the surface gravity g correlates with the mass M and the radius R according to

$$g = \frac{GM}{R^2}(1+z)\,, \tag{4.5}$$

where z, the gravitational redshift on the stellar surface, is defined by

$$(1+z) = \left(1 - \frac{2\,GM}{c^2 R}\right)^{-\frac{1}{2}}\,, \tag{4.6}$$

CCOs are very promising objects to constrain the NS mass and radius by modelling the surface gravity and atmosphere (see e.g. Ho & Heinke, 2009; Suleimanov et al., 2014; Klochkov et al., 2015).

The possible presence of isolated NSs in SNRs allows for a systematic search for them by analysing X-ray observations of these extended objects. As described in the following chapter, the Galactic SNR G96.0+2.0 can be considered a promising candidate for this search.

4.3 The Galactic Supernova Remnant G96.0+2.0

The SNR G96.0+2.0 was discovered by Kothes et al. (2005) in the Perseus spiral arm of the Milky Way galaxy analysing data from the *Canadian Galactic Plane Survey* (CGPS; Taylor et al., 2003). It is a shell-type SNR located at a right ascension (J2000) of $21^{\mathrm{h}}\,30^{\mathrm{m}}\,33^{\mathrm{s}}$ and a declination of $+54^\circ\,00'$ (Kothes et al., 2006) in a stellar wind bubble. Due to the tenuous surrounding medium, the SNR lacks material to interact with and, thus, can only lose energy inefficiently, which causes it to be rather faint. Figure 4.3 shows the remnant in the 1420 MHz radio band. As can be seen there, the shell of the remnant is well defined on one side, where Kothes et al. (2005) identified the edge of the stellar wind bubble based on the H I distribution, and fades away towards the interior of the cavity.

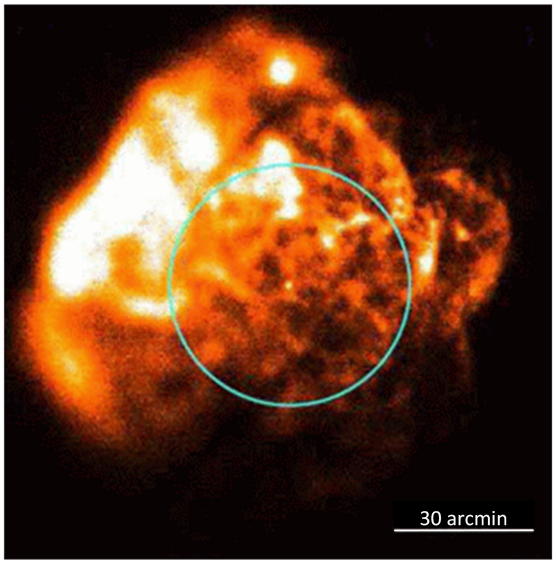

Figure 4.2: The central compact object in the SNR Puppis A. The blue circle marks the 30 arcmin central region within which the neutron star RX J0822-4300 can clearly be seen. The image was taken with ROSAT, operating in the 0.1–2.4 keV band. (Hui & Becker, 2006, modified)

Its appearance suggests that the remnant could expand freely in all directions so far due to a dent that the progenitor star must have produced in the H I distribution with its strong stellar wind. Based on this, Kothes et al. (2005) classified G96.0+2.0 to be the remnant of a type Ib/c supernova explosion. This means an associated compact object can be expected to exist as well. It is not clear whether the SNR is still at its earliest stage (Kothes et al., 2005; Sun et al., 2011) or already at the beginning of the adiabatically expanding phase (Kothes et al., 2006). But in any case its early stage of development makes it plausible to assume that a potentially associated, thermally emitting compact object, if present, will still be hot enough to be detected in X-rays. This makes G96.0+2.0 a suitable object to search for an associated compact object, preferably a CCO, as is the focus of this work.

In addition, the whole SNR fits into XMM-Newton's FOV of $\sim 30'$. Based on the visible arc-like structure of the remnant, Kothes et al. (2005) estimate its diameter to be $26'$, which, at a distance of 4 kpc as determined by them, corresponds to a size of 30 pc. The distance estimate can be useful for the analysis of the point sources in the FOV as it allows to get luminosity values for them from the spectral analysis. Together with the low Galactic photoelectric absorption that can be expected due to the remnant's location far from the Galactic centre, this adds to G96.0+2.0 being an ideal object for the intended study.

4.4 The Available Dataset

The first and, so far, only X-ray observation of G96.0+2.0 was obtained with XMM-Newton (observation ID: 0803450201) on 05 May 2017 during the satellite's revolution 3187. The total duration of the observation was ∼37 ks. Table 4.1 shows specifics for

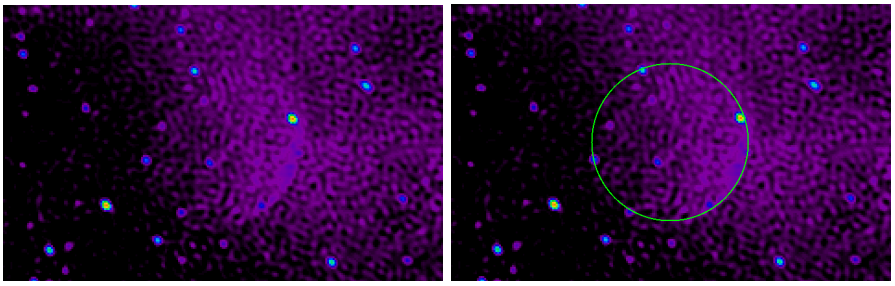

Figure 4.3: Radio image of G96.0+2.0 at 1420 MHz. The image was taken from the CGPS (available at `http://www.cadc-ccda.hia-iha.nrc-cnrc.gc.ca/en/cgps/`) and is shown without any region marker for a clearer illustration of the border of the shell (left) and with the position and the estimated size of 26′ of the SNR indicated in green (right).

Table 4.1: EPIC exposures of the XMM-Newton observation of G96.0+2.0.

Detector	Exposure ID	Mode	Filter	Duration (ks)	Exposure time* (ks)
MOS1	S001	Full Window	Medium	36.6	35.8
MOS2	S002	Full Window	Medium	36.5	36.3
pn	S003	Full Window	Medium	34.9	34.0

* after filtering for good-time intervals

the available EPIC exposures, including the individual effective exposure durations. For each of the three EPIC detectors, MOS1, MOS2 and pn, a single, uninterrupted exposure exists and they were all operated in Full Frame Mode with the medium filters being used. The duration of the pn exposure is slightly shorter mainly due to an offset map being created before starting the pn exposure, which is the standard procedure to correct the energy offsets of all pixels.

As in Full Frame Mode all CCDs are read out[73], the whole EPIC FOV of 30′ is used, allowing to cover the entire supernova remnant with an expected extent of 26′ (see Chapter 4.3). Also, the use of the Full Frame Mode sets the time resolution available for the timing analysis carried out within the scope of this work to 2.6 s for the MOS detectors and to 73.4 ms for the pn detector. Its much higher time resolution makes the pn camera the main instrument amongst the three EPIC detectors to search for pulsations of neutron stars, which, as known so far, can have rotation periods in the range from 1.4 ms (Hessels et al., 2006) up to 6.67 h (De Luca et al., 2006; Braun et al., 2019), though all but a few exceptions of the observed pulsating neutron stars show periods below 12 s.

Besides the EPIC data, a set of exposures in the optical was obtained with the OM. It was operated in Image Mode using its visual (V) filter, which has a passband from 510 nm to 580 nm (Mason et al., 2001). The maximum exposure time for the Image Mode of the OM is generally set to 5 ks to prevent the memory of the camera to be affected by cosmic rays, the minimum exposure time recommended to achieve a high

[73] with the exception of MOS1 CCD3, CCD6 and half of CCD4, which were damaged due to micrometeoroid hits before this observation took place

Table 4.2: OM exposures of the XMM-Newton observation of G96.0+2.0.

Exposure	Mode	Filter	Duration (s)
S006	Image	V	5000
S007	Image	V	1119
S401	Image	V	4999
S402	Image	V	4999
S403	Image	V	5001
S404	Image	V	5000
S405	Image	V	1119
S406	Image	V	1120
S407	Image	V	1119
S408	Image	V	1120

efficiency is 1 ks (*XMM-Newton Users Handbook*, ESA: XMM-Newton SOC, 2018b). Due to these limitations, OM observations are usually split into several exposures. In the present case, ten OM exposures are available for analysis. Their individual durations are given in Table 4.2. With only $17'$, the FOV of the OM is smaller than the EPIC FOV, but the higher number of sources that can be detected in the optical and the better spatial resolution make the OM an ideal supporting instrument for astrometric corrections.

Also, two RGS exposures are available for high spectral resolution spectroscopy. However, the RGSs are intended to be used for the spectral analysis of single, bright point sources located close to the on-axis position and only have a small FOV of $5'$. Therefore, the data of these exposures was not of interest concerning the search for a compact object amongst all sources visible in the vicinity of the SNR and details of the RGS exposures shall not be discussed further at this point.

4.5 EPIC Data Reduction

To ensure that the data reduction was performed with updated public calibration files, the raw ODFs, rather than the already processed PPS files, as well as the newest CCFs available at the time of the analysis were used. All basic data processing was done using SAS version 16.0.0, together with the HEAsoft package, version 6.19. The initial standard steps were performed following the instructions given in *The XMM-Newton ABC Guide* and the *Users Guide to the XMM-Newton Science Analysis System*. First, a Calibration Index File (CIF) was created with the task `cifbuild` to access the correct CCFs for the observation and with the task `odfingest` housekeeping and calibration information relevant for running SAS were extracted. Calibrated EPIC event lists were obtained by running the tasks `emchain`, for the MOS detectors, and `epchain`, for the pn detector.

The EPIC data were then processed in two different ways. For imaging purposes, the XMM Extended Source Analysis Software (ESAS) package, which is implemented in SAS, was used. This package contains tasks that facilitate the analysis of extended sources, like SNRs. Their extent over the satellite's FOV and their often relatively

faint emission make their analysis more susceptible to background issues and, thus, careful consideration of different background components, like the quiescent particle background, soft proton background, cosmic particle background and solar wind charge exchange, is necessary (Snowden et al., 2008), which is what ESAS is optimized for.

Applying the ESAS tasks as suggested in the *ESAS Cookbook* (Snowden & Kuntz, 2014)[74], `mos-filter` and `pn-filter` were run, which automatically filter for soft proton flares, applying the method described in detail in Kuntz & Snowden (2008), and provide diagnostic files which can be examined to detect possible anomalous states of the MOS CCDs. The filtering result, which shows the observation times that were kept for imaging, is shown in Figure 4.4 for the pn detector, the respective results for the MOS detectors are provided in the appendix (Figures B.1 and B.2). The diagnostic files to check for anomalous CCD states of the MOS detectors include images in the 0.2–0.9 keV band, which allow for detecting the higher background below 1 keV that is indicative of an anomalous state. Figure 4.5 shows these images for both MOS detectors. As MOS2 CCD5, which is known to be in a recurrent state of high instrumental noise (Smith et al., 2019), shows an enhanced low energy background, it was excluded from further processing.

Using the tasks `mos-spectra` and `pn-spectra`, separate images were created for each of the individual EPIC detectors for the whole FOV for the 0.4–8.0 keV and 0.4–3.0 keV bands respectively, together with a number of intermediate files necessary for further processing. After creating images of the quiescent particle background with `mos-back` and `pn-back`, a combined, exposure-corrected and particle background-subtracted image was obtained for each of the two energy bands using the `adapt_900` task. These two images are shown in Figure 4.6. In the wider energy range image, increased X-ray radiation can be seen outside the expected SNR boundary in the south-west where Kothes et al. (2005) expect the wall of the H I cavity G96.0+2.0 resides in and where the SNR shell is brighter at their considered radio frequencies of 408 MHz and 1420 MHz. The FOV does not cover the immediate environment to the north-east and, also, there is no bright, extended X-ray emission coming from within the SNR boundary. The 0.4–3.0 keV image covers the lower part of the XMM energy range, at which a potential CCO is expected to be brightest (see e.g. Park et al., 2006; Klochkov et al., 2015, 2016; Gotthelf & Halpern, 2018). It is, thus, used for further illustration purposes regarding the analysis of the visible point sources following in this work.

As mentioned before, besides the data reduction and image creation with ESAS, the data were also processed another way. Figure 4.4 shows that in the present case, the standard filtering algorithm applied in the ESAS routine excludes a large part of the pn data, which has an enhanced count rate in more than half of the observation. However, the light curve does not show the typical strong peaks indicative of soft proton flares and the corresponding increase present in the pn corner light curve rather suggests the cause of the rise being instrumental high-energy particle background (Snowden & Kuntz, 2014) as events resulting from low energy particles focused by the mirrors are not induced in the detector corners, which are unexposed to the sky (De Luca & Molendi, 2004).

As there is no severe contamination with soft proton flaring and because, compared with extended sources, the background is less problematic for the often brighter point sources, for which a suitable, local background region for background subtraction can

[74] available at `https://heasarc.gsfc.nasa.gov/docs/xmm/esas/cookbook/xmm-esas.html`

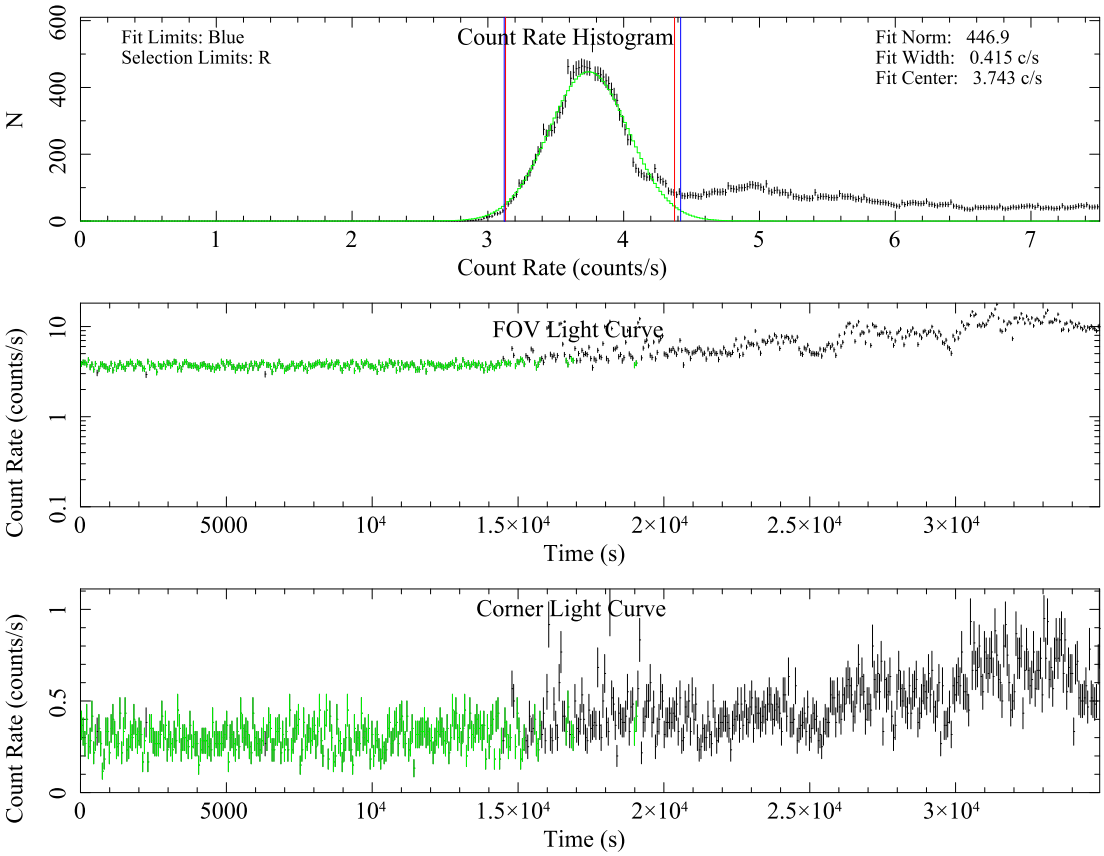

Figure 4.4: ESAS temporal filtering result for the pn data of G96.0+2.0. *Top panel*: histogram for the FOV light curve in the 2.5–8.5 keV energy band, showing the distribution of the count rate with the number N of occurrences; *Middle panel*: FOV light curve in the 2.5–8.5 keV energy band; *Bottom panel*: light curve from the detector corners in the 2.5–8.5 keV energy band. The green data were kept by the filtering algorithm for further analysis, the black data were excluded.

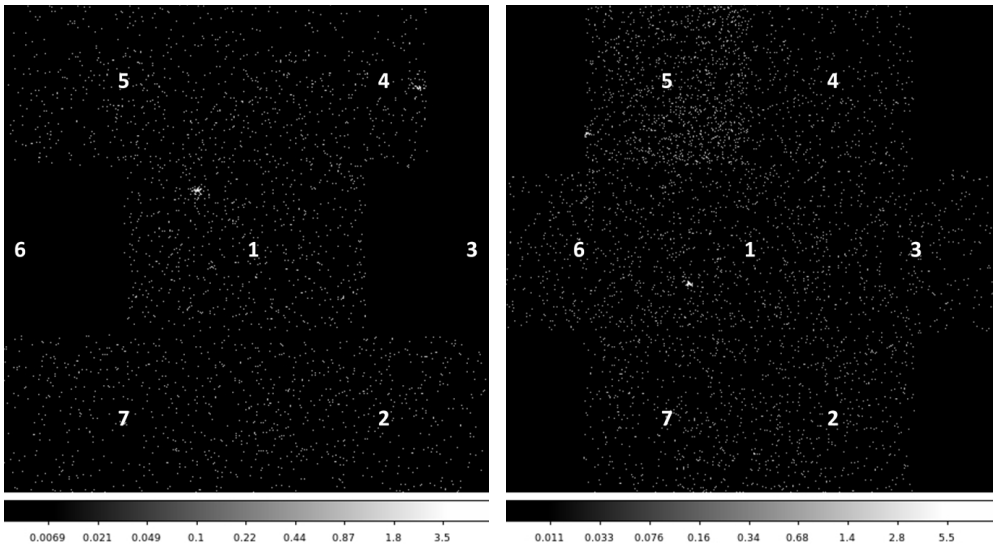

Figure 4.5: MOS soft band event images from the ESAS processing of the G96.0+2.0 observation. The images include the events in the 0.2–0.9 keV band. The numbers give the CCD IDs. On the left side, in the MOS1 image, CCD3 and CCD6 are missing as they were lost due to micrometeorite hits before the observation was performed. Also, half of CCD4 shows an increased background since CCD3 was hit and is, thus, also excluded. The image for MOS2 on the right shows a slightly enhanced low energy background of CCD5, indicating that it is in an anomalous state.

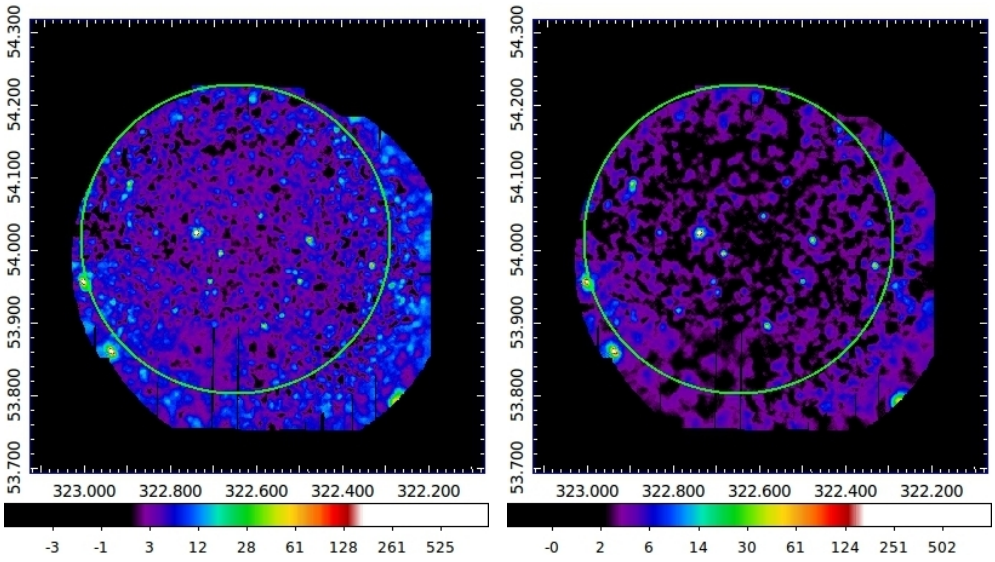

Figure 4.6: X-ray images of G96.0+2.0 in the 0.4–8.0 keV (left) and 0.4–3.0 keV (right) bands. Both images were adaptively smoothed with a factor of 50 counts and a threshold of 0.02 being set to exclude regions with low exposures. The right ascension (horizontal axis) and declination (vertical axis) are given in degrees, the colour index shows the counts per second and square degree in logarithmic scale. Just as for the radio image in Figure 4.3, the green circle marks the assumed outer boundary of the SNR.

usually be found within the FOV, the data were only processed with ESAS tasks for imaging purposes and an independent way of reducing the data was chosen for the analysis of the point sources. Again, the general SAS guidelines described in the standard SAS manuals mentioned at the beginning of this chapter were followed. All event selection as well as the creation of spectra and light curves was done with the SAS task `evselect`.

Based on the calibrated event lists already obtained with `emchain` and `epchain`, light curves were created considering only events matching the selection criteria suggested for the GTI filtering: using only valid single events (‘`PATTERN==0`’) that comply with the standard FLAG filters (‘`#XMMEA_EM`’ for MOS, ‘`#XMMEA_EP`’ for pn) and setting a lower energy limit of 10 keV (‘`PI > 10000`’), with an additional upper limit of 12 keV in the case of pn (‘`PI in [10000:12000]`’). To define the GTIs, the same procedure which was already described in Chapter 3.5.1 was applied. Figures 4.7, B.3 and B.4 show that this method, unlike the ESAS routine, did not lead to an extreme exclusion of pn time frames actually free of soft proton flares, thus leaving higher statistics for the analysis of the point sources. With the determined GTI count limits of 17.0 cts, 26.6 cts and 58.6 cts for MOS1, MOS2 and pn, respectively, a GTI-file was created for each of the detectors using the task `tabgtigen`. The resulting GTI filtered exposure times are given in Table 4.1.

Clean event files were then obtained by using the GTI count thresholds for temporal filtering, including all valid events in the case of MOS (‘`PATTERN <= 12`’) and all single and double events in the case of pn (‘`PATTERN <= 4`’). Furthermore, the energy was limited to the recommended ranges (‘`PI in [300:12000]`’ for MOS, ‘`PI in [300:15000]`’ for pn) and, again, the standard FLAG filters (‘`#XMMEA_EM`’/‘`#XMMEA_EP`’) were set. In addition, MOS2 CCD5 was excluded as it had already been revealed by the ESAS routines that the CCD was in an anomalous state of enhanced low-energy background during the observation. For the spectral analysis, the pn FLAGs were further reduced to the more restrictive ‘`FLAG==0`’ selection as suggested by the guidelines. Before performing any timing analysis, a barycentric correction was applied to the data with the SAS task `barycen` to compensate for the effects the satellite’s movement has on the arrival times of the photons.

4.6 Source Detection

After the initial data reduction, the XMM SAS task `edetect_chain` was used to search for X-ray point sources within the FOV of each EPIC detector. The search was carried out in the 0.4–3.0 keV band as a potential CCO would have a rather soft spectrum with the bulk of the flux being detected within this energy range. The `edetect_chain` task was run for each EPIC detector individually as different binning values are recommended in the user guides for creating MOS and pn images due to the detectors’ different pixel sizes. Following these recommendations, a bin size of 22 was used for MOS and a bin size of 82 was used for pn. In order to be able to run `edetect_chain`, attitude files had to be created with the `atthkgen` task first and images in the 0.4–3.0 keV energy band and with the above mentioned recommended binning were obtained with `evselect`.

The `edetect_chain` task itself allows for running a chain of several subtasks necessary for source detection with one single command. These subtasks are described in more detail in the *Users Guide to the XMM-Newton Science Analysis System* and

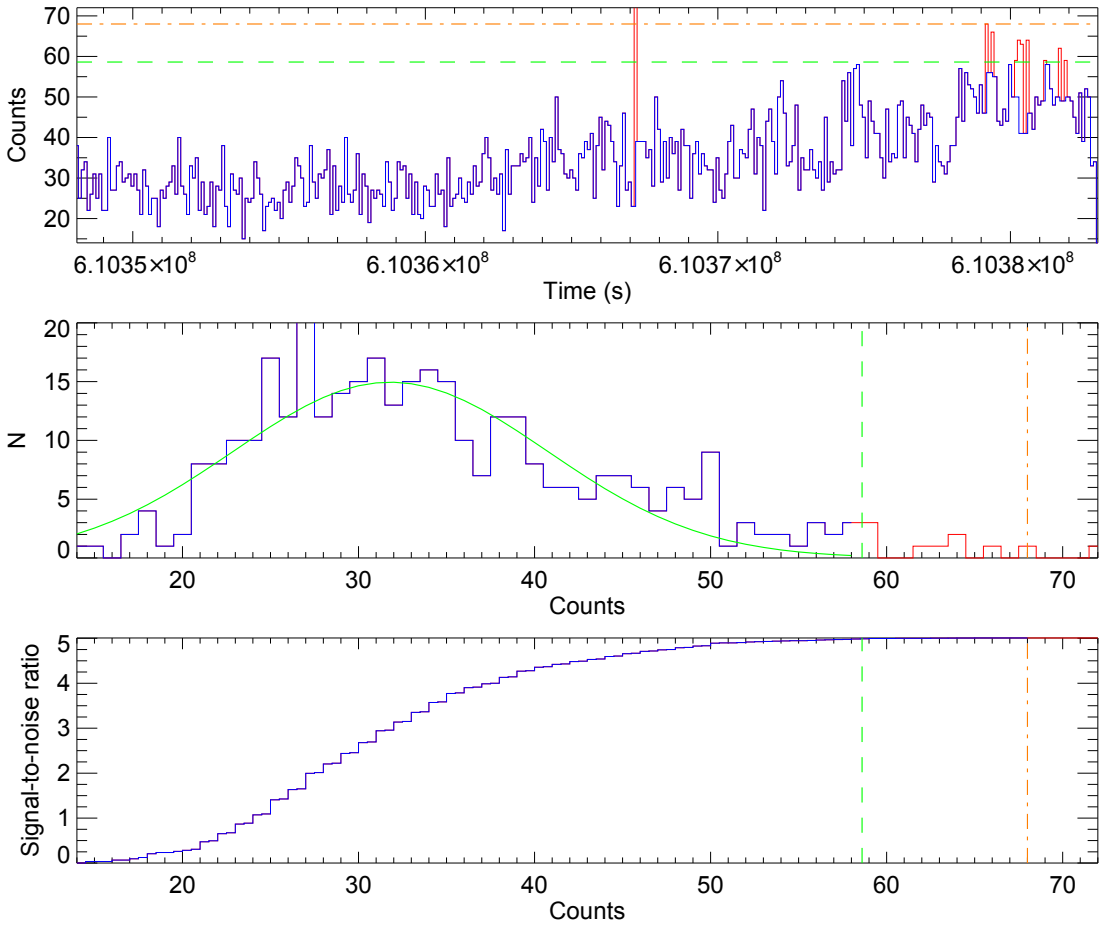

Figure 4.7: Screening for soft proton flares in the pn data of G96.0+2.0. *Top panel*: light curve in the 10.0–12.0 keV energy band with a binning of 100 s; *Middle panel*: histogram for the light curve in the 10.0–12.0 keV energy band, showing the distribution of counts with the number N of occurrences; *Bottom panel*: S/N for the 10.0–12.0 keV energy band. The green, dashed line shows the Gaussian threshold at three times sigma above the mean value. The orange, dash-dotted line indicates the threshold set by the maximum S/N. The more conservative of the thresholds, in this case the Gaussian threshold, is selected to decide which data to keep (blue) and which data to reject (red) for further analysis.

shall, thus, only be summarised here. At the beginning of this chain, `eexpmap` is run to generate an exposure map to compensate for spatial differences in the detector efficiency and a detection mask, which defines the FOV areas that are screened for sources, is created with the `emask` task. After that, the source detection is performed with `eboxdetect` in its local detection mode to provide a first source list as input for the next task, `esplinemap`, which creates a background map from the source free regions. For the detection likelihood $\mathcal{L}$, a value of 8 was chosen as recommended to not miss any sources. This likelihood is defined as

$$\mathcal{L} = -\ln p \tag{4.7}$$

with the probability p of a Poissonian random fluctuation of the background counts in a source's detection box (by default a 5×5 pixel window) that leads to them being at least as high as the number of source counts detected, which would result in the assumed source counts actually being caused by the background. After the background maps are obtained, they are used in a second run of `eboxdetect`, this time in its map detection mode, to reach a higher sensitivity for the source detection. Once this is done, the final source list is obtained with `emldetect` by doing a maximum likelihood fit of the PSF, which is contained in the CCFs, to the distribution of the source counts to derive, among others, the source location and count rate fit parameters. The minimum detection likelihood for a source to be included in the source list was set to 10 as it is recommended to set it slightly higher than the likelihood used for the `eboxdetect` run.[75] The chain in addition runs `esensmap` as a last step to generate a sensitivity map that takes vignetting into account to show the detection limit for each detector pixel, which can be useful should a source not have been detected in the detection process.

To combine the individual source lists obtained for the three EPIC cameras, the SAS task `srcmatch` was used with the parameter '`maxerr`' being set to 3 so sources from different lists were correlated with each other only if their positions matched within a confidence level of three times the standard deviation σ. A value of $1.5''$ was used for the systematic position error according to Pietsch et al. (2004), Watson et al. (2009) and the maximum 1σ astrometric error given in the current technical note on the *EPIC Status of Calibration and Data Analysis* (Smith et al., 2019).

Eventually, 22 sources were detected in total and region files for the data extraction were created for all of them using the SAS task `srcdisplay`. In Figure 4.8 the sources are tagged with the source ID taken from the final, combined source list obtained with `srcmatch`. The three sources #1, #3 and #8 are closest to the assumed centre of the SNR where a potential CCO would be expected. The circles marking the sources show the source extraction regions used and, following Klochkov et al. (2015, 2016), their size corresponds to a radius r_{extr} that encompasses at least 90% of the source photon energy under the PSF in the 0.4–3.0 keV band. This radius was determined with the SAS task `region` with its '`radiusstyle`' parameter being set to '`enfrac`'. As `region` requires an eventlist as input, it was run for each EPIC detector individually and in the end for each source the largest of the three radii was selected and rounded to the nearest integer. In Table 4.3, the extraction radius r_{extr} is listed for each source, together with the coordinates in right ascension (RA) and declination (Dec). The total 1σ confidence level position error σ_{tot} includes the circular statistical error σ_{stat} given by the source

[75] `http://xmm-tools.cosmos.esa.int/external/sas/current/doc/eboxdetect/node3.html`

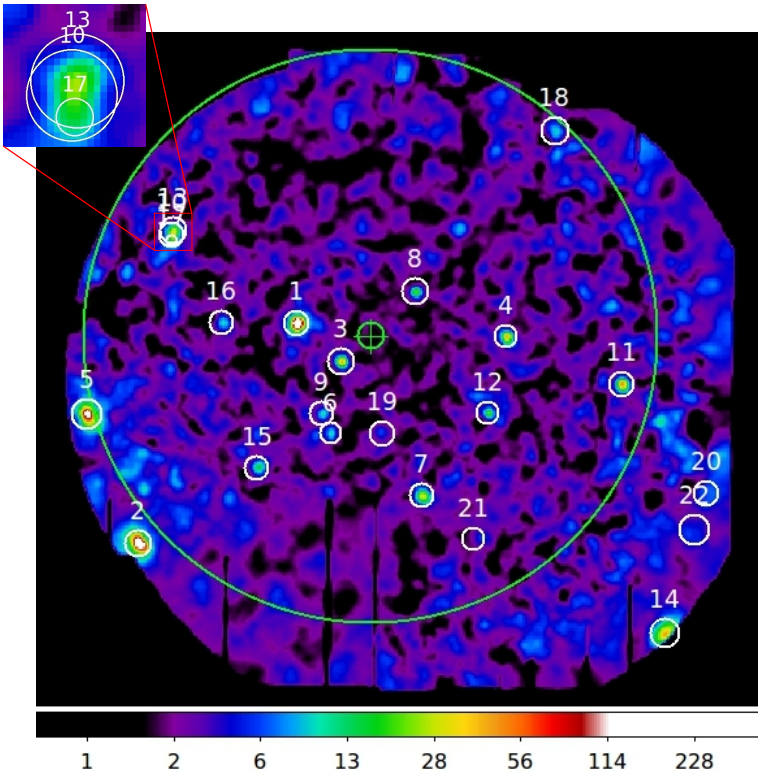

Figure 4.8: Point sources detected in the 0.4–3.0 keV band XMM data of G96.0+2.0. The white circles mark the source extraction regions, which encompass ∼90% of the source energy. The numeric tags correspond to the source IDs in the final source list. For the illustration of the source positions, the same image of the observation was used as shown in Figure 4.6, right-hand side, with an additional Gaussian smoothing with a kernel radius of 2 pixels for a clearer presentation of the point sources. The colour index shows the counts per second and square degree in logarithmic scale. The green circle marks the assumed outer boundary of the SNR with the centre being located at the position of the green cross hairs pointer.

detection process routines as well as the 1.5″ systematic error σ_{sys} which, conforming to error propagation, sum up quadratically (Watson et al., 2009; Pineau et al., 2011):

$$\sigma_{\mathrm{tot}} = \sqrt{{\sigma_{\mathrm{stat}}}^2 + {\sigma_{\mathrm{sys}}}^2}\,. \tag{4.8}$$

Table 4.3 also shows in which EPIC detector's data the individual sources were detected and gives the total EPIC source counts registered by the source detection chain as an indication of the statistics available for the source analysis. Reasons for sources not being detected with all three detectors are: the sources were not within a camera's FOV, source positions were overlapping with CCD gaps or the respective detection likelihood was too low for a detection to be included in a camera's source list.

The background regions were defined for each source individually considering the recommendations of the *XMM Science Operations Centre* (Smith et al., 2019). In the

Table 4.3: Source list for the point source detections in the 0.4–3.0 keV band XMM data of G96.0+2.0. The source position is given in right ascension (RA) and declination (Dec) with the position error σ_{tot} being the quadratic sum of the statistical and systematic errors. The extraction radius r_{extr} encompasses at least 90% of the source energy. In the detection columns, a cross marks the detection of a source with the MOS1 (m1), MOS2 (m2) or pn detector, respectively, a dash indicates a non-detection. For the total EPIC counts, the counts determined for each of the three cameras in the source detection process were summed up.

Source	RA*	Dec*	σ_{tot}	r_{extr}	Detection			EPIC
ID	h m s	° ′ ″	″	″	m1	m2	pn	counts
1	21 30 57.81	+54 01 30.31	1.52	34	x	x	x	1312 ± 54
2	21 31 45.45	+53 51 41.33	1.54	36	x	–	x	978 ± 36
3	21 30 44.36	+53 59 48.78	1.60	35	x	x	x	306 ± 23
4	21 29 54.42	+54 00 55.98	1.66	31	x	x	x	203 ± 19
5	21 32 01.17	+53 57 25.55	1.62	40	x	x	–	186 ± 17
6	21 30 47.51	+53 56 36.34	1.93	29	x	–	–	25 ± 7
7	21 30 19.98	+53 53 51.50	1.79	32	x	–	x	90 ± 13
8	21 30 21.94	+54 02 54.67	1.80	35	x	x	–	60 ± 10
9	21 30 50.17	+53 57 28.88	1.92	32	x	–	x	67 ± 13
10	21 31 35.81	+54 05 26.57	2.34	34	x	–	–	31 ± 9
11	21 29 19.49	+53 58 45.89	1.76	34	x	–	x	142 ± 17
12	21 29 59.85	+53 57 30.97	2.00	31	–	x	x	76 ± 13
13	21 31 35.36	+54 05 37.29	1.98	35	–	x	x	103 ± 15
14	21 29 06.74	+53 47 39.75	2.15	39	–	–	x	106 ± 15
15	21 31 09.63	+53 55 03.70	2.09	32	–	–	x	75 ± 13
16	21 31 20.70	+54 01 30.75	2.52	32	–	–	x	45 ± 11
17	21 31 35.57	+54 05 10.07	2.59	14	–	–	x	39 ± 10
18	21 29 39.55	+54 10 02.65	2.58	37	–	–	x	48 ± 12
19	21 30 31.82	+53 56 34.82	3.23	34	–	–	x	43 ± 12
20	21 28 54.12	+53 53 54.17	2.93	34	–	–	x	59 ± 13
21	21 30 04.18	+53 51 55.00	2.60	31	–	–	x	41 ± 11
22	21 28 57.70	+53 52 16.92	3.06	40	–	–	x	46 ± 12

* J2000

case of MOS, the first priority choice for the background was an annulus around the source region with an inner radius of two times the source extraction radius and an outer radius of three times the source extraction radius. In cases where this was not possible, either due to other point sources within this area or due to the annulus covering in part other CCDs than the source region, a circular region encompassing an area of similar size was positioned in the source's vicinity instead, also keeping a distance of about two times the source extraction radius. For pn, an annulus around the source is not recommended as this would include out-of-time events from the source that are gathered in the readout direction during the readout of the CCD. Thus, an elliptical background region was defined on the source CCD, positioned at approximately the same `RAWY` coordinate value as the source region to limit differences in the CTIs.

4.7 Optical Counterparts

4.7.1 Astrometric Correction

In the course of searching for a possible CCO related with G96.0+2.0, a central NS without an optical counterpart would already be a good indication of a potential candidate (see Section 4.2.2). A cross-match of the source positions with data listed in optical source catalogues can be performed to search for such a counterpart. But before conducting the search, the positions obtained from the source detection process require an astrometric correction to compensate for the systematic offset of the XMM pointing.

As, for example, in Ducci et al. (2014) and Saeedi et al. (2016), one possibility to correct for these position offsets is the use of bright point sources in the FOV of the X-ray instruments that can be associated with optical or infrared counterparts which are already known to be foreground stars or point-like background objects, like AGNs, and take their position entries in catalogues as a reference. In the present case, this method was not considered suitable as G96.0+2.0 is a Galactic object and, thus, the view is more limited by Galactic absorption. Only 22 point sources were detected, with which a statistically sufficient precision could not be achieved.

Instead, the optical data of the OM telescope on board XMM-Newton was used to determine the offset of the spacecraft pointing. With only $17'$, the FOV of the OM is smaller than the $\sim 30'$ FOV of the EPIC detectors, but, as can be seen in Figure 4.9 when comparing the OM image with the image taken from the *Digital Sky Survey System* (DSS) of the *Canadian Astronomy Data Centre* (CADC)[76], the number of optical sources that can be correlated with optical catalogues is still much higher than the point-sources available in the X-ray observation. The risk of false matches is minimized as the existence of a significant number of counterparts in the optical catalogue can be expected, which is not necessarily the case for sources detected in X-ray data. Also, a better spatial resolution can be achieved in the optical[77] and the higher count rates generally observed in the optical allow for a statistically more precise positioning.

The OM data were processed with the OM Image Mode specific `omichain` processing chain included in SAS, which automatically generates output files for analysis from the raw OM input, including the necessary corrections, source detection and astrometry. For the astrometric correction, the option for a direct cross-correlation of the source positions

[76] `http://www.cadc-ccda.hia-iha.nrc-cnrc.gc.ca/en/dss/`
[77] see Chapter 3.2 for details on the angular resolution of the XMM instruments

Figure 4.9: Comparison of the OM image (left) with CADC DSS data (right) of the same FOV. The large, diffuse structures in the OM image are artefacts, caused, for example, by stray light or by photons of bright sources that are reflected from the detector structure. In both images, the central, coloured cross marks the XMM pointing position.

with the *United States Naval Observatory* (USNO)-B1.0 catalogue (Monet et al., 2003) was used. In the end, a weighted mean $\Delta\alpha = -0.156'' \, (\pm 0.008'')$ was determined for the offset of the right ascension and $\Delta\delta = 0.303'' \, (\pm 0.008'')$ for the offset of the declination. The positions of the X-ray sources were corrected with these systematic offsets before cross-matching them with catalogues to search for counterparts potentially associated with them.

4.7.2 Cross-Match of the Source Positions with Optical Catalogues

To search for potential optical counterparts that would support a NS's classification as a CCO, the X-Match service of the *Strasbourg Astronomical Data Center* (CDS, French: *Centre de Données Astronomiques de Strasbourg*) was used, which provides an easy cross-match of input source lists with a wide variety of source catalogues available for different wavelength ranges. The position errors of the corrected positions as well as the position errors of the online catalogues were considered. A 3σ confidence level with a probability of 99.7% was chosen to conduct the search. To do so, X-Match applies the method developed by Pineau et al. (2011), as the deviations between the measured X-ray source positions and the coordinates of the catalogue counterparts constitute a two-dimensional problem where the probability density of the position errors follows a Rayleigh distribution (Watson et al., 2009). In this case, the 99.7% selection criterion conforms to

$$d \leq 3.43935 \sqrt{{\sigma_{\mathrm{list}}}^2 + {\sigma_{\mathrm{cat}}}^2} \tag{4.9}$$

with the distance d between the X-ray and optical source positions and the position errors from the X-ray source list (σ_{list}) and from the selected catalogue (σ_{cat}). As a maximum distance, the default value of $5''$ was set to prevent the matching of sources with a distance too large to make an actual correlation seem likely.

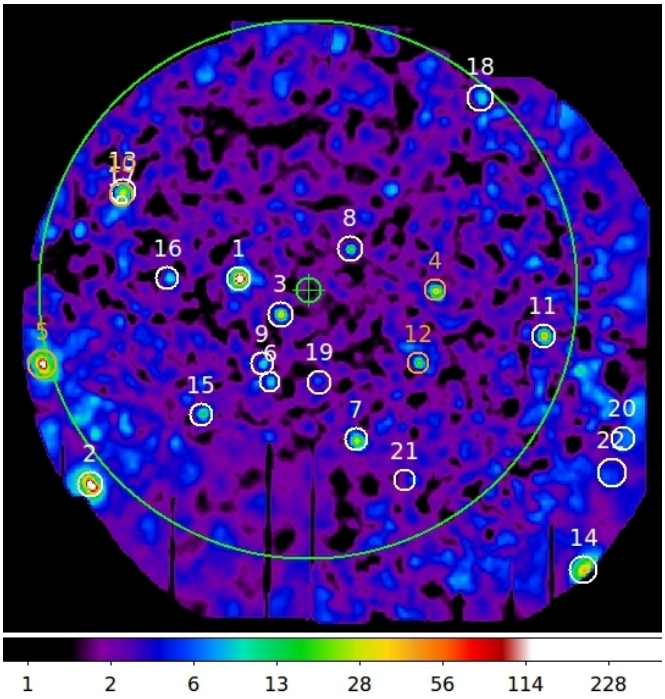

Figure 4.10: Result of the search for optical counterparts to the X-ray sources in the G96.0+2.0 FOV. Sources for which potential optical counterparts were found in the optical catalogues available online are marked in white, sources #4, #5, #10 and #12 are marked in orange as no such counterparts exist in the catalogues considered. The X-ray image is conform with the one shown and annotated in more detail in Figure 4.8.

Large area astronomical catalogues with a depth sufficient to expect potential counterparts for the detected X-ray sources to be included were chosen for the cross-match. With the optical catalogues USNO-B.1.0 (see previous chapter), GSC 2.3 (*Guide Star Catalog*; Lasker et al., 2008) and Gaia Data Release 1 (DR1; Gaia Collaboration et al., 2016), potential counterparts were found for all sources except #4, #5, #10 and #12, which are highlighted in Figure 4.10. As can be seen there, none of them is located at immediate proximity to the SNR centre, which would have been a first indication of a CCO. A cross-match with the *Sloan Digital Sky Survey* (SDSS) DR12 (Alam et al., 2015) was also attempted but the catalogue did not cover the FOV observed with XMM. Another cross-match with Gaia Data was performed after the second data release (Gaia Collaboration et al., 2018) got available, but again no optical counterparts were found for the four sources mentioned above.

To slightly enlarge the number of consulted catalogues for an increased reliability of the cross-match results, near-infrared (IR) data was included in the search for counterparts as well. The *Two Micron All Sky Survey* (2MASS; Cutri et al., 2003) and the extended catalogue of the *Wide-field Infrared Survey Explorer* (AllWISE; Wright et al., 2010; Cutri et al., 2014) both confirmed the absence of any counterparts for sources #4, #5, #10 and #12 in the considered energy range.

4.8 Spectral and Timing Analysis

4.8.1 Methods

In order to categorize the X-ray point sources detected, a spectral and timing analysis was performed using the methods described in this section. Finding pulsations with frequencies below a few seconds would unambiguously prove the NS nature of a source (Lyne & Graham-Smith, 2012). The maximum frequency which can be detected is limited as derived from the Nyquist-Shannon sampling theorem[78], which describes a common problem in signal processing and states that a continuous signal can only be properly reconstructed if the sampling, meaning its conversion into discrete values, is done with a sampling rate ν_{sampling} more than twice as high as the maximum frequency ν_{max} in the original signal (e.g. Nyquist, 1928; Shannon, 1949):

$$\nu_{\mathrm{sampling}} > 2\,\nu_{\mathrm{max}}\,. \tag{4.10}$$

That implies that the maximum frequency which can be reconstructed from the discrete values in a sample, generally known as the Nyquist frequency ν_{Nyquist}, is half the sampling rate:

$$\nu_{\mathrm{Nyquist}} = \frac{1}{2}\,\nu_{\mathrm{sampling}}\,. \tag{4.11}$$

If this condition is not met, aliasing will occur, which means frequencies that are higher than the Nyquist frequency are recognized as lower frequencies, leading to a distortion of the reconstruction result.

In the present case, the Nyquist frequency is determined by the time resolution of the detector and is equivalent to twice its value. While the MOS cameras, with their time resolution of 2.6 s in Full Frame Mode (see Chapter 3.2.3), sets a limit of 5.2 s to detectable pulsation periods, the pn detector's corresponding time resolution of 73.4 ms enables the user to search for periods down to 146.8 ms. Thus, pn is the instrument to be used in this case to search for pulsations as periods relevant in the classification of an object as a NS can be detected.

A commonly used method to search for pulsations is the Z^2_m test, which was introduced by Buccheri et al. (1983) and Buccheri (1988) to search for pulses in the gamma-ray emission of radio pulsars where the problem of weak signals with only sparse photon detections had to be faced. Thus, this method is a particularly useful tool to analyse the temporal features of the point sources in the observation at hand as the statistics of the individual sources are rather poor (see Table 4.3), especially when considering that only the pn counts are useful here to search for pulses coming from NSs.

To apply the test, a phase value ϕ_i in the interval between 0 and 1 is ascribed to the barycentrically corrected arrival times t_i of each photon i:

$$\phi_i = \text{fractional part of} \left(\nu \Delta t_i + \frac{\dot{\nu} \Delta t_i^2}{2} + \frac{\ddot{\nu} \Delta t_i^3}{6} \right) ; \quad i = 1, ..., n \tag{4.12}$$

[78] sometimes also referred to as e.g. Whittaker–Kotelnikov–Shannon theorem, Nyquist theorem, Nyquist-Shannon theorem or sampling theorem

with the total number of photons n, the pulse frequency ν and $\Delta t_i = t_i - t_0$ being the difference between t_i and the barycentrically corrected arrival time t_0 of the first photon. As finding any pulsation would already help with the source characterization in this case, only the frequency itself, not its temporal variation, is of interest here and, thus, it is sufficient to just consider the first term in equation 4.12.

Next, the phase values obtained are Fourier-analysed. The Z^2_m test is based on the Rayleigh test, where the Rayleigh power nR^2 describes the probability of a pulse being present at a particular frequency:

$$nR^2 = \frac{1}{n}\left(\left(\sum_{i=1}^{n}\cos\phi_i\right)^2 + \left(\sum_{i=1}^{n}\sin\phi_i\right)^2\right) . \tag{4.13}$$

The Rayleigh test assumes a purely sinusoidal signal whereas the further developed Z^2_m test is also sensitive to more complex phase structures by summing the power over multiple harmonics m,

$$Z^2_m = \frac{2}{n}\sum_{k=1}^{m}\left(\left(\sum_{i=1}^{n}\cos k\phi_i\right) + \left(\sum_{i=1}^{n}\sin k\phi_i\right)\right) , \tag{4.14}$$

with commonly two harmonics used so it is possible to not only detect single-peaks in the signal but also double-peak structures (Brazier, 1994). To evaluate the significance of a detection, the probability density function (pdf), which in the case of $m = 2$ is

$$pdf(Z^2_2) = \frac{1}{2}\exp\left(-\frac{Z^2_2}{2}\right) \tag{4.15}$$

with $2m = 4$ degrees of freedom (dof), can be used (Bendat & Piersol, 2010). Detections of pulsations would support the characterization of the X-ray sources in question. If no pulsations are found, though, it might be a hint at a homogeneous surface emission of a possible CCO (Ho & Heinke, 2009; Klochkov et al., 2013, 2015, 2016; Doroshenko et al., 2018) but further techniques need to be applied then to find out about a potential NS nature of a source.

Light curves of the sources were not considered to be the right basis with which to conduct the search for pulsations as the usual epoch folding technique, which involves a reallocation of the time bins to phase bins, does not work satisfactorily for low photon numbers (Buccheri et al., 1983). A look at the light curves is still worthwhile, though, as also variations on longer time scales can provide insight into a source's properties. For example, irregular flaring could indicate the presence of magnetic activity, as in the case of SGRs and AXPs, and/or of accretion (Kaspi & Beloborodov, 2017; Walter & Ferrigno, 2017). Thus, also light curves, created from the barycentrically and background corrected data, were used within the scope of this work to analyse the detected X-ray point sources.

Besides the temporal investigation of the sources, an analysis of their spectra is absolutely essential for looking into the nature and different properties of astronomical sources. In the following, suitable models to search for NSs, particularly CCOs, that could be associated with the SNR, are introduced. The terms in parentheses behind the model name give the corresponding command to call the model component in the

HEAsoft subprogramme Xspec, which was used for the spectral fitting. Details on the models are given in the *Xspec Users' Guide* (Arnaud et al., 2018):

- Blackbody model (`bbody`): This model describes blackbody radiation, which is thermally emitted by different types of astronomical objects. It is defined with the function $\mathcal{F}_{\texttt{bb}}(E)$ as

$$\mathcal{F}_{\texttt{bb}}(E) = K_{\texttt{bb}} \times \frac{8.0525 E^2 \mathrm{d}E}{(k_\mathrm{B}T)^4 \left(\exp\left(\frac{E}{k_\mathrm{B}T}\right) - 1\right)} \tag{4.16}$$

  where E denotes the energy, T the temperature in Kelvin, k_B the Boltzmann constant[79] and $K_{\texttt{bb}}$ the normalisation parameter which derives from the source's luminosity L_{39} in units of $10^{39}\,\mathrm{erg\,s^{-1}}$ and its distance d_{10} in units of 10 kpc:

$$K_{\texttt{bb}} = \frac{L_{39}}{d_{10}}\,. \tag{4.17}$$

  Blackbody spectra with temperatures $k_\mathrm{B}T$ of circa 0.2–0.5 keV are typical for CCOs (Pavlov et al., 2004; Mereghetti, 2011; De Luca, 2017) and would, thus, support the characterization of a source as such.

- Power-law model (`pow`): With the power-law component, on the other hand, non-thermal emission, e.g. in the form of synchrotron radiation, can be modelled. The model itself has already been introduced in Chapter 3.3.2. A power law with a photon index Γ of about 1–2 could indicate that the X-ray emission originates from a young radio pulsar (Pavlov et al., 2009) or, with Γ having a value between $\sim$1.4 and $\sim$2.5, from a background AGN (Ishibashi & Courvoisier, 2010; Ananna et al., 2020).

- Hydrogen atmosphere NS model (`hatm`): Introduced by Klochkov et al. (2015) and Suleimanov et al. (2017), this model is intended to be used for the spectra of hydrogen NS atmospheres, assuming a weak magnetic field with a neglectable influence. The general principle of the model is a linear interpolation between computed model spectra provided for a grid of the effective temperature T between 1×10^6 K and 4×10^6 K, with steps of 0.05×10^6 K, and the logarithmic surface gravity acceleration, $\log(g)$, between 13.7 and 14.9, with steps of 0.15. For the fit, the free parameters are the effective temperature T, the mass M and radius R of the NS and the normalization $K_{\texttt{atm}}$,

$$K_{\texttt{atm}} = \frac{A}{d_{10}^2}\,, \tag{4.18}$$

  where d_{10} is, again, the distance in units of 10 kpc and A is the emitting area as a fraction of the total NS surface and takes a value between 0 and 1. Being intended to be used for weakly magnetized NSs, the model is particularly suitable for the study of CCOs and its applicability in this respect has already been successfully tested (e.g. Klochkov et al., 2015, 2016; Doroshenko et al., 2018).

[79] $k_\mathrm{B} \approx 8.617 \times 10^{-5}\,\mathrm{eV\,K^{-1}}$ (Mohr et al., 2016)

Table 4.4: Energy ranges used to search for pulsations with the Z_m^2 test. Ranges were selected within which the background was not highly dominating to increase the S/N.

Source ID	Energy range (keV)
1	0.5–2.0
2	0.4–1.5
3	0.8–1.5
4	0.9–5.0
5	1.0–5.0
7	0.6–1.2
11	0.9–1.5
13	0.6–1.1
14	0.4–1.1

- Carbon atmosphere NS model (`carbatm`): Based on Suleimanov et al. (2014, 2017), the carbon atmosphere model works similarly to the hydrogen atmosphere model mentioned before, following the same principle of computed models being provided for a T-log (g)-grid. The temperature values run from 0.5×10^6 K to 10×10^6 K, with steps of 0.05×10^6 K, the log (g) values and the free parameters are the same as in the previous case. Again, a non-magnetic atmosphere is assumed, which makes this model just as well useful for analysing CCOs.

When fitting the models for astronomical objects to the spectra, also the Galactic photoelectric absorption due to gas and dust in the Milky Way needs to be taken into account. To do so, the photoelectric absorption model `phabs`, defined as

$$\mathcal{F}_{\texttt{phabs}} = \exp\left(-N_{\mathrm{H}}\sigma_{\mathrm{x}}(E)\right) \tag{4.19}$$

with the hydrogen column N_{H} in units of $10^{22}\,\mathrm{atoms\,cm^{-2}}$ and the energy-dependent cross-section σ_{x} (Balucinska-Church & McCammon, 1992), which does not include Thomson scattering, was used as a multiplicative component in all spectral fits. According to the task `nh`, part of the FTOOLS (Blackburn, 1995) subpackage included in HEASOFT, the Galactic hydrogen column N_{H} in the direction of G96.0+2.0 is about $1.0{\times}10^{22}\,\mathrm{atoms\,cm^{-2}}$.

For a detailed spectral and timing analysis, the statistics need to be sufficient so that only the point sources with the highest X-ray count detections were considered at this stage of the analysis, with a minimum of 90 total EPIC source counts being set as a limit. As Table 4.3 shows, only nine of the 22 detected sources, namely sources #1, #2, #3, #4, #5, #7, #11, #13 and #14, which are highlighted in Figure 4.11, meet this requirement. At a first glance at the spectra (see Figure 4.12), for each of these sources an energy range (see Table 4.4) was defined within which the background was not highly dominating. To search for pulsations in the pn data with the Z_m^2 test, the data were limited to these energies to increase the S/N.

At first, source #1 was of special interest as, with the highest number of EPIC counts, it has the best statistics and is at the same time located close to the centre of the

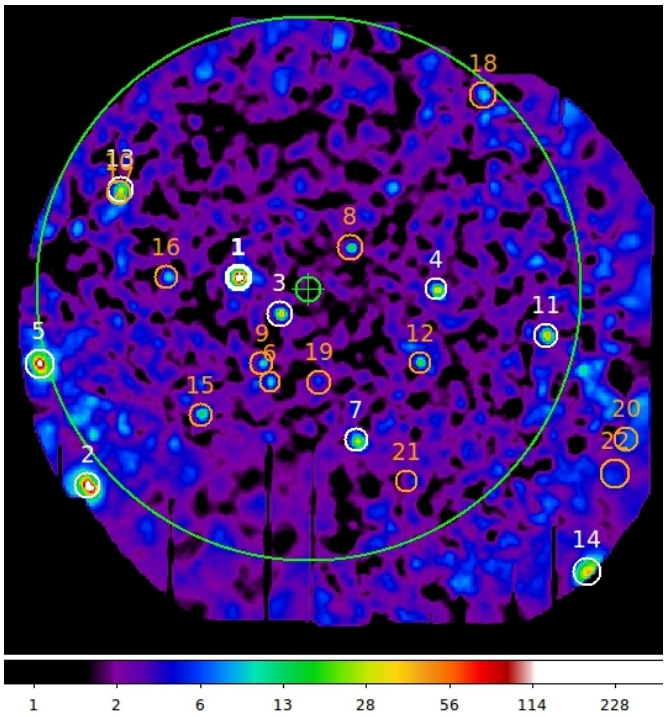

Figure 4.11: Point sources in the G96.0+2.0 FOV suitable for the spectral and timing analysis. Sources highlighted in white have more than 90 total EPIC counts and were, thus, considered at this stage of the analysis. The data of the sources marked in orange were considered insufficient for a detailed spectral and timing analysis. Source #1 is marked in bold as the focus was first set on it. The X-ray image is conform with the one shown and annotated in more detail in Figure 4.8.

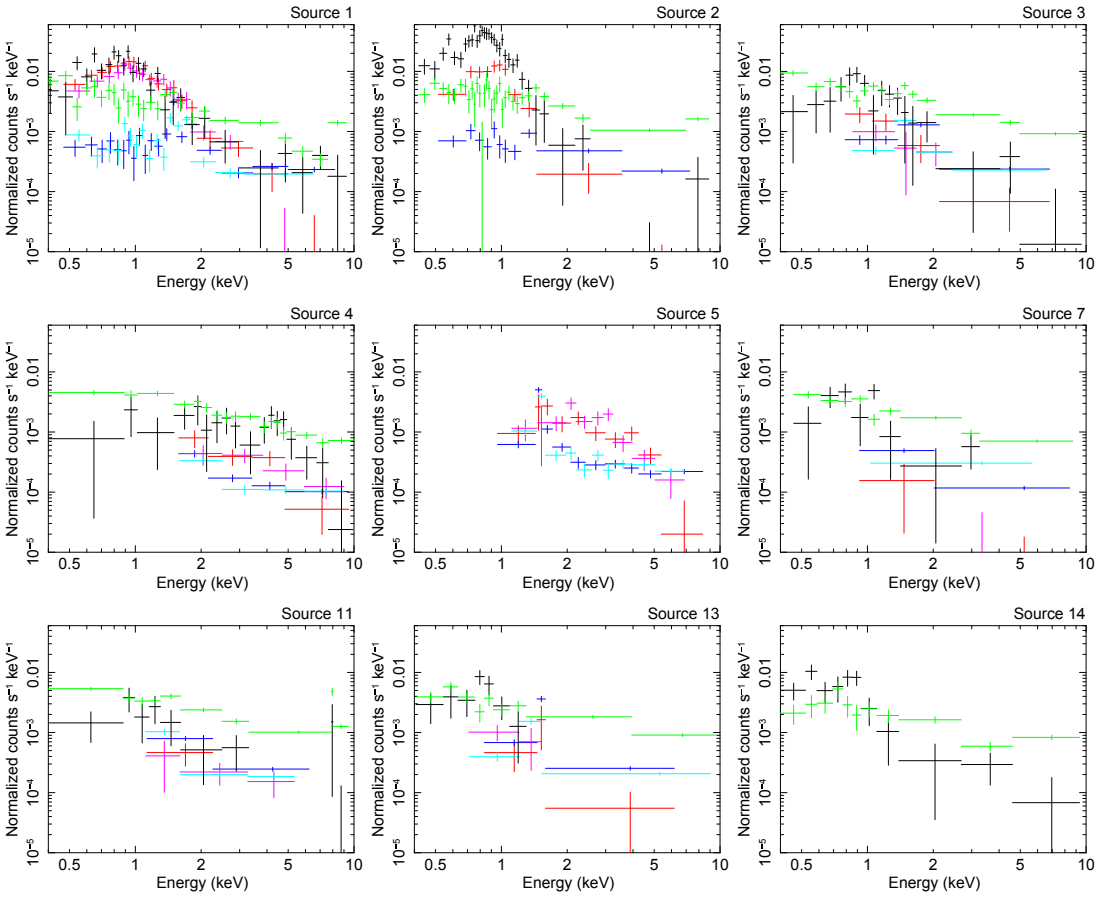

Figure 4.12: Spectra for the point sources with the highest number of counts in the G96.0+2.0 FOV. Source spectra are red (MOS1), magenta (MOS2) and black (pn), background spectra are blue (MOS1), cyan (MOS2) and green (pn). The data were grouped with a minimum of 25 counts per bin and rebinned to get a minimum significance of 1σ per bin with an upper limit of 5 bins being combined. Source #2 was only covered by MOS1 and pn, source #5 was only covered by the MOS cameras and source #14 only by the pn detector.

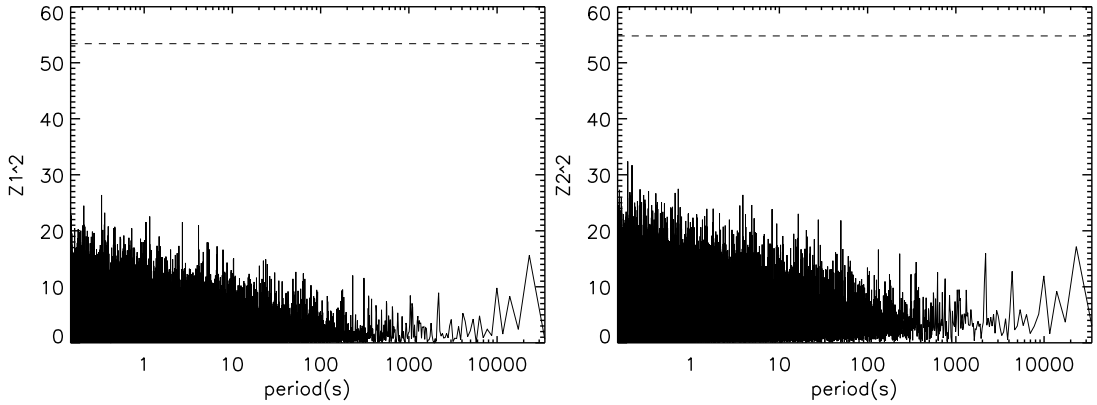

Figure 4.13: Z_m^2 test for source #1 in the G96.0+2.0 FOV. The result for one harmonic is shown on the left, the result for two harmonics on the right. The dashed lines indicate the 5σ significance level.

SNR. In addition, the finding of a potential optical counterpart does not automatically imply that the X-ray and optical emission are actually related, which still leaves the possibility of source #1 being a CCO, for which the lack of an optical counterpart is characteristic (Pavlov et al., 2004; De Luca, 2008; Halpern & Gotthelf, 2010). As the source also shows a very soft spectrum, with a peak below 1 keV, the focus was first set on this candidate.

4.8.2 A Promising Candidate

In the course of analysing the possibility of source #1 being an object that can potentially be associated with G96.0+2.0, first the astronomical database SIMBAD[80] (short for *Set of Identifications, Measurements and Bibliography for Astronomical Data;* Wenger et al., 2000) of the CDS was checked for an entry related to the optical counterpart. A hit might already have given information about the nature of the source and an understanding of whether or not the optical and X-ray emission are actually related, but no such identification was found.

Next, the Z_m^2 test was applied to the barycentrically corrected data of source #1. Figure 4.13 shows the results for one and two harmonics. The test was performed for the whole range of periods for which Z_m^2 could be calculated and for both, one and two harmonics, to be able to double-check the results. Also, with a higher number of harmonics the sensitivity for sinusoidal signals decreases while at the same time more complex structures can be detected. In the plots, the 5σ significance level is given, which indicates the level at which a peak constitutes an obvious detection of pulsation. But no peak, not even with a lower significance, is present. Though this means no pulsation could be found, particularly not with periods below a few seconds, which would have proven a neutron star nature of source #1, this result supports the idea of a homogeneously emitting surface as might be expected for a CCO (e.g. Klochkov et al., 2016; Gotthelf & Halpern, 2018; Posselt & Pavlov, 2018). Spectral analysis can help to reinforce this assumption by examining if the spectrum of the source can be fitted with a blackbody model.

[80] `http://simbad.u-strasbg.fr/simbad/`

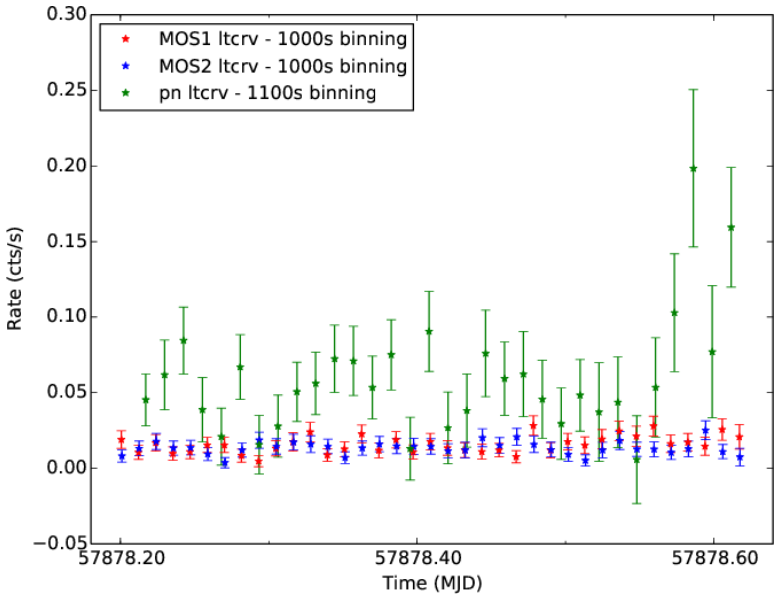

Figure 4.14: Light curve for source #1.

To look for variability on longer time scales, the source and background light curves were created from the barycentrically corrected data with `evselect` and the background subtracted light curve, Figure 4.14, was then obtained using the SAS tool `epiclccorr`. Due to statistical Poissonian noise, negative count rate values can occur if the time bin size is small, particularly with low statistics. The data were, thus, binned with a factor of 1000 s in the case of MOS and with a factor of 1100 s in the case of pn to get count rate values above zero throughout. The pn data show a higher count rate in the light curve, which is due to the pn detector being more sensitive than the MOS cameras (Carter & Read, 2007) and not having a reflection grating stack in its light path. Only in the pn data an increase in the count rate can be seen towards the end of the observation. As there is no such increase in the MOS data and as a corresponding increase in the count rate was already detected and classified as being of instrumental origin in the process of GTI filtering (see Chapter 4.5), this feature is not related to the source and no flaring behaviour could be detected.

For the spectral analysis, the extracted EPIC spectra of source #1 in the 0.4–8.0 keV energy range were simultaneously fitted in XSPEC with the previously introduced power-law model `pow`, the blackbody model `bb` and the atmosphere models `hatm` and `carbatm`, respectively. Each of these models was combined with the photoelectric absorption model `phabs`.

Using the atmosphere models, the mass was first set to 1.4 $M_{\odot}$ to be able to try to either figure out the object's radius by freezing the value of the distance or to check its distance by setting the radius to a few kilometres (∼10 km), as is typical for NSs. For the distance, 4 kpc, as given in the literature (Kothes et al., 2005), were assumed, which corresponds to a model normalization of 6.25 if the emission comes from the whole surface of the source. A homogeneous emission from the surface can be assumed for CCOs and, also, the lack of pulsations supports this assumption. Unfortunately, the spectrum could not be fitted with the atmosphere models, neither with the mass being fixed nor with it running freely, mostly due to the mass M and radius R parameters

reaching values that lead to a $\log(g)$ which was not covered by the T-$\log(g)$-grid of the model. To examine a possible NS nature further, also the neutron star models `nsx` (Ho & Heinke, 2009), which contains spectral templates for non-magnetic helium atmospheres, and `nsmaxg` (Ho et al., 2008), for magnetic hydrogen atmospheres, were tested but could not be fitted. This inapplicability of the models rather supports the idea of source #1 not being a thermally emitting NS.

In the upper two sections of Table 4.5, the parameters of the fits with the power-law model and with the blackbody model are given. First, the models were fitted with the hydrogen column density parameter, N_{H}, left free. Besides the quality of the fit being unsatisfactory, with χ^2_{red} being 1.392 and 1.527 for 61 dof, respectively, N_{H} ended up too low to match the determined value of $1.0{\times}10^{22}\,\mathrm{cm}^{-2}$, particularly in the case of the blackbody model. Fixing N_{H} to the expected value led to an even poorer goodness of the fits for both models.

The third section in Table 4.5 contains the parameters for a fit with both, the blackbody and the power-law model, together to allow for a combination of thermal and non-thermal emission. If N_{H} is allowed to run freely, this leads to an obvious improvement of the goodness of the fit with χ^2_{red} being 1.059 for 59 dof. Still, N_{H} only reaches about half the value expected. A fixed value slightly impairs the fit, though it is still better than any of the fits with the single models, and leads to an extremely high photon index Γ. Thus, the fit with the free N_{H} parameter is to be preferred. The low temperature $k_{\mathrm{B}}T$ of $0.12\,(+0.04/-0.04)$[81] keV and the high photon index Γ of $3.17\,(+0.96/-0.74)$ are both indicative of a soft source.

As an identification of source #1 as a NS could not be achieved with the spectral modelling, a way to analyse if the X-ray emission and the potential optical counterpart are actually related was pursued. In Figure 4.15, the astrometrically corrected position of source #1 can be seen in an optical image observed with the Palomar Observatory showing the according region of the sky. The associated optical source lies within the 3σ confidence limits but, as long as not proven otherwise, there is still the chance of the optical emission being caused by a different source. Finding a connection between the optical and X-ray emission would disprove the possibility of the source being a CCO candidate.

Thus, and because the source has been characterized as having soft X-ray emission, the hot diffuse gas emission model `mekal` (Kaastra & Mewe, 2000) was used to test for a hot star nature of the source. The model is based on the calculations by Mewe et al. (1985, 1986), Kaastra (1992) and Liedahl et al. (1995) for optically thin high-temperature plasmas, taking line emission of a number of elements[82] into account. The main model parameters are the temperature $k_{\mathrm{B}}T$, the hydrogen density n_{H} per cm^{-3}, the metal abundances, the redshift z and the normalization

$$K_{\texttt{mekal}} = \frac{1}{4\pi(d_{\mathrm{a}}(1+z))^2} \times 10^{-14} \int n_{\mathrm{e}} n_{\mathrm{H}} \mathrm{d}V \tag{4.20}$$

with the angular diameter distance d_{a} and with the electron density n_{e} and n_{H} integrated over the volume V. Only the temperature and the normalization were left running free

[81] Errors are 90% confidence limits for all fitting parameters.

[82] namely hydrogen (H), helium (He), carbon (C), nitrogen (N), oxygen (O), neon (Ne), sodium (Na), magnesium (Mg), aluminium (Al), silicon (Si), sulphur (S), argon (Ar), calcium (Ca), iron (Fe) and nickel (Ni)

Table 4.5: Fit parameters for source #1 in the G96.0+2.0 FOV, both for the $N_{\rm H}$ parameter left free and for it being frozen to the value of $1.0{\times}10^{22}\,{\rm cm}^{-2}$ as determined with the FTOOLS task `nh`. The parameters for different models are separated by horizontal lines. The models applied are, from top to bottom: power law, blackbody, power law and blackbody combined and a triple use of `mekal`. The errors given are the 90% confidence limits.

parameter	$N_{\rm H}$ free	$N_{\rm H}$ frozen
$N_{\rm H}$ $(10^{22}\,{\rm cm}^{-2})$	$0.41\,^{+0.11}_{-0.09}$	1.00
Γ	$4.35\,^{+0.67}_{-0.55}$	$7.91\,^{+0.23}_{-0.24}$
norm.	$1.01\,^{+0.42}_{-0.27}{\times}10^{-4}$	$5.56\,^{+0.33}_{-0.33}{\times}10^{-4}$
$\chi^2_{\rm red}$ (dof)	1.392 (61)	2.009 (62)
$N_{\rm H}$ $(10^{22}\,{\rm cm}^{-2})$	$0.02\,^{+0.07}_{-0.02}$	1.00
$k_{\rm B}T$ (keV)	$0.26\,^{+0.03}_{-0.03}$	$0.09\,^{+0.01}_{-0.01}$
norm.	$9.67\,^{+3.03}_{-1.14}{\times}10^{-7}$	$3.37\,^{+1.40}_{-0.97}{\times}10^{-4}$
$\chi^2_{\rm red}$ (dof)	1.527 (61)	3.506 (62)
$N_{\rm H}$ $(10^{22}\,{\rm cm}^{-2})$	$0.46\,^{+0.36}_{-0.20}$	1.00
Γ	$3.17\,^{+0.96}_{-0.74}$	$8.27\,^{+0.24}_{-0.24}$
norm.	$4.43\,^{+6.22}_{-2.43}{\times}10^{-5}$	$5.12\,^{+0.37}_{-0.38}{\times}10^{-4}$
$k_{\rm B}T$ (keV)	$0.12\,^{+0.04}_{-0.04}$	$0.57\,^{+0.13}_{-0.11}$
norm.	$1.03\,^{+24.86}_{-0.79}{\times}10^{-5}$	$4.75\,^{+1.34}_{-1.23}{\times}10^{-7}$
$\chi^2_{\rm red}$ (dof)	1.059 (59)	1.346 (60)
$N_{\rm H}$ $(10^{22}\,{\rm cm}^{-2})$	$0.79\,^{+0.14}_{-0.09}$	1.00
$k_{\rm B}T_1$ (keV)	$0.08\,^{+0.08}_{-0.08}$	$0.08\,^{+0.01}_{-0.08}$
norm.	$0.06\,^{+0.22}_{-0.06}$	$0.47\,^{+0.08}_{-0.19}$
$k_{\rm B}T_2$ (keV)	$0.19\,^{+0.06}_{-0.02}$	$0.24\,^{+0.05}_{-0.06}$
norm.	$1.57\,^{+1.83}_{-1.50}{\times}10^{-3}$	$9.59\,^{+28.01}_{-4.80}{\times}10^{-4}$
$k_{\rm B}T_3$ (keV)	$1.74\,^{+0.53}_{-0.35}$	$1.80\,^{+0.57}_{-0.48}$
norm.	$5.88\,^{+1.05}_{-1.06}{\times}10^{-5}$	$5.72\,^{+1.79}_{-1.11}{\times}10^{-5}$
$\chi^2_{\rm red}$ (dof)	1.084 (57)	1.172 (58)

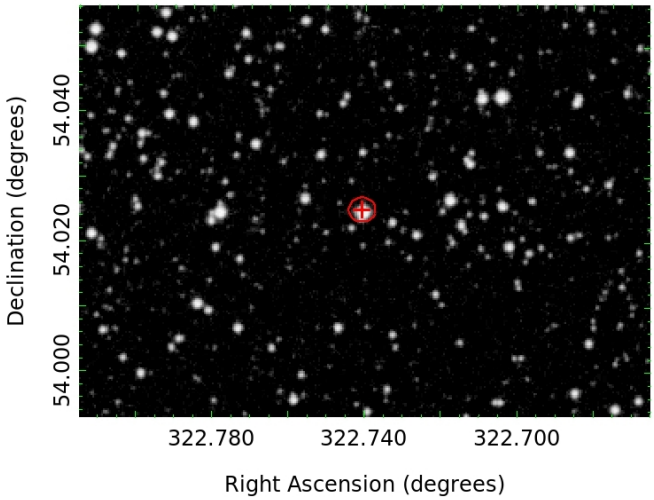

Figure 4.15: Position of X-ray source #1 on top of an optical image from the Palomar Observatory Sky Survey, taken with the 1.2 m Samuel Oschin Telescope. The red cross marks the astrometrically corrected position determined for source #1. The red ellipse shows the 3σ confidence region, which encompasses the potential optical counterpart (USNO-B1.0 designation: 1440-0361458). The image was obtained with the DSS of the Space Telescope Science Institute, STScI (available at `https://archive.stsci.edu/cgi-bin/dss_form/`).

during the fitting process, as for the other `mekal` parameters, the default parameters were kept.

Following the hot star analysis of Nazé (2009), different model compositions were tested, including up to three `mekal` components with either one common absorption component (`phabs`) affecting all of them or an individual absorption component for each of them. The best fit was achieved combining three `mekal` models with a common absorption handling: `phabs` × (`mekal` + `mekal` + `mekal`). In the bottom section of Table 4.5, the parameter values of the fit are given, again for both cases, N_{H} running freely and being frozen to the predicted value of $1.0{\times}10^{22}\,\mathrm{cm}^{-2}$.

With χ^2_{red} being 1.084 for 57 *dof* in the case of N_{H} left unfrozen, the model represents the data well, as shown with the fitted spectrum in Figure 4.16, and also the hydrogen column density N_{H}, being $0.79\,(+0.14/-0.09){\times}10^{22}\,\mathrm{cm}^{-2}$, is much closer to the expected value than in previous fitting attempts with the other models. Even when freezing N_{H} again, the goodness of the fit is still better. Independent of whether or not N_{H} was fixed, the first temperature reaches ∼0.08 keV, the lowest value allowed in XSPEC, the second temperature is ∼0.2 keV and the hardest temperature is just below ∼2 keV. With these values, the fit matches the triple `mekal` model description for O- and B-type stars in Nazé (2009) perfectly well, together with the normalizations behaving in the same way as described there: being lower for the higher temperatures, with the softest component clearly dominating. Source #1 has, thus, been characterized as being a hot foreground star and discarded as a possible candidate for a compact object associated with G96.0+2.0.

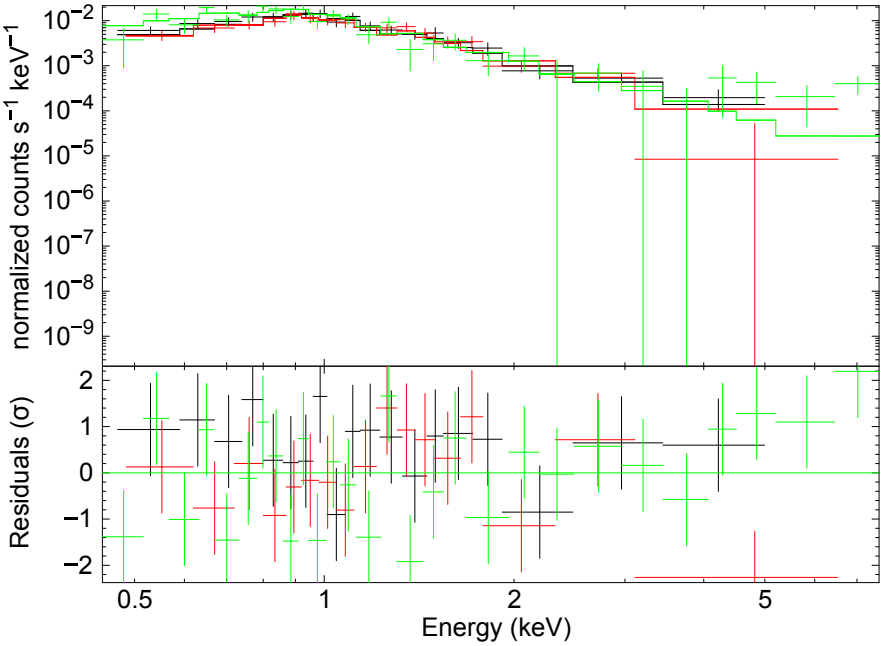

Figure 4.16: Spectrum of source #1 fitted with a triple `mekal` model. N_{H} was left running freely and χ^2_{red} of the fit is 1.084 for 57 dof.

4.8.3 Extended Analysis

As source #1 was no longer qualified for being a potential candidate for a compact object associated with the SNR, the same analysis steps were performed for the other detected X-ray sources with a decent number of EPIC counts (>90) detected in the 0.4–3.0 keV range. These objects are sources #2, #3, #4, #5, #7, #11, #13 and #14 (see Table 4.3).

To search for pulsations of these sources, again the Z^2_m test was applied to the pn data for the energy ranges given in Table 4.4 above. The results for two harmonics are shown in Figure 4.17, with the exception of source #5, which was not covered by the pn detector. Source #13 shows slight peaks at ∼1.896 s with Z^2_2 being ∼35.748 and at ∼3.792 s with Z^2_2 being ∼36.628. This accounts for detection probabilities just below 3σ. Also, no according peaks were detected in the one harmonic plots (see Figure B.5), which were created to double check the results and be able to evaluate whether or not a signal is indeed indicative of pulsation. Considering the not quite conclusive detection probability and the missing of mirror patterns in the one harmonic results, these peaks are most probably only due to noise. The same applies to the slight peaks of source #7 at ∼0.208 s, ∼0.223 s and ∼0.251 s and of source #11 at ∼0.210 s, which also do not have any corresponding peaks in the one harmonic plots. All in all, pulsations could not be detected for any of the sources.

For the timing analysis on longer time scales to look for flaring, the light curves for each of the eight sources were created with the same binning of 1000 s in the case of MOS and 1100 s in the case of pn as for source #1. As can be seen in Figure 4.18, the light curves did not show any flaring behaviour. Only the instrumental rise in the pn data discussed before (see Chapter 4.8.2) is visible again in the light curves of the brightest sources. Also the partially poorer statistics become apparent as even the large

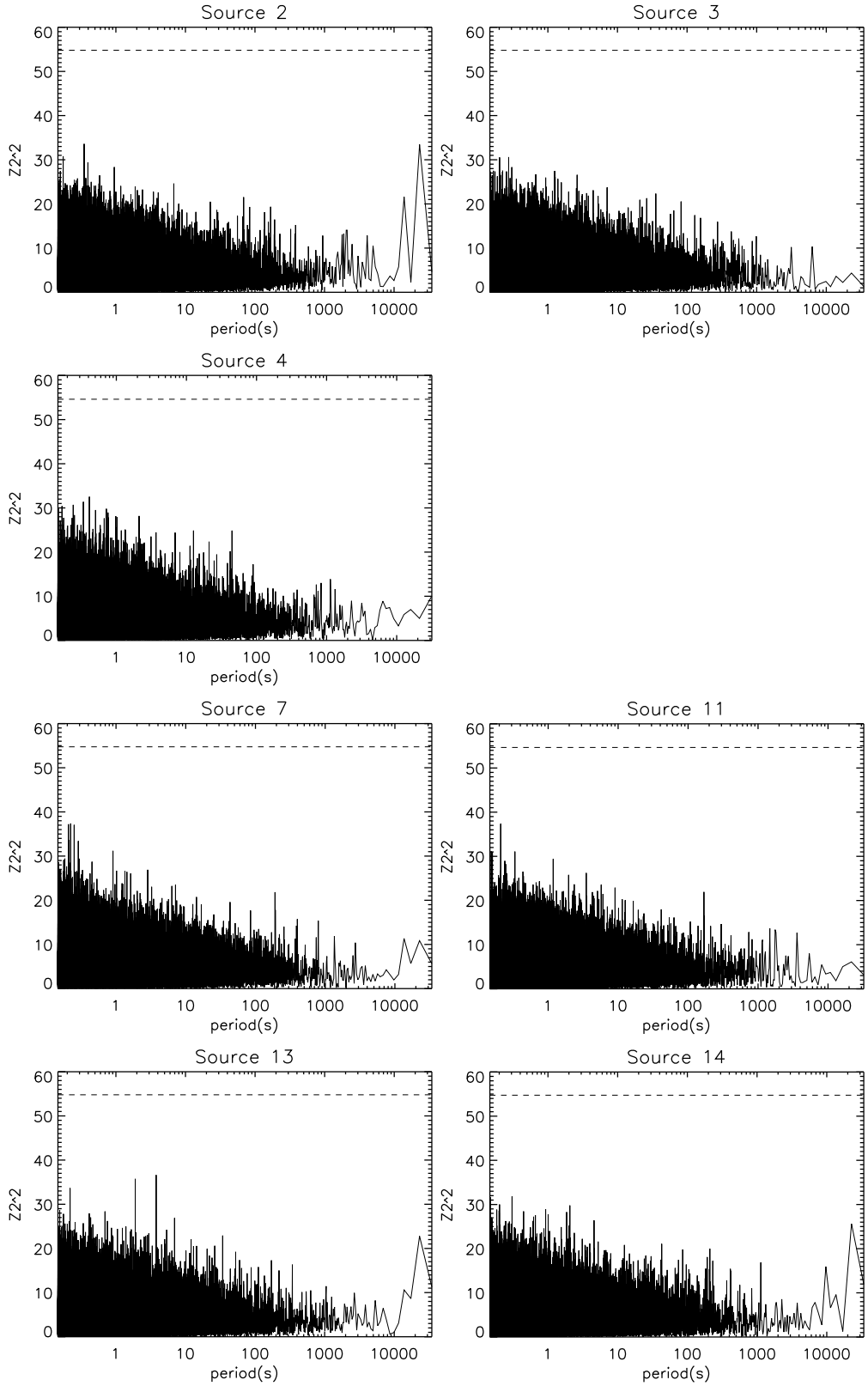

Figure 4.17: Z_m^2 test with two harmonics for seven of the eight remaining sources with more than 90 EPIC counts in the G96.0+2.0 FOV. Source #5 is missing as it was not covered by the pn detector. The dashed lines indicate the 5σ significance level.

Table 4.6: Fit parameters for sources in the G96.0+2.0 FOV best fitted with a blackbody model. The errors given are the 90% confidence limits.

parameter	source #2	source #5
N_{H} ($10^{22}\,\mathrm{cm}^{-2}$)	$0.78^{+0.25}_{-0.20}$	$0.82^{+0.71}_{-0.52}$
$k_{\mathrm{B}}T$ (keV)	$0.09^{+0.02}_{-0.01}$	$0.85^{+0.19}_{-0.15}$
norm.	$2.36^{+15.96}_{-1.84}\times10^{-4}$	$2.66^{+0.57}_{-0.43}\times10^{-6}$
χ^2_{red} (dof)	0.984 (47)	1.157 (16)

Table 4.7: Fit parameters for sources in the G96.0+2.0 FOV best fitted with a power-law model. The errors given are the 90% confidence limits.

parameter	source #4
N_{H} ($10^{22}\,\mathrm{cm}^{-2}$)	$1.56^{+2.18}_{-1.34}$
Γ	$1.34^{+1.06}_{-0.86}$
norm.	$1.18^{+4.73}_{-0.87}\times10^{-5}$
χ^2_{red} (dof)	0.753 (27)

time bins were not sufficient to minimize the statistical noise and get count rate values above zero in all cases. All things considered, no timing properties could be discovered that could hint at e.g. rotation and/or accretion processes of the sources.

The poor statistics were also problematic in the spectral analysis of the sources. For each of the eight sources, basically the same models used to analyse source #1 were tested, namely the blackbody model `bbody`, the power-law model `pow`, a combination of the two, the atmosphere models `hatm` and `carbatm` as well as the hot plasma model `mekal` applied in single, double and triple form. The spectra were fitted again in the 0.4–8.0 keV range. Just as for source #1, attempts to fit any of these sources with the atmosphere models did not succeed, again mostly due to the parameters reaching limits not covered by the models. Thus, only results from the fitting with the other models shall be discussed in more detail in the following. In Table 4.6 the best fit parameters are given for the sources best fitted with a blackbody model, namely sources #2 and #5, Table 4.7 contains the parameters for a best fit with a power-law model, which applied only to source #4, and in Table 4.8 the fit parameters for sources #3, #7, #11 and #13, which were best fitted with a single `mekal` model, can be found. For source #14 the combination of the `mekal` model with a blackbody model (Table 4.9) led to a clear improvement of the fit. Figures 4.19 and 4.20 contain the corresponding fitted spectra for the sources mentioned.

At the beginning of the spectral analysis of these sources, special attention was given to sources #3 and #4, as source #3 is the next closest source to the SNR centre after source #1 and source #4 is the most centrally located source for which no optical counterpart was found. Thus, these two sources offered the best chance of still finding a CCO after source #1 had to be dismissed. In the case of source #3, the best fit was achieved with a single use of the `mekal` model (see Table 4.8). Besides the good quality of the fit and a temperature matching the values given in Nazé (2009) for hot stars, the

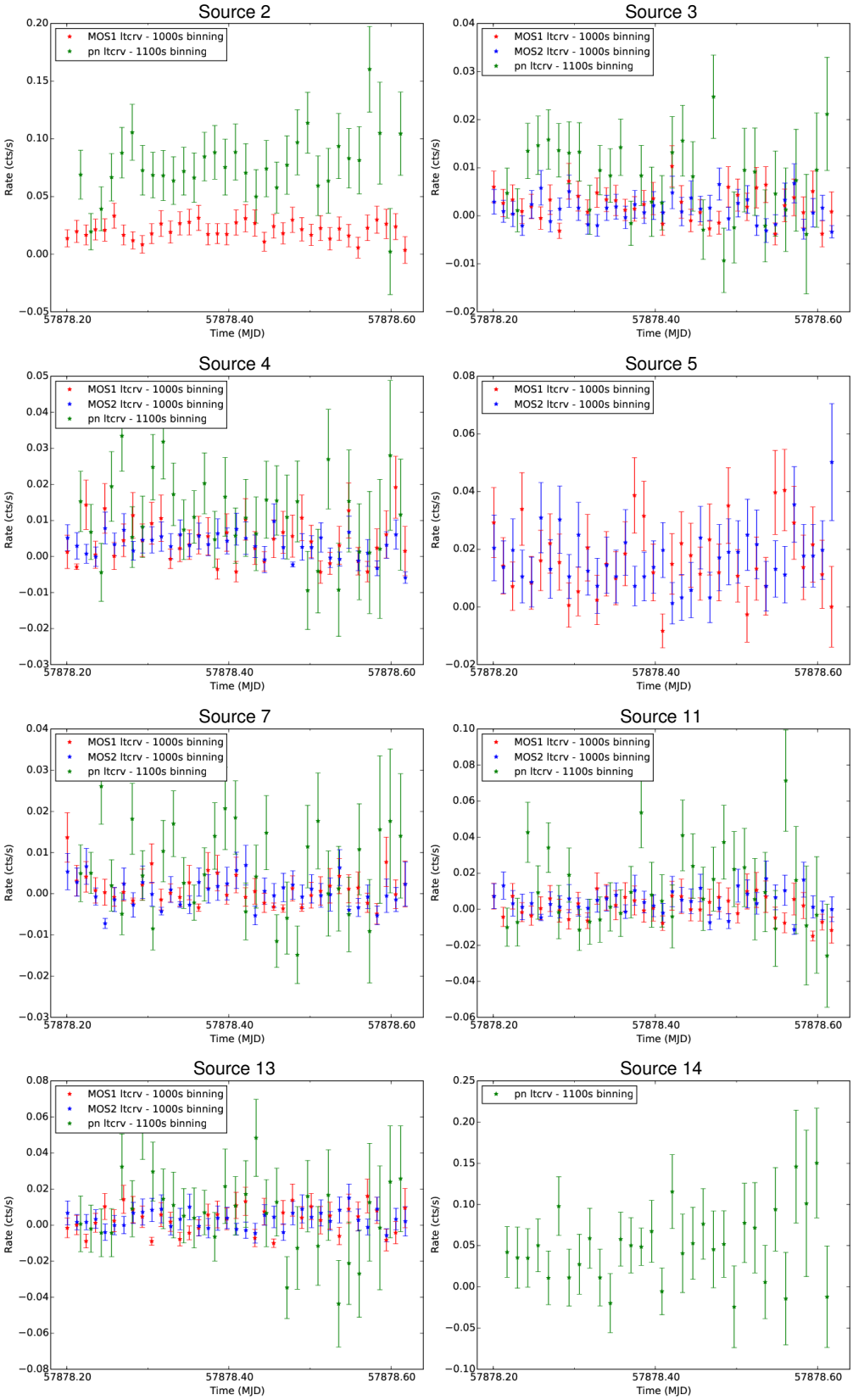

Figure 4.18: Light curves of the eight remaining sources with more than 90 EPIC counts in the G96.0+2.0 FOV.

Table 4.8: Fit parameters for sources in the G96.0+2.0 FOV best fitted with a single `mekal` model. The errors given are the 90% confidence limits.

parameter	source #3	source #7
$N_{\rm H}$ ($10^{22}\,{\rm cm}^{-2}$)	$0.72^{+0.25}_{-0.28}$	$0.41^{+0.53}_{-0.41}$
$k_{\rm B}T$ (keV)	$0.59^{+0.16}_{-0.15}$	$0.33^{+0.23}_{-0.19}$
norm.	$2.27^{+2.43}_{-1.29}\times10^{-5}$	$1.14^{+94.71}_{-1.14}\times10^{-5}$
$\chi^2_{\rm red}$ (dof)	1.037 (32)	1.428 (13)

parameter	source #11	source #13
$N_{\rm H}$ ($10^{22}\,{\rm cm}^{-2}$)	$0.86^{+0.45}_{-0.41}$	$1.20^{+75198.8}_{-1.20}\times10^{-5}$
$k_{\rm B}T$ (keV)	$0.61^{+0.26}_{-0.22}$	$0.54^{+0.15}_{-0.39}$
norm.	$3.89^{+6.45}_{-2.63}\times10^{-5}$	$3.55^{+1366.45}_{-0.84}\times10^{-6}$
$\chi^2_{\rm red}$ (dof)	1.327 (21)	1.009 (18)

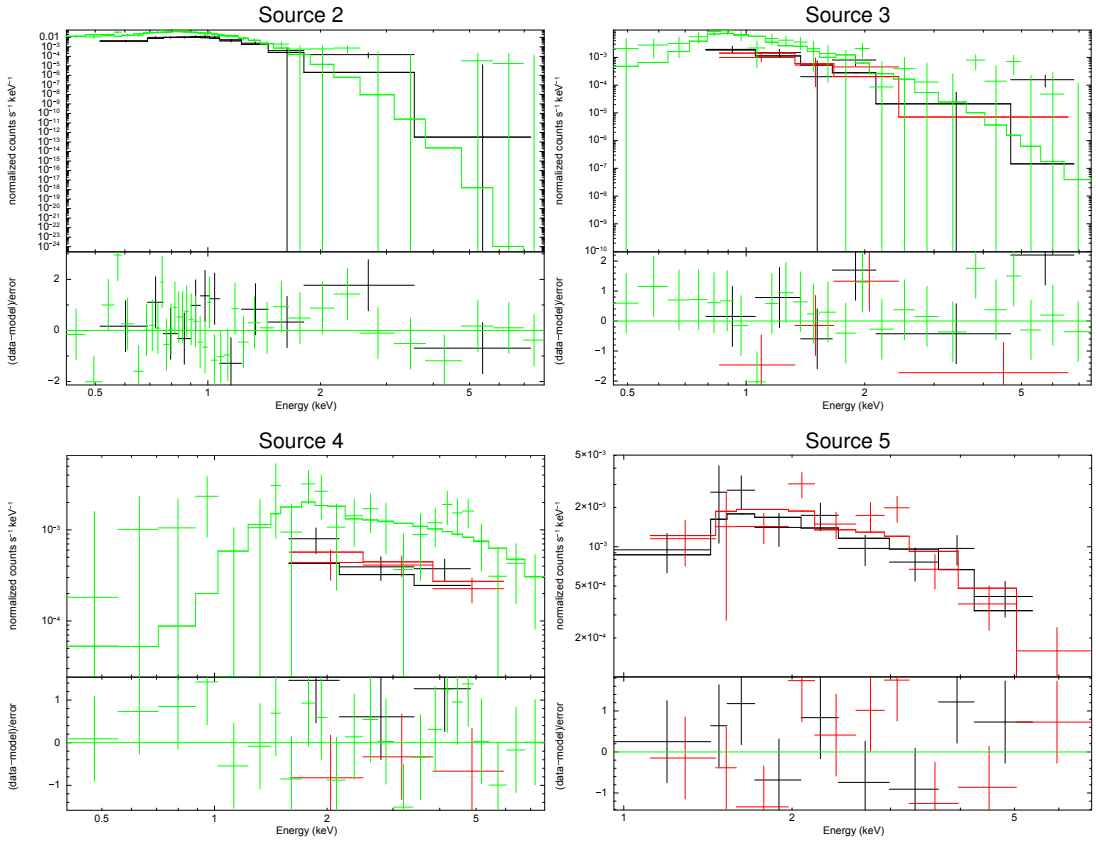

Figure 4.19: Best fit spectra and residuals for sources #2, #3, #4 and #5. Sources #2 and #5 were fitted with a blackbody model, source #3 with a single `mekal` model and source #4 with a power-law model. MOS1 data are black, MOS2 data red and pn data green. Source #2 was only covered by MOS1 and pn, source #5 was only covered by the MOS cameras. The data were grouped with a minimum of 25 counts per bin.

Table 4.9: Fit parameters for sources in the G96.0+2.0 FOV best fitted with a combined blackbody (bb) and `mekal` model. The errors given are the 90% confidence limits.

parameter	source #14
$N_{\rm H}$ ($10^{22}\,{\rm cm}^{-2}$)	$1.05^{+0.15}_{-0.33}$
$k_{\rm B}T_{\rm bb}$ (keV)	$0.99^{+1.61}_{-0.47}$
norm.$_{\rm bb}$	$7.93^{+17.29}_{-5.06}\times10^{-7}$
$k_{\rm B}T_{\texttt{mekal}}$ (keV)	$0.08^{+0.05}_{-0.08}$
norm.$_{\texttt{mekal}}$	$0.50^{+0.58}_{-0.49}$
$\chi^2_{\rm red}$ (dof)	1.178 (10)

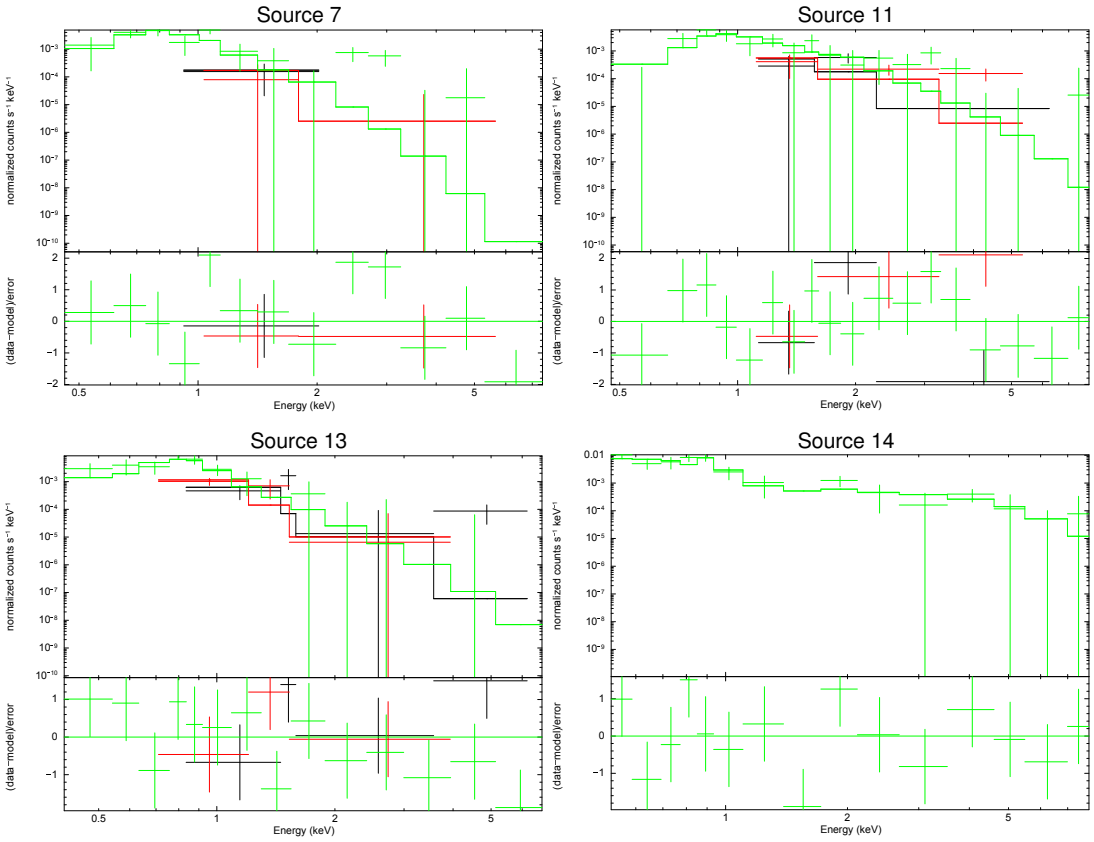

Figure 4.20: Best fit spectra and residuals for sources #7, #11, #13 and #14. Sources #7, #11 and #13 were fitted with a single `mekal` model and source #14 with a combined blackbody and `mekal` model. MOS1 data are black, MOS2 data red and pn data green. Source #14 was only covered by the pn detector. The data were grouped with a minimum of 25 counts per bin.

hydrogen column of $0.72\,(+0.25/-0.28)\times10^{22}\,\mathrm{cm}^{-2}$ is similar to the one obtained with the best fit of source #1 above, which was $0.79\,(+0.14/-0.09)\times10^{22}\,\mathrm{cm}^{-2}$. Thus, this model is the preferred one even though a blackbody or power-law model also led to good χ^2_{red} values of $\sim$0.99 for 32 dof. As for the blackbody model, the hydrogen column was too low by two orders of magnitude. With the power-law model, the hydrogen column of $0.54\,(+0.43/-0.26)\times10^{22}\,\mathrm{cm}^{-2}$ would have been acceptable but a rather high photon index of $4.70\,(+2.57/-1.47)$ suggested the source to be of a soft nature and supported the classification of it as a hot star. Source #3 was, therefore, also dropped as a potential candidate associated with G96.0+2.0.

As for source #4, the best fit could be obtained with the power-law model (Table 4.7). It resulted in an adequate photon index of $1.34\,(+1.06/-0.86)$, usual for young radio pulsars with a PWN but also for background AGNs. As no pulsations were found to indicate a NS nature of the source, which could also be due to its axis being oriented in a way so that we miss the narrow beam of pulsed emission, a radio counterpart was searched for using X-Match again, together with the data of the NVSS, the NRAO (National Radio Astronomy Observatory) VLA (Very Large Array) Sky Survey (Condon et al., 1998). The relevant part of the sky is covered by the catalogue, but no radio counterpart could be found for source #4 to support a pulsar classification. But the beam of the radio emission could just as well be completely missing our line of sight. A possible background AGN nature of the source can be doubted as also no optical counterpart could be found for source #4 (see Chapter 4.7.2). While the `mekal` model to test for a possible hot star nature of the source could clearly be dismissed due to it resulting in temperature values several tens of magnitudes too high, the statistics did not allow for a definite preference between the power law and the blackbody model. The latter led to a χ^2_{red} of 0.709 for 27 dof, quite similar to the quality of the simple power-law fit. The hydrogen column is rather low with $0.08\,(+1.16/-0.08)\times10^{22}\,\mathrm{cm}^{-2}$, but the expected value of about $1.0\times10^{22}\,\mathrm{cm}^{-2}$ is still within the error. But with $1.45\,(+0.43/-0.21)\,\mathrm{keV}$ the temperature $k_{\mathrm{B}}T$ of the fit is higher than expected for a possible CCO candidate. Attempts to improve the fit with a combination of a blackbody and power-law model, as sometimes also successfully applied to the spectra of young pulsars (e.g. McGowan et al., 2004; Hebbar et al., 2020), resulted in implausible parameter values for either one of the model components.

Similarly, no obvious preference of one model could be found for source #2. Only a power-law model could be dismissed due to the bad quality of the fit with χ^2_{red} being 2.700 for 47 dof. The spectrum of the source was clearly better fitted with a blackbody model (Table 4.6), resulting in a χ^2_{red} of 0.984 for 47 dof and an absorption column of $0.78\,(+0.25/-0.20)\times10^{22}\,\mathrm{cm}^{-2}$, which matches the values already obtained with the best fits of sources #1 and #3 quite well. Besides source #2 being located too far off from the centre of the SNR to be a CCO (see Figure 4.11), also the temperature of the blackbody fit, being $0.09\,(+0.02/-0.01)\,\mathrm{keV}$, which corresponds to $\sim10^6\,\mathrm{K}$, is below the expected value for CCOs but still matches typical values for the surface temperature of NSs (Longair, 2011). The luminosity derived from the normalization with an assumed distance of 4 kpc for an object related to the SNR is $\sim10^{35}\,\mathrm{erg\,s^{-1}}$, higher than the typical luminosities of 10^{33}–$10^{34}\,\mathrm{erg\,s^{-1}}$ observed for CCOs (Seward & Charles, 2010) but within the range of luminosities observed for NSs. Also fits with the `mekal` model led to acceptable results. A single `mekal` use resulted in a χ^2_{red} of 1.132 for 47 dof and a typical temperature of $0.26\,(+0.05/-0.03)\,\mathrm{keV}$, which matches

the SIMBAD classification of the potential optical counterpart as a normal star. With $0.56\,(+0.09/-0.12)\times10^{22}\,\mathrm{cm}^{-2}$, the absorption column is slightly lower than the one for the blackbody model. The fits with the blackbody and the `mekal` model, which show much better results than the power-law model, at least clearly suggest a thermal origin of the source's emission.

The spectral analysis of region #5 lead to more obvious results. From all trials with the `mekal` model a single use resulted in the best χ^2_{red} with 1.188 for 16 dof, but generally the lowest absorption column that could be obtained with this model was already twice as high as expected. Though a high absorption column can indicate a dense medium environment around an object, also the temperatures in the `mekal` fits were higher than expected for hot stars. The power-law model fit had a χ^2_{red} of 1.225 for 16 dof. Even though N_{H}, with about $2\times10^{22}\,\mathrm{cm}^{-2}$, is equally high as in the case of the best `mekal` fit, a reasonable photon index of $2.33\,(+0.86/-0.69)$ could be obtained. With a blackbody model (Table 4.6), the goodness of the fit was slightly better with χ^2_{red} being 1.157 for 16 dof, the hydrogen absorption column of $0.82\,(+0.71/-0.52)\times10^{22}\,\mathrm{cm}^{-2}$ was conform with the values from the other unambiguous best fits of sources #1 and #3 and a promising temperature of $0.85\,(+0.19/-0.15)\,\mathrm{keV}$ was obtained. At the expected distance of $\sim$4 kpc for a compact object associated with G96.0+2.0, the normalization of $2.66\,(+0.57/-0.43)\times10^{-6}$ corresponds to a luminosity of the order of $10^{33}\,\mathrm{erg\ s}^{-1}$. Although source #5, which is one of the few sources in the FOV for which no potential optical counterpart could be found, is located at the border of the SNR (see Figure 4.11) and, thus, too far from the centre to be a CCO, its luminosity also matches the values typical for other types of compact objects like rotation-powered pulsars (Possenti et al., 2002). A combination of a blackbody and a power-law component resulted in a slightly worse fit with an unusually low photon index. Even though the neutron star atmosphere models `hatm` and `carbatm` were not recommended by their goodness of fit and fit parameter values, it is worth mentioning that sources #5 and #4 are the only two sources in the set to which these models could be applied without reaching the limits of the underlying T-$\log(g)$-grid.

For the remaining four sources, #7, #11, #13 and #14, the use of the `mekal` model led to satisfying fits. But only in the case of sources #11 and #13 the results obtained with a single `mekal` component (Table 4.8) were clearly preferable. Regarding source #11 it led to a fit with χ^2_{red} being 1.327 for 21 dof. Again, with $0.86\,(+0.45/-0.41)\times10^{22}\,\mathrm{cm}^{-2}$ the absorption column has about the same value as for the above-mentioned best fits of sources #1, #3 and #5 and the temperature of $0.61\,(+0.26/-0.22)\,\mathrm{keV}$ is within the hot star limits in Nazé (2009). The fit for source #13 had a χ^2_{red} of 1.009 for 19 dof. Only due to its high upper error the absorption column of $1.20\,(+75198.8/-1.20)\times10^{17}\,\mathrm{cm}^{-2}$ can still be considered to be as expected, while the temperature of $0.54\,(+0.15/-0.39)\,\mathrm{keV}$ matches the typical values for hot stars perfectly. For source #7, only a power-law model could clearly be dismissed with χ^2_{red} being 3.568 for 13 dof. The single `mekal` and the blackbody models led to equally good results. The fit with `mekal` resulted in a χ^2_{red} of 1.428 for 13 dof, the one for the blackbody model in a χ^2_{red} of 1.441 for 13 dof. Both fits show a rather low absorption column, $0.41\,(+0.53/-0.41)\times10^{22}\,\mathrm{cm}^{-2}$ in the case of `mekal` and $0.59\,(+1.52/-0.26)\times10^{22}\,\mathrm{cm}^{-2}$ in the case of the blackbody model. With $0.11\,(+0.10/-0.06)\,\mathrm{keV}$, the temperature in the blackbody fit is rather low, while the `mekal` temperature of $0.33\,(+0.23/-0.19)\,\mathrm{keV}$ is again consistent with the typical temperatures for hot stars. As for source #14, of all the single component

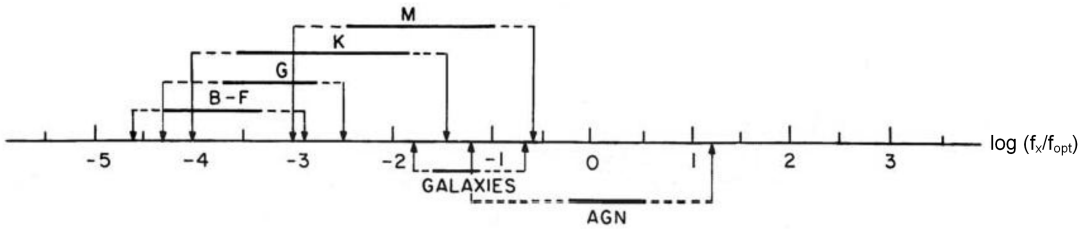

Figure 4.21: X-ray-to-optical flux ratios of stars of type B–M, galaxies and AGNs. The classification is based on X-ray fluxes in the 0.3–3.5 keV band and the visual magnitude. (Maccacaro et al., 1988, modified)

models tested the use of `mekal` led to the best fit as well, but with a χ^2_{red} of 1.605 for 12 *dof* its quality was still worse than for any other source. A fit with a single power-law model had a comparable quality with χ^2_{red} being 1.545 for 12 *dof*, but with a quite high photon index Γ of $\sim$10 it indicated that the source is of a very soft nature. With a χ^2_{red} of 1.832 (12 *dof*) a single blackbody component resulted in a worse fit than the other models. However, in the case of source #14 the fit could be clearly improved by combining a `mekal` and a blackbody component (Table 4.9), leading to χ^2_{red} being 1.178 for 10 *dof*. The absorption column, with $1.05\,(+0.15/-0.33)\times10^{22}\,\mathrm{cm}^{-2}$, is as expected and the two thermal components with temperatures of $0.99\,(+1.61/-0.47)$ keV and $0.08\,(+0.05/-0.08)$ keV for the blackbody and `mekal`, respectively, confirm the source's soft nature. The values suggest a thermal origin that matches a stellar nature, which is supported by an according entry in the SIMBAD database for the source's location.

4.9 X-ray-to-Optical Flux and Hardness Ratios

Two alternative options to find out about the nature of the detected sources, including the sources with insufficient counts for spectral fitting, are the analyses of the X-ray-to-optical flux ratios and the hardness ratios. The X-ray-to-optical flux ratio can help to classify an object by indicating whether its X-ray or optical emission is dominating. Although CCOs do not have optical counterparts, calculating the X-ray-to-optical flux ratio of the sources can support the classification done with the spectral analysis so far and hint at other types of compact objects that might be associated with the SNR. For those sources in the FOV for which a potential optical counterpart was found (see Figure 4.10), the ratio between the X-ray flux (f_{x}) and the optical flux (f_{opt}) was calculated according to Maccacaro et al. (1988):

$$\log\left(\frac{f_{\mathrm{x}}}{f_{\mathrm{opt}}}\right) = \log f_{\mathrm{x}} + \frac{m_{\mathrm{v}}}{2.5} + 5.37\,, \tag{4.21}$$

where m_{v} is the visual magnitude. Figure 4.21 shows the corresponding classification for stars as well as background AGNs and galaxies, which can usually be found in X-ray observations. A value of $\log(f_{\mathrm{x}}/f_{\mathrm{opt}}) \gtrsim 1.3$ thus hints at less common objects like X-ray binaries and only isolated NSs can even show extremely high ratios of up to $\log(f_{\mathrm{x}}/f_{\mathrm{opt}}) \approx 5$ and higher (Stocke et al., 1991, 1995).

The X-ray flux for each detected source with a potential optical counterpart, including all sources except for #4, #5, #10 and #12, was determined as in Maccacaro

et al. (1988) for the 0.3–3.5 keV band. To do so, the online version of the Portable, Interactive Multi-Mission Simulator (WebPIMMS) tool[83] was used to convert the count rates from the 0.4–3.0 keV band, given by the SAS task `edetect_chain` for the EPIC detector which had shown the highest detection likelihood for the source. Besides giving the count rates as input, a spectral model needs to be assumed in order to determine the fluxes, for which an absorbed power law was used here with $N_{\mathrm{H}} = 1.0{\times}10^{22}\,\mathrm{atoms\,cm^{-2}}$ as determined before (see Chapter 4.8.1) and a photon index of 1.7 as applied for the XMM-Newton Slew Survey Clean Source Catalogue (Saxton et al., 2008).[84]

As for the optical magnitude, the mean G-band magnitude of the respective potential optical counterpart was taken from the Gaia catalogue. The band is broader than the classical visual band but this is sufficient for a first separation of optically bright sources from sources bright in X-rays. The resulting X-ray-to-optical flux ratios are shown in Figure 4.22. For sources with two potential optical counterparts, namely sources #3, #15, #16, #20 and #21, the X-ray-to-optical flux ratio was calculated for both respectively.

To check the results obtained with WebPIMMS, as they are based on a generally assumed single power-law model, the X-ray flux was also extracted from the best spectral fits for the sources which had both, a potential optical counterpart and enough counts for spectral fitting, using the Xspec model `cflux`. Figure 4.23 shows the according X-ray-to-optical flux ratio. The X-ray flux is even slightly lower in this case, resulting in an also slightly lower flux ratio.

The two figures show that all sources have a dominating optical component. This means they are no candidates for a NS, should the optical counterpart actually be related to them, and a more precise allocation on the X-ray-to-optical flux scale was not expedient in the scope of this work. Even the two sources that appeared brightest in X-rays, sources #1 and #2, which are almost an order of magnitude brighter in X-rays than most of the other sources, seem to have strong optical counterparts as well as they are located in the lower range of the flux ratio values. The exact values used in the process of determining the X-ray-to-optical flux ratios are all listed in the appendix (Table A.7).

Further information about a source's spectral properties, this time including the sources without a potential optical counterpart, can be obtained by calculating hardness ratios. A hardness ratio HR compares the count rate H in a harder energy band with the count rate S in a softer band and is defined as:

$$HR = \frac{H - S}{H + S}\,. \tag{4.22}$$

Three bands were used for the analysis: 0.4–2.0 keV, 2.0–4.5 keV and 4.5–10.0 keV. The count rates for these bands were determined with the Xspec task `edetect_chain` for the detector which had the maximum detection likelihood in the 0.4–3.0 keV source detection run. Hardness ratios $HR1$ and $HR2$ were calculated for the two softer bands and the two harder bands, respectively. The count rates for the different bands and the hardness ratios are given in the appendix in Table A.8. Sources #14, #20 and #22 had to be excluded as they were not detected with `edetect_chain` in the newly defined

[83] available at `https://heasarc.gsfc.nasa.gov/cgi-bin/Tools/w3pimms/w3pimms.pl`
[84] available at `https://heasarc.gsfc.nasa.gov/w3browse/all/xmmslewcln.html`

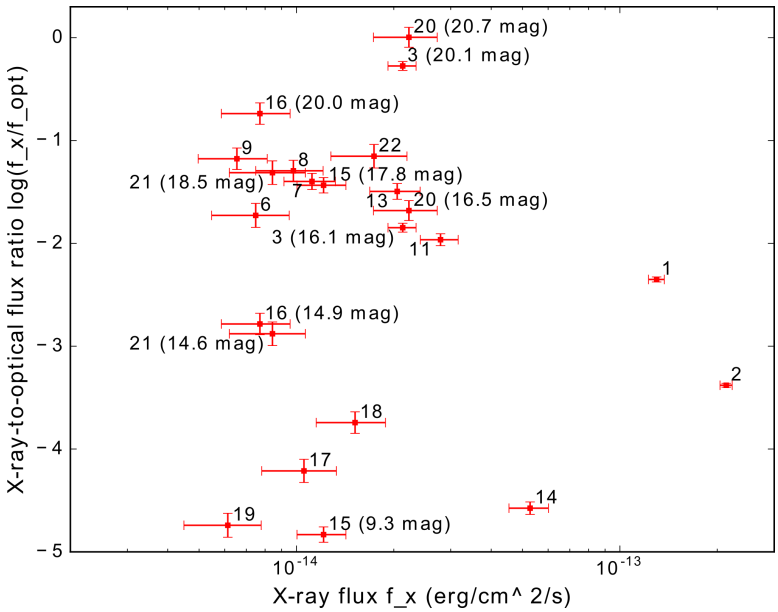

Figure 4.22: X-ray-to-optical flux ratio with X-ray fluxes determined using WebPIMMS. The numbers assigned to the data points correspond to the source numbers assigned to the sources in this work. For sources with two potential optical counterparts, the respective optical magnitude is given in parentheses.

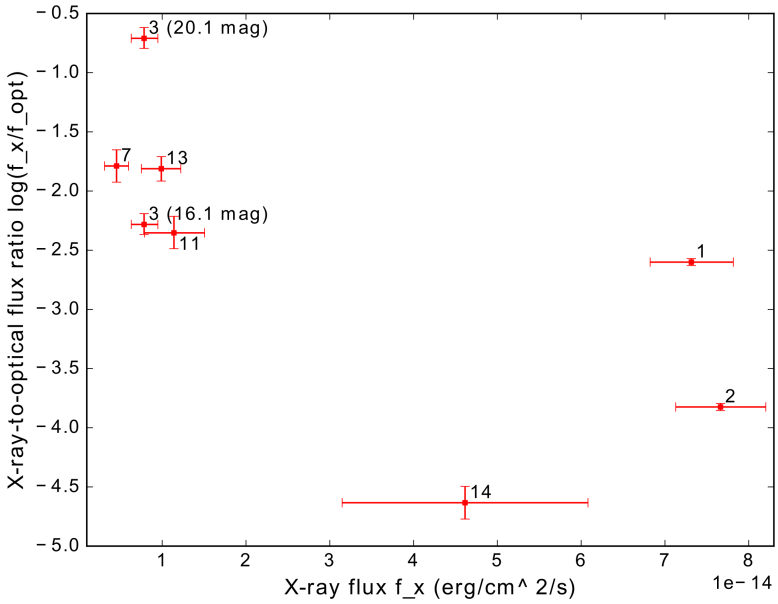

Figure 4.23: X-ray-to-optical flux ratio with X-ray fluxes determined using `cflux`. The numbers assigned to the data points correspond to the source numbers assigned to the sources in this work. For source #3, which has two potential optical counterparts, the respective optical magnitude is given in parentheses.

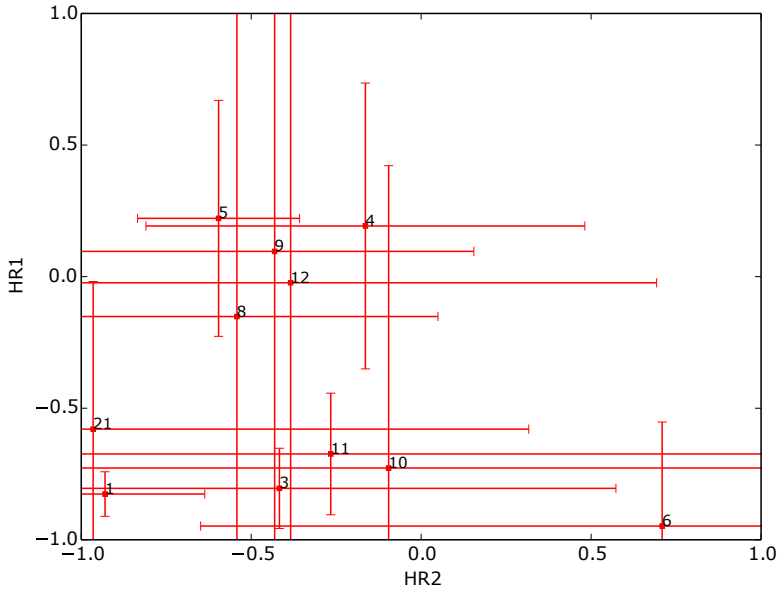

Figure 4.24: Hardness ratios based on count rates in the 0.4–2.0 keV, 2.0–4.5 keV and 4.5–10.0 keV bands.

energy bands. For some sources $HR\,2$ could not be calculated due to the low statistics in the higher band. The same holds true for $HR\,1$ in a couple of cases. In Figure 4.24, $HR\,1$ is plotted against $HR\,2$.

There seem to be two groups of sources, those with $HR\,1 \lesssim -0.5$ and those above this value. As for the first group, this position in the hardness ratio diagram is typical, though not conclusive, for stars (Brunner et al., 2008) and SNRs (Pietsch et al., 2004). Normal galaxies and AGNs are often found there as well but can also be located at $HR\,1 \gtrsim -0.5$ (Brunner et al., 2008). Pulsars and X-ray binaries usually have a higher hardness ratio in the soft bands than stars (Sturm et al., 2013). It is worth mentioning that all sources without an optical counterpart, namely #4, #5 #10 and #12, are located here (in case of source #10 at least within the errors). Unfortunately, as AGNs, pulsars and X-ray binaries are also on the same hardness level in the harder bands (Sturm et al., 2013), no differentiation between the usual AGNs and potential pulsar or binary candidates can be made here.

Magnetars appear hard in the soft band comparison too, but in the hard bands they tend to be even softer than other compact objects or AGNs (Lin et al., 2012). As for middle-aged thermally cooling isolated NSs, they are of such a soft nature (Haberl, 2007) that they have an imperceptible hard component and also stay at lower hardness ratio levels in the soft range (Lin et al., 2012). All sources in Table A.8 for which no $HR\,2$ could be calculated and which have a $HR\,1 \lesssim -0.5$ could, thus, match this property, namely sources #2, #7, #13 and #15–19. But alternative options for these sources, like normal stars, cannot be excluded based on the hardness ratio analysis alone. The spectra of CCOs are harder due to their younger age and higher temperature, which is why they can be expected to occupy the same spot as AGNs, pulsars and X-ray binaries in the hardness ratio diagram above. However, since the sources located closest to the SNR centre could be spectrally analysed in more detail in Chapters 4.8.2 and 4.8.3 and

did not fulfil the requirements to be categorised as a CCO candidate, the presence of such an object in Figure 4.24 seems unlikely.

4.10 Discussion

Table 4.10 gives an overview of which analysis steps were performed for each source, respectively, and the resulting source classification. All in all, the presence of a possible CCO is unlikely. Though the absence of variability features in the data does not automatically imply the absence of a NS that could be associated with the SNR, a CCO would be expected to be located in the centre of the SNR. As for G96.0+2.0, there is no X-ray source directly at the estimated centre of the remnant and the characteristics of the three closest sources, #1, #3 and #8, suggest them to be of a different nature than a CCO and, in general, none of the sources could be fitted with a blackbody model with the parameters typical for CCOs.

The best spectral fits with the `mekal` model in the case of sources #1 and #3 clearly classify them as normal stars. This is supported by their negative X-ray-to-optical flux ratios and their position in the hardness ratio diagram (see Figure 4.24). The poor statistics did not allow for a decent spectral fit for source #8, but the X-ray-to-optical flux ratio around -1 indicates a normal star or background AGN nature alike, which are both consistent with the hardness ratio values.[85]

The same accounts for source #9, which shows similar properties. Sources #7, #11 and #13, for which spectral fits could be obtained, show softer spectra, which, together with the best fit being obtained with the `mekal` model, make a normal star nature seem most likely. The same holds true for source #14, for which the `mekal` and the blackbody model were combined and for which a SIMBAD entry supported the classification. Except for sources #2, #4, #5, #10 and #12, which are discussed below, all remaining sources show a low X-ray-to-optical flux ratio and soft nature but not enough statistics to perform a more detailed spectral analysis. Sources #15–19 also seem to be normal stars due to their negative X-ray-to-optical flux ratios combined with the very soft spectra. The counts at higher energies were so low that the higher hardness ratio $HR\,2$ could not even be calculated. Except for source #16, matching entries of stellar objects could be found in the SIMBAD database, too. As opposed to these sources, the hardness ratio analysis of sources #6 and #21 showed them to be harder, with sufficient counts detected in all energy bands considered. Thus, a background AGN nature, which would also be consistent with the X-ray-to-optical flux ratio, seems to be as much possible as a stellar nature. With only the results of the X-ray-to-optical flux ratio analysis given, both options, a background AGN and a stellar nature, also remain for sources #20 and #22.

More can be said about source #2. It also has a low X-ray-to-optical flux ratio, but the spectral fitting, though also possible with the `mekal` model, showed a blackbody spectrum with a temperature and estimated luminosity within the range observed for NSs. As the very soft nature shown in the hardness ratio analysis would also be consistent with middle-aged thermally emitting isolated NSs (Haberl, 2007; Lin et al., 2012), it seems that the optical counterpart found for this source might not actually

[85] The values would also suggest a normal galaxy nature, but this option was considered less likely for all sources as G96.0+2.0 is located in the Galactic plane and, thus, faint background objects can be expected to be unobservable due to absorption.

Table 4.10: Summary of the analysis of the point sources in the G96.0+2.0 FOV. For each source the analysis steps which were executed as well as the resulting source classification are given.

Source ID	spectral fitting	X-ray/optical flux ratio	hardness ratio	SIMBAD entry	proposed source type(s)
1	✓	✓	✓	–	normal star
2	✓	✓	✓	✓	neutron star[1], normal star
3	✓	✓	✓	–	normal star
4	✓	–	✓	–	background AGN[2], rotation-powered pulsar[3], X-ray binary[4]
5	✓	–	✓	–	rotation-powered pulsar[5]
6	–	✓	✓	–	normal star, background AGN
7	✓	✓	✓	–	normal star
8	–	✓	✓	–	normal star, background AGN
9	–	✓	✓	–	normal star, background AGN
10	–	–	✓	–	late-type star, background AGN[2], rotation-powered pulsar[3], X-ray binary[6]
11	✓	✓	✓	–	normal star
12	–	–	✓	–	late-type star, background AGN[2], rotation-powered pulsar[3], X-ray binary[4]
13	✓	✓	✓	–	normal star
14	✓	✓	–	✓	normal star
15	–	✓	✓	✓	normal star
16	–	✓	✓	–	normal star
17	–	✓	✓	✓	normal star
18	–	✓	✓	✓	normal star
19	–	✓	✓	✓	normal star
20	–	✓	–	–	normal star, background AGN
21	–	✓	✓	–	normal star, background AGN
22	–	✓	–	–	normal star, background AGN

[1] assuming the detected optical counterpart is not actually associated with the X-ray source
[2] assuming the optical emission is obscured
[3] assuming the beam of pulsed X-ray and radio emission does not cross our line-of-sight
[4] assuming variability on longer timescales and an obscured optical counterpart
[5] reinforced by the presence of a radio counterpart
[6] assuming variability on longer timescales and either an obscured optical counterpart or an association with sources #13 and/or #17

be related to it and the low X-ray-to-optical flux ratio is only due to a mismatch. A better positional accuracy could be achieved with a follow-up observation with Chandra (Doroshenko et al., 2019) to ascertain whether or not the optical and X-ray emission originate from one and the same source.

As for the four sources for which no potential optical counterpart could be found at all, only #4 and #5 had high enough statistics for spectral fitting. For sources #10 and #12 only the hardness ratios could be obtained, which show large error bars and, thus, any assumptions with respect to the nature of the sources, e.g. optically faint late-type stars, AGNs with an obscured optical counterpart, binaries with a faint optical companion or pulsars with a beam out of our line of sight, can only be made vaguely. The overlap of the extraction region (with ∼90% of the source energy) of source #10 with those of sources #13 and #17 (see Figure 4.10) might hint at a binary scenario with the optical counterpart being detected for the latter sources. This could be supported by further observations to investigate variability on longer time scales.

A more precise analysis could be done for sources #4 and #5. The best fit with a power law with a photon index of $1.34\,(+1.06/-0.86)$ in the case of source #4 is compatible with the source being a background AGN or a young pulsar. In the first case an optical counterpart would be expected whereas in the latter case there is no pulsation to support the classification and, also, a cross-correlation with the NVSS catalogue did not result in a match with a potential radio counterpart. That a blackbody model also leads to an acceptable fit makes it even hard to tell for sure whether the emission is of thermal or non-thermal origin and a combination of both could not be reinforced by a successful fit with a combination of the two model components. It might be possible for the source to be a pulsar whose pulsing beam, both in radio and in X-rays, does not cross our line of sight so that we also do not see the thermal emission from the hotter surface near the magnetic poles, as described by e.g. Greenstein & Hartke (1983) and De Luca et al. (2005), but a dominating synchrotron emission. The hard nature of the source also leaves an X-ray binary with an obscured optical emission as an option. In this case, again, variability on longer time scales could give more insight.

The best prospect for a confirmation of a NS nature, however, offers source #5. It also does not have an optical counterpart but is the only one of the 22 detected X-ray point sources which has a radio counterpart, as was derived from the cross-match with the NVSS catalogue (source designation: NVSS J213200+535726) and as shown in Figure 4.25. The hardness of the X-ray spectrum and the estimated luminosity following from the fit with a blackbody model also do not contradict a possible NS nature, though both, either a thermal or a non-thermal fit, were possible. Unfortunately, source #5 is located at the border of the SNR and was only covered by the two MOS detectors but not the pn detector, which would have allowed for a better time resolution. No indications of pulsation could be found in the MOS data, as Figures 4.26 and B.6 illustrate with the Z^2_m test for the second and first harmonics, respectively. But with these detectors the timing analysis could only be performed down to periods of 5.2 s, which means that there is a great chance the pulsing signal of a possible pulsar cannot be resolved. Follow-up observations, both in X-rays and in the radio band, would make a search for pulsations at lower periods possible and could, thus, give enough evidence to characterize the source as a NS that could potentially be associated with the SNR.

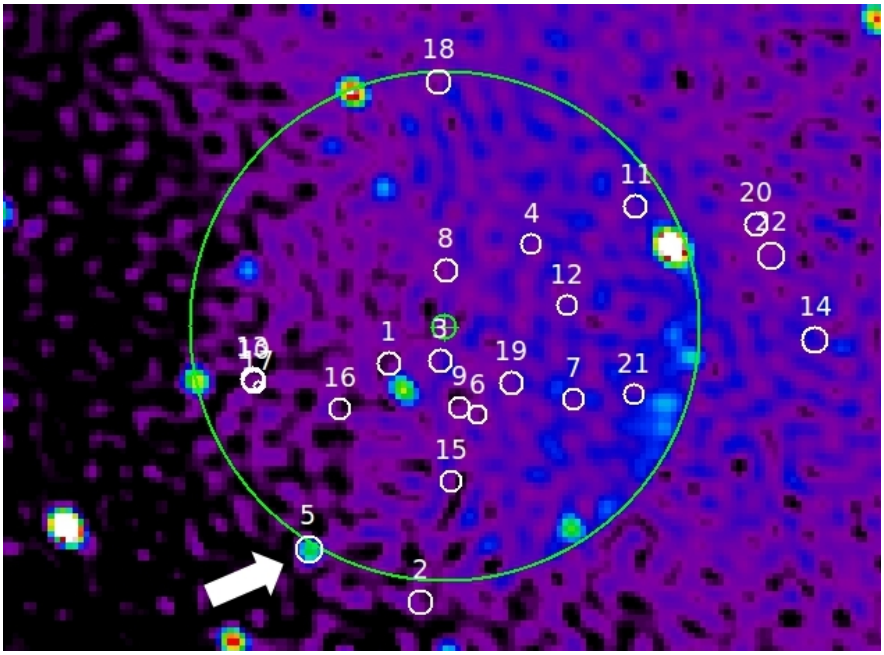

Figure 4.25: Radio image of G96.0+2.0 with the detected X-ray sources. Again, the white circles encompass ∼90% of the source energy in X-rays, the numeric tags correspond to the source IDs in the final source list and the green circle marks the assumed outer boundary of the SNR with the centre being located at the position of the green cross hairs pointer. (The radio image was taken from the CGPS, available at `http://www.cadc-ccda.hia-iha.nrc-cnrc.gc.ca/en/cgps/`.)

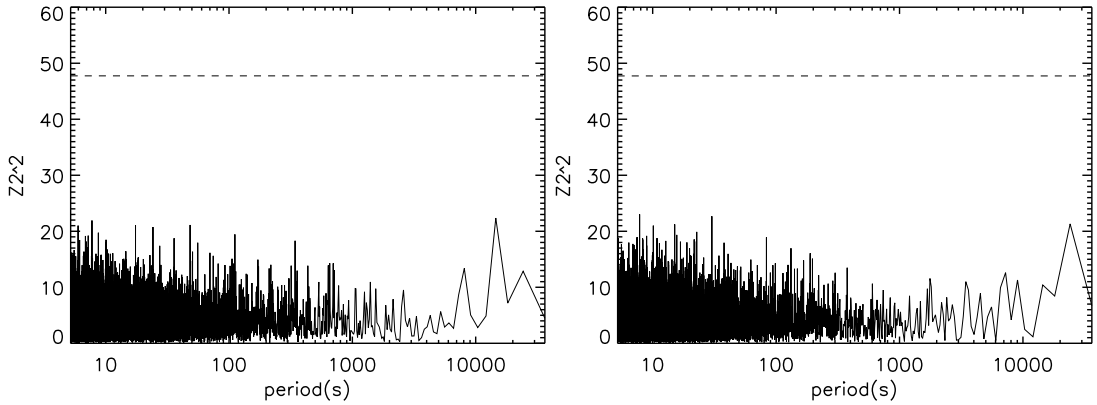

Figure 4.26: Z_m^2 test with two harmonics for source #5 based on the MOS data (left: MOS1, right: MOS2). The dashed lines indicate the 5σ significance level.

CHAPTER 5

Summary and Outlook

In the scope of this thesis, two topics related to XMM-Newton were focussed on. The first one concerns the improvement of the on-axis effective area calibration of the three cameras constituting the XMM EPIC because discrepancies in the source flux derived with each of them separately showed their effective area calibration requires a re-alignment. For this purpose, the CORRAREA tool by Guainazzi et al. (2014), which has been a non-default option in the XMM SAS for users so far, was revised and developed further in this work. It is a current priority issue of the XMM calibration team at ESAC to provide the users with a default correction of the effective area calibration uncertainties, to which the outcome of this work largely contributes. The second topic presented in this thesis concerns the analysis of an XMM observation of the SNR G96.0+2.0 to search for a compact object, with a focus on NSs, that can be associated with this SNR with the aim of increasing the number of known SNR–NS–pairs and, potentially, even find a CCO, which is considered to be a virtually ideal object to study the equation of state of superdense matter. The conducted steps, obtained results and the future outlook for the two topics are summarized in the following two sections.

5.1 Status and Future Prospects of CORRAREA

Since CORRAREA has not been considered to be fully validated and, thus, to not be sufficiently reliable and suitable to be used for a default correction of scientific data, it has originally only been implemented in the XMM SAS as a non-default option for estimation purposes. The tool applies an energy-dependent correction factor to the data, based on a correction function that is empirically determined from the MOS-to-pn residual ratio obtained with stacked spectra of selected sources according to the *stack and fit* approach. With the final aim in mind to make CORRAREA a tool for a default correction of the on-axis effective area, the procedure to determine the correction function was revised and recalibrated in the scope of this work, together with an automation of the required steps as far as practicable.

The stacking process executed by the developed automation scripts was first validated by reproducing the approximate correction function of the original, already implemented CORRAREA version. Regarding the procedure to determine the correction function, different aspects were revised for the recalibration and the either new or changed steps were implemented into the script package (with the exception of steps concerning manual screening). The revision and recalibration involved the following aspects. First, a new approach to select GTIs was applied to allow for an exclusion of periods with high solar proton flare background individually adjusted to each observation. Second, the selection criteria were revised, mainly to include all imaging modes and filter

types, and applied to an updated, considerably extended version of the *XMM-Newton Serendipitous Source Catalogue*. The images of all 344 selected sources were manually screened, next, to examine their suitability for use. 82 sources were excluded, mostly due to extended emission or crowded fields being present around the source, either chip gaps or bad columns located close to the source or the source being positioned too far from the on-axis position despite the according selection criterion being set before. Also, new, individual background regions were defined for each exposure, mainly to account for instrument specifics and the science mode used, and the maximum source extraction radius that might be used for each source in the sample was determined (for each of the two detector types, respectively). Last but not least, a new method to evaluate the presence of pile-up in each exposure was implemented into the procedure, making use of the MOS diagonal patterns amongst other things. All in all, a sample of 163 pile-up free sources suitable to be used for the Corrarea correction was defined in the course of this work.

Besides this recalibration with a revision of certain steps, also different analyses were conducted to validate the applicability of the correction:

- A comparison of the results for different filters, particularly to justify the inclusion of thick filter observations, could not be done since no sufficient number of observations with only the thick filters in use was available. However, the overall small number of thick filter uses in the sample made any substantial influence of the thick filters on the obtained correction functions seem unlikely.

- A comparison of the MOS-to-pn residual ratios for different source extraction radii was done to examine whether or not the determined individual maximum source region radii might be used for each source instead of a common radius. The analysis showed a small but systematic difference between the residual ratios obtained for the different radii. This difference could be largely ascribed to the PSF calibration, which was improved at ESAC at the time.

- The new, recalibrated PSF calibration files created at ESAC were successfully tested in the scope of this work using the developed script package to provide an independent validation.

- A comparison of the residual ratios obtained with the different science modes involved mainly showed deviations at energies above 7 keV. By stacking the spectra of sources observed in different science modes, an uncommonly high residual ratio was discovered, revealing a problem of the original stacking method with respect to the combination of different modes, most likely due to an incorrect weighting of the response files.

- Using only FF mode observations from the pile-up free sample assembled here, recalibrated correction functions for MOS1 and MOS2 (since pn served as the reference instrument for the cross-calibration) were determined with the revised, largely automated procedure presented in this work. It was successfully shown that the new correction functions reduce the inconsistencies that are noticeable when comparing the source fluxes obtained with the three EPIC cameras, respectively, and they may be used as a recalibrated update for the original non-default Corrarea correction.

Currently the *fit and stack* approach is implemented into the routine as an alternative option at the *Institute for Astronomy and Astrophysics Tübingen* (IAAT) in collaboration with the ESAC.[86] This will allow for a new comparison of the two stacking approaches with the changes that were introduced in this work with respect to the original procedure. Depending on the final choice of which approach to stick to, either the higher systematic errors expected to be introduced with the *fit and stack* approach and its reliability at higher energies (which might be problematic because of negative spectral bins that can result from background subtraction in the case of low statistics) need to be examined or the weighting of the response files in the *stack and fit* approach has to be adjusted to be able to combine sources observed with different imaging modes. In both cases, the outcomes obtained for each science mode separately have to be compared again and before different modes are combined to determine further refined correction functions it has to be ensured that the applicability of a correction function on scientific observations is mode-independent. Besides an analysis of the mode dependency, two more validation steps are strongly recommended before finally switching to a default usage of Corrarea. First, a renewed comparison of the results for different source extraction radii should be done since the new PSF calibration files which were tested in the scope of this work have been implemented into the set of public calibration files. Second, it has to be ensured that a correction function potentially suitable for the default correction does not introduce any new features to spectral data. The script package developed for automation as part of this work significantly eases these follow-up tasks as well as any future updates. Also, the source sample presented here is sufficiently large for the default correction to be based on it and the required, more time-intensive manual screening steps as described in this work could be concluded.

The presentation of this work at various meetings, particularly the XMM calibration meetings and the meetings of the IACHEC (International Astronomical Consortium for High Energy Calibration), captured the interest of the community. The continuation of the project is actively pursued with an ongoing collaboration of the IAAT and the ESAC and the potential is seen to include other X-ray satellite missions in the effective area cross-calibration with the methods applied here.

5.2 The Study of G96.0+2.0

To search for a compact object associated with G96.0+2.0, the first X-ray observation of the SNR, which was obtained with XMM-Newton, was analysed in the scope of this work. After the initial data processing, a search for X-ray point sources in the 0.4–3.0 keV band was conducted, leading to 22 detections. For all point sources, optical counterparts were searched for. To do so, the source positions determined in X-rays were astrometrically corrected, first. The required systematic position offsets were determined by making use of the positions of optical sources observed with the OM and comparing them with entries of optical sources in the USNO-B1.0 catalogue. Using the CDS X-Match service, the corrected positions of the detected X-ray sources were then cross-matched with several optical and near-infrared catalogues. Potential counterparts were found for all but four sources.

[86] At the time of publication of this work, a new, updated non-default Corrarea version had been released, based on the further developed script package including the *fit and stack* approach and making use of the source sample presented here (Smith et al., 2021).

Next, the spectral fitting and timing analyses were performed for all sources, followed by an analysis of the X-ray-to-optical flux ratios and the hardness ratios. No pulsations or irregular variability could be detected. In the course of the analysis of the spectral properties, most sources could be identified as a normal star or as being either a normal star or a background AGN. In summary, no obvious indication of the presence of a NS could be found in the XMM observation of G96.0+2.0. The possibility of the SNR having an associated CCO could be excluded altogether. However, while no definite classification of a source as a NS was possible based on the observation and most detected point sources could be ruled out as potential NS candidates, five sources were identified which are worth further analysis with respect to a NS nature and their potential association with the SNR.

The sources tagged #10 and #12 in this thesis lacked optical counterparts but their statistics did not allow for a more detailed analysis so that a longer observation or an observation with more sensitive instruments, like the ones provided by the future ATHENA mission, would be required for a classification. But the analysis of sources #2, #4 and particularly #5 showed these sources to be far more promising. A potential optical counterpart was found for source #2 and the spectrum was found to be of thermal origin, with both a hot diffuse gas emission model (`mekal`) and a blackbody model leading to acceptable fits. The derived physical parameters left both a normal, hot star nature and a neutron star nature open as options, the latter on the assumption of a mismatched optical counterpart. In this case, a follow-up observation with a higher positional accuracy, for example with Chandra, could help to verify or dismiss the corresponding optical source as an actual counterpart. As for source #4, the best fit was obtained with a power law model and the best fit parameters suggested a background AGN nature and a young, rotation-powered pulsar alike. However, an acceptable fit was also achieved with a blackbody model and, with the spectrum being rather hard, also an X-ray binary nature has to be considered. The missing of both an optical and a radio counterpart as well as the lack of any sign of variability complicated a more concrete classification. However, source #5 was shown to meet several characteristics expected from a NS without contradiction and its confirmation as the compact object associated with G96.0+2.0 would automatically dismiss the other potential candidates identified in this work. Its best fit was obtained with a blackbody model with the physical parameters derived from it suggesting a compact object, most likely a rotation-powered pulsar, at the distance of the SNR. To support this classification, which was also consistent with the hardness ratio analysis, source #5 was found to be the only source in the FOV with a radio counterpart while at the same time lacking an optical counterpart. Since the source was not covered by the pn detector, the observation did not provide the full timing capabilities of XMM-Newton in this case and a good chance remains to detect pulsations below a few seconds with a follow-up observation with XMM (possibly combined with radio observations) specifically targeting source #5. If pulsations below a few seconds are revealed, it will be an unambiguous evidence for a NS nature of this promising candidate identified here. A following detailed study of the object may then profit from an implemented default correction of the XMM on-axis effective area calibration based on the work presented in the first part of this thesis.

Glossary

2MASS	Two Micron All Sky Survey
ACIS	Advanced CCD Imaging Spectrometer
AGN	Active Galactic Nucleus
ARF	Ancilliary Response File
ASCA	Advanced Satellite for Cosmology and Astrophysics
ATHENA	Advanced Telescope for High-Energy Astrophysics
AXP	Anomalous X-Ray Pulsar
BH	Black Hole
CADC	Canadian Astronomy Data Centre
CCD	Charge Coupled Device
CCF	Current Calibration File
CCO	Central Compact Object
CDS	Centre de Données Astronomiques de Strasbourg (Strasbourg Astronomical Data Center)
CGPS	Canadian Galactic Plane Survey
CIF	Calibration Index File
CTI	Charge Transfer Inefficiency
Dec	Declination
DR	Data Release
DSS	Digitized Sky Survey
EPIC	European Photon Imaging Camera
eRosita	Extended Roentgen Survey with an Imaging Telescope Array
ESA	European Space Agency
ESAC	European Space Astronomy Centre
ESAS	Extended Source Analysis Software
ESOC	European Space Operations Centre
FF	Full Frame
FITS	Flexible Image Transport System
FOV	Field Of View
GTI	Good Time Interval
GSC	Guide Star Catalog
HEAsoft	High Energy Astrophysics Software
HMXB	High-Mass X-ray Binary
IAAT	Institute for Astronomy and Astrophysics Tübingen
IACHEC	International Astronomical Consortium for High Energy Calibration
ID	Identifier
IR	Infrared
LMXB	Low-Mass X-ray Binary
LW	Large Window

MOC	Mission Operations Centre
MOS	Metal Oxide Semiconductor
N	Number
NASA	National Aeronautics and Space Administration
NRAO	National Radio Astronomy Observatory
NS	Neutron Star
NVSS	NRAO (National Radio Astronomy Observatory) VLA (Very Large Array) Sky Survey
ODF	Observation Data File
OM	Optical Monitor
OoT	Out of Time
PPS	Pipeline Processing Subsystem
PSF	Point Spread Function
PWN	Pulsar Wind Nebula
RA	Right Ascension
RGS	Reflection Grating Spectrometer
RMF	Response Matrix File
ROSAT	Röntgensatellit
SAS	Science Analysis System
SDSS	Sloan Digital Sky Survey
SGR	Soft Gamma Repeater
SIMBAD	Set of Identifications, Measurements and Bibliography for Astronomical Data
SN	Supernova
SNR	Supernova Remnant
S/N	Signal-to-Noise Ratio
SOC	Science Operations Centre
SRG	Spectrum-Roentgen-Gamma
STScI	Space Telescope Science Institute
SW	Small Window
USNO	United States Naval Observatory
V	Visual
VLA	Very Large Array
WebPIMMS	Online Version of the Portable, Interactive Multi-Mission Simulator
WD	White Dwarf
WFI	Wide Field Imager
WISE	Wide-Field Infrared Survey Explorer
XDINS	X-ray Dim Isolated Neutron Star
XMM	X-ray Multi-Mirror
Xspec	X-Ray Spectral Fitting Package

A	fraction of the emitting area on a neutron star surface
c	speed of light in vacuum
$\mathcal{C}$	CORRAREA correction function
d	distance
$d_{\mathbf{a}}$	angular diameter distance
d_{10}	distance in units of 10 kpc

dof	degrees of freedom
$\mathbf{e}^-$	electron
E	energy
f	fraction of mass available for nuclear fusion
$f_{\mathbf{opt}}$	optical flux
$f_{\mathbf{x}}$	X-ray flux
$\mathcal{F}_{\mathtt{bb}}$	function of the blackbody model
$\mathcal{F}_{\mathtt{phabs}}$	function of the photoelectric absorption model `phabs`
$\mathcal{F}_{\mathtt{pow}}$	function of the powerlaw model
g	surface gravity acceleration
G	gravitational constant
H	count rate in the hard energy band
HR	hardness ratio
i	index for photons
j	index for the MOS cameras
k	index for harmonics
$k_{\mathbf{B}}$	Boltzmann constant
$K_{\mathtt{atm}}$	normalization parameter of the neutron star atmosphere models
$K_{\mathtt{bb}}$	normalization parameter of the blackbody model
$K_{\mathtt{mekal}}$	normalization parameter of the mekal model
$K_{\mathtt{pow}}$	normalization parameter of the powerlaw model
L	luminosity
L_{39}	luminosity in units of $10^{39}\,\mathrm{erg\,s^{-1}}$
$\mathcal{L}$	likelihood
m	number of harmonics
$m_{\mathbf{v}}$	apparent visual magnitude
M	mass of an astronomical object
$\mathbf{n}$	neutron
n	number of photons
$n_{\mathbf{e}}$	electron density
$n_{\mathbf{H}}$	hydrogen density
$N_{\mathbf{H}}$	hydrogen column density
nR^2	Rayleigh power
$\mathbf{p}$	proton
p	probability
pdf	probability density function
P	pressure
r	distance to the centre of a star
$r_{\mathbf{extr}}$	extraction radius
R	radius of an astronomical object
$\mathcal{R}$	residual ratio
S	count rate in the soft energy band
t_0	arrival time of the first photon
t	arrival time of a photon
Δt	difference between the arrival time of a photon and the arrival time of the first photon
T	effective temperature

V	volume
z	redshift
Z	atomic number
Z_m^2	statistical probability variable of the so-called Z_m^2 test
Z_2^2	statistical probability variable of the Z_m^2 test for two harmonics
α	best fit parameter of the CORRAREA correction function
β	best fit parameter of the CORRAREA correction function
γ	best fit parameter of the CORRAREA correction function
Γ	photon index of the power law model
δ	best fit parameter of the CORRAREA correction function
$\Delta\alpha$	right ascension offset
$\Delta\delta$	declination offset
ε	mass energy released by fusion
$\theta_{\mathbf{c}}$	critical incidence angle
μ	mean value
ν	pulse frequency
$\nu_{\mathbf{e}}$	electron neutrino
$\nu_{\mathbf{max}}$	maximum frequency in a signal
$\nu_{\mathbf{Nyquist}}$	Nyquist frequency
$\nu_{\mathbf{sampling}}$	sampling frequency
ρ	density
σ	standard deviation
$\sigma_{\mathbf{cat}}$	source catalogue position error
$\sigma_{\mathbf{list}}$	source list position error
$\sigma_{\mathbf{stat}}$	statistical position error
$\sigma_{\mathbf{sys}}$	systematic position error
$\sigma_{\mathbf{tot}}$	total position error
$\sigma_{\mathbf{x}}$	photoelectric cross-section
$\tau_{\mathbf{ms}}$	timescale for a star to be on the main sequence
$\tau_{\mathbf{nuc}}$	nuclear timescale
ϕ	phase value in the interval 0 to 1 for the photon arrival time
$\chi^2_{\mathbf{red}}$	reduced chi-squared for goodness of fit testing

Bibliography

Alam, S.; Albareti, F.D.; Allende Prieto, C.; Anders, F.; Anderson, S.F.; et al. (2015): The Eleventh and Twelfth Data Releases of the Sloan Digital Sky Survey: Final Data from SDSS-III, *The Astrophysical Journal Supplement Series*, 219:12.

Ananna, T.T.; Treister, E.; Urry, C.M.; Ricci, C.; Hickox, R.C.; et al. (2020): Accretion History of AGNs. II. Constraints on AGN Spectral Parameters Using the Cosmic X-Ray Background, *The Astrophysical Journal*, 889(1):17.

Arnaud, K.; Gordon, G.; Dorman, B. (2018): "Xspec - An X-Ray Spectral Fitting Package: User's Guide for Version 12.10.1".

Arnaud, K.; Smith, R.; Siemiginowska, A. (2011): Handbook of X-ray Astronomy, *Cambridge University Press*.

Arnaud, K.A. (1996): XSPEC: The First Ten Years. In: G.H. Jacoby; J. Barnes (eds), Astronomical Data Analysis Software and Systems V, vol. 101 of the *Astronomical Society of the Pacific Conference Series*, p. 17.

Baade, W.; Zwicky, F. (1934): Cosmic Rays from Super-Novae, *Proceedings of the National Academy of Science*, 20(5):259–263.

Balucinska-Church, M.; McCammon, D. (1992): Photoelectric Absorption Cross Sections with Variable Abundances, *The Astrophysical Journal*, 400:699.

Becker, W. (2009): X-Ray Emission from Pulsars and Neutron Stars. In: W. Becker (ed.), Astrophysics and Space Science Library, vol. 357 of the *Astrophysics and Space Science Library*, *Springer*, pp. 91–140.

Bendat, J.; Piersol, A. (2010): Random Data: Analysis and Measurement Procedures. Wiley Series in Probability and Statistics, *Wiley*.

Beznogov, M.V.; Yakovlev, D.G. (2015): Statistical Theory of Thermal Evolution of Neutron Stars - II. Limitations on Direct Urca Threshold, *Monthly Notices of the Royal Astronomical Society*, 452(1):540–548.

Bischoff-Kim, A.; Provencal, J.L.; Bradley, P.A.; Montgomery, M.H.; ... Heinitz, C. ...; et al. (2019): GD358: Three Decades of Observations for the In-depth Asteroseismology of a DBV Star, *The Astrophysical Journal*, 871(1):13.

Blackburn, J.K. (1995): FTOOLS: A FITS Data Processing and Analysis Software Package. In: R.A. Shaw; H.E. Payne; J.J.E. Hayes (eds), Astronomical Data Analysis Software and Systems IV, vol. 77 of the *Astronomical Society of the Pacific Conference Series*, pp. 367–370.

Braun, C.; Safi-Harb, S.; Fryer, C.L. (2019): Progenitors and Explosion Properties of Supernova Remnants Hosting Central Compact Objects: I. RCW 103 Associated with the Peculiar Source 1E 161348-5055, *Monthly Notices of the Royal Astronomical Society*, 489(3):4444–4463.

Brazier, K.T.S. (1994): Confidence Intervals from the Rayleigh Test, *Monthly Notices of the Royal Astronomical Society*, 268:709.

Briel, U.G.; Aschenbach, B.; Balasini, M.; Braeuninger, H.W.; Burkert, W.; et al. (2000): In-Orbit Performance of the EPIC-PN CCD Camera on Board XMM-Newton. In: J.E. Truemper; B. Aschenbach (eds), X-Ray Optics, Instruments, and Missions III, vol. 4012 of the *Society of Photo-Optical Instrumentation Engineers (SPIE) Conference Series*, pp. 154–164.

Brunner, H.; Cappelluti, N.; Hasinger, G.; Barcons, X.; Fabian, A.C.; et al. (2008): XMM-Newton Observations of the Lockman Hole: X-Ray Source Catalogue and Number Counts, *Astronomy & Astrophysics*, 479(1):283–300.

Buccheri, R. (1988): The Problem of Period Detection in Sources of Hard Gamma-Ray Emission, *Space Science Reviews*, 49:197–206.

Buccheri, R.; Bennett, K.; Bignami, G.F.; Bloemen, J.B.G.M.; Boriakoff, V.; et al. (1983): Search for Pulsed Gamma-Ray Emission from Radio Pulsars in the COS-B Data, *Astronomy & Astrophysics*, 128:245–251.

Carter, J.A.; Read, A.M. (2007): The XMM-Newton EPIC Background and the Production of Background Blank Sky Event Files, *Astronomy & Astrophysics*, 464:1155–1166.

Chadwick, J. (1932): Possible Existence of a Neutron, *Nature*, 129:312.

Chandrasekhar, S. (1931): The Maximum Mass of Ideal White Dwarfs, *The Astrophysical Journal*, 74:81.

Condon, J.J.; Cotton, W.D.; Greisen, E.W.; Yin, Q.F.; Perley, R.A.; et al. (1998): The NRAO VLA Sky Survey, *The Astronomical Journal*, 115:1693–1716.

Cutri, R.M.; Skrutskie, M.F.; van Dyk, S.; Beichman, C.A.; Carpenter, J.M.; et al. (2003): VizieR Online Data Catalog: 2MASS All-Sky Catalog of Point Sources (Cutri+ 2003), *VizieR Online Data Catalog*, II/246.

Cutri, R.M.; et al. (2014): VizieR Online Data Catalog: AllWISE Data Release (Cutri+ 2013), *VizieR Online Data Catalog*, II/328.

De Luca, A. (2008): Central Compact Objects in Supernova Remnants. In: C. Bassa; Z. Wang; A. Cumming; V.M. Kaspi (eds), 40 Years of Pulsars: Millisecond Pulsars, Magnetars and More, vol. 983 of the *American Institute of Physics Conference Series*, pp. 311–319.

De Luca, A. (2017): Central Compact Objects in Supernova Remnants. In: International Conference Physics of Neutron Stars - 2017. 50 years after., vol. 932 of the *Journal of Physics Conference Series*, p. 012006.

De Luca, A.; Caraveo, P.A.; Mereghetti, S.; Negroni, M.; Bignami, G.F. (2005): On the Polar Caps of the Three Musketeers, *The Astrophysical Journal*, 623(2):1051–1069.

De Luca, A.; Caraveo, P.A.; Mereghetti, S.; Tiengo, A.; Bignami, G.F. (2006): A Long-Period, Violently Variable X-ray Source in a Young Supernova Remnant, *Science*, 313(5788):814–817.

De Luca, A.; Molendi, S. (2004): The 2-8 keV Cosmic X-Ray Background Spectrum as Observed with XMM-Newton, *Astronomy & Astrophysics*, 419:837–848.

Den Herder, J.W.; Brinkman, A.C.; Kahn, S.M.; Brand uardi-Raymont, G.; Thomsen, K.; et al. (2001): The Reflection Grating Spectrometer on Board XMM-Newton, *Astronomy & Astrophysics*, 365:L7–L17.

Dennerl, K.; Briel, U.G.; Haberl, F.; Hartner, G.D.; Krause, N.; et al. (1999): Determination and Correction of the Charge Transfer Efficiency of the pn-CCD Camera. In: O.H. Siegmund; K.A. Flanagan (eds), EUV, X-Ray, and Gamma-Ray Instrumentation for Astronomy X, vol. 3765 of the *Proceedings of the Society of Photo-Optical Instrumentation Engineers (SPIE)*, pp. 232–243.

Dorman, B.; Arnaud, K.A. (2001): Redesign and Reimplementation of XSPEC. In: J. Harnden F. R.; F.A. Primini; H.E. Payne (eds), Astronomical Data Analysis Software and Systems X, vol. 238 of the *Astronomical Society of the Pacific Conference Series*, p. 415.

Doroshenko, V.; Malyshev, D.; Pühlhofer, G.; Dincel, B.; Sasaki, M.; et al. (2019): XMM-Newton and Fermi/LAT View on the Supernova Remnant 3C434.1, *Astronomy & Astrophysics*, 631:A179.

Doroshenko, V.; Suleimanov, V.; Santangelo, A. (2018): CXOU J160103.1-513353: Another Central Compact Object with a Carbon Atmosphere?, *Astronomy & Astrophysics*, 618:A76.

Ducci, L.; Kavanagh, P.J.; Sasaki, M.; Koribalski, B.S. (2014): XMM-Newton Observation of the Interacting Galaxies NGC 1512 and NGC 1510, *Astronomy & Astrophysics*, 566:A115.

ESA: XMM-Newton SOC (2018)a: "Users Guide to the XMM-Newton Science Analysis System", issue 14.0.

ESA: XMM-Newton SOC (2018)b: "XMM-Newton Users Handbook", issue 2.16.

Friedman, H.; Lichtman, S.W.; Byram, E.T. (1951): Photon Counter Measurements of Solar X-Rays and Extreme Ultraviolet Light, *Physical Review*, 83(5):1025–1030.

Gaia Collaboration; Brown, A.G.A.; Vallenari, A.; Prusti, T.; de Bruijne, J.H.J.; et al. (2018): Gaia Data Release 2. Summary of the Contents and Survey Properties, *Astronomy & Astrophysics*, 616:A1.

Gaia Collaboration; Prusti, T.; de Bruijne, J.H.J.; Brown, A.G.A.; Vallenari, A.; et al. (2016): The Gaia Mission, *Astronomy & Astrophysics*, 595:A1.

Gendreau, K.C.; Arzoumanian, Z.; Okajima, T. (2012): The Neutron Star Interior Composition ExploreR (NICER): an Explorer Mission of Opportunity for Soft X-Ray Timing Spectroscopy. In: T. Takahashi; S.S. Murray; J.W. den Herder (eds), Space Telescopes and Instrumentation 2012: Ultraviolet to Gamma Ray, vol. 8443 of the *Proceedings of the Society of Photo-Optical Instrumentation Engineers (SPIE)*, 844313.

Giacconi, R. (2003): Nobel Lecture: The Dawn of X-Ray Astronomy, *Reviews of Modern Physics*, 75(3):995–1010.

Giacconi, R.; Branduardi, G.; Briel, U.; Epstein, A.; Fabricant, D.; et al. (1979): The Einstein (HEAO 2) X-Ray Observatory., *The Astrophysical Journal*, 230:540–550.

Giacconi, R.; Gursky, H.; Paolini, F.R.; Rossi, B.B. (1962): Evidence for X Rays From Sources Outside the Solar System, *Physical Review Letter*, 9(11):439–443.

Giacconi, R.; Gursky, H.; Waters, J.R. (1964): Two Sources of Cosmic X-Rays in Scorpius and Sagittarius, *Nature*, 204(4962):981–982.

Giacconi, R.; Reidy, W.P.; Vaiana, G.S.; van Speybroeck, L.P.; Zehnpfennig, T.F. (1969): Grazing-Incidence Telescopes for X-Ray Astronomy, *Space Science Reviews*, 9:3–57.

Gold, T. (1968): Rotating Neutron Stars as the Origin of the Pulsating Radio Sources, *Nature*, 218(5143):731–732.

Gold, T. (1969): Rotating Neutron Stars and the Nature of Pulsars, *Nature*, 221(5175):25–27.

Gondoin, P.; Aschenbach, B.R.; Beijersbergen, M.W.; Egger, R.; Jansen, F.A.; et al. (1998): Calibration of the First XMM Flight Mirror Module: I. Image Quality. In: R.B. Hoover; A.B. Walker (eds), X-Ray Optics, Instruments, and Missions, vol. 3444 of the *Society of Photo-Optical Instrumentation Engineers (SPIE) Conference Series*, pp. 278–289.

Gotthelf, E.V.; Halpern, J.P. (2018): The First Glitch in a Central Compact Object Pulsar: 1E 1207.4-5209, *The Astrophysical Journal*, 866(2):154.

Gotthelf, E.V.; Halpern, J.P.; Alford, J. (2013): The Spin-Down of PSR J0821-4300 and PSR J1210-5226: Confirmation of Central Compact Objects as Anti-Magnetars, *The Astrophysical Journal*, 765(1):58.

Grant, C.E. (2011): Charge-Coupled Devices. In: Handbook of X-Ray Astronomy, *Cambridge University Press*, pp. 39–58.

Greenstein, G.; Hartke, G.J. (1983): Pulselike Character of Blackbody Radiation from Neutron Stars., *The Astrophysical Journal*, 271:283–293.

Guainazzi, M. (2014): "Instrumental Limits to X-Ray Astronomy Knowledge", presented at the 14th meeting of the High Energy Astrophysics Division.

Guainazzi, M.; Saxton, R.; Stuhlinger, M.; Smith, M.; Freyberg, M.; et al. (2014): "CORRAREA: a New Tool to Estimate the Impact of Effective Area EPIC Inter-Calibration Uncertainties" (XMM-Newton CCF Release Note XMM-CCF-REL-321; previously XMM-CAL-SRN-0321).

Güdel, M. (2009): A Decade of X-ray Astronomy with XMM-Newton, *Astronomy & Astrophysics*, 500(1):595–596.

Haberl, F. (2007): The Magnificent Seven: Magnetic Fields and Surface Temperature Distributions, *Astrophysics and Space Science*, 308(1-4):181–190.

Halpern, J.P.; Gotthelf, E.V. (2010): Spin-Down Measurement of PSR J1852+0040 in Kesteven 79: Central Compact Objects as Anti-Magnetars, *The Astrophysical Journal*, 709(1):436–446.

Hebbar, P.R.; Heinke, C.O.; Ho, W.C.G. (2020): X-Ray Spectral Analysis of the Neutron Star in SNR 1E 0102.2-7219, *Monthly Notices of the Royal Astronomical Society*, 491(2):1585–1599.

Hertzsprung, E. (1911): Über die Verwendung Photographischer Effektiver Wellenlängen zur Bestimmung von Farbenäquivalenten, *Publikationen des Astrophysikalischen Observatoriums zu Potsdam*, 22(63).

Hessels, J.W.T.; Ransom, S.M.; Stairs, I.H.; Freire, P.C.C.; Kaspi, V.M.; et al. (2006): A Radio Pulsar Spinning at 716 Hz, *Science*, 311(5769):1901–1904.

Hewish, A.; Bell, S.J.; Pilkington, J.D.H.; Scott, P.F.; Collins, R.A. (1968): Observation of a Rapidly Pulsating Radio Source, *Nature*, 217(5130):709–713.

Ho, W.C.G.; Heinke, C.O. (2009): A Neutron Star with a Carbon Atmosphere in the Cassiopeia A Supernova Remnant, *Nature*, 462:71–73.

Ho, W.C.G.; Potekhin, A.Y.; Chabrier, G. (2008): Model X-Ray Spectra of Magnetic Neutron Stars with Hydrogen Atmospheres, *The Astrophysical Journal Supplement Series*, 178:102–109.

Hui, C.Y.; Becker, W. (2006): X-Ray Observations of RX J0822-4300 and Puppis-A, *Astronomy & Astrophysics*, 454(2):543–552.

Ishibashi, W.; Courvoisier, T.J.L. (2010): X-ray Power Law Spectra in Active Galactic Nuclei, *Astronomy & Astrophysics*, 512:A58.

Ishida, M.; Tsujimoto, M.; Kohmura, T.; Stuhlinger, M.; Smith, M.; et al. (2011): Cross Spectral Calibration of Suzaku, XMM-Newton, and Chandra with PKS 2155-304 as an Activity of IACHEC, *Publications of the Astronomical Society of Japan*, 63:S657–S668.

Jagoda, N.; Austin, G.; Mickiewicz, S.; Goddard, R. (1972): The UHURU X-Ray Instrument, *IEEE Transactions on Nuclear Science*, 19(1):579.

Jansen, F.; Lumb, D.; Altieri, B.; Clavel, J.; Ehle, M.; et al. (2001): XMM-Newton Observatory. I. The Spacecraft and Operations, *Astronomy & Astrophysics*, 365:L1–L6.

Jethwa, P.; Saxton, R.; Guainazzi, M.; Rodriguez-Pascual, P.; Stuhlinger, M. (2015): When is Pile-Up Important in the XMM-Newton EPIC Cameras?, *Astronomy & Astrophysics*, 581:A104.

Joye, W.A.; Mandel, E. (2003): New Features of SAOImage DS9. In: H.E. Payne; R.I. Jedrzejewski; R.N. Hook (eds), Astronomical Data Analysis Software and Systems XII, vol. 295 of the *Astronomical Society of the Pacific Conference Series*, p. 489.

Kaastra, J.S. (1992): An X-Ray Spectral Code for Optically Thin Plasmas. In: Internal SRON-Leiden Report, updated version 2.0.

Kaastra, J.S.; Mewe, R. (2000): Coronal Plasmas Modeling and the MEKAL code. In: M.A. Bautista; T.R. Kallman; A.K. Pradhan (eds), Atomic Data Needs for X-Ray Astronomy, pp. 161–165.

Kaspi, V.M. (2000): Neutron Star/Supernova Remnant Associations. In: M. Kramer; N. Wex; R. Wielebinski (eds), IAU Colloq. 177: Pulsar Astronomy - 2000 and Beyond, vol. 202 of the *Astronomical Society of the Pacific Conference Series*, p. 485.

Kaspi, V.M.; Beloborodov, A.M. (2017): Magnetars, *Annual Review of Astronomy & Astrophysics*, 55(1):261–301.

Kettula, K.; Nevalainen, J.; Miller, E.D. (2013): Cross-Calibration of Suzaku/XIS and XMM-Newton/EPIC Using Galaxy Clusters, *Astronomy & Astrophysics*, 552:A47.

Klochkov, D.; Pühlhofer, G.; Suleimanov, V.; Simon, S.; Werner, K.; et al. (2013): A Non-Pulsating Neutron Star in the Supernova Remnant HESS J1731-347/G353.6-0.7 with a Carbon Atmosphere, *Astronomy & Astrophysics*, 556:A41.

Klochkov, D.; Suleimanov, V.; Pühlhofer, G.; Yakovlev, D.G.; Santangelo, A.; et al. (2015): The Neutron Star in HESS J1731-347: Central Compact Objects as Laboratories to Study the Equation of State of Superdense Matter, *Astronomy & Astrophysics*, 573:A53.

Klochkov, D.; Suleimanov, V.; Sasaki, M.; Santangelo, A. (2016): Study of a New Central Compact Object: The Neutron Star in the Supernova Remnant G15.9+0.2, *Astronomy & Astrophysics*, 592:L12.

Kothes, R.; Fedotov, K.; Foster, T.J.; Uyaniker, B. (2006): A Catalogue of Galactic Supernova Remnants from the Canadian Galactic Plane Survey. I. Flux Densities, Spectra, and Polarization Characteristics, *Astronomy & Astrophysics*, 457(3):1081–1093.

Kothes, R.; Uyaniker, B.; Reid, R.I. (2005): Two New Perseus Arm Supernova Remnants Discovered in the Canadian Galactic Plane Survey, *Astronomy & Astrophysics*, 444:871–881.

Kuntz, K.D.; Snowden, S.L. (2008): The EPIC-MOS Particle-Induced Background Spectra, *Astronomy & Astrophysics*, 478:575–596.

Landau, L.D. (1932): To the Stars Theory, *Physikalische Zeitschriften der Sowjetunion*, 1:285.

Large, M.I.; Vaughan, A.E.; Mills, B.Y. (1968): A Pulsar Supernova Association?, *Nature*, 220(5165):340–341.

Lasker, B.M.; Lattanzi, M.G.; McLean, B.J.; Bucciarelli, B.; Drimmel, R.; et al. (2008): The Second-Generation Guide Star Catalog: Description and Properties, *The Astronomical Journal*, 136:735–766.

Lattimer, J.M.; Prakash, M. (2001): Neutron Star Structure and the Equation of State, *The Astrophysical Journal*, 550(1):426–442.

Lattimer, J.M.; Prakash, M. (2004): The Physics of Neutron Stars, *Science*, 304(5670):536–542.

Lattimer, J.M.; Prakash, M. (2007): Neutron Star Observations: Prognosis for Equation of State Constraints, *Physics Report*, 442(1-6):109–165.

Leahy, D.A.; Morsink, S.M.; Chou, Y. (2011): Constraints on the Mass and Radius of the Neutron Star XTE J1807-294, *The Astrophysical Journal*, 742(1):17.

Liedahl, D.A.; Osterheld, A.L.; Goldstein, W.H. (1995): New Calculations of Fe L-shell X-Ray Spectra in High-Temperature Plasmas, *The Astrophysical Journal Letters*, 438:L115–L118.

Lin, D.; Webb, N.A.; Barret, D. (2012): Classification of X-Ray Sources in the XMM-Newton Serendipitous Source Catalog, *The Astrophysical Journal*, 756(1):27.

Longair, M.S. (2011): High Energy Astrophysics, *Cambridge University Press*.

Longinotti, A.L.; de La Calle, I.; Bianchi, S.; Guainazzi, M.; Dovciak, M. (2008): FERO (Finding Extreme Relativistic Objects): Statistics of Relativistic Broad Fe Kalpha Lines in AGN. In: Revista Mexicana de Astronomia y Astrofisica Conference Series, vol. 32 of the *Revista Mexicana de Astronomia y Astrofisica Conference Series*, pp. 62–64.

Lorimer, D.R.; Kramer, M. (2012): Handbook of Pulsar Astronomy, *Cambridge University Press*.

Lumb, D.H.; Schartel, N.; Jansen, F.A. (2012): X-ray Multi-Mirror Mission (XMM-Newton) Observatory, *Optical Engineering*, 51(1):011009-011009-11.

Lyne, A.; Graham-Smith, F. (2012): Pulsar Astronomy, *Cambridge University Press*.

Maccacaro, T.; Gioia, I.M.; Wolter, A.; Zamorani, G.; Stocke, J.T. (1988): The X-Ray Spectra of the Extragalactic Sources in the Einstein Extended Medium Sensitivity Survey, *The Astrophysical Journal*, 326:680–690.

Manchester, R.N.; Hobbs, G.B.; Teoh, A.; Hobbs, M. (2005): The Australia Telescope National Facility Pulsar Catalogue, *The Astronomical Journal*, 129(4):1993–2006.

Mason, K.O.; Breeveld, A.; Much, R.; Carter, M.; Cordova, F.A.; et al. (2001): The XMM-Newton Optical/UV Monitor Telescope, *Astronomy & Astrophysics*, 365:L36–L44.

McGowan, K.E.; Zane, S.; Cropper, M.; Kennea, J.A.; Córdova, F.A.; et al. (2004): XMM-Newton Observations of PSR B1706-44, *The Astrophysical Journal*, 600(1):343–350.

Melrose, D.B.; Rafat, M.Z. (2017): Pulsar Radio Emission Mechanism: Why no Consensus?, *Journal of Physics Conference Series*, 932:012011.

Mereghetti, S. (2008): The Strongest Cosmic Magnets: Soft Gamma-Ray Repeaters and Anomalous X-Ray Pulsars, *The Astronomy & Astrophysics Review*, 15(4):225–287.

Mereghetti, S. (2011): X-Ray Emission from Isolated Neutron Stars, *Astrophysics and Space Science Proceedings*, 21:345–363.

Mereghetti, S. (2013): Pulsars and Magnetars, *Brazilian Journal of Physics*, 43(5-6):356–368.

Mewe, R.; Gronenschild, E.H.B.M.; van den Oord, G.H.J. (1985): Calculated X-radiation from Optically Thin Plasmas. V, *Astronomy & Astrophysics Supplement*, 62:197–254.

Mewe, R.; Lemen, J.R.; van den Oord, G.H.J. (1986): Calculated X-radiation from Optically Thin Plasmas. VI - Improved Calculations for Continuum Emission and Approximation Formulae for Nonrelativistic Average Gaunt Factors, *Astronomy & Astrophysics Supplement*, 65:511–536.

Mohr, P.J.; Newell, D.B.; Taylor, B.N. (2016): CODATA Recommended Values of the Fundamental Physical Constants: 2014, *Reviews of Modern Physics*, 88(3):035009.

Monet, D.G.; Levine, S.E.; Canzian, B.; Ables, H.D.; Bird, A.R.; et al. (2003): The USNO-B Catalog, *The Astronomical Journal*, 125:984–993.

Morsink, S.M.; Leahy, D.A. (2011): Multi-Epoch Analysis of Pulse Shapes from the Neutron Star SAX J1808.4-3658, *The Astrophysical Journal*, 726(1):56.

Morton, D.C. (1964): Neutron Stars as X-Ray Sources, *The Astrophysical Journal*, 140:460.

Mück, B. (2014): Low-Mass X-Ray Binary Studies with XMM-Newton. Dissertation, Eberhard Karls Universität Tübingen.

NASA/GSFC XMM-Newton Guest Observer Facility (2018): "The XMM-Newton ABC Guide: An Introduction to XMM-Newton Data Analysis", version 5.0, 2018.

Natalucci, L. (2013): "Scientific Satellites Cross-Calibration: the IACHEC Activity", presented at the 1st COSPAR Symposium.

Nazé, Y. (2009): Hot Stars Observed by XMM-Newton. I. The Catalog and the Properties of OB Stars, *Astronomy & Astrophysics*, 506:1055–1064.

Ness, J.U.; Parmar, A.N.; Valencic, L.A.; Smith, R.; Loiseau, N.; et al. (2014): XMM-Newton Publication Statistics, *Astronomische Nachrichten*, 335:210.

Nevalainen, J.; David, L.; Guainazzi, M. (2010): Cross-Calibrating X-ray Detectors with Clusters of Galaxies: an IACHEC Study, *Astronomy & Astrophysics*, 523:A22.

Nyquist, H. (1928): Certain Topics in Telegraph Transmission Theory, *Transactions of the American Institute of Electrical Engineers*, 47(2):617–644.

Ofengeim, D.D.; Kaminker, A.D.; Klochkov, D.; Suleimanov, V.; Yakovlev, D.G. (2015): Analysing Neutron Star in HESS J1731-347 from Thermal Emission and Cooling Theory, *Monthly Notices of the Royal Astronomical Society*, 454(3):2668–2676.

Oppenheimer, J.R.; Volkoff, G.M. (1939): On Massive Neutron Cores, *Physical Review*, 55(4):374–381.

Özel, F.; Freire, P. (2016): Masses, Radii, and the Equation of State of Neutron Stars, *Annual Review of Astronomy & Astrophysics*, 54:401–440.

Pacini, F. (1967): Energy Emission from a Neutron Star, *Nature*, 216(5115):567–568.

Pacini, F. (1968): Rotating Neutron Stars, Pulsars and Supernova Remnants, *Nature*, 219(5150):145–146.

Park, T.; Kashyap, V.L.; Siemiginowska, A.; van Dyk, D.A.; Zezas, A.; et al. (2006): Bayesian Estimation of Hardness Ratios: Modeling and Computations, *The Astrophysical Journal*, 652:610–628.

Pavlov, G.G.; Kargaltsev, O.; Wong, J.A.; Garmire, G.P. (2009): Detection of X-Ray Emission from the Very Old Pulsar J0108-1431, *The Astrophysical Journal*, 691(1):458–464.

Pavlov, G.G.; Sanwal, D.; Teter, M.A. (2004): Central Compact Objects in Supernova Remnants. In: F. Camilo; B.M. Gaensler (eds), Young Neutron Stars and Their Environments, vol. 218 of the *International Astronomical Union Symposium*, pp. 239–246.

Pfeffermann, E. (2008): Imaging Proportional Counters. In: J.E. Trümper; G. Hasinger (eds), The Universe in X-Rays, *Springer*, pp. 21–28.

Pietsch, W.; Misanovic, Z.; Haberl, F.; Hatzidimitriou, D.; Ehle, M.; et al. (2004): XMM-Newton Survey of the Local Group Galaxy M33, *Astronomy & Astrophysics*, 426:11–24.

Pineau, F.X.; Motch, C.; Carrera, F.; Della Ceca, R.; Derrière, S.; et al. (2011): Cross-Correlation of the 2XMMi Catalogue with Data Release 7 of the Sloan Digital Sky Survey, *Astronomy & Astrophysics*, 527:A126.

Policarpo, A.J.P.L.; Alves, M.A.F.; Dos Santos, M.C.M.; Carvalho, M.J.T. (1972): Improved Resolution for Low Energies with Gas Proportional Scintillation Counters, *Nuclear Instruments and Methods*, 102(2):337–348.

Popov, S.B.; Kaurov, A.A.; Kaminker, A.D. (2015): Central Compact Objects in Kes 79 and RCW 103 as 'Hidden' Magnetars with Crustal Activity, *Publications of the Astronomical Society of Australia*, 32:e018.

Posselt, B.; Pavlov, G.G. (2018): Upper Limits on the Rapid Cooling of the Central Compact Object in Cas A, *The Astrophysical Journal*, 864(2):135.

Possenti, A.; Cerutti, R.; Colpi, M.; Mereghetti, S. (2002): Re-Examining the X-Ray Versus Spin-Down Luminosity Correlation of Rotation Powered Pulsars, *Astronomy & Astrophysics*, 387:993–1002.

Predehl, P.; Andritschke, R.; Arefiev, V.; Babyshkin, V.; Batanov, O.; et al. (2021): The eROSITA X-Ray Telescope on SRG, *Astronomy & Astrophysics*, 647:A1.

Read, A.M.; Guainazzi, M.; Sembay, S. (2014): Cross-Calibration of the XMM-Newton EPIC pn and MOS On-Axis Effective Areas Using 2XMM Sources, *Astronomy & Astrophysics*, 564:A75.

Rosen, S.R.; Webb, N.A.; Watson, M.G.; Ballet, J.; Barret, D.; et al. (2016): The XMM-Newton Serendipitous Survey. VII. The Third XMM-Newton Serendipitous Source Catalogue, *Astronomy & Astrophysics*, 590:A1.

Russell, H.N. (1914): Relations Between the Spectra and Other Characteristics of the Stars, *Popular Astronomy*, 22:275–294.

Saeedi, S.; Sasaki, M.; Ducci, L. (2016): XMM-Newton Study of the Draco Dwarf Spheroidal Galaxy, *Astronomy & Astrophysics*, 586:A64.

Santangelo, A.; Madonia, R. (2014): Fifty Years of X-Ray Astronomy: A Look Back and Into the (Near) Future, *Astroparticle Physics*, 53:130–151.

Santos-Lleo, M.; Schartel, N.; Tananbaum, H.; Tucker, W.; Weisskopf, M.C. (2009): The First Decade of Science with Chandra and XMM-Newton, *Nature*, 462:997–1004.

Sartore, N.; Tiengo, A.; Mereghetti, S.; De Luca, A.; Turolla, R.; et al. (2012): Spectral Monitoring of RX J1856.5-3754 with XMM-Newton. Analysis of EPIC-pn Data, *Astronomy & Astrophysics*, 541:A66.

Sasaki, M.; Heinitz, C.; Warth, G.; Pühlhofer, G. (2014): XMM-Newton Observation of the Galactic Supernova Remnant W51C (G49.1-0.1), *Astronomy & Astrophysics*, 563:A9.

Saxton, R.D.; Read, A.M.; Esquej, P.; Freyberg, M.J.; Altieri, B.; et al. (2008): The First XMM-Newton Slew Survey Catalogue: XMMSL1, *Astronomy & Astrophysics*, 480:611–622.

Schartel, N.; Jansen, F.; Ward, M.J. (2017): XMM-Newton: Status and Scientific Perspective, *Astronomische Nachrichten*, 338:354–359.

Schellenberger, G.; Reiprich, T.H.; Lovisari, L.; Nevalainen, J.; David, L. (2015): XMM-Newton and Chandra Cross-Calibration Using HIFLUGCS Galaxy Clusters. Systematic Temperature Differences and Cosmological Impact, *Astronomy & Astrophysics*, 575:A30.

Schwartz, D.A. (2011): Optics. In: Handbook of X-Ray Astronomy, *Cambridge University Press*, pp. 6–22.

Sedov, L.I. (1959): Similarity and Dimensional Methods in Mechanics, *Academic Press*.

Seward, F.D.; Charles, P.A. (2010): Exploring the X-Ray Universe, *Cambridge University Press*.

Shannon, C.E. (1949): Communication in the Presence of Noise, *Proceedings of the Institute of Radio Engineers*, 37(1):10–21.

Shklovsky, I.S. (1967): On the Nature of the Source of X-Ray Emission of Sco XR-1, *The Astrophysical Journal Letters*, 148:L1.

Smith, M.J.S.; ex rel. EPIC Consortium (2019): "EPIC Status of Calibration and Data Analysis" (XMM-Newton Calibration Technical Note XMM-SOC-CAL-TN-0018), version 3.12.

Smith, M.J.S.; Pommranz, C.; Heinitz, C.; Stuhlinger, M. (2021): "Update of the CORRAREA Empirical EPIC Effective Area Correction" (XMM-Newton CCF Release Note XMM-CCF-REL-382).

Snowden, S.L.; Kuntz, K.D. (2014): "Cookbook for Analysis Procedures for XMM-Newton EPIC Observations of Extended Objects and the Diffuse Background", version 5.9.

Snowden, S.L.; Mushotzky, R.F.; Kuntz, K.D.; Davis, D.S. (2008): A Catalog of Galaxy Clusters Observed by XMM-Newton, *Astronomy & Astrophysics*, 478:615–658.

Staelin, D.H.; Reifenstein, E.C. (1968): Pulsating Radio Sources Near the Crab Nebula, *Science*, 162(3861):1481–1483.

Staubert, R.; Trümper, J.E. (2008): Overview. In: J.E. Trümper; G. Hasinger (eds), The Universe in X-Rays, *Springer*, pp. 3–4.

Stocke, J.T.; Morris, S.L.; Gioia, I.M.; Maccacaro, T.; Schild, R.; et al. (1991): The Einstein Observatory Extended Medium-Sensitivity Survey. II. The Optical Identifications, *The Astrophysical Journal Supplement Series*, 76:813.

Stocke, J.T.; Wang, Q.D.; Perlman, E.S.; Donahue, M.E.; Schachter, J.F. (1995): Discovery of a Candidate Old, Isolated Neutron Star in the Field of a Galactic Cirrus Cloud, *The Astronomical Journal*, 109:1199.

Strüder, L.; Briel, U.; Dennerl, K.; Hartmann, R.; Kendziorra, E.; et al. (2001): The European Photon Imaging Camera on XMM-Newton: The pn-CCD Camera, *Astronomy & Astrophysics*, 365:L18–L26.

Strüder, L.; Meidinger, N. (2008): CCD Detectors. In: J.E. Trümper; G. Hasinger (eds), The Universe in X-Rays, *Springer*, pp. 51–71.

Sturm, R.; Haberl, F.; Pietsch, W.; Ballet, J.; Hatzidimitriou, D.; et al. (2013): The XMM-Newton Survey of the Small Magellanic Cloud: The X-Ray Point-Source Catalogue, *Astronomy & Astrophysics*, 558:A3.

Suleimanov, V.F.; Klochkov, D.; Pavlov, G.G.; Werner, K. (2014): Carbon Neutron Star Atmospheres, *The Astrophysical Journal Supplement Series*, 210:13.

Suleimanov, V.F.; Klochkov, D.; Poutanen, J.; Werner, K. (2017): Probing the Possibility of Hotspots on the Central Neutron Star in HESS J1731-347, *Astronomy & Astrophysics*, 600:A43.

Sun, X.H.; Reich, P.; Reich, W.; Xiao, L.; Gao, X.Y.; et al. (2011): A Sino-German $\lambda 6$ cm Polarization Survey of the Galactic Plane. VII. Small Supernova Remnants, *Astronomy & Astrophysics*, 536:A83.

Tanaka, Y.; Inoue, H.; Holt, S.S. (1994): The X-Ray Astronomy Satellite ASCA, *Publications of the Astronomical Society of Japan*, 46:L37–L41.

Tauris, T.M.; Kaspi, V.M.; Breton, R.P.; Deller, A.T.; Keane, E.F.; et al. (2015): Understanding the Neutron Star Population with the SKA. In: Advancing Astrophysics with the Square Kilometre Array (AASKA14), vol. 215 of the *Proceedings of Science*, 039.

Taylor, A.R.; Gibson, S.J.; Peracaula, M.; Martin, P.G.; Landecker, T.L.; et al. (2003): The Canadian Galactic Plane Survey, *The Astronomical Journal*, 125(6):3145–3164.

Taylor, G. (1950): The Formation of a Blast Wave by a Very Intense Explosion. I. Theoretical Discussion, *Proceedings of the Royal Society of London Series A*, 201(1065):159–174.

Tolman, R.C. (1939): Static Solutions of Einstein's Field Equations for Spheres of Fluid, *Physical Review*, 55(4):364–373.

Trümper, J.E.; Hasinger, G. (2008): The Universe in X-Rays, *Springer*.

Tsujimoto, M.; Guainazzi, M.; Plucinsky, P.P.; Beardmore, A.P.; Ishida, M.; et al. (2011): Cross-Calibration of the X-Ray Instruments Onboard the Chandra, INTEGRAL, RXTE, Suzaku, Swift, and XMM-Newton Observatories Using G21.5-0.9, *Astronomy & Astrophysics*, 525:A25.

Tuohy, I.; Garmire, G. (1980): Discovery of a Compact X-ray Source at the Center of the SNR RCW 103., *The Astrophysical Journal Letters*, 239:L107–L110.

Turner, M.J.L.; Abbey, A.; Arnaud, M.; Balasini, M.; Barbera, M.; et al. (2001): The European Photon Imaging Camera on XMM-Newton: The MOS Cameras, *Astronomy & Astrophysics*, 365:L27–L35.

Vink, J. (2012): Supernova Remnants: the X-ray Perspective, *The Astronomy & Astrophysics Review*, 20:49.

Walter, R.; Ferrigno, C. (2017): X-Ray Pulsars. In: A.W. Alsabti; P. Murdin (eds), Handbook of Supernovae, *Springer/Cham*, pp. 1385–1399.

Watson, M.G.; Schröder, A.C.; Fyfe, D.; Page, C.G.; Lamer, G.; et al. (2009): The XMM-Newton Serendipitous Survey. V. The Second XMM-Newton Serendipitous Source Catalogue, *Astronomy & Astrophysics*, 493:339–373.

Webb, N.A.; Coriat, M.; Traulsen, I.; Ballet, J.; Motch, C.; et al. (2020): The XMM-Newton Serendipitous Survey. IX. The Fourth XMM-Newton Serendipitous Source Catalogue, *Astronomy & Astrophysics*, 641:A136.

Weigert, A.; Wendker, H.J.; Wisotzki, L. (2009): Astronomie und Astrophysik: Ein Grundkurs, *Wiley*.

Weiler, M. (2018): Revised Gaia Data Release 2 Passbands, *Astronomy & Astrophysics*, 617:A138.

Weisskopf, M.C.; Brinkman, B.; Canizares, C.; Garmire, G.; Murray, S.; et al. (2002): An Overview of the Performance and Scientific Results from the Chandra X-Ray Observatory, *Publications of the Astronomical Society of the Pacific*, 114(791):1–24.

Wenger, M.; Ochsenbein, F.; Egret, D.; Dubois, P.; Bonnarel, F.; et al. (2000): The SIMBAD Astronomical Database. The CDS Reference Database for Astronomical Objects, *Astronomy & Astrophysics Supplement*, 143:9–22.

Wolter, H. (1952): Spiegelsysteme Streifenden Einfalls als Abbildende Optiken für Röntgenstrahlen, *Annalen der Physik*, 445(1-2):94–114.

Wright, E.L.; Eisenhardt, P.R.M.; Mainzer, A.K.; Ressler, M.E.; Cutri, R.M.; et al. (2010): The Wide-Field Infrared Survey Explorer (WISE): Mission Description and Initial On-Orbit Performance, *The Astronomical Journal*, 140:1868–1881.

XMM-Newton Survey Science Centre Consortium (2010): "The XMM-Newton Serendipitous Source Catalogue: 2XMMi-DR3 User Guide to the Catalogue", release 1.0.

Yakovlev, D.G.; Haensel, P.; Baym, G.; Pethick, C. (2013): Lev Landau and the Concept of Neutron Stars, *Physics Uspekhi*, 56(3):289-295.

APPENDIX A

Additional Tables

Table A.1: List of the 46 sources included in the original CORRAREA version. The sources are referred to with the IDs (OBSID) of the respective observations from which they were selected. Also given are the GTI-filtered exposure times used for the original CORRAREA version as given in Read et al. (2014), see Chapter 3.3.1, as well as the GTI-filtered exposure times resulting from the revised GTI-filtering method from the recalibration described in Chapter 3.5.1. One observation was excluded in the recalibrated version as it was found to be located too close to the pn CCD4 chip border.

OBSID	Original exp. GTI (ks)	Revised exp. GTI (ks)	OBSID	Original exp. GTI (ks)	Revised exp. GTI (ks)
0056340201	12.4	9.5	0204040101	75.6	69.8
0067750101	23.6	17.9	0204040301	56.4	49.0
0084140101	35.3	33.4	0205010101	26.3	23.3
0084140501	12.4	10.8	0205390301	49.1	48.2
0086360301	54.5	39.8	0206580101	36.9	34.2
0086360401	26.9	21.8	0207130401	11.7	9.7
0092850501	38.9	34.5	0300240501	25.8	24.2
0100240701	15.5	14.0	0300630301	17.6	15.9
0101440601	34.7	32.2	0300910301	13.0	19.1
0101441501	37.1	31.3	0303340101	44.7	41.8
0106860101	23.4	17.1	0304320201	68.5	64.7
0112521001	7.9	7.5	0304320301	36.1	27.8
0112850201	16.5	12.5	0304320801	37.8	32.3
0112880101	28.1	26.7	0306630201	91.4	89.3
0124900101	29.7	25.0	0402560901	48.0	–
0146390101	17.3	13.3	0405090101	96.1	89.9
0147670201	12.1	11.2	0405690201	36.1	33.7
0147920601	12.1	11.5	0405690501	25.8	22.8
0151390101	46.3	41.9	0502220301	69.1	66.9
0152940101	39.4	30.0	0510181701	44.6	39.8
0153250101	54.7	43.9	0555020201	24.9	24.1
0200480101	30.2	29.2	0555650201	96.4	93.4
0201290301	18.2	16.9	0555650301	92.8	81.8

Table A.2: Observations excluded from the new source sample in the image screening process. The reasons for their exclusion are marked with "1" in the columns following the observation ID (OBSID).

OBSID	Crowded fields	Chip gaps/ Bad columns	Extended emission	Other
	(0 = no; 1 = yes)			
0046340101	0	0	1	0
0086770101	0	0	1	0
0094360601	1	0	1	0
0109060201	0	0	1	0
0111130701	0	0	1	0
0112880801	1	0	0	0
0112960101	0	0	1	0
0123110201	0	1	1	0
0135721401	0	0	1	1*
0135721501	0	0	1	0
0135721701	0	0	1	0
0135721901	0	0	1	0
0135722001	0	0	1	0
0135722101	0	0	1	1*
0135722501	0	0	1	0
0143370101	1	0	1	0
0152020101	1	0	1	0
0200530401	0	1	0	0
0203540801	1	0	0	0
0204610101	1	0	1	0
0205590301	0	0	1	0
0205590401	0	0	1	0
0206080101	0	0	1	0
0305540701	1	0	0	0
0306230101	1	0	1	0
0400560301	1	0	1	0
0402560901	0	1	0	0
0404980101	1	0	1	0
0405320801	1	0	1	0
0412982201	0	0	1	0
0412982301	0	0	1	0
0412983201	0	0	1	0
0412983301	0	0	1	0
0502120101	0	0	1	0
0504480201	0	0	0	1††
0505140201	1	0	1	0
0505140401	1	0	1	0
0505140501	1	0	1	0

continued on next page...

* detectors have mixed modes with the main modes not overlapping in time

† off-axis source

†† GTI-filtered exposure time too short for proper screening

... continuation of table A.2

OBSID	Crowded fields	Chip gaps/ bad columns	Extended emission	Other
	(0 = no; 1 = yes)			
0505720201	1	0	1	0
0505720301	1	0	1	0
0505720401	1	0	1	0
0505720501	1	0	1	0
0505720601	1	0	1	0
0506340101	0	0	0	1†
0551690201	1	0	1	0
0600660201	1	0	0	0
0650510501	0	0	1	0
0650560201	1	0	1	0
0650560301	1	0	1	0
0650560401	1	0	1	0
0657800101	0	0	1	0
0670950101	0	1	0	0
0674210301	1	0	1	0
0691250301	0	0	0	1†
0692840201	1	0	1	0
0692840501	1	0	1	0
0693850501	1	0	0	1†
0693851201	1	0	0	1†
0694580101	0	1	0	0
0720690101	1	0	0	1†
0722370201	1	0	1	0
0723450101	1	0	1	0
0723450201	1	0	1	0
0724840301	1	0	0	0
0729561301	1	0	1	0
0740060501	0	0	1	0
0742230101	1	0	0	0
0742590301	1	0	0	0
0743050301	0	0	1	0
0743050801	0	0	1	0
0760870101	1	0	1	0
0763500201	1	0	1	0
0791580101	0	0	1	0
0791580401	0	0	1	0
0791580501	0	0	1	0
0791580601	0	0	1	0
0791580701	0	0	1	0
0791580801	0	0	1	0
0791580901	0	0	1	0
0791581001	0	0	1	0
0791581101	0	0	1	0
0791581201	0	0	1	0

Table A.3: Pile-up free sources of the new, extended sample. Besides the observation ID (OBSID), the revolution number (Rev.), the source coordinates (in right ascension, RA, and declination, Dec) and the GTI-filtered exposure time (Exp. GTI) are given. Also, the mode, filter, source count rate and the maximum radius to be used for the source extraction region (max. $r_{\rm extr}$) are given for pn, MOS1 (m1) and MOS2 (m2), respectively. The modes are Full Frame (FF), Large Window (LW) and Small Window (SW); the filters are thin (t), medium (m) and thick (T).

		RA*	Dec*	Mode			Filter			Count rate* (cts s^{-1})			Exp. GTI	Max. $r_{\rm extr}$ ($''$)		
OBSID	Rev.	h m s	$^\circ$ $'$ $''$	pn	m1	m2	pn	m1	m2	pn	m1	m2	(ks)	pn	m1	m2
0006220201	0197	12 35 36.67	−39 54 33.93	FF	FF	FF	m	T	T	1.18	0.29	0.30	33.9	60	60	60
0024140101	0231	04 19 47.61	+15 37 39.44	FF	FF	FF	T	T	T	0.69	0.18	0.18	45.0	45	60	60
0029340101	0238	06 41 19.10	+82 16 02.45	LW	LW	LW	m	m	m	2.31	0.62	0.63	35.9	35	60	60
0029340201	0700	06 41 19.10	+82 16 01.96	LW	LW	LW	m	m	m	2.89	0.80	0.81	41.0	35	60	60
0044740201	0273	11 50 41.79	+01 45 52.60	FF	FF	FF	T	T	T	0.47	0.11	0.12	44.3	45	60	60
0067750101	0311	14 58 21.95	−31 40 07.31	FF	FF	FF	t	t	t	1.23	0.32	0.32	17.9	40	60	60
0084140501	0395	02 08 38.16	+35 23 13.00	FF	FF	FF	t	m	m	1.55	0.44	0.45	10.7	35	60	60
0086360401	0230	04 18 31.10	+28 27 16.24	FF	FF	FF	m	m	m	1.13	0.32	0.32	22.1	40	40	40
0090070101	0462	01 46 12.57	−39 23 06.09	FF	LW	LW	m	m	m	0.93	0.26	0.27	28.0	35	60	60
0092850501	0373	14 09 23.91	+26 18 20.83	FF	FF	FF	t	t	t	1.09	0.29	0.29	34.9	40	40	40
0101040301	0178	10 23 30.57	+19 51 54.48	FF	FF	FF	m	m	m	1.15	0.37	0.38	32.4	35	35	35
0106860101	0157	03 18 19.88	−66 29 10.65	FF	FF	FF	m	m	m	0.93	0.31	0.30	17.2	30	30	30
0109080301	0443	13 23 49.53	+65 41 48.18	LW	LW	LW	t	t	t	2.94	0.75	0.77	7.9	35	60	60
0109080501	0549	14 17 00.82	+44 56 06.39	LW	LW	LW	t	t	t	1.78	0.43	0.45	19.8	35	60	60
0109080601	0489	14 46 45.95	+40 35 05.83	LW	LW	LW	t	t	t	1.22	0.30	0.32	15.8	35	60	60
0109080701	0444	10 51 43.87	+33 59 26.97	LW	LW	LW	t	t	t	1.41	0.38	0.40	17.7	30	60	60
0109080801	0445	11 17 06.43	+44 13 33.42	LW	LW	LW	t	t	t	0.79	0.26	0.25	33.0	35	60	60
0109080901	0453	14 29 43.11	+47 47 26.39	LW	LW	LW	t	t	t	1.39	0.37	0.39	33.9	30	60	60
0109130601	0415	18 38 20.38	−65 25 38.21	LW	SW	SW	t	t	t	1.87	0.59	0.60	6.8	40	45	50
0110890201	0159	07 08 41.49	−49 33 06.76	FF	LW	LW	m	m	m	1.45	0.35	0.36	38.0	35	60	60

continued on next page...

* as in the *XMM-Newton Serendipitous Source Catalogue*, version 3XMM-DR7

... continuation of table A.3

OBSID	Rev.	RA	Dec	Mode			Filter			Count rate (cts s^{-1})			Exp. GTI	Max. r_{extr} ($''$)		
		h m s	° ′ ″	pn	m1	m2	pn	m1	m2	pn	m1	m2	(ks)	pn	m1	m2
0111220201	0158	06 15 36.20	+71 02 15.58	FF	FF	FF	m	m	m	0.95	0.27	0.27	37.0	35	35	35
0111251501	0422	21 15 40.98	−58 40 53.61	LW	SW	SW	t	t	t	2.48	0.77	0.80	12.4	35	35	35
0111290101	0349	09 50 48.42	+39 26 50.64	LW	LW	LW	t	t	t	2.08	0.57	0.59	17.3	30	60	60
0111290601	0482	14 27 35.61	+26 32 14.63	FF	FF	FF	t	t	t	0.76	0.23	0.23	27.1	35	60	60
0111291001	0496	15 14 43.09	+36 50 50.70	LW	LW	LW	t	t	t	1.84	0.51	0.52	14.4	25	25	25
0114090101	0051	05 39 54.27	−28 39 55.81	FF	LW	FF	m	m	m	0.90	0.30	0.29	31.4	35	60	60
0144570101	0648	13 47 15.65	+17 27 25.55	FF	LW	LW	T	T	T	1.41	0.35	0.36	37.5	40	60	60
0148680101	0661	13 11 52.17	+27 52 44.63	FF	FF	FF	T	T	T	0.68	0.16	0.17	39.1	40	60	60
0151390101	0630	10 41 17.16	+06 10 16.96	FF	FF	FF	t	t	t	0.72	0.22	0.22	41.9	35	60	60
0152940101	0660	13 38 15.88	+04 32 33.39	FF	FF	FF	t	t	t	1.25	0.43	0.43	30.0	35	60	60
0200910101	0944	04 13 40.33	+11 12 14.93	LW	LW	LW	m	m	m	1.87	0.67	0.69	29.4	35	60	60
0201290301	0813	09 44 31.71	+03 58 05.53	FF	FF	FF	t	t	t	1.00	0.28	0.30	16.8	35	45	45
0202860101	0902	22 02 01.92	−31 52 09.98	LW	LW	LW	t	t	t	1.88	0.64	0.64	21.6	40	60	60
0203542001	0872	04 14 12.79	+28 12 14.50	FF	FF	SW	m	m	m	1.41	0.42	0.44	28.8	25	25	25
0203770201	0842	14 19 03.81	−13 10 44.60	LW	LW	LW	t	t	t	1.54	0.46	0.47	18.0	40	60	60
0205390301	0831	13 53 15.88	+63 45 45.95	FF	FF	FF	m	m	m	0.74	0.19	0.19	48.2	30	45	45
0205770101	0738	08 07 27.78	−76 32 00.98	FF	LW	LW	t	t	t	1.21	0.40	0.40	92.3	30	60	60
0206100101	0899	08 06 22.95	+15 27 31.12	LW	SW	SW	t	t	t	0.63	0.11	0.12	41.9	40	50	50
0206580101	0939	13 22 24.47	−16 43 42.64	FF	FF	FF	m	m	m	0.63	0.17	0.17	34.1	35	50	50
0300240501	1129	13 06 26.13	−40 24 52.40	FF	FF	FF	t	t	t	1.14	0.38	0.39	24.2	40	60	60
0300480301	1081	08 54 48.87	+20 06 30.64	LW	LW	LW	m	m	m	1.29	0.36	0.37	23.6	35	60	60
0300630301	1120	02 40 08.18	−23 09 15.79	FF	FF	FF	t	t	t	1.01	0.28	0.29	15.8	30	60	60
0301500101	1041	04 21 59.43	+19 32 06.35	FF	LW	SW	m	m	m	0.85	0.29	0.29	39.4	35	60	45
0302900101	1117	14 03 19.65	−41 22 58.46	FF	FF	FF	t	t	t	1.11	0.29	0.28	97.6	35	60	60

continued on next page...

... continuation of table A.3

OBSID	Rev.	RA h m s	Dec ° ′ ″	Mode pn	Mode m1	Mode m2	Filter pn	Filter m1	Filter m2	Count rate (cts s^{-1}) pn	Count rate (cts s^{-1}) m1	Count rate (cts s^{-1}) m2	Exp. GTI (ks)	Max. r_{extr} (″) pn	Max. r_{extr} (″) m1	Max. r_{extr} (″) m2
0305920201	1096	11 40 08.72	+03 07 11.40	FF	FF	FF	t	t	t	0.71	0.16	0.16	35.6	35	60	60
0306560301	1064	08 07 27.71	−76 32 00.64	FF	LW	LW	m	m	m	0.37	0.09	0.09	63.5	40	60	60
0306630101	1101	12 30 54.11	+11 00 11.22	FF	FF	FF	t	m	m	1.28	0.31	0.31	59.2	45	60	60
0306630201	1103	12 30 54.12	+11 00 11.17	FF	FF	FF	t	m	m	1.36	0.33	0.33	89.5	45	60	60
0400200101	1288	14 05 16.23	+25 55 34.27	LW	LW	LW	m	m	m	2.64	0.63	0.65	20.0	35	60	60
0400200201	1289	14 05 16.21	+25 55 34.12	LW	LW	LW	m	m	m	1.90	0.48	0.47	5.7	35	60	60
0401060201	1271	08 54 48.84	+20 06 30.47	LW	LW	LW	m	m	m	1.02	0.30	0.30	43.6	35	60	60
0405090101	1255	03 18 19.89	−66 29 10.92	FF	FF	FF	m	m	m	0.89	0.29	0.28	89.8	30	30	30
0405690201	1272	13 29 38.61	+58 25 05.51	FF	FF	FF	m	m	m	1.17	0.32	0.33	33.3	40	60	60
0405690501	1275	13 29 38.62	+58 25 05.56	FF	FF	FF	m	m	m	0.86	0.24	0.25	22.8	35	60	60
0500750101	1483	14 03 19.62	−41 22 58.19	FF	FF	FF	t	t	t	1.03	0.27	0.26	51.6	35	60	60
0502220301	1441	08 31 41.71	+52 45 17.47	FF	FF	FF	m	m	m	0.31	0.10	0.09	67.0	35	60	60
0502630201	1533	08 54 48.82	+20 06 30.62	LW	LW	LW	m	m	m	1.01	0.30	0.30	38.4	35	60	60
0506200301	1360	07 08 41.50	−49 33 06.74	LW	SW	SW	m	m	m	2.46	0.48	0.54	37.8	35	40	45
0550950101	1648	01 11 27.58	−38 05 00.47	LW	LW	LW	m	m	m	0.38	0.09	0.09	95.5	35	60	60
0550970101	1609	15 56 58.95	−79 14 03.27	FF	LW	LW	m	m	m	0.71	0.26	0.26	55.4	35	60	60
0553300301	1667	02 41 04.80	−08 15 20.84	FF	FF	FF	m	m	m	0.69	0.22	0.22	48.4	35	60	60
0553300401	1772	02 41 04.80	−08 15 20.93	FF	FF	FF	m	m	m	0.70	0.22	0.23	54.5	40	60	60
0554710801	2032	07 08 41.46	−49 33 06.63	LW	SW	SW	m	m	m	0.34	0.08	0.08	65.1	30	30	30
0555650201	1598	16 15 34.55	−22 42 41.71	FF	FF	FF	m	m	m	0.65	0.18	0.18	93.4	40	60	60
0555650301	1599	16 15 34.56	−22 42 41.86	FF	FF	FF	m	m	m	0.64	0.18	0.17	82.2	40	50	50
0560180701	1632	07 48 33.70	−67 45 07.73	FF	FF	FF	m	m	m	0.67	0.18	0.18	27.6	40	60	60
0561580401	1885	08 19 29.00	+70 42 19.34	FF	FF	FF	m	m	m	1.40	0.40	0.36	25.0	35	60	60
0601400201	2198	00 57 22.64	−46 48 03.57	FF	LW	LW	m	m	m	0.77	0.21	0.21	47.7	35	60	60

continued on next page...

... continuation of table A.3

OBSID	Rev.	RA	Dec	Mode			Filter			Count rate (cts s^{-1})			Exp. GTI	Max. r_{extr} ($''$)		
		h m s	° ′ ″	pn	m1	m2	pn	m1	m2	pn	m1	m2	(ks)	pn	m1	m2
0601560201	1737	11 23 32.27	−08 39 30.69	LW	LW	LW	m	m	m	2.85	0.76	0.75	11.9	40	60	60
0602290101	1723	09 35 38.94	+35 48 34.17	FF	FF	FF	T	T	T	0.98	0.24	0.24	56.1	35	60	60
0602490101	1744	01 57 49.05	−21 54 05.84	LW	LW	LW	m	m	m	0.99	0.25	0.24	47.6	40	60	60
0603980101	1745	00 13 09.14	+05 35 40.95	FF	FF	FF	m	m	m	1.30	0.32	0.31	50.6	40	60	60
0604060101	1842	23 09 49.11	+21 35 16.62	FF	FF	FF	t	t	t	0.68	0.19	0.19	38.8	40	60	60
0605090101	1769	05 05 45.73	−23 51 13.76	FF	FF	FF	t	t	t	0.84	0.28	0.29	24.8	35	60	60
0605560401	1698	07 48 33.71	−67 45 07.69	FF	FF	FF	t	t	t	0.56	0.15	0.14	39.7	35	60	60
0605560501	1751	07 48 33.82	−67 45 07.59	FF	FF	FF	t	t	t	0.50	0.13	0.13	76.9	35	60	60
0606150101	1746	11 29 16.74	−04 24 06.85	FF	FF	FF	m	m	m	0.22	0.07	0.07	88.9	35	60	60
0651120101	1958	04 35 27.38	+24 14 58.71	FF	FF	FF	m	m	m	0.32	0.09	0.08	98.7	25	25	25
0651330601	1999	11 17 06.40	+44 13 33.29	LW	LW	LW	t	t	t	1.03	0.32	0.32	19.6	35	35	35
0651690101	1927	07 48 33.71	−67 45 07.68	FF	FF	FF	t	t	t	0.47	0.13	0.12	49.0	35	60	60
0653380301	1943	14 03 19.66	−41 22 58.33	FF	FF	FF	t	t	t	1.24	0.32	0.32	108.8	30	60	60
0653380401	2039	14 03 19.65	−41 22 58.24	FF	FF	FF	t	t	t	1.18	0.30	0.29	91.5	35	60	60
0653380501	2040	14 03 19.67	−41 22 58.16	FF	FF	FF	t	t	t	1.14	0.29	0.29	95.1	40	60	60
0655050101	1915	00 15 28.92	−39 13 18.45	FF	FF	FF	t	t	t	0.91	0.27	0.26	108.1	40	60	60
0670880501	2263	09 06 31.88	+16 46 11.84	FF	FF	FF	m	m	m	0.58	0.17	0.17	50.4	35	60	60
0672130101	2115	00 42 42.51	+40 51 51.84	FF	FF	FF	t	t	t	0.36	0.11	0.11	78.2	35	60	60
0672130601	2119	00 42 42.51	+40 51 52.86	FF	FF	FF	t	t	t	0.41	0.13	0.12	67.5	35	60	60
0672130701	2120	00 42 42.53	+40 51 52.95	FF	FF	FF	t	t	t	0.40	0.12	0.12	74.6	35	60	60
0672530301	2104	19 05 25.94	+42 27 39.96	LW	SW	SW	m	m	m	2.58	0.75	0.76	22.3	35	40	50
0673270101	2121	16 33 23.61	+47 18 58.61	LW	LW	LW	t	t	t	0.84	0.23	0.24	20.1	35	50	50
0673270201	2154	16 33 23.57	+47 18 58.79	LW	LW	LW	t	t	t	0.85	0.24	0.24	21.0	35	50	50
0673580201	2127	13 25 19.37	−38 24 52.47	LW	LW	LW	t	t	t	2.43	0.55	0.53	73.5	35	60	60

continued on next page...

... continuation of table A.3

OBSID	Rev.	RA h m s	Dec ° ′ ″	Mode pn	Mode m1	Mode m2	Filter pn	Filter m1	Filter m2	Count rate (cts s^{-1}) pn	Count rate (cts s^{-1}) m1	Count rate (cts s^{-1}) m2	Exp. GTI (ks)	Max. r_{extr} (″) pn	Max. r_{extr} (″) m1	Max. r_{extr} (″) m2
0673580301	2129	13 25 19.37	−38 24 52.48	LW	LW	LW	t	t	t	1.48	0.31	0.30	69.8	35	60	60
0673580401	2131	13 25 19.36	−38 24 52.26	LW	LW	LW	t	t	t	2.71	0.59	0.57	103.4	35	60	60
0673730101	2100	09 48 57.32	+00 22 25.53	LW	LW	LW	m	m	m	1.35	0.39	0.39	29.5	35	60	60
0690200301	2425	16 05 26.25	−19 48 18.60	FF	FF	FF	T	T	T	1.18	0.27	0.26	28.1	45	60	60
0690330101	2445	07 48 33.74	−67 45 07.35	FF	FF	FF	t	t	t	0.41	0.11	0.10	89.4	30	50	50
0690600401	2298	00 42 51.98	+41 31 07.85	FF	FF	FF	t	t	t	1.10	0.38	0.38	81.0	35	60	60
0690870501	2504	02 34 37.86	−08 47 16.48	SW	SW	SW	t	t	t	2.07	0.62	0.61	97.4	40	40	50
0691100201	2384	06 19 27.56	−65 53 08.82	FF	FF	SW	t	t	m	1.04	0.28	0.28	26.5	35	60	50
0694170101	2401	13 06 26.12	−40 24 52.53	FF	SW	SW	t	t	t	0.39	0.12	0.11	91.4	35	40	50
0694651501	2854	12 48 15.23	+17 46 26.49	SW	SW	SW	t	t	t	4.63	0.74	0.70	8.1	35	40	50
0700381801	2353	01 27 45.95	−73 32 56.49	FF	FF	FF	t	m	m	1.09	0.35	0.35	29.1	35	40	40
0701780101	2458	09 45 41.93	−14 19 35.03	SW	SW	SW	m	m	m	3.30	1.13	1.16	12.1	35	40	50
0720110301	2479	14 17 59.55	+25 08 12.66	SW	SW	SW	t	t	t	2.53	0.80	0.79	49.2	40	45	50
0720110401	2483	14 17 59.55	+25 08 12.73	SW	SW	SW	t	t	t	6.20	2.09	2.09	51.4	40	45	40
0720110501	2487	14 17 59.55	+25 08 12.71	SW	SW	SW	t	t	t	4.18	1.37	1.39	54.4	40	25	40
0720110601	2489	14 17 59.55	+25 08 12.73	SW	SW	SW	t	t	t	6.49	2.18	2.22	51.4	40	30	25
0720110701	2491	14 17 59.55	+25 08 12.77	SW	SW	SW	t	t	t	5.15	1.71	1.70	53.3	40	15	25
0720110801	2493	14 17 59.55	+25 08 12.73	SW	SW	SW	t	t	t	5.00	1.66	1.68	52.0	45	45	50
0720110901	2494	14 17 59.55	+25 08 12.70	SW	SW	SW	t	t	t	4.53	1.50	1.50	52.0	40	45	40
0720111001	2495	14 17 59.53	+25 08 12.42	SW	SW	SW	t	t	t	4.64	1.51	1.52	52.7	40	30	45
0720111101	2496	14 17 59.55	+25 08 12.72	SW	SW	SW	t	t	t	5.96	1.98	2.04	45.3	40	35	25
0720111201	2497	14 17 59.55	+25 08 12.69	SW	SW	SW	t	t	t	5.73	1.90	1.91	54.1	40	15	30
0720111301	2498	14 17 59.55	+25 08 12.75	SW	SW	SW	t	t	t	5.26	1.75	1.74	47.4	40	45	40
0720111401	2499	14 17 59.55	+25 08 12.72	SW	SW	SW	t	t	t	4.52	1.47	1.48	52.1	35	30	45

continued on next page...

... continuation of table A.3

OBSID	Rev.	RA	Dec	Mode			Filter			Count rate (cts s^{-1})			Exp. GTI	Max. r_{extr} ($''$)		
		h m s	° ′ ″	pn	m1	m2	pn	m1	m2	pn	m1	m2	(ks)	pn	m1	m2
0720111501	2570	14 17 59.55	+25 08 12.74	SW	SW	SW	t	t	t	4.26	1.36	1.36	46.3	40	45	50
0720111601	2593	14 17 59.56	+25 08 13.39	SW	SW	SW	t	t	t	6.07	1.96	1.96	52.8	45	50	50
0720280101	2599	14 48 51.03	−40 08 46.24	FF	FF	FF	t	t	t	1.04	0.34	0.34	19.9	35	60	60
0721220101	2587	17 03 30.38	+45 40 47.17	SW	SW	SW	m	m	m	7.57	1.96	1.89	19.7	45	45	50
0721220301	2588	17 03 30.39	+45 40 47.71	SW	SW	SW	m	m	m	8.83	2.26	2.19	23.5	45	45	50
0722610101	2530	05 21 01.40	−25 21 45.19	FF	FF	FF	m	m	m	0.52	0.16	0.16	34.3	35	60	60
0723130301	2596	14 03 19.67	−41 22 58.25	FF	FF	FF	t	t	t	1.04	0.26	0.26	34.0	35	60	60
0724820101	2516	18 36 58.26	−59 24 07.77	SW	SW	SW	t	t	t	7.06	2.54	2.57	101.1	35	40	50
0724820201	2537	18 36 58.19	−59 24 07.63	SW	SW	SW	t	t	t	5.19	1.87	1.88	91.7	40	40	50
0727760301	2706	18 56 36.06	−37 54 36.19	SW	SW	SW	t	t	t	5.70	0.92	0.88	70.9	45	30	45
0727761001	3075	18 56 36.01	−37 54 36.85	SW	SW	SW	t	t	t	5.49	0.90	0.83	67.2	45	35	45
0727960301	2486	11 31 51.52	−12 31 58.63	SW	SW	SW	t	t	t	1.72	0.48	0.48	67.9	35	40	45
0740610201	2691	05 22 18.70	−08 39 58.18	FF	FF	FF	T	T	T	0.72	0.18	0.22	51.7	30	60	60
0741260101	2667	11 38 50.86	−23 21 34.11	SW	SW	SW	t	t	t	4.37	1.35	1.37	91.9	35	40	45
0741390101	2650	04 39 38.74	−53 11 31.24	SW	SW	SW	m	m	m	2.99	0.62	0.60	22.9	35	40	50
0741390201	2662	13 55 16.56	+56 12 45.21	SW	SW	SW	m	m	m	5.05	1.10	1.08	22.8	35	40	50
0741390301	2648	23 43 28.54	−14 55 30.57	SW	SW	SW	m	m	m	3.40	0.77	0.73	29.3	40	45	50
0741390401	2667	13 55 16.51	+56 12 45.13	SW	SW	SW	m	m	m	2.32	0.50	0.49	10.4	35	40	45
0742490101	2803	03 17 38.61	−66 33 03.80	FF	FF	FF	m	m	m	0.26	0.08	0.08	80.5	35	60	60
0743830501	2765	02 34 37.86	−08 47 16.43	SW	SW	SW	t	t	t	9.02	2.34	2.27	108.9	45	50	50
0744240101	2682	14 24 38.11	+22 56 00.71	FF	FF	FF	t	t	t	0.49	0.14	0.14	76.9	35	60	60
0744290101	2789	15 59 09.63	+35 01 47.49	SW	SW	SW	m	m	m	2.50	0.63	0.61	17.9	40	40	50
0744440101	2753	12 46 35.25	+02 22 08.83	SW	SW	SW	t	t	t	7.04	1.57	1.52	35.6	35	45	50
0744440201	2754	12 46 35.29	+02 22 09.40	SW	SW	SW	t	t	t	8.57	1.94	1.88	39.4	35	40	50

continued on next page...

... continuation of table A.3

OBSID	Rev.	RA h m s	Dec ° ′ ″	Mode pn	Mode m1	Mode m2	Filter pn	Filter m1	Filter m2	Count rate (cts s^{-1}) pn	Count rate (cts s^{-1}) m1	Count rate (cts s^{-1}) m2	Exp. GTI (ks)	Max. r_{extr} (″) pn	Max. r_{extr} (″) m1	Max. r_{extr} (″) m2
0744440501	2766	12 46 35.27	+02 22 09.42	SW	SW	SW	t	t	t	7.21	1.62	1.56	103.7	35	45	50
0744450101	2673	11 59 41.01	−19 59 24.61	LW	LW	LW	t	t	t	1.74	0.50	0.49	105.9	35	60	60
0744450301	2773	01 40 17.07	−00 50 02.94	LW	LW	LW	t	t	t	2.33	0.61	0.59	81.8	45	50	50
0744450401	2674	11 59 41.01	−19 59 24.66	LW	LW	LW	t	t	t	1.76	0.50	0.50	53.9	35	60	60
0744490401	2744	22 36 46.48	−12 32 42.74	LW	LW	LW	t	t	t	1.43	0.49	0.49	78.3	35	60	60
0744490501	2746	22 36 46.51	−12 32 42.67	LW	LW	LW	t	t	t	0.94	0.32	0.33	30.4	35	60	60
0744500201	2689	04 21 59.43	+19 32 06.32	FF	FF	LW	m	m	m	0.55	0.17	0.16	36.1	40	60	60
0744500301	2694	04 21 59.44	+19 32 06.33	FF	FF	LW	m	m	m	1.02	0.30	0.31	39.7	45	60	60
0744500401	2700	04 21 59.43	+19 32 06.29	FF	FF	LW	m	m	m	1.03	0.31	0.32	38.2	40	60	60
0761040101	2883	19 07 16.27	+44 01 08.28	FF	FF	FF	t	t	m	0.78	0.24	0.23	50.8	30	60	60
0761220101	2853	14 13 14.88	−03 12 27.85	SW	SW	SW	t	t	t	7.73	2.70	2.73	119.6	40	40	50
0761500201	2822	08 54 48.81	+20 06 31.86	LW	LW	LW	t	t	t	2.74	0.72	0.70	58.5	35	60	60
0761510301	2902	08 14 41.92	+21 29 18.48	FF	FF	FF	t	t	t	1.30	0.26	0.30	32.9	35	50	50
0764010101	2929	22 49 37.15	−19 16 26.31	FF	FF	FF	t	t	t	0.31	0.09	0.09	53.7	35	60	60
0764170101	2851	00 57 20.36	−22 22 55.28	SW	SW	SW	t	m	t	10.05	2.14	2.21	106.1	35	40	45
0764370201	2914	22 05 10.29	−01 55 21.10	FF	FF	FF	t	m	m	0.63	0.19	0.19	47.1	40	60	60
0780561301	3038	13 25 19.28	−38 24 52.29	LW	LW	LW	t	t	t	2.94	0.65	0.61	124.5	35	60	60
0780561501	3043	13 25 19.36	−38 24 52.25	LW	LW	LW	t	t	t	1.92	0.40	0.38	116.3	35	60	60
0780561701	3045	13 25 19.35	−38 24 52.07	LW	LW	LW	t	t	t	2.15	0.47	0.44	115.5	35	60	60
0792180101	3046	13 25 19.23	−38 24 52.02	LW	LW	LW	t	t	t	2.11	0.48	0.47	120.0	35	60	60
0792180201	3048	13 25 19.32	−38 24 52.27	LW	LW	LW	t	t	t	2.70	0.58	0.55	123.9	35	60	60
0792180301	3049	13 25 19.36	−38 24 52.43	LW	LW	LW	t	t	t	1.18	0.25	0.23	107.1	35	60	60
0792180501	3052	13 25 19.36	−38 24 53.02	LW	LW	LW	t	t	t	2.43	0.54	0.51	119.1	35	60	60

Table A.4: Sources of the new, extended sample for which the presence of pile-up can only be evaluated vaguely. The same description of the content applies as for Table A.3.

		RA	Dec	Mode			Filter			Count rate (cts s^{-1})			Exp. GTI	Max. r_{extr} ($''$)		
OBSID	Rev.	h m s	° ′ ″	pn	m1	m2	pn	m1	m2	pn	m1	m2	(ks)	pn	m1	m2
0017940101	0196	13 05 42.37	+18 01 03.71	FF	SW	SW	t	t	t	2.41	0.71	0.72	39.9	35	30	35
0061540101	0238	06 52 12.34	+74 25 37.71	FF	FF	FF	m	m	m	1.54	0.51	0.52	8.0	35	60	60
0067540201	0477	00 48 47.15	+31 57 24.78	FF	LW	LW	m	m	m	2.31	0.76	0.77	2.5	40	60	60
0084140101	0217	02 08 38.40	+35 23 13.02	FF	FF	FF	t	m	m	1.40	0.39	0.41	33.2	35	60	60
0101441501	0410	04 24 12.44	+14 45 29.64	FF	FF	FF	m	m	m	1.69	0.43	0.43	31.2	45	60	60
0102040201	0175	11 31 09.52	+31 14 05.60	FF	LW	LW	t	t	T	2.19	0.61	0.50	11.7	40	60	60
0102040301	0182	10 30 59.09	+31 02 55.75	FF	LW	LW	t	t	T	2.08	0.58	0.47	20.5	40	60	60
0103861801	0449	11 01 01.81	+11 02 48.51	FF	SW	SW	m	m	m	2.41	0.72	0.73	6.3	35	30	45
0109080401	0478	13 54 35.72	+18 05 18.05	LW	LW	LW	t	t	t	2.80	0.74	0.74	6.9	35	60	60
0109130201	0468	01 23 54.33	−35 03 55.18	LW	SW	SW	t	t	t	2.79	1.03	1.05	8.2	35	40	45
0111290301	0446	11 18 30.28	+40 25 54.05	LW	LW	LW	t	t	t	2.73	0.68	0.72	14.2	35	60	60
0112880401	0135	04 59 34.83	+01 47 00.69	FF	FF	FF	T	T	T	1.72	0.46	0.47	15.6	30	60	60
0140190101	0675	03 23 15.31	−49 31 06.16	FF	SW	SW	t	t	t	2.12	0.52	0.54	25.2	30	35	45
0146390101	0604	19 01 40.81	−36 52 33.75	FF	FF	FF	m	m	m	1.66	0.59	0.58	13.3	30	30	30
0147670201	0576	13 37 39.80	−12 57 25.57	FF	FF	FF	t	t	t	1.61	0.49	0.49	10.9	35	60	60
0148000201	0512	04 26 00.69	−57 12 02.06	LW	SW	SW	m	m	m	2.83	0.80	0.85	10.9	30	35	45
0153250101	0615	05 46 46.32	−71 08 52.07	FF	FF	FF	t	t	t	1.92	0.39	0.40	43.8	35	60	60
0301040101	1104	13 31 46.51	+29 16 35.67	LW	FF	FF	m	m	m	1.44	0.35	0.36	29.2	35	60	60
0304320201	1017	13 00 22.16	+28 24 02.65	FF	FF	FF	m	t	t	1.55	0.42	0.42	64.9	40	60	60
0510010701	1389	00 06 19.55	+20 12 10.59	LW	FF	FF	t	m	m	1.98	0.48	0.48	16.1	35	60	60

continued on next page...

... continuation of table A.4

OBSID	Rev.	RA h m s	Dec ° ′ ″	Mode pn	Mode m1	Mode m2	Filter pn	Filter m1	Filter m2	Count rate (cts s^{-1}) pn	Count rate (cts s^{-1}) m1	Count rate (cts s^{-1}) m2	Exp. GTI (ks)	Max. r_{extr} (″) pn	Max. r_{extr} (″) m1	Max. r_{extr} (″) m2
0550350101	1650	01 34 16.88	−42 58 25.99	FF	FF	FF	t	t	t	1.49	0.38	0.38	21.0	35	60	60
0550640101	1689	05 16 21.20	−10 33 41.35	LW	SW	SW	m	m	m	2.92	0.73	0.86	65.9	30	35	45
0653380201	1942	14 03 19.66	−41 22 58.48	FF	FF	FF	t	t	t	1.28	0.33	0.32	78.2	35	60	60
0701990101	2403	05 20 29.62	−69 31 54.50	FF	FF	FF	m	m	m	1.08	0.35	0.34	17.6	35	40	40
0721110101	2569	01 23 45.73	−58 48 20.49	SW	SW	SW	m	m	m	12.60	3.41	3.29	49.4	35	40	50
0723130401	2597	14 03 19.64	−41 22 58.15	FF	FF	FF	t	t	t	1.11	0.29	0.27	31.4	40	60	60
0743910301	2738	05 00 46.09	−70 44 36.63	FF	FF	FF	t	m	m	1.43	0.47	0.46	20.9	35	60	60
0780560101	3037	13 25 19.45	−38 24 52.47	LW	LW	LW	t	t	t	2.74	0.60	0.58	52.2	35	60	60
0780561401	3039	13 25 19.45	−38 24 52.32	LW	LW	LW	t	t	t	2.75	0.59	0.56	113.9	35	60	60

Table A.5: Clearly piled-up sources remaining after the source selection and image screening. The same description of the content applies as for Table A.3.

		RA	Dec	Mode			Filter			Count rate (cts s^{-1})			Exp. GTI	Max. r_{extr} ($''$)		
OBSID	Rev.	h m s	° ′ ″	pn	m1	m2	pn	m1	m2	pn	m1	m2	(ks)	pn	m1	m2
0008220201	0199	12 51 41.94	+27 32 26.30	FF	LW	LW	T	T	T	3.37	1.00	1.03	35.3	40	60	60
0056340201	0420	16 32 32.16	+82 32 16.53	FF	FF	FF	t	m	m	2.17	0.65	0.66	9.5	35	60	60
0086360301	0230	04 18 31.10	+28 27 16.31	FF	FF	FF	m	m	m	1.87	0.48	0.49	39.9	40	40	40
0090050701	0233	05 19 49.69	−45 46 43.55	FF	SW	SW	t	t	t	3.99	1.24	1.26	3.0	35	35	45
0100240701	0127	15 32 23.21	−08 32 00.88	FF	FF	FF	m	m	m	2.15	0.62	0.66	13.1	40	60	60
0101440501	0135	04 28 34.49	+15 57 43.79	FF	FF	FF	T	T	T	2.11	0.55	0.57	37.1	45	60	60
0101440601	0138	04 24 12.49	+14 45 29.50	FF	FF	FF	m	m	m	2.28	0.58	0.61	32.1	40	60	60
0103060401	0255	21 51 55.54	−30 27 53.45	LW	FF	FF	m	m	m	2.27	0.69	0.70	20.9	35	35	35
0103860201	0267	22 36 56.01	−22 13 15.77	FF	SW	SW	m	m	m	3.70	1.10	1.11	4.5	35	35	45
0103860901	0188	01 20 19.65	−44 07 42.86	FF	SW	SW	m	m	m	2.50	0.73	0.74	17.7	35	35	45
0103861201	0274	22 19 18.53	+12 07 53.16	FF	SW	SW	m	m	m	2.63	0.69	0.71	7.6	35	35	40
0110890101	0387	13 25 19.41	−38 24 52.26	FF	LW	LW	m	m	m	2.43	0.57	0.59	51.6	35	60	60
0111970301	0341	04 09 11.36	−71 17 42.13	FF	SW	SW	m	m	t	2.59	0.78	0.81	14.7	55	50	40
0111970701	0454	11 38 26.82	+03 22 07.10	FF	LW	SW	m	m	t	4.17	1.26	1.35	9.7	40	60	50
0112521001	0428	09 57 53.29	+69 03 48.13	FF	FF	FF	t	t	t	2.17	0.69	0.70	7.4	30	60	60
0112600501	0355	20 46 20.86	−02 48 44.88	FF	LW	LW	m	m	m	4.38	1.23	1.28	7.5	40	60	60
0112850201	0469	11 30 07.03	−14 49 27.13	FF	FF	FF	t	t	t	1.88	0.60	0.60	12.5	35	60	60
0112880101	0565	11 31 55.27	−34 36 27.45	FF	FF	FF	m	m	m	2.07	0.52	0.54	26.8	30	60	60
0124900101	0082	12 31 31.39	+64 14 18.37	FF	FF	FF	t	t	t	2.17	0.61	0.62	25.0	40	60	60
0143430101	0704	07 19 14.52	+65 57 44.28	FF	SW	SW	t	t	t	3.10	0.87	0.89	3.1	35	40	50
0144840101	0602	07 57 01.31	+63 06 02.21	FF	FF	FF	m	m	m	1.64	0.51	0.50	3.8	35	60	60

continued on next page...

... continuation of table A.5

OBSID	Rev.	RA h m s	Dec ° ′ ″	Mode pn	Mode m1	Mode m2	Filter pn	Filter m1	Filter m2	Count rate (cts s^{-1}) pn	Count rate (cts s^{-1}) m1	Count rate (cts s^{-1}) m2	Exp. GTI (ks)	Max. r_{extr} (″) pn	Max. r_{extr} (″) m1	Max. r_{extr} (″) m2
0145800101	0658	12 30 54.12	+11 00 11.27	FF	FF	FF	t	m	m	1.56	0.38	0.38	46.2	40	60	60
0147920601	0539	22 02 01.86	−31 52 10.76	FF	FF	FF	t	t	t	2.02	0.65	0.66	11.5	45	60	60
0152670101	0707	21 57 05.87	−69 41 23.28	FF	SW	SW	m	t	t	4.33	1.34	1.37	14.3	35	40	50
0157360101	0561	13 08 48.19	+21 27 06.73	FF	LW	LW	t	t	t	2.64	0.54	0.56	24.7	35	60	60
0163560101	0743	13 08 48.15	+21 27 06.62	FF	LW	LW	t	t	t	2.68	0.54	0.56	23.4	30	60	60
0164571201	1033	14 08 17.10	−03 46 17.73	FF	FF	FF	t	m	t	1.35	0.40	0.42	18.4	40	60	60
0200470101	0797	08 19 29.00	+70 42 19.24	FF	LW	LW	m	m	m	3.46	1.03	1.03	36.8	35	60	60
0200480101	0915	02 28 15.20	−40 57 14.39	FF	FF	FF	t	t	t	1.72	0.39	0.41	29.2	35	60	60
0200530501	1180	10 56 27.24	+07 00 36.07	LW	FF	FF	m	m	m	1.86	0.49	0.50	21.4	35	60	60
0200960101	0971	09 09 55.90	+54 29 16.86	FF	FF	FF	m	m	m	2.34	0.61	0.61	55.8	35	60	60
0200980101	0879	09 57 53.31	+69 03 48.37	LW	FF	FF	t	t	t	1.73	0.55	0.56	70.8	35	60	60
0202180301	1014	12 42 10.61	+33 17 02.67	FF	LW	LW	t	t	t	5.13	1.34	1.32	9.9	40	60	60
0204040101	0823	13 00 22.17	+28 24 02.91	FF	FF	FF	m	t	t	1.99	0.53	0.54	69.8	40	60	60
0204040301	0841	13 00 22.16	+28 24 02.54	FF	FF	FF	m	t	t	1.49	0.40	0.41	49.1	45	60	60
0205010101	0816	12 20 06.83	+29 16 50.62	FF	FF	FF	t	m	m	1.77	0.48	0.49	23.3	35	60	60
0207130401	0948	14 44 14.67	+06 33 06.73	FF	FF	FF	t	m	m	2.09	0.56	0.56	9.7	50	50	50
0300910301	1068	09 22 47.03	+51 20 37.95	FF	FF	FF	t	t	t	1.85	0.40	0.41	19.1	35	60	60
0301890101	1085	01 05 16.86	−58 26 15.15	FF	LW	LW	m	m	m	4.16	1.04	1.05	86.4	35	60	60
0303340101	1102	01 36 54.46	−35 09 52.17	FF	FF	FF	t	t	t	3.11	0.65	0.66	41.8	35	60	60
0304320301	1016	13 00 22.18	+28 24 02.82	FF	FF	FF	m	t	t	1.44	0.38	0.38	27.7	40	60	60
0304320801	1189	13 00 22.16	+28 24 02.83	FF	FF	FF	m	t	t	2.00	0.53	0.53	32.4	40	60	60
0305900301	1016	13 08 48.16	+21 27 07.21	FF	SW	SW	t	t	t	2.67	0.53	0.54	11.8	35	40	50
0305900401	1025	13 08 48.16	+21 27 06.97	FF	SW	SW	t	t	t	2.64	0.52	0.53	11.5	35	40	50
0305900601	1115	13 08 48.14	+21 27 07.02	FF	SW	SW	t	t	t	2.68	0.53	0.54	14.2	35	40	50

continued on next page...

... continuation of table A.5

OBSID	Rev.	RA	Dec	Mode			Filter			Count rate (cts s^{-1})			Exp. GTI	Max. r_{extr} ($''$)		
		h m s	° ′ ″	pn	m1	m2	pn	m1	m2	pn	m1	m2	(ks)	pn	m1	m2
0414580101	1350	22 02 01.88	−31 52 10.41	FF	LW	LW	T	T	T	3.85	1.31	1.34	30.7	35	60	60
0504480301	1496	14 42 44.41	−00 39 55.83	FF	FF	FF	m	m	m	0.89	0.26	0.30	24.4	35	60	60
0510181701	1528	02 31 55.28	−71 18 07.00	FF	FF	FF	t	m	t	1.59	0.50	0.51	39.8	40	60	60
0553720101	1678	16 15 14.97	−28 37 33.43	FF	LW	LW	m	m	m	2.65	0.96	0.95	41.1	35	60	60
0555020101	1544	12 31 36.54	+70 44 14.41	FF	LW	LW	t	t	t	5.41	1.47	1.48	13.2	35	60	60
0555020201	1558	11 59 41.01	−19 59 24.62	FF	FF	FF	t	t	t	2.17	0.61	0.62	24.1	35	60	60
0556030101	1670	12 56 11.16	−05 47 21.90	FF	LW	LW	t	t	t	5.08	1.49	1.46	19.0	35	60	60
0601780201	1837	11 13 49.75	+09 35 10.72	FF	FF	FF	m	m	m	1.92	0.55	0.52	13.0	35	60	60
0601781701	1825	11 09 41.58	−03 39 26.95	FF	FF	FF	m	m	m	1.90	0.49	0.50	9.4	35	60	60
0650790101	1957	04 26 20.80	+15 37 05.82	FF	LW	LW	T	T	T	3.16	0.85	0.85	29.2	40	60	60
0652330101	2027	08 36 56.21	−78 56 45.65	FF	LW	FF	m	T	m	2.20	0.46	0.55	30.1	40	60	60
0654650301	2007	12 13 45.27	+36 37 54.59	FF	FF	FF	m	m	m	1.73	0.55	0.56	9.3	35	60	60
0673580101	2126	13 25 19.35	−38 24 52.72	FF	LW	LW	t	t	t	3.04	0.66	0.64	64.9	35	60	60
0690870101	2493	02 34 37.84	−08 47 16.14	FF	FF	FF	t	t	t	1.91	0.58	0.57	16.6	40	60	60
0693781501	2417	05 16 11.41	−00 08 59.20	SW	SW	SW	m	m	m	14.44	4.14	4.14	93.3	35	40	50
0721790101	2557	22 18 32.76	+19 25 20.23	FF	FF	FF	t	t	t	1.52	0.43	0.42	27.9	40	60	60
0722480201	2747	12 48 15.23	+17 46 26.48	SW	SW	SW	t	t	t	16.30	2.65	2.52	26.7	40	40	50
0724431101	2542	21 07 58.15	−05 17 42.12	SW	SW	SW	t	t	t	3.52	0.68	0.70	34.4	35	35	50
0727760201	2618	18 56 36.02	−37 54 37.58	SW	LW	LW	t	t	t	5.41	1.07	0.98	61.1	60	60	60
0727760401	2794	18 56 36.08	−37 54 37.11	SW	LW	LW	t	t	t	5.44	1.07	0.99	60.1	60	60	60
0727760601	2977	18 56 36.13	−37 54 37.10	SW	LW	LW	t	t	t	5.45	1.03	0.95	36.6	60	60	60
0727780401	3057	15 55 43.05	+11 11 24.34	SW	SW	SW	m	m	m	14.97	3.67	3.54	27.5	35	40	50
0740590101	2743	21 31 01.88	+23 20 05.61	SW	LW	LW	m	m	m	5.16	1.27	1.23	39.8	35	60	60
0743830601	2771	02 34 37.83	−08 47 16.21	SW	SW	SW	t	t	t	14.22	3.61	3.55	100.2	45	45	35
0761510201	2900	08 01 01.41	+18 48 40.79	FF	FF	FF	t	t	t	1.84	0.35	0.39	21.4	35	60	60

Table A.6: Exposures excluded from observations (listed with their observation ID: OBSID) in the new sample.

OBSID	excluded exposures
0029340101	mos1U002, mos2U002
0061540101	mos1U002, mos2U002
0114090101	mos1S001, mos2S003
0200960101	mos1U002, mos2U002, pnU014
0400200101	mos1U002, mos2U002
0414580101	mos1S005, mos2S006, pnS002
0653380201	mos1U002
0672130701	mos1U002, mos2U002, pnU014
0673730101	mos1U004, mos2U004
0694170101	mos1U003, mos2U003
0720111101	mos1S001, mos2S002
0744450401	mos1S001, mos1S012, mos1S014, mos2S002, mos2S013, mos2S015, pnS011, pnS016
0764010101	mos1S001, mos2S002
0792180301	mos1U003, mos1U004, mos2U003, mos2U004, pnU014

Table A.7: Calculation of the X-ray-to-optical flux ratio for the point sources in the G96.0+2.0 FOV. The X-ray flux was determined in two ways, with WebPIMMS based on the count rate of the detector with the maximum detection likelihood and for those sources which had enough counts for spectral fitting also in Xspec with `cflux`. For sources #3, #15, #16, #20 and #21, two optical counterparts were found, respectively. No according counterparts were found for sources #4, #5, #10 and #12 and they are, thus, not included.

				WebPIMMS		`cflux`	
Source ID	Optical magnitude[1]	Detector used	Count rate[2] (10^{-3} cts s^{-1})	0.3–3.5 keV flux (erg cm^{-2} s^{-1})	$\log(f_x/f_{opt})$	0.3–3.5 keV flux (erg cm^{-2} s^{-1})	$\log(f_x/f_{opt})$
1	12.913	MOS2	13.54±0.76	$(1.299\pm0.073)\times10^{-13}$	-2.35 ± 0.02	$(7.315^{+0.502}_{-0.491})\times10^{-14}$	$-2.60^{+0.03}_{-0.03}$
2	9.803	pn	62.22±2.68	$(2.132\pm0.092)\times10^{-13}$	-3.38 ± 0.02	$(7.663^{+0.540}_{-0.534})\times10^{-14}$	$-3.82^{+0.03}_{-0.03}$
3	16.134	pn	6.22±0.62	$(2.131\pm0.212)\times10^{-14}$	-1.85 ± 0.04	$(7.838^{+1.646}_{-1.528})\times10^{-15}$	$-2.28^{+0.09}_{-0.08}$
	20.065				-0.28 ± 0.04		$-0.71^{+0.09}_{-0.08}$
6	17.569	MOS1	7.80±0.21	$(7.482\pm2.014)\times10^{-15}$	-1.73 ± 0.12		
7	17.959	pn	3.26±0.59	$(1.117\pm0.202)\times10^{-14}$	-1.40 ± 0.08	$(4.552^{+1.432}_{-1.433})\times10^{-15}$	$-1.79^{+0.14}_{-0.14}$
8	18.362	MOS2	1.02±0.24	$(9.785\pm2.302)\times10^{-15}$	-1.29 ± 0.10		
9	19.091	pn	1.91±0.46	$(6.545\pm1.576)\times10^{-15}$	-1.18 ± 0.10		
11	15.549	pn	8.14±1.09	$(2.789\pm0.374)\times10^{-14}$	-1.96 ± 0.06	$(1.140^{+0.366}_{-0.351})\times10^{-14}$	$-2.35^{+0.14}_{-0.13}$
13	17.058	pn	5.98±1.06	$(2.049\pm0.363)\times10^{-14}$	-1.50 ± 0.08	$(9.895^{+2.323}_{-2.378})\times10^{-15}$	$-1.81^{+0.10}_{-0.10}$
14	8.331	pn	15.40±2.15	$(5.277\pm0.737)\times10^{-14}$	-4.58 ± 0.06	$(4.614^{+1.467}_{-1.467})\times10^{-14}$	$-4.63^{+0.14}_{-0.14}$
15	17.777	pn	3.54±0.61	$(1.213\pm0.209)\times10^{-14}$	-1.44 ± 0.07		
	9.285	pn			-4.83 ± 0.07		
16	20.011	pn	2.25±0.54	$(7.710\pm1.850)\times10^{-15}$	-0.74 ± 0.10		
	14.897	pn			-2.78 ± 0.10		
17	10.985	pn	3.08±0.80	$(1.055\pm0.274)\times10^{-14}$	-4.21 ± 0.11		
18	11.764	pn	4.43±1.07	$(1.518\pm0.367)\times10^{-14}$	-3.74 ± 0.10		
19	10.252	pn	1.79±0.48	$(6.134\pm1.645)\times10^{-15}$	-4.74 ± 0.12		
20	16.502	pn	6.50±1.45	$(2.227\pm0.497)\times10^{-14}$	-1.68 ± 0.10		
	20.714	pn			0.00 ± 0.10		
21	18.478	pn	2.46±0.65	$(8.430\pm2.227)\times10^{-15}$	-1.31 ± 0.11		
	14.562	pn			-2.88 ± 0.11		
22	18.093	pn	5.07±1.34	$(1.737\pm0.459)\times10^{-14}$	-1.15 ± 0.11		

[1] in the Gaia (Gaia Collaboration et al., 2016) G-band, ∼330–1050 nm (Weiler, 2018)
[2] as determined by the Xspec task `edetect_chain` in the 0.4–3.0 keV range for the detector with the maximum detection likelihood

Table A.8: Hardness ratios for the point sources in the G96.0+2.0 FOV. The count rates were determined with the XSPEC task `edetect_chain` for the detector which had the maximum detection likelihood in the 0.4–3.0 keV source detection. Source #14, #20 and #22 are missing as they were not detected in the `edetect_chain` runs with the energy bands used here.

Source ID	Detector used	Count rate 0.4–2.0 keV (10^{-3} cts s^{-1})	Count rate 2.0–4.5 keV (10^{-3} cts s^{-1})	Count rate 4.5–10.0 keV (10^{-3} cts s^{-1})	$HR1$[1]	$HR2$[1]
1	MOS2	13.785±0.774	1.313±0.252	0.047±0.101	−0.83±0.08	−0.93±0.29
2	pn	61.584±2.648	0.537±0.499	0.000±0.635	−0.98±0.06	–
3	pn	6.153±0.595	0.667±0.265	0.274±0.242	−0.80±0.15	−0.42±0.99
4	pn	3.255±0.563	4.807±0.606	3.453±0.613	0.19±0.54	−0.16±0.65
5	MOS2	4.501±0.708	7.062±0.869	1.785±0.641	0.22±0.45	−0.60±0.24
6	MOS1	0.759±0.204	0.020±0.057	0.120±0.094	−0.95±0.40	−0.71±1.36
7	pn	3.009±0.549	0.489±0.288	0.000±0.148	−0.72±0.30	–
8	MOS2	0.748±0.206	0.551±0.167	0.164±0.113	−0.15±1.36	−0.54±0.59
9	pn	1.218±0.388	1.479±0.564	0.587±0.323	0.10±2.04	−0.43±0.59
10	MOS1	6.013±4.622	0.950±0.878	0.784±1.283	−0.73±1.15	−0.10±9.41
11	pn	7.589±1.026	1.479±0.564	0.858±0.751	−0.67±0.23	−0.27±1.57
12	MOS2	0.440±0.231	0.420±0.190	0.187±0.137	−0.02±14.92	−0.38±1.08
13	pn	6.250±1.063	0.000±0.137	0.000±0.427	–	–
15	pn	3.358±0.571	0.156±0.210	0.000±0.209	−0.91±0.26	–
16	pn	1.828±0.478	0.602±0.311	0.000±0.112	−0.50±0.52	–
17	pn	2.971±0.756	0.166±0.272	0.000±0.243	−0.89±0.38	–
18	pn	4.395±0.996	0.154±0.416	0.000±1.218	−0.93±0.35	–
19	pn	1.907±0.461	0.000±0.061	0.000±0.105	–	–
21	pn	1.919±0.565	0.511±0.385	0.009±0.256	−0.58±0.56	−0.97±1.28

[1] $HR1$ compares the 0.4–2.0 keV and 2.0–4.5 keV bands, $HR2$ the 2.0–4.5 keV and 4.5–10.0 keV bands

APPENDIX B

Additional Figures

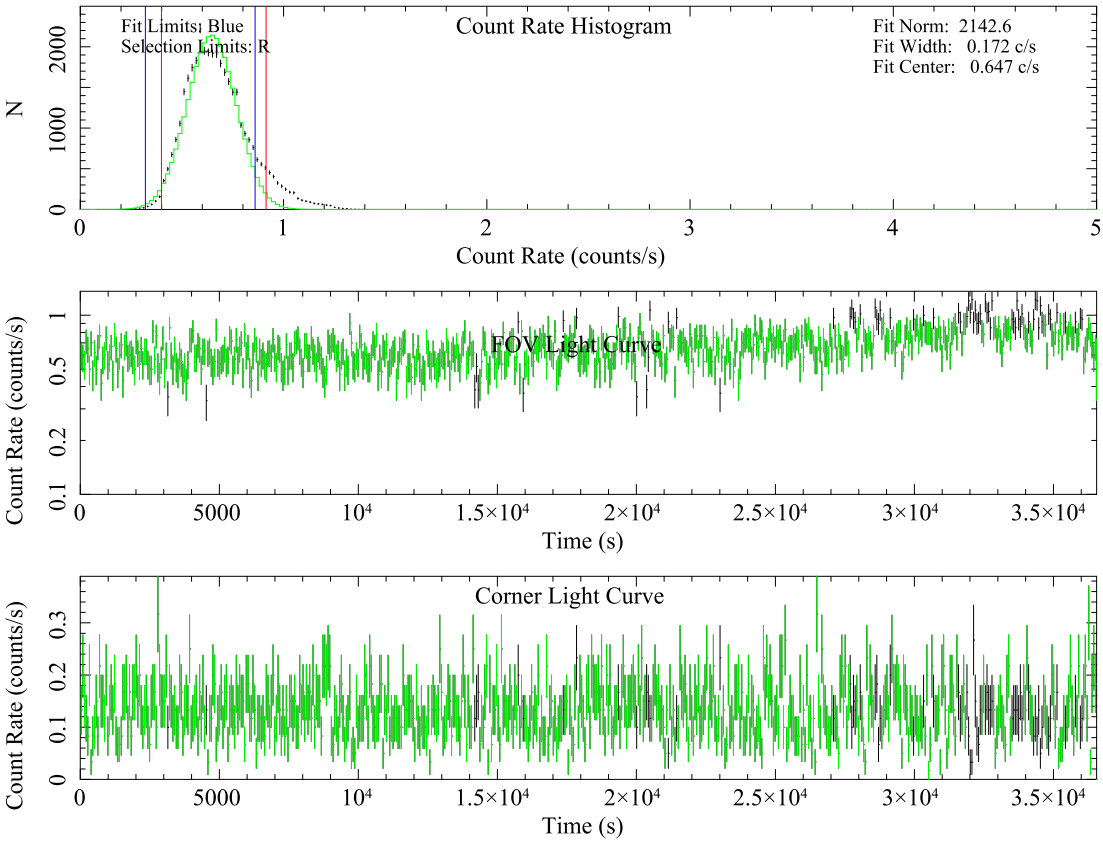

Figure B.1: ESAS temporal filtering result for the MOS1 data of G96.0+2.0. *Top panel*: histogram for the FOV light curve in the 2.5–8.5 keV energy band, showing the distribution of the count rate with the number N of occurrences; *Middle panel*: FOV light curve in the 2.5–8.5 keV energy band; *Bottom panel*: light curve from the detector corners in the 2.5–8.5 keV energy band. The green data were kept by the filtering algorithm for further analysis, the black data were excluded.

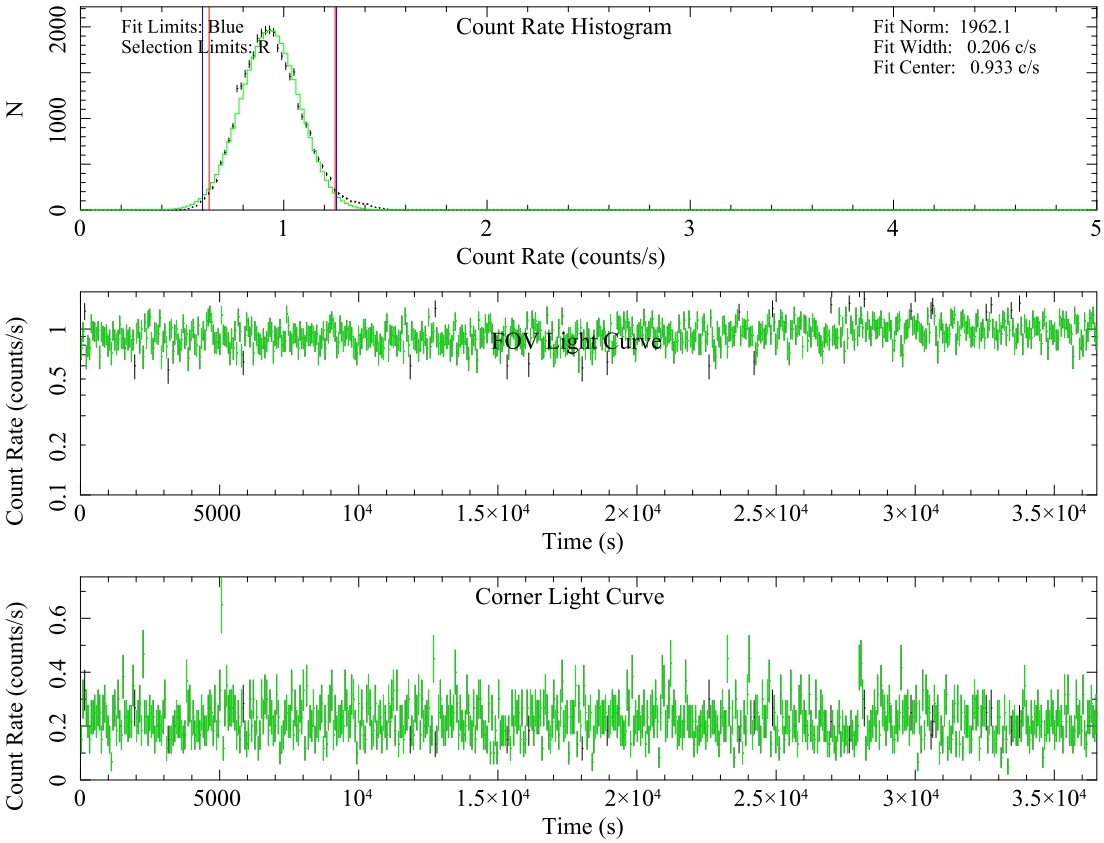

Figure B.2: ESAS temporal filtering result for the MOS2 data of G96.0+2.0. *Top panel*: histogram for the FOV light curve in the 2.5–8.5 keV energy band, showing the distribution of the count rate with the number N of occurrences; *Middle panel*: FOV light curve in the 2.5–8.5 keV energy band; *Bottom panel*: light curve from the detector corners in the 2.5–8.5 keV energy band. The green data were kept by the filtering algorithm for further analysis, the black data were excluded.

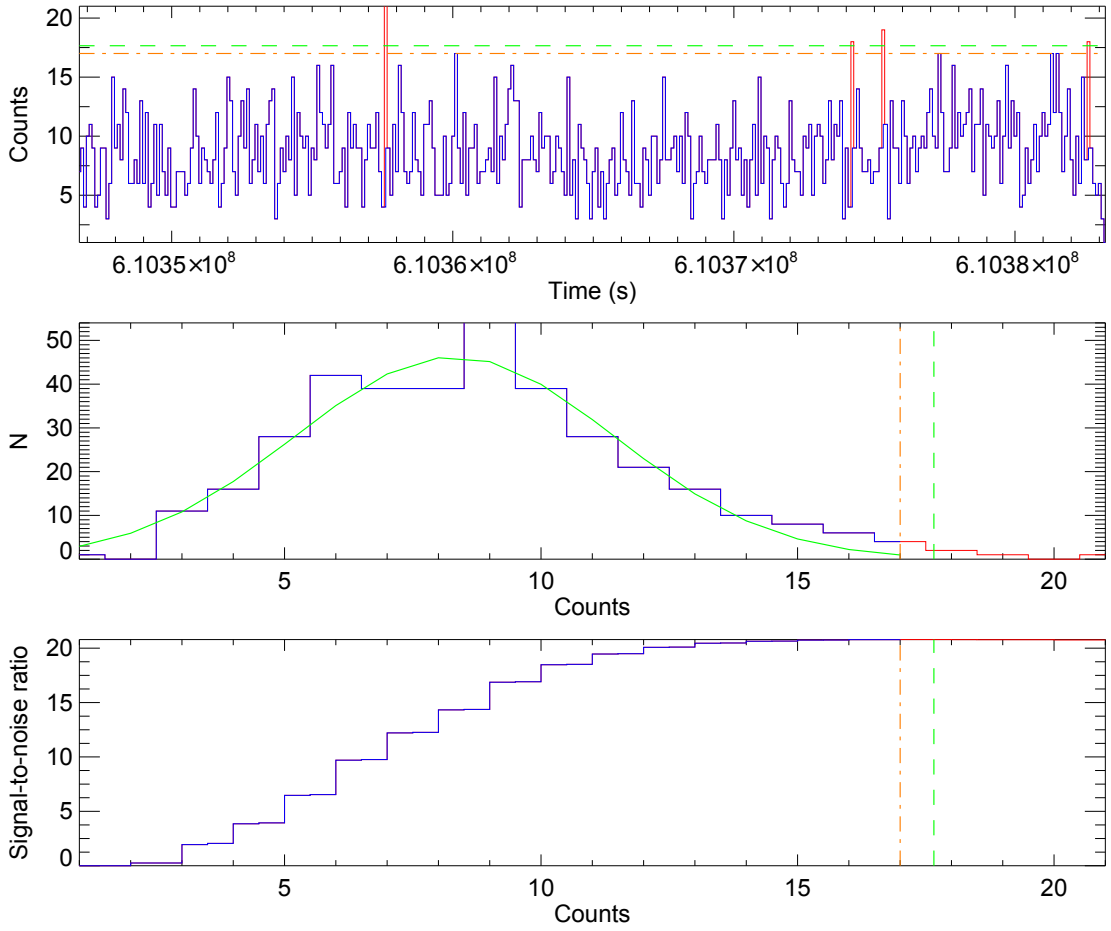

Figure B.3: Screening for soft proton flares in the MOS1 data of G96.0+2.0. *Top panel*: light curve for energies > 10.0 keV with a binning of 100 s; *Middle panel*: histogram for the light curve with energies > 10.0 keV, showing the distribution of counts with the number N of occurrences; *Bottom panel*: S/N for energies > 10.0 keV. The green, dashed line shows the Gaussian threshold at three times sigma above the mean value. The orange, dash-dotted line indicates the threshold set by the maximum S/N. The more conservative of the thresholds, in this case the S/N threshold, is selected to decide which data to keep (blue) and which data to reject (red) for further analysis.

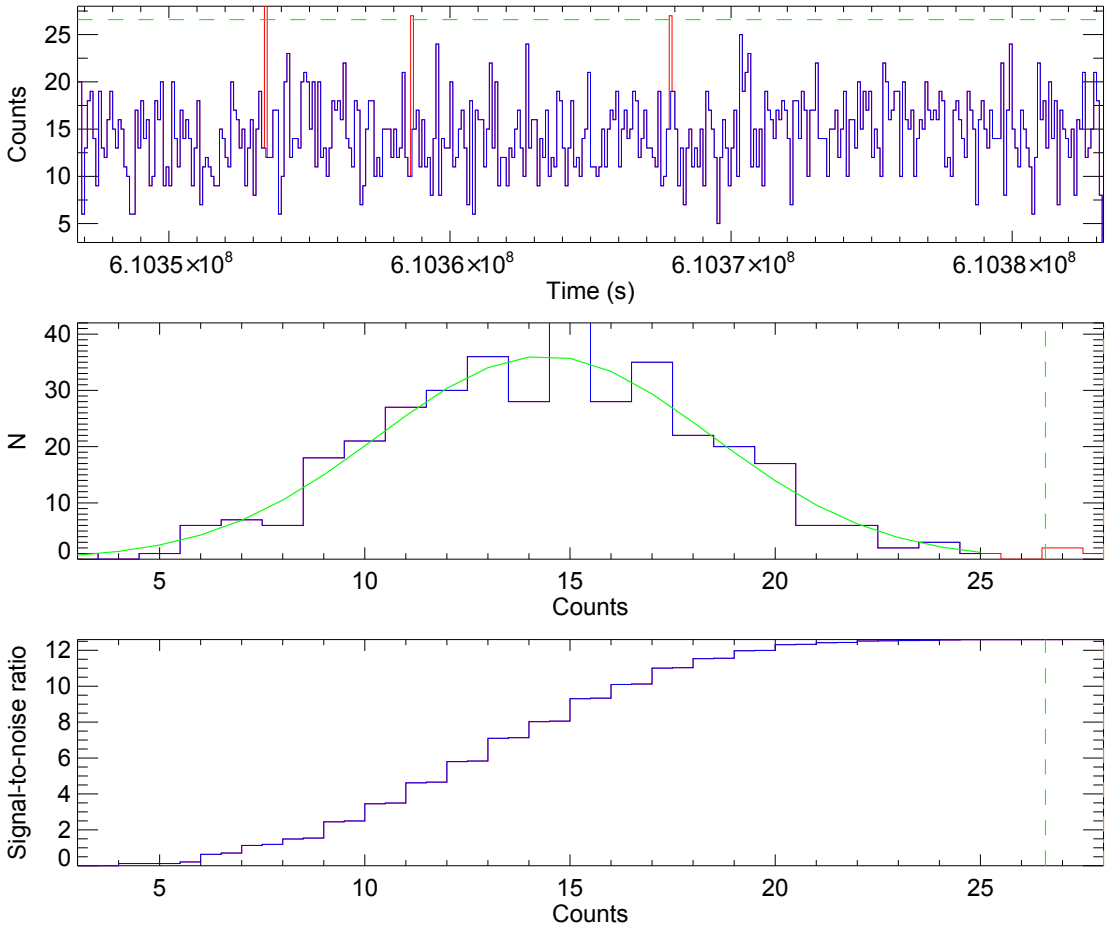

Figure B.4: Screening for soft proton flares in the MOS2 data of G96.0+2.0. *Top panel*: light curve for energies > 10.0 keV with a binning of 100 s; *Middle panel*: histogram for the light curve with energies > 10.0 keV, showing the distribution of counts with the number N of occurrences; *Bottom panel*: S/N for energies > 10.0 keV. The green, dashed line shows the Gaussian threshold at three times sigma above the mean value. The orange, dash-dotted line indicates the threshold set by the maximum S/N. The more conservative of the thresholds, in this case the Gaussian threshold, is selected to decide which data to keep (blue) and which data to reject (red) for further analysis.

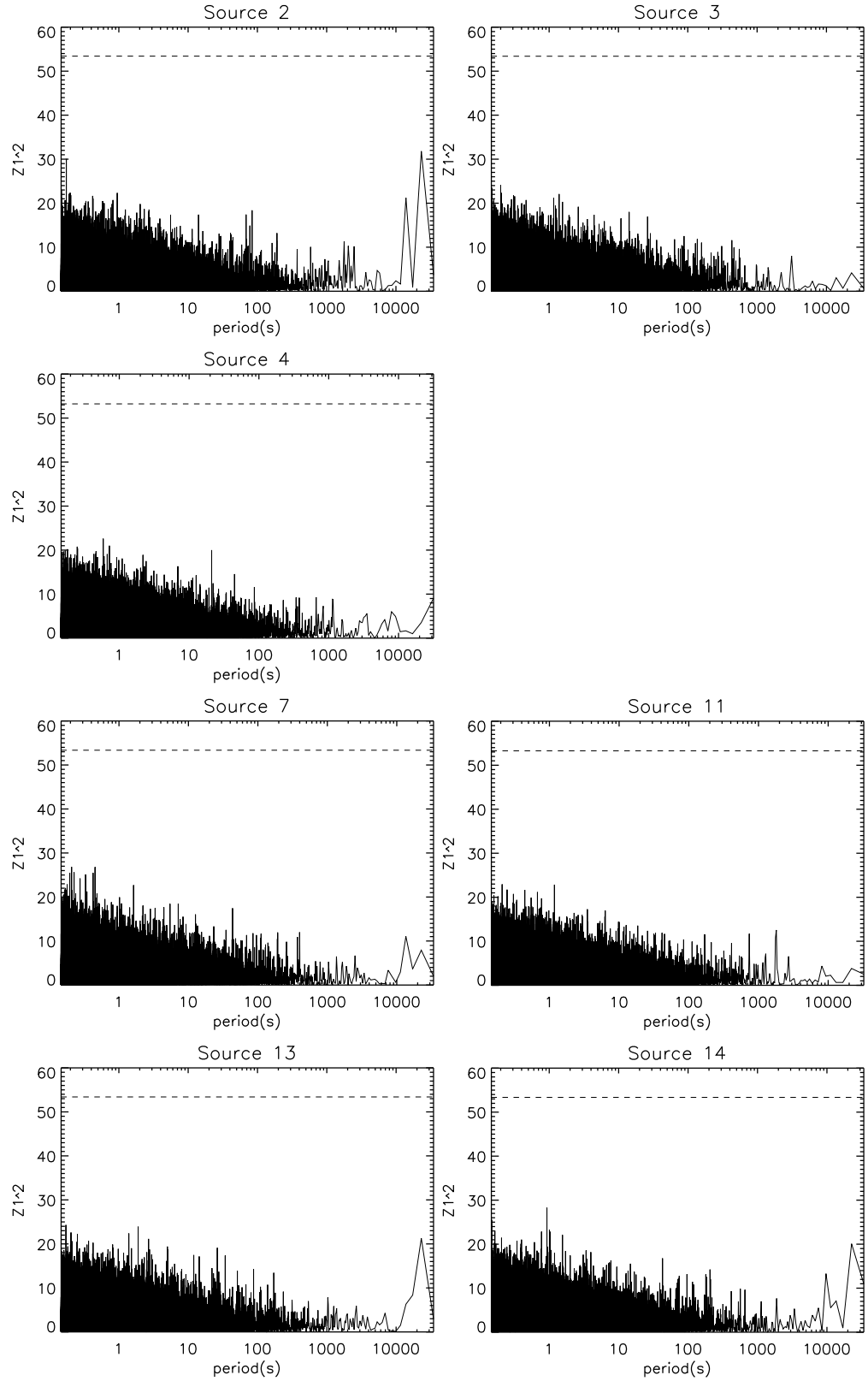

Figure B.5: Z_m^2 test with one harmonic for seven of the eight remaining sources with more than 90 EPIC counts in the G96.0+2.0 FOV. Source #5 is missing as it was not covered by the pn detector. The dashed lines indicate the 5σ significance level.

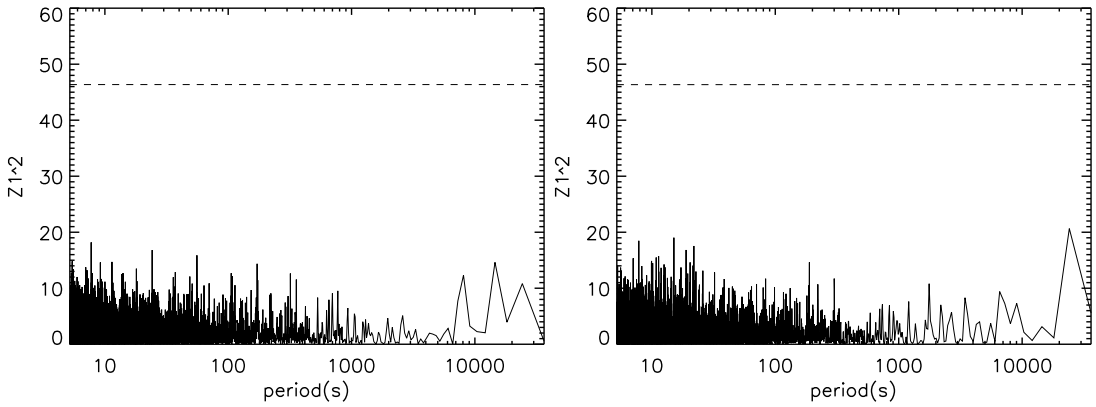

Figure B.6: Z_m^2 test with one harmonic for source #5 based on the MOS data (left: MOS1, right: MOS2). The dashed lines indicate the 5σ significance level.

Acknowledgements

Working on this thesis and on the presented projects has been a profound journey and I would like to say a big thank you to everyone who has supported me in one way or another over the past years. My special thanks go to...

... Prof. Dott. Andrea Santangelo for welcoming me to his group, for supervising this work and for his contagious dedication to science. Thank you, Andrea, for having given me this opportunity to work on such interesting research projects and to learn so much. Thank you for your guidance, for a great time at the institute and for always having been so encouraging, supportive and understanding.

... Dr. Jan-Christoph Tenzer for his big support with this work and for his patience as the go-to person for many different matters. Thank you, Chris, for all your help and advice, for the amazing trips to conferences, for taking the trouble of dealing with bureaucracy a lot and for organizing the BBQs, ice cream and sailing.

... Dr. Victor Doroshenko for his interesting topic suggestions, tips and advice concerning the analysis of compact objects. Thank you, Victor, for your constructive feedback, for contributing your knowledge and ideas and for always being available for questions.

... Michael Smith for entrusting me with this important calibration topic and for all his help with it. Thank you, Michael, for all the effort and time you put into the project, for your contribution and many replies and for the productive and enjoyable meetings at ESAC.

... Dr. Martin Stuhlinger for his calibration-related contribution to this work. Thank you, Martin, for your big help, particularly with the pile-up issue, and for a great time at conferences and during my trips to Madrid.

... Dr. Sara Saeedi for her support concerning data analysis and for having been a great friend all these years. Thank you, Sarah, for sharing your knowledge, for the warm atmosphere in the office and for all the fun and the many joyful moments.

... Christian Pommranz for carrying on "our" calibration project and for his help with the final steps regarding this thesis. Thank you, Christian, for the effective teamwork and for making a smooth handover possible.

... the colleagues at the XMM-Newton EPIC Calibration and Operations Meeting and the IACHEC members for the friendly welcome, for taking an interest in the topic and for the helpful discussions and suggestions. In particular, I wish to thank Lucia Ballo, Jacobo Ebrero and Ivan Valtchanov for their help with the image screening, Matteo Guainazzi for preparing the ground for this calibration work and for providing initial information and Peter and Bärbel Kretschmar for their hospitality and friendship.

... all colleagues at the IAAT for the general helpfulness and the friendly atmosphere. Thank you, in particular, to my office mates for making the everyday office life so pleasant and to everyone who has made the lunch and coffee breaks, the dinners and the evenings/nights at the telescope so much fun. Also, thank you for the great teamwork to all fellow team members participating in the organization of public events, especially the annual Children's University Research Day.

... my long-time university friends Carola, Büsra and Hannah for the emotional support and for the relaxing diversion.

... all my family and friends for their patience every time I was "too busy" again.

... my sister and brother, my brother- and sister-in-law and my nieces for enriching every day.

... my parents for our wonderful family life and their endless love and support, without which this work would not exist and for which I am grateful beyond words.
Danke, Mama & Papa - für alles!

This work was partially supported by the Bundesministerium für Wirtschaft und Energie through Deutsches Zentrum für Luft- und Raumfahrt (DLR, grants FKZ 50 OG 1902 and 50 OG 1602).

This work is based on observations obtained with XMM-Newton, an ESA science mission with instruments and contributions directly funded by ESA Member States and NASA. This research has made use of data obtained from the 3XMM and 4XMM XMM-Newton Serendipitous Source Catalogues compiled by the 10 institutes of the XMM-Newton Survey Science Centre selected by ESA. This research has made use of the XMM-Newton Science Analysis Software (SAS) provided by the XMM-Newton Science Operations Centre (SOC) and of the XMM-Newton Extended Source Analysis Software (ESAS) developed at the NASA/GSFC XMM-Newton Guest Observer Facility (GOF) in cooperation with the XMM-Newton SOC. This research has made use of the SAOImage DS9 tool developed at the Smithsonian Astrophysical Observatory. This research has made use of data, software and web tools obtained from the High Energy Astrophysics Science Archive Research Center (HEASARC), a service of the Astrophysics Science Division at NASA/GSFC and of the Smithsonian Astrophysical Observatory's High Energy Astrophysics Division. This research has made use of the SIMBAD database, VizieR catalogue access tool and cross-match service provided by and operated at CDS, Strasbourg, France. This research has made use of NASA's Astrophysics Data System Bibliographic Services.